The Effect of High Pressure on Structural Oddities

Russell D. L. Johnstone

A thesis submitted in fulfilment of the requirements for the degree of Doctor of Philosophy to the School of Chemistry, University of Edinburgh

September 2009

Declaration

I declare that this thesis was written by me and that the work detailed in this thesis is my own, or I have contributed substantially to such work, except where specific reference is made to the work of another.

Russell. D. L. Johnstone

Abstract

This thesis describes the effect of pressure on crystal structures that are in some way unusual. The aim was to investigate whether pressure could be used to force these 'structural oddities' to conform to more conventional behaviour. In many cases pressure-induced phase transitions were observed, and the driving forces of these are considered.

L-serine monohydrate crystallises with layers of hydrogen bonded serine molecules. Layers are linked together by H-bonds from the donor atoms of water molecules. The orientation of the water molecules between the layers is uncommon for other layered hydrates in the CSD. A single crystal of serine hydrate undergoes a pressure-induced phase transition at 5 GPa, which is characterised by a rotation of the water molecules to an orientation which is more frequently observed. PIXEL calculations show that the transition is driven by the *PV* term in the equation $G = U - TS + PV$. An attempt to reproduce the transition in another layered hydrate with a similar topology was partially successful in the compression of S-4-sulfo-L-phenylalanine monohydrate, which undergoes a similar phase transition at 1 GPa.

Methyl 2-(9H-carbazol-9-yl)benzoate crystallises unusually with eight molecules in the asymmetric unit ($Z' = 8$). Compression of a single crystal results in a phase transition at *ca*. 5 GPa to give a $Z' = 2$ polymorph. The *PV* term is an important contributor to the driving force of the transition. The geometries of the molecules in phase-II are significantly less stable than in phase-I, and as pressure is released on phase-II the need to adopt a more stable molecular conformation eventually outweighs the *PV* advantage. The $Z' = 8$ structure is eventually re-established at 4.6 GPa. This work illustrates how low Z' polymorphs of the same structure are not always the thermodynamically more stable forms.

When recrystallised *in situ* from a 4:1 by volume solution of methanol and ethanol, a new polymorph of salicylamide is obtained at 0.2 GPa. The ambient pressure phase appears in the CSD to contain a number of abnormally short H…H contacts. We find this model to be incorrect, and have re-determined the structure to find no short H…H contacts. PIXEL and DFT calculations indicate that the high-pressure polymorph is favoured over the ambient phase by the *PV* term, the zero point energy and entropy. Low completeness that often occurs as a result of shading from the high-pressure cell was improved by the inclusion of multiple crystals within the sample chamber.

Bianthrone changes colour from yellow to green on grinding, though this does not occur when subjected to hydrostatic pressure to 6.5 GPa. There is, however, a subtle colour change from bright yellow to dark orange as pressure is applied, and it is likely that this is caused by changes in the π-π stacking distances. This work highlights how a system can react differently to hydrostatic and non-hydrostatic conditions.

Dedication

This thesis is dedicated to George Scott Johnstone, a brilliant geologist and grandfather. Thank you for (unknowingly) convincing me to undertake this PhD.

Acknowledgements

First of all, I would like to thank Professor Simon Parsons for giving me the opportunity to do this PhD. I have thoroughly enjoyed working for you over the past three years. Thank you also for teaching me about the finer things in life, like dessert wine, whisky and ridiculously posh tea.

Thanks to the Parsons group which has changed beyond recognition over the past three years. You have given me some incredible memories. In particular, I would like to acknowledge Stephen Moggach, Pete Wood and Fraser White for their invaluable help with practical work, theory and computers.

I express my gratitude to the EPSRC and the CCDC for sponsorship. Thanks especially to Elna Pidcock (my boss at the CCDC) who has been a great help with project suggestions and proof reading.

Thanks to the STFC for provision of synchrotron and INS beam time, and also to the EastCHEM Research Computing Facility for access to software and computing facilities.

I would also like to show my appreciation to Stuart Parker for collection of the INS data in Chapter 5.

Thank you so much to family, you were, as always, extremely supportive and helpful. I know you still find it hard to believe that I am actually doing this PhD. Thanks also to the Poddar family for their much valued support and encouragement.

Finally, I would like to say a huge thank you to my wife Anita, you have the patience of a saint. I am sorry for being a big grump over the last couple of months, hopefully I will never have to write a thesis again!

Abbreviations

ADP	Anisotropic displacement parameters
BTM	Betaine monohydrate
CAM	L-Cysteic acid monohydrate
CCD	Charge-coupled device
CCDC	Cambridge Crystallographic Data Centre
CSD	Cambridge Structural Database
DAC	Diamond anvil cell
DFT	Density functional theory
EOS	Equation of state
EPSRC	Engineering and Physical Sciences Research Council
GPa	Gigapascal
INS	Inelastic neutron scattering
IR	Infrared
NMR	Nuclear magnetic resonance
RMS	Root mean square
SPM	S-4-Sulfo-L-phenylalanine monohydrate
STFC	Science and Technology Facilities Council
TiZr	Titanium-Zirconium
WC	Tungsten carbide
X-N	X-ray-Neutron
ZPE	Zero point energy

Contents

Chapter 1

Introduction

1.1 High-Pressure Crystallography

Crystallographic data recorded on molecular compounds at high pressure (1000's of atmospheres) are at present very limited by comparison with the volume of data available at non-ambient temperatures. The current version of the Cambridge Structural Database (Macrae *et al.*, 2008) contains 453 entries which feature the word 'pressure' (excluding 'blood pressure'). Although this number is small in comparison to the total number of entries in the CSD (483,021 in May 2009), it has quadrupled since 2003 (114 entries) (Dawson, 2003). This recent rise reflects the growing interest and expertise in the area of high-pressure crystallography, though advances in technology, computer software and the accessibility of synchrotron sources have contributed considerably.

A range of systems has now been studied at pressure, including amino acids (Moggach, Parsons *et al.*, 2008), pharmaceuticals (Fabbiani & Pulham, 2006), and transition metal complexes (Moggach & Parsons, 2009a). Polymeric structures have been examined (Boldyreva *et al.*, 2006), but the overwhelming majority of studies have focused on molecular compounds (404 out of the 453 entries). The attraction of studying simple organic systems is also evident from the data (333 out of the 404 entries).

The work presented in this thesis focuses on the effect of pressure on organic molecular single crystal structures which appear in some way to be anomalous. The aim is to investigate whether pressure can be used to force these 'structural oddities' to conform to more conventional behaviour. In addition to this, the driving forces behind pressure-induced phase transitions for a number of the featured compounds are explored in some detail.

1.1.1 High-pressure equipment

The standard tool for high pressure crystallography is the diamond anvil cell (DAC), which comprises two vertically opposed gem-quality diamond anvils, a metal gasket (typically made of tungsten, steel or rhenium) and some means for supporting them (Figure 1.1a). A hole (usually 200-300 μm in diameter) is drilled in the centre of the gasket by spark erosion to provide a small cylindrical sample

chamber, which is sealed shut by the flat faces (culets) of the two opposing diamonds. Pressure can then be applied to the sample within the chamber by the application of force in the directions of the arrows shown in Figure 1.1a.

For the application of hydrostatic pressure to a single crystal, the Merrill Bassett design of DAC (Merrill & Bassett, 1974) (Figure 1.1b) is most commonly used. The cell is suitable for a range of techniques including X-ray diffraction and Raman spectroscopy.

In Merrill and Bassett's original design, beryllium backing disks are employed to provide support to the diamond anvils as pressure is applied. A more recent design of cell employs conically ground tungsten carbide backing disks (see below). Each backing disc has a hole at its centre, forming a window for optical observation of the sample. The backing discs are held in position by two steel plates, and can be shifted laterally by the tightening of three grub screws to enable alignment of the diamond faces with each other. Each plate has a conical hole at its centre (half-opening angle typically 40˚) to allow the transmission of X-rays to and from the sample. Pressure is applied via the tightening of three Allen screws (Figure 1.1b) which force the two steel plates together.

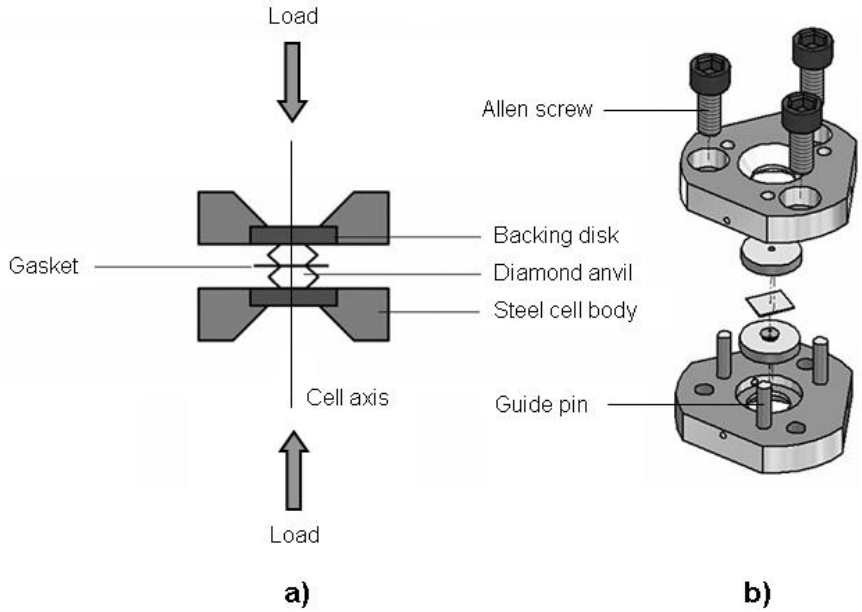

Figure 1.1: a) The basic components of a diamond anvil cell (DAC). b) The Merrill Bassett design. Figure taken from Moggach, Parsons *et al.* (2008).

The whole assembly is small enough to be placed on a standard diffractometer (Figure 1.2a). However, prior to this, the cell must be super-glued to a small metal table which can then be attached to a standard goniometer head (Figure 1.2b).

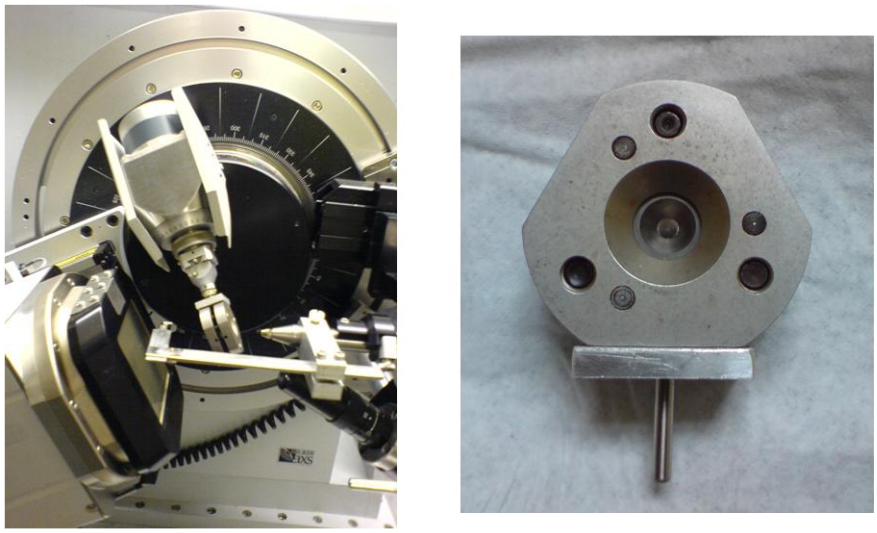

a) b)

Figure 1.2: The Merrill Bassett DAC a) mounted on the Bruker-Nonius APEX-II diffractometer on station 9.8 at the STFC synchrotron facility in Daresbury, b) attached to the mounting table prior to data collection.

1.1.2 The sample

In the majority of cases described in this thesis a crystal was grown under ambient conditions, mounted in the pressure cell and diffraction data collected at a series of increasing pressures. In order to prevent the sample from crushing upon tightening of the screws, a hydrostatic medium must be included in the sample chamber. A popular medium consists of a 16:3:1 by volume mix of methanol, ethanol and water, which remains fluid up to *ca.* 10 GPa (Miletich *et al.*, 2000). Other common hydrostatic media are given in Table 1.1. Gases (shown in bold in Table 1.1) can be used for pressures > 10 GPa; these materials crystallise at fairly low pressures, but their low-shear strengths mean that conditions are hydrostatic well beyond these limits. However, gases are relatively troublesome to load into a pressure cell.

Medium	Maximum GPa of (quasi) hydrostaticity
Silicon oil	< 2.0
Water	2.5
Isopropyl alcohol	4.3
Glycerine:water (3:2)	5.3
Petroleum ether	6
Pentane:isopentane (1:1)	7.4
Methanol	8.6
Methanol:ethanol (4:1)	10.4
Methanol:ethanol:water (16:3:1)	14.5
Hydrogen	177
Helium	60-70
Neon	16
Argon	9
Xenon	55
Nitrogen	13

Table 1.1: Some common pressure-transmitting media. Data taken from Miletich *et al.* (2000).

A small ruby chip is also included in the sample chamber. Ruby has a fluorescence transition, the frequency of which is dependent on pressure. Measurement of the ruby fluorescence lines therefore enables the pressure inside the cell to be determined (Piermarini *et al.*, 1975).

An alternative method to studying crystals grown at ambient conditions is to crystallise *in situ* at pressure. If the compound of interest is a liquid at or near ambient temperature, the liquid sample can be first frozen by application of pressure, and then redissolved by heating to leave a crystal as the cell cools. Examples of compounds studied by this method are methanol (Allan *et al.*, 1998), ethanol, acetic acid (Allan & Clark, 1999) and acetone (Allan *et al.*, 1999). In each case new high-pressure phases were formed.

The method just described is applicable only to relatively simple molecular compounds: more complex compounds melt at too high a temperature for the method to be feasible. Instead, a saturated solution of the material is loaded into the DAC and pressure is applied to the liquid in order to induce crystallisation. The resulting polycrystalline material is then melted back to a small seed crystallite, which is

allowed to grow into a single crystal upon cooling. This method was used to induce a new solvate of paracetamol at 0.62 GPa (Fabbiani *et al.*, 2003), and in this thesis, a new polymorph of salicylamide was formed at 0.2 GPa when recrystallised from a 4:1 by volume mix of methanol: ethanol (see chapter 5).

1.1.3 Data collection and processing

All high-pressure data in this thesis were collected on a three-circle Bruker-Nonius APEX-II diffractometer (Figure 1.2a) which employs a CCD detector, and has a fixed value of χ at 54.75˚.

The restricted view of the sample caused by the body of the high-pressure cell presents many problems, and one of them is centring of the cell on the diffractometer. An initial approximate method is to align the sample optically. It is important to be able to focus the telescope or video camera during the procedure because the diamonds act as lenses which displace the image of the sample. This method works well for centring the sample in the directions perpendicular to the cell axis (Figure 1.1a). In the direction parallel to the cell axis, the sample is obscured by the gasket, but the cell can be approximately centred by ensuring that images viewed from either side of the cell are both in focus. A more accurate way to centre in this direction is to acquire two images of the direct beam through the sample at two separate values of ω which are equal in magnitude and opposite in sign (usually 25° and -25°). If the sample is properly centred, then subtraction of the two images will result in pixel values of zero at the position of the direct beam. Details of this procedure are given in Dawson *et al.* (2004). Note that this procedure centres the gasket hole rather than the sample itself.

During data collection, the sample can be obscured by the cell body from *i*) the detector or *ii*) the X-ray beam, and this places restrictions on the values of ω and φ that can be used in a collection strategy. A typical strategy used for high-pressure data collection for a DAC with half opening angle of 40˚ is given in Table 1.2. Similar strategies were used for high-pressure data throughout this thesis. The sequence consists of eight runs of 0.3˚ ω scans which are chosen to ensure the angle

between the incident beam and the cell axis is never more than 40˚, and that no more than 80% of the detector is shaded.

Run no.	Range of ω	2θ (˚)	φ (˚)
1	-10 to -40	-28	90
2	40 to -25	28	90
3	-155 to -220	-28	90
4	-140 to -170	28	90
5	-155 to -220	-28	270
6	-140 to -170	28	270
7	-10 to -40	-28	270
8	40 to -25	28	270

Table 1.2: A typical high-pressure data collection strategy for a DAC with a half opening angle of 40˚ (Dawson *et al.*, 2004).

Indexing of high-pressure data can suffer from problems associated with contamination of the diffraction pattern by diamond reflections and powder lines from the backing seat and gasket material (Figure 1.3a). Contamination by scattering from the beryllium backing disks used in Merrill and Bassett's original cell design can be eliminated with the use of a beryllium-free cell which employs BOEHLER ALMAX™ cut diamonds and WC backing discs (Moggach, Allan *et al.*, 2008) (Figure 1.3b).

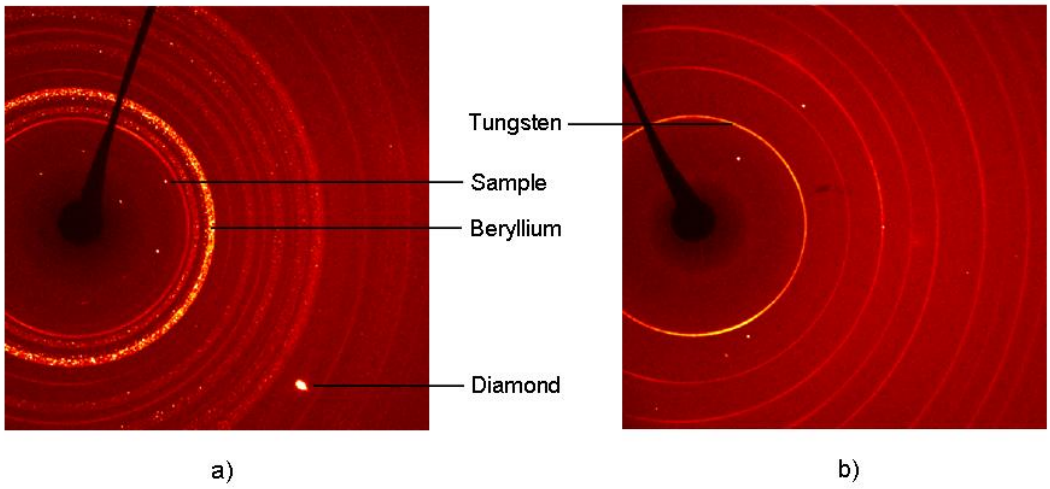

Figure 1.3: Diffraction images from a Merrill Bassett diamond anvil cell a) with beryllium backing disks, b) the beryllium-free design.

Standard indexing programs are not usually sufficient for high-pressure data, and an effective method is first to remove contaminating peaks manually using a reciprocal lattice viewer (Figure 1.4).

Figure 1.4: Harvested reflections in the Bruker-Nonius reciprocal lattice viewer RLATT. Images (a) and (b) are before and after editing respectively. Figure taken from Moggach, Parsons *et al.* (2008).

Integration of high-pressure data is also problematic as large portions of the detector are shaded by the steel body of the pressure cell. In order to get around this difficulty, a set of *dynamic masks* can be produced using the locally written program ECLIPSE (Dawson *et al.*, 2004). The program SAINT (Bruker-Nonius, 2006), which was used throughout this work for integration, uses these masks to determine which regions of the detector should be ignored. (Figure 1.5).

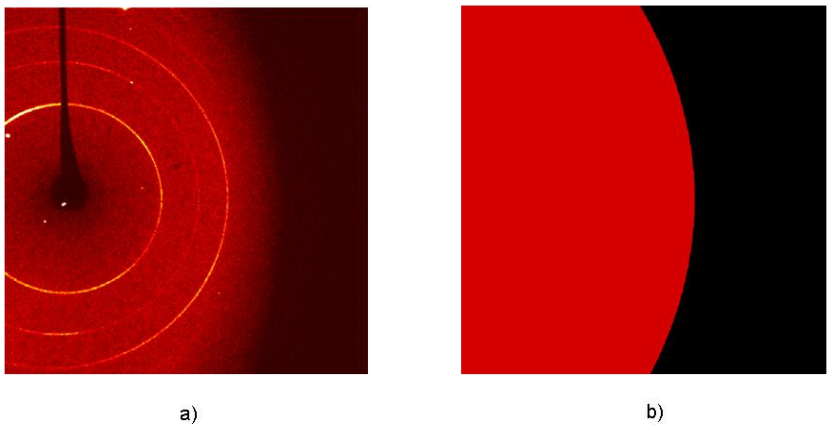

Figure 1.5: a) A frame from a high-pressure data collection where there is severe shading from the cell, b) the corresponding dynamic mask (the black region is masked).

Once integration has taken place, an empirical 'multi-scan' absorption correction can be applied using the program SADABS (Sheldrick, 2004). Prior to applying this correction it is usually advantageous to remove reflections with poor profiles for which the diffracted beam makes an angle with the cell axis within 2° of the nominal opening angle of the cell. This can be performed in the program SHADE (Parsons, 2004).

1.1.4 Structure solution and refinement

The low completeness of high-pressure data can lead to problems with structure solution, especially when a new high-pressure phase is formed which often results in a deterioration of the crystal quality. In this thesis, it was possible to solve all new high-pressure phases using the direct methods programs SIR92 (Altomare *et al.*, 1994) and SIR2004 (Burla *et al.*, 2005). In other work simulated annealing methods originally designed for solution of structures from powder data have been found to be very useful. Charge flipping can also be used provided the intensities of missing reflections are first estimated using maximum entropy (Palatinus & Gervais, 2007; Palatinus *et al.*, 2007).

High-pressure data invariably suffer from systematic errors which are still present even after the corrections described above are applied. The use of robust-resistant weighting schemes during merging (Blessing, 1997) using the program SORTAV (Blessing, 1987) has been found to be an effective way of treating this (Dawson *et al.*, 2004). In addition, outliers that persist can be eliminated during refinement with the use of robust-resistant weight modifiers (Prince, 1982; Prince & Nicholson, 1983).

1.1.5 The use of synchrotrons in high-pressure crystallography

All high-pressure data in this thesis were collected on Station 9.8 at the STFC synchrotron facility in Daresbury (Cernik *et al.*, 1997), which became the world's leading facility for high-throughput high-pressure single-crystal diffraction. The Daresbury facility closed in August 2008, and more recent work has been carried out on beam-line I19 at the DIAMOND Light Source.

One of the main advantages that synchrotron sources have over standard diffractometers for high-pressure data collection is the increased intensity of the beam. This is very important as samples are necessarily small, and usually quite weakly diffracting. In addition, some of the beam is absorbed by the diamonds and the beryllium backing discs (if present) during data collection. Although data collections can, and often are, carried out using laboratory sources, synchrotron data sets are usually of much better resolution and much quicker to measure (1 hr compared to at least 1 day).

Another advantage is the tuneability of the wavelength of the X-ray beam. The opening angle of the pressure cell (usually 80˚) restricts the volume of reciprocal space that can be accessed. Wavelengths of ≤ 0.5 Å are commonly used for high-pressure data collection in order to increase the size of the Ewald sphere and 'squeeze in' more of the diffraction pattern. Table 1.3 shows how much of an improvement this can make to the overall completeness. In this study of the single molecule magnet Mn_{12}-acetate (space group *I*-4), two data sets were collected using the same sample at λ = 0.6909 and 0.4577 Å on Station 9.8. The improvement in completeness and data quality at λ = 0.4577 is readily apparent.

λ/Å	$R1[F>4\sigma(F)]$	No. unique data with $F>4\sigma(F)$	Total unique data	d_{min}/Å	% Completeness to d = 0.8 Å
0.6909	0.0564	1646	1927	0.80	55
0.4577	0.0575	2892	5765	0.57	77

Table 1.3: Coverage statistics as a function of wavelength for Mn_{12}-acetate at high pressure. Data taken from Moggach & Parsons (2009b).

1.2 A Survey of Molecular Structures at Pressure

Though high-pressure research is a mature field in mineralogy and condensed matter physics, studies of the effect of pressure on molecular systems are less common (see above). In order to gain an overview of the classes of molecular materials which have been studied, an initial data set was created from the 404

molecular structures that appear in the CSD with the word 'pressure' associated with them. From this data set, structures which were studied at pressures between 0.1 and 10 GPa were selected leaving a total of 269 entries. The entries removed mostly refer to ambient-pressure determinations, or those for which the pressure of the determination is not given. The data set contains 97 different compounds. An additional 71 entries taken from unpublished work by the Edinburgh group (corresponding to 7 more compounds) were appended to the final data set. These data are listed in a spreadsheet available in the electronic supplemental material.

1.2.1 The effect of pressure on the volume of molecular structures

The effect of pressure on the volume of a material can be measured using the bulk modulus *K*, which is the inverse of the compressibility, and is defined as

$$K = -V(\partial P / \partial V)_T$$

where V = volume, P = pressure and T = temperature. K is determined by fitting an ideal equation of state (a mathematical expression, which relates volume to pressure and/or temperature) to pressure-volume data. An example of commonly used EOS is the Vinet equation (Vinet *et al.*, 1987; Vinet *et al.*, 1986),

$$P = 3K\frac{(1-f_v)}{f_v^2}\exp\left(\frac{3}{2}(K'-1)(1-f_v)\right)$$

where $f_v = V/V_o$ (V_o is the initial volume) and K' is the pressure derivative of the bulk modulus. The Birch-Murnaghan equation of state (Birch, 1947) is also commonly used.

If the value of the bulk modulus is large then this implies that the material is incompressible, for example, diamond, the hardest material known has a bulk modulus of 440 GPa. In contrast, molecular solids typically have $K < 30$ GPa (Angel, 2004). K' is also a useful parameter as it gives a measure of the rate of compression at low pressure. A large value of K' indicates a large amount of compression at low

pressure, and for molecular compounds it is usually relatively high. For example, $MgSiO_3$ (a perovskite) has K = 261 GPa and K' = 4, whilst the amino acid alanine has K = 13.6 GPa and K' = 6.7.

In order for an accurate determination of an equation of state, precise unit cell volumes are required. The more pressure-volume points available over the range of several GPa the better: in mineralogy papers an excess of ten data points over ranges of 2-5 GPa is normal. Moreover it is important that the dataset is finely sampled in the low-pressure region in order to define K'. Regrettably, most single crystal studies of molecular crystals do not meet these requirements and accurate compressibility data are still sparse, despite the recent interest in the area.

Therefore, in order to assess how molecular structures are affected by pressure, an alternative method has been applied. A general rule for a wide range of molecular crystal structures is that the average volume required for a non-hydrogen atom is approximately 18 $Å^3$. This figure was initially proposed by Kempster & Lipson (1972) who observed that for a data set of 40 arbitrarily chosen organic crystal structures which contained carbon, nitrogen, oxygen and hydrogen atoms, the relationship between the unit cell volumes and the number of atoms they contained (excluding hydrogen) was approximately linear.

The '18 $Å^3$ rule' has been used by crystallographers for over 30 years to aid structure solution by providing an initial estimate of Z (the number of formula units per unit cell), without any prior knowledge of the density (which is often complicated and time-consuming to measure) from the equation

$$Z = (V / 18) / N$$

where V is the unit cell volume and N is the number of non-H atoms per formula unit.

A graph of the average non-hydrogen volume *vs.* pressure for the 269 high-pressure molecular structures mined from the CSD is given in Figure 1.6. Outliers are shown in red, and were chosen as being > 23 $Å^3$ or < 13 $Å^3$ in the pressure range $0.1 \leq P \leq 2$ GPa; > 19 $Å^3$ in the pressure range $2 < P \leq 5$ GPa and > 18 $Å^3$ in the

pressure range $5 < P \leq 10$ GPa. The severe outliers which have unusually large average non-H volumes are labelled I, II, III and IV in Figure 1.6, and are from compounds CH_2I_2; CH_4; $2(CH_4),H_2$ and CH_4, $2(H_2)$ respectively. The large volumes arise from the low numbers of non-H atoms per formula unit.

From Figure 1.6 it can be seen that overall, the average non-H volume gradually decreases as pressure increases. The decrease appears to be rapid at first when the structures are most compressible and *K*' is largest, then after *ca*. 2 GPa the curve flattens out significantly. If the line of best fit in Figure 1.6 is a good representation of the trend, then at *ca.* 10 GPa, a rule of 12-13 $Å^3$ per non-H atom may be more appropriate.

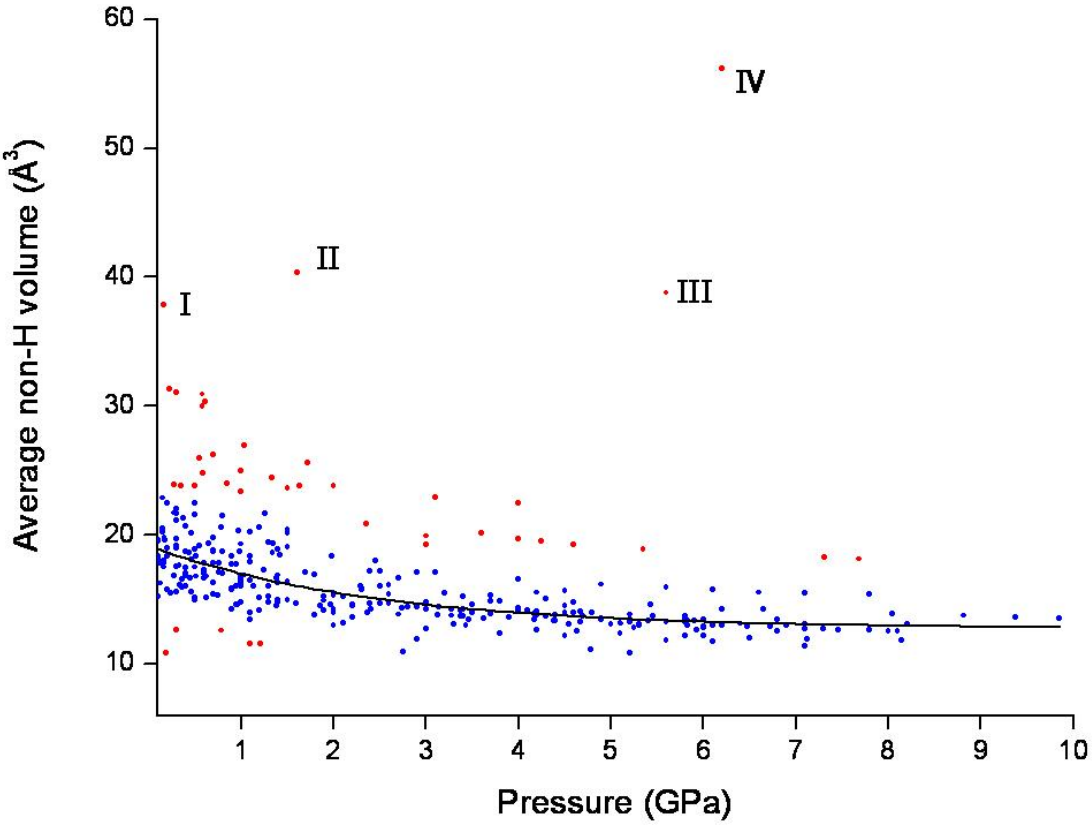

Figure 1.6: A graph of the average volume of non-hydrogen atoms in molecular structures at pressure. Outliers are shown as red points.

1.2.2 Intermolecular contact distances as a function of pressure

As molecular structures are compressed, voids decrease in size and molecules move much closer together, and as a result, intermolecular interactions tend to shorten considerably. This is in contrast to *intra*molecular distances and angles, which are relatively incompressible up to 10 GPa. It is observed that within this pressure regime, intermolecular contact distances do not compress to distances below those of ambient pressure structures in the CSD. In order to illustrate this, the 269 molecular structures were analysed for contact distances in OH…O, NH…O and CH…O interactions. These were then compared to ambient pressure contact distances in the CSD.

The results are shown as histograms in Figures 1.7 to 1.9. In each case the minimum contact distances in the high-pressure structures are never shorter than those observed at ambient conditions. In addition, the peaks of the distributions for the structures at high pressure occur at shorter distances than at ambient pressure, showing that the average contact distances are shorter in the high-pressure structures.

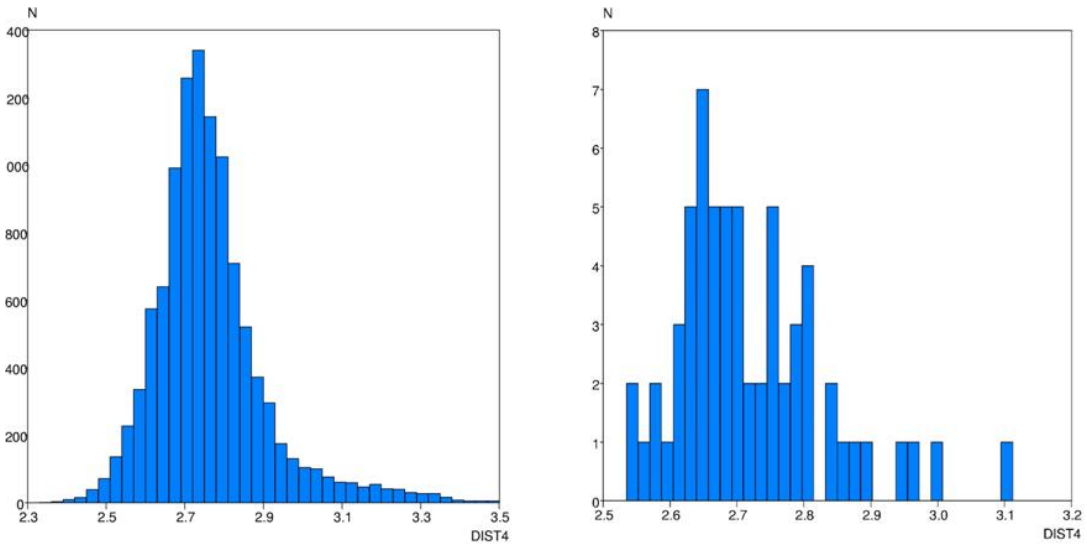

Figure 1.7: Histograms of O…O distances (in Å) for OH…O contacts in the CSD a) at ambient pressure and b) at high pressure. In (a) the shortest distance is 2.358 Å CSD refcode = ADESIM and the median is 2.780 Å. In (b) the shortest distance is 2.548 Å CSD refcode = HXACAN12 and the median is 2.693 Å.

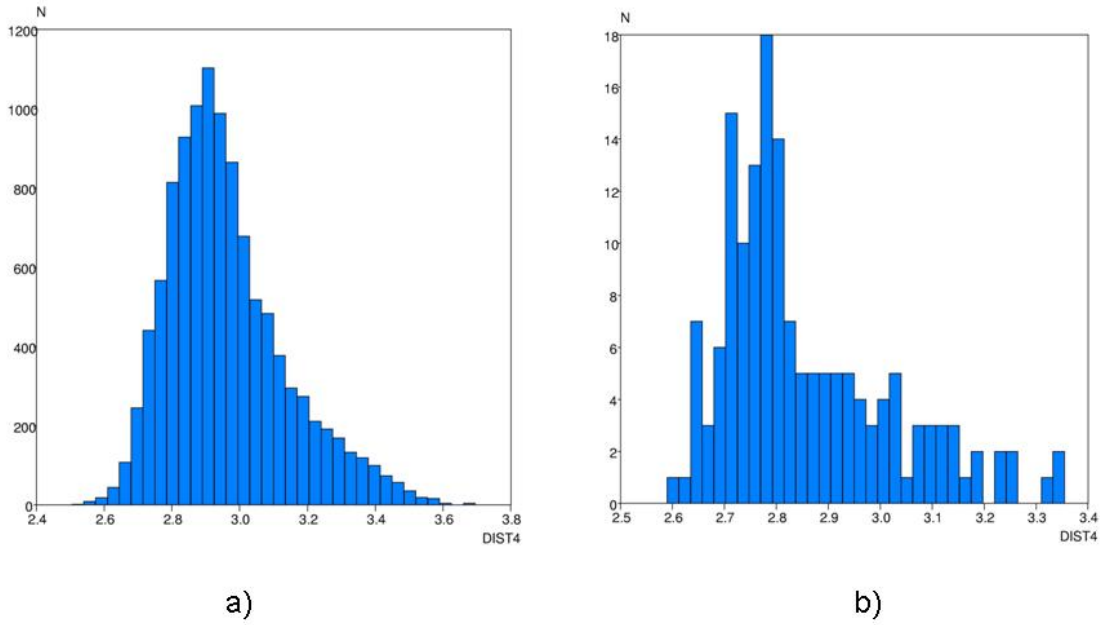

Figure 1.8: Histograms of N…O distances (in Å) for NH…O contacts in the CSD a) at ambient pressure and b) at high pressure. In (a) the shortest distance is 2.520 Å CSD refcode = BAMNAF and the median is 2.930 Å. In (b) the shortest distance is 2.593 Å CSD refcode = GLYCIN68 and the median is 2.806 Å.

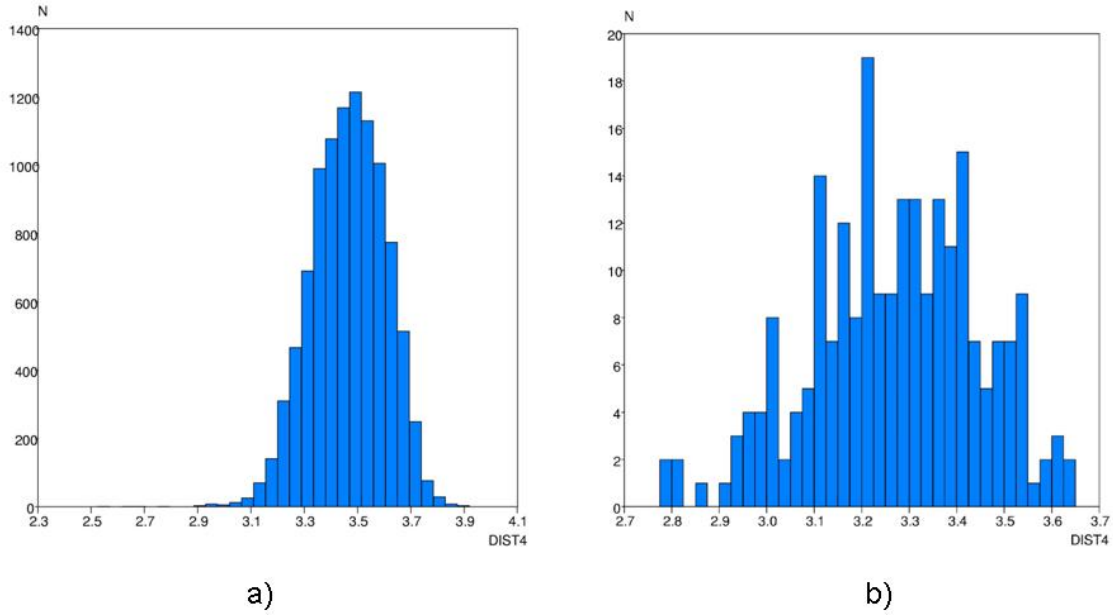

Figure 1.9: Histograms of C…O distances (in Å) for CH…O contacts in the CSD a) at ambient pressure and b) at high pressure. In (a) the shortest distance is 2.378 Å CSD refcode = AKIFAB and the median is 3.405 Å. In (b) the shortest distance is 2.791 Å CSD refcode = GLYCIN41 and the median is 3.277 Å.

1.2.3 Pressure-induced polymorphism in molecular compounds

The 269 molecular structures were further analysed for the occurrence of pressure-associated polymorphism. This was done by searching for entries which contained any of the words 'polymorph', 'phase' or 'form'. This resulted in a total of 54 different compounds. In addition to these data, four of the seven appended structures (not featured in the CSD) are known to exhibit polymorphism, giving a total of 58 structures (half of the total number of *different* compounds in the original data set of 296). The structures are listed in Table 1.4 with their CSD refcodes. It is clear that pressure is a very effective means to induce phase transitions in molecular crystals.

Compound Name	**CSD refcode**	**Compound Name**	**CSD refcode**
Acetic acid	ACETAC	L-serine	LSERIN
Adamantane	ADAMAN	bis(N,N-Dimethylethylenediammonium) (m2-chloro)-nonachloro-di-antimonate(iii)	MENTIJ
Adamantanone	ADMNTB	Methanol	METHOL
Benzene	BENZEN	2,5-bis(4-Nitrophenyl)-(1,3,4)-oxadiazole	NAGHOT
2-Oxopyrrolidineacetamide	BISMEV	Ethynylbenzene	NIMRIK
Carbon tetrachloride	CARBTC	3-*t*-Butylsalicylaldoxime	NIRJII
bis(tricarbonyl-(triphenylphosphine)-cobalt)	CEDBUJ	1,1,2,2-Tetrachloroethane	OCUJOM
bis(bis(Ethylenedithio-tetrathiafulvalene) tri-iodide	CILHIO	Phenanthrene	PHENAN
Dodecadeuterocyclohexane	CYCHEX	Phenol	PHENOL
bis(Ethylenedithio)-tetrathiafulvalene tri-iodide	DATREV	Pentadeuteropyridinium nitrate	PYRDHN
p-Dichlorobenzene	DCLBEN	Pyrene	PYRENE
1,2-Dichloroethane	DCLETH	2-Fluorophenol	QAMWEH
Diiodomethane	DIMETH	4-Fluorophenol	QQQBNG
bis(bis(Ethylenedithio)-tetrathiafulvalene) dicyano-silver	DUSBEY	N,N-Dimethylethylenediammonium pentachloroantimonate(iii)	REYFUW

(a)

Compound Name	CSD refcode	Compound Name	CSD refcode
Ethanol	ETANOL	2-hydroxybenzaldehyde oxime	SALOXM
1,2-diaminoethane	ETDIAM	Thiourea	THIOUR
Tetradeutero-ethylene	ETHLEN	(tris(2-((Pyrrol-2-yl)methyleneamino)ethyl)amine)-manganese(iii)	TRPAMN
1,3-Cyclohexanedione	FACRIK	2-Methyl-2-propanol	VATSAK
Cyclopropylamine	FIGYID	1-Azonia-4-azabicyclo(2,2,2)octane bromide	WOLZAY
Formic acid	FORMAC	bis(N-(2-Pyridylmethylene)-4-amino-1,1':4',1''-terphenyl)-diisothiocyanato-iron(ii) methanol solvate	XECMIB
Glycine	GYLCIN	Bromochloromethane	YISBIM
Chlorotrimethylsilane	GUHHAS	Methane bis(dihydrogen)	ZOSXOU
Cyclopentanol	HEGHUX	1,4-Di-iodobenzene	ZZZPRO
Acetone	HIXHIF	Methane	ZZZWEQ
4-Hydroxyacetanilide	HXACAN	N,N'-bis(Pyridin-4-ylmethyl)ethanediamide di-iodobutadiyne	WANNUV
Squaric acid	KECYBU	**L-serine monohydrate**	**-N/A-**
Cyclobutanol	KETVEK	**S-4-sulfo-L-Phenylalanine monohydrate**	**-N/A-**
L-Cysteine	LCYSTN	**Salicylamide**	**-N/A-**
L-alpha-leucine	LEUCIN	**Methyl 2-(9H-carbazol-9-yl)benzoate**	**-N/A-**

(b)

Table 1.4: Molecular crystal structures taken from the CSD which exhibit pressure-related polymorphism. The four entries in bold at the bottom right of the table are data from the Edinburgh group which do not currently feature in the CSD.

1.3 Understanding phase transitions in molecular structures

1.3.1 Driving forces for phase transitions

In Section 1.2 it was shown that high-pressure polymorphism in molecular compounds is not uncommon. Little is known, however, about the forces which drive these transitions. Understanding how and why a transition occurs is important as it could ultimately lead to the prediction and even the control of polymorphism in the solid state. One area where the control of phase transitions is extremely important is the pharmaceutical industry where drugs may be placed under pressure during tabletting.

We have also seen in Section 1.2 that unusually short intermolecular interactions are not formed in the regime 0 – 10 GPa. This observation would appear to imply that formation of short intermolecular interactions is avoided at high pressure because such interactions would be located in repulsive regions of their potentials, and in order to avoid this situation a phase transition occurs to relieve this build up of strain, either by lengthening the interaction, or by breaking it.

Accordingly, phase transitions in L-serine (Moggach *et al.*, 2005) and L-cysteine (Moggach *et al.*, 2006) occurred when N…O and S…S distances reached the lower limits for these interactions defined in searches of the CSD. Similarly, an analysis of the compression of small molecule single crystal structures (Wood, McKinnon *et al.*, 2008) has shown that in the pressure regime 0-10 GPa, H…H contacts do not appear to compress below a distance of 1.7Å. Structures which were compressed near to this limit were seen either to undergo a phase transition or to undergo collapse of the sample into an amorphous or polycrystalline mass. In the same publication, a search of the CSD for ambient pressure organic structures showed that the frequency of H…H contacts as a function of distance drops off drastically between 1.9 and 1.7 Å.

The idea of rationalising a phase transition based solely on intermolecular contact distances is intuitively appealing, but perhaps a little naïve because it considers only the contribution of internal energy (U) to free energy. The full expression for the free energy (G) is

$$G = U - TS + PV$$

and it is clear that the pressure × volume term (PV) will become increasingly significant as pressure increases. In order to assess the relative importance of the U and PV terms it is important to quantify them. A relatively new technique called the PIXEL method provides a way of observing how the lattice energies of crystal structure are perturbed as pressure is applied. If a transition is indeed driven by the need to relieve repulsive intermolecular interactions, then there will be an increase in

the stability of the lattice energy through the transition, and the *U*-term will be important in driving the transition.

1.3.2 The PIXEL method

The PIXEL method (also known as the *semi-classical density sums* method), developed by Gavezzotti (2005) is a computational technique, which enables the calculation of packing energies by considering whole molecule-molecule interactions, rather than a more conventional atom-atom approach. Calculations of intermolecular interaction energies can be performed with the program OPIX (Gavezzotti, 2003a) to enable the computation of both full lattice and specific dimer energies. The total energy of each interaction can be further broken down into four constituent terms: Coulombic, polarisation, dispersion and repulsion. The technique provides a relatively quick and simple alternative to methods like *ab initio* calculations, which are often time-consuming, and has the advantage that it can be performed on a normal desk-top computer.

PIXEL calculations are very sensitive to the positions of hydrogen atoms and if required, X–H distances in the molecule are extended to the standard neutron lengths before calculations are performed. Apart from this, the geometry of the molecule is taken unchanged from the crystal structure, and a standard quantum mechanical package, for example, GAUSSIAN03 (Frisch *et al.*, 2004) used to produce a three-dimensional electron density map of the molecule. This is done at the MP2/6-31G** level of theory, and the resulting electron density map is output in the form of a grid of pixels with dimensions 0.08 x 0.08 x 0.08 Å.

In order to expedite ensuing calculations, the pixels are ‘condensed’ into larger ones; the level of condensation depends on the type of calculation being performed. After the grid has been modified, a spherical cluster of molecules must be created using the space group of the crystal. For small organic molecules the radius of the cluster is usually set at 18 Å.

A useful way of describing how the PIXEL method works is to illustrate how the Coulombic term is derived. Coulombic energies in a PIXEL calculation are pair-wise additive and are calculated as sums of pixel–pixel, pixel–nucleus and nucleus–

nucleus terms. Each pixel has its own charge, as does each atomic nucleus, and the formula for each calculation is the standard electrostatic potential energy equation

$$E_{COUL} = \left(\frac{q_1 q_2}{4\pi\varepsilon^o r} \right)$$

where q_1 and q_2 are the charges on the pixel or nucleus and r is the distance between them. Similar procedures are used for summation of the polarisation, dispersion and repulsion components. However, for these three terms, four empirical parameters are used which are optimised to reproduce experimental sublimation enthalpies for a range of organic molecular crystal structures. Summation of the four energy terms gives the total energy.

PIXEL lattice energies are found to compare well with experimental sublimation enthalpies (usually to within ±10 kJ mol^{-1}), and tests have also shown that the results compare well to intermolecular perturbation theory (Gavezzotti, 2003b) and periodic DFT calculations (Wood, Francis *et al.*, 2008).

1.3.3 Testing the theory

The pressure-induced phase transition in salicylaldoxime (Wood *et al.*, 2006) provided the first test case for the distance based theory described above. As pressure is applied to salicylaldoxime-I, a hydrogen bond and a π…π interaction both shorten towards the limit of their contact distances based on searches performed on the CSD for chemically similar compounds. As the phase transition occurs, both contacts are relieved. PIXEL calculations showed that the interaction energies of both contacts became rapidly destabilising as pressure was applied, and the phase transition resulted in a significant stabilisation of the lattice energy by *ca*. 25 kJ mol^{-1}. Therefore, in this case the theory was proven to be correct.

However, when the theory was tested on L-serine, the phase transition resulted in a significant *destabilisation* of the intermolecular lattice energy by *ca*. 50 kJ mol^{-1}, and no intermolecular contacts became rapidly destabilising as pressure was applied, even though the contact distances reached the lower limits determined from

a search of the CSD. In contrast to salicylaldoxime, the phase transition in L-serine was accompanied by a significant drop in the unit cell volume *and* a change in the molecular geometry of the serine molecules to an arrangement which was more stable by *ca.* 40 kJ mol^{-1}. When both of these factors were taken into account, it was found that the phase transition resulted in a significant stabilisation of the lattice enthalpy term by *ca.* 13 kJ mol^{-1}. Therefore, the driving force of the transition could be seen as being controlled by the *PV* term in the equation for the free energy (see section 1.3.1).

1.3.4 Structural oddities

Observed crystal structures are located at free-energy minima. Molecular structures are characterised by large numbers of structural parameters, and when expressed as a minimisation problem there are potentially a huge number of ways of defining a free energy minimum. This is what makes *ab initio* structure prediction so difficult. This being said, there are a number of rules which many stable structures appear to obey.

An example of a rule which characterises 'normal' behaviour was first outlined by Etter in relation to H-bonded structures (Etter, 1990). It is usually found that structures are directed by pairing-up of the strongest H-bond donors with the strongest acceptors. Another common feature of molecular structures is that they have low numbers of molecules in the asymmetric unit (Anderson *et al.*, 2006). The 18 $Å^3$ is another rule which is often found to be obeyed to within a few $Å^3$ (Kempster & Lipson, 1972; Roman *et al.*, 1993). A further observation is that the geometry of molecules in a crystal is usually very close to its most stable conformation, though there is a compromise between this and efficient packing (Glusker, 1994). In addition, we have already seen that small organic crystal structures tend not to exhibit short H…H contacts under ambient conditions (Wood, McKinnon *et al.*, 2008).

Nevertheless exceptions to the usual rules of crystal packing do occur, and these cases might be described as 'structural oddities'. The aim of the work in this

thesis was to examine whether pressure would induce such oddities to behave more normally. Each of the compounds featured in this thesis is in some way unusual.

L-serine monohydrate was chosen for its unusual packing: layers of serine molecules are linked together via H-bonds from water molecules in the arrangement shown in Figure 1.10a. Searches of the CSD for layered hydrates indicate that the orientation shown in Figure 1.10b is more commonplace. It is likely that the orientation of the water in Figure 1.10b takes up less volume between the layers, allowing for more efficient packing.

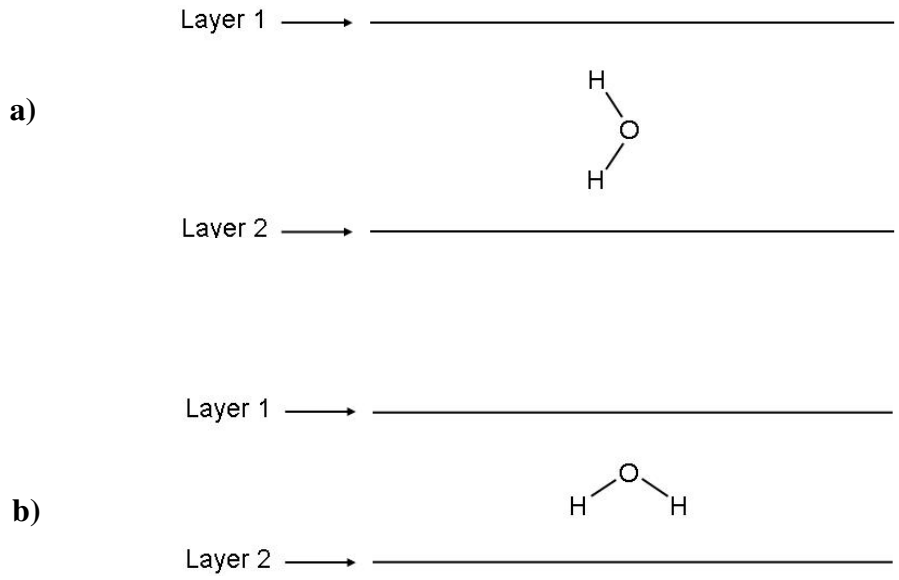

Figure 1.10: Two types of orientation of the water molecules in layered hydrates. In a) the layers are linked together through H-bonding from the donor atoms of the water molecules, in b) the H-bonds are formed to the same layer.

Methyl 2-(9H-carbazol-9-yl)benzoate was chosen as it crystallises under ambient conditions with eight molecules in the asymmetric unit. This is an extremely rare phenomenon: currently only 0.02% of structures in the CSD have $Z' = 8$. The crystal structure of salicylamide is also unusual because it appears to have a number of short H…H contacts, each under 2.0 Å (X-H distances normalised to standard neutron values). Finally, bianthrone was selected as it unusually changes colour from yellow to green on grinding.

1.4 References

Allan, D. R. & Clark, S. J. (1999). *Physical Review B: Condensed Matter and Materials Physics* **60**, 6328-6334.

Allan, D. R., Clark, S. J., Brugmans, M. J. P., Ackland, G. J. & Vos, W. L. (1998). *Physical Review B: Condensed Matter and Materials Physics* **58**, R11809-R11812.

Allan, D. R., Clark, S. J., Ibberson, R. M., Parsons, S., Pulham, C. R. & Sawyer, L. (1999). *Chemical Communications* **8**, 751-752.

Altomare, A., Cascarano, G., Giacovazzo, C., Guagliardi, A., Burla, M. C., Polidori, G. & Camalli, M. (1994). *Journal of Applied Crystallography* **27**, 435-435.

Anderson, K. M., Goeta, A. E., Hancock, K. S. B. & Steed, J. W. (2006). *Chemical Communications* **20**, 2138-2410.

Angel, R. J. (2004). High Pressure Crystallography. NATO Science Series II, edited by A. Katrusiak & P. F. McMillan, pp. 21-36.

Birch, F. (1947). *Physical Review* **71**, 809-824.

Blessing, R. H. (1987). *Crystallography Reviews* **1**, 3-58.

Blessing, R. H. (1997). *Journal of Applied Crystallography* **30**, 421-426.

Boldyreva, E. V., Ahsbahs, H., Chernyshev, V. V., Ivashevskaya, S. N. & Oganov, A. R. (2006). *Zeitschrift fuer Kristallographie* **221**, 186-197.

Bruker-Nonius (2006). *SAINT version 7, Program for integration of area detector data.* Bruker-AXS, Madison, Wisconsin, USA.

Burla, M. C., Caliandro, R., Camalli, M., Carrozzini, B., Cascarano, G. L., Caro, L. D., Giacovazzo, C., Polidori, G. & Spagna, R. (2005). *Journal of Applied Crystallography* **38**, 381-388.

Cernik, R. J., Clegg, W., Catlow, C. R. A., Bushnell-Wye, G., Flaherty, J. V., Greaves, G. N., Burrows, I., Taylor, D. J., Teat, S. J. & Hamichi, M. (1997). *Journal of Synchrotron Radiation* **4**, 279-286.

Dawson, A. (2003). PhD thesis, The University of Edinburgh.

Dawson, A., Allan, D. R., Parsons, S. & Ruf, M. (2004). *Journal of Applied Crystallography* **37**, 410-416.

Etter, M. C. (1990). *Accounts of Chemical Research* **23**, 120-126.

Fabbiani, F. P. A., Allan, D. R., Dawson, A., David, W. I. F., McGregor, P. A., Oswald, I. D. H., Parsons, S. & Pulham, C. R. (2003). *Chemical Communications* **24**, 3004-3005.

Fabbiani, F. P. A. & Pulham, C. R. (2006). *Chemical Society Reviews* **35**, 932-942.

Frisch, M. J., Trucks, G. W., Schlegel, H. B., Scuseria, G. E., Robb, M. A., Cheeseman, J. R., J. A. Montgomery, J., Vrevren, T., Kudin, K. N., Burant, J. C., Millam, J. M., Iyengar, S. S., Tomasi, J., Barone, V., Mennucci, B., Cossi, M., Scalmani, G., Rega, N., Petersson, G. A., Nakatsuji, H., Hada, M., Ehara, M., Toyota, K., Fukuda, R., Hasegawa, J., Ishida, M., Nakajima, T., Honda, Y., Kitao, O., Nakai, H., Klene, M., Li, X., Knox, J. E., Hratchian, H. P., Cross, J. B., Bakken, V., Adamo, C., Jaramillo, J., Gomperts, R., Stratmann, R. E., Yazyev, O., Austin, A. J., Cammi, R., Pomelli, C., Ochterski, J. W., Ayala, P. Y., Morokuma, K., Voth, G. A., Salvador, P., Dannenberg, J. J., Zakrzewski, V. G., Dappricj, S., Daniels, A. D., Strain, M. C., Farkas, O., Malick, D. K., Rabuck, A. D., Raghavachari, K., Foresman, J. B., Oritz, J. V., Cui, Q., Baboul, A. G., Clifford, S., Cioslowski, J., Stefanov, B. B., Liu, G., Liashenko, A., Piskorz, P., Komaromi, I., Martin, R. L., Fox, D. J., Keith, T., Al-Laham, M. A., Peng, C. Y., Nanayakkara, A., Challacombe, M., Gill, P. M. W., Johnson, B., Chen, W., Wong, M. W., Gonzalez, C. & Pople, J. A. (2004). *Gaussian 03 revision E.01.* Gaussian, Inc., Wallington CT., USA.

Gavezzotti, A. (2003a). *OPIX - A computer program package for the calculation of intermolecular interactions and crystal energies.* University of Milano, Milan, Italy.

Gavezzotti, A. (2003b). *CrystEngComm* **5**, 249-438.

Gavezzotti, A. (2005). *Zeitschrift fuer Kristallographie* **220**, 499-510.

Glusker, J. P. (1994). Crystal Structure Analysis for Chemists and Biologists, p. 456. Wiley-VCH, Inc.

Kempster, C. J. E. & Lipson, H. (1972). *Acta Crystallographica., Section B* **28**, 3674.

Macrae, C. F., Bruno, I. J., Chisholm, J. A., Edgington, P. R., McCabe, P., Pidcock, E., Rodriguez-Monge, L., Taylor, R., Streek, J. v. d. & Wood, P. A. (2008). *Journal of Applied Crystallography* **41**, 466-470.

Merrill, L. & Bassett, W. A. (1974). *Review of Scientific Instruments* **45**, 290-294.

Miletich, R., Allan, D. R. & Kuhs, W. F. (2000). *Reviews in Mineralogy and Geochemistry* **41**, 445-519.

Moggach, S. A., Allan, D. R., Clark, S. J., Gutmann, M. J., Parsons, S., Pulham, C. R. & Sawyer, L. (2006). *Acta Crystallographica, Section B* **62**, 296-309.

Moggach, S. A., Allan, D. R., Morrison, C. A., S. Parsons & Sawyer, L. (2005). *Acta Crystallographica, Section B* **61**, 58-68.

Moggach, S. A., Allan, D. R., Parsons, S. & Warren, J. E. (2008). *Journal of Applied Crystallography* **41**, 249-251.

Moggach, S. A. & Parsons, S. (2009a). *Specialist Periodic Reports: Spectroscopic Properties of Inorganic and Organometallic Compounds* **40**, 324-354.

Moggach, S. A. & Parsons, S. (2009b). *Spectroscopic Properties of Inorganic and Organometallic Compounds* **40**, 324-354.

Moggach, S. A., Parsons, S. & Wood, P. A. (2008). *Crystallography Reviews* **14**, 143-184.

Palatinus, L. & Gervais, C. (2007). *Journal of Applied Crystallography* **40**, 786-790.

Palatinus, L., Walter, S. & Gervais, C. (2007). *Journal of Applied Crystallography* **40**, 456-462.

Parsons, S. (2004). *SHADE- Program for empirical absorption corrections to high pressure data.* The University of Edinburgh, Edinburgh, United Kingdom.

Piermarini, G. J., Block, S., Barnett, J. D. & Forman, R. A. (1975). *Journal of Applied Physics* **46**, 2774-2780.

Prince, E. (1982). Mathematical Techniques in Crystallography and Materials Science, p. 192. New York, USA: Springer-Verlag.

Prince, E. & Nicholson, W. L. (1983). *Acta Crystallographica, Section A* **39**, 407-410.

Roman, P., Guzman-Miralles, C. & Luque, A. (1993). *Acta Crystallographica, Section B* **49,** 383-386.

Sheldrick, G. M. (2004). *SADABS Version 2004-1, Program for absorption corrections to area detector data.* Bruker-AXS, Madison, Wisconsin, USA.

Vinet, P., Ferrante, J., Rose, J. H. & Smith, J. R. (1987). *Journal of Geophysical Research* **92**, 9319-9325.

Vinet, P., Ferrante, J., Smith, J. R. & Rose, J. H. (1986). *Journal of Physics C* **19**, L467-L473.

Wood, P. A., Forgan, R. S., Henderson, D., Parsons, S., Pidcock, E., Tasker, P. A. & Warren, J. E. (2006). *Acta Crystallographica Section B* **62**, 1099-1111.

Wood, P. A., Francis, D., Marshall, W. G., Moggach, S. A., Parsons, S., Pidcock, E. & Rohl, A. L. (2008). *CrystEngComm* **10**, 1154-1166.

Wood, P. A., McKinnon, J. J., Parsons, S., Pidcock, E. & Spackman, M. A. (2008). *CrystEngComm* **10**, 368-376.

Chapter 2

High-Pressure Polymorphism in L-Serine Monohydrate: Identification of Driving Forces in High Pressure Phase Transitions and Implications for Pressure-Induced Protein Denaturation*

* Johnstone, R. D. L., Francis, D., Lennie, A. R., Marshall, W. G., Moggach, S. A., Parsons, S., Pidcock, E. & Warren, J. E. (2008). *CrystEngComm* 10, 1758-1769.

2.1 Abstract

At ambient pressure the crystal structure of L-serine monohydrate (L-serine monohydrate-I) contains H-bonded layers of zwitterionic serine molecules linked by H-bonds to water molecules. The waters act as donors to oxygen atoms on carboxylate and alcohol groups in separate layers. This phase remains stable from ambient pressure to 4.5 GPa; the most prominent structural change in this range is a reduction in the interlayer distance. On increasing the pressure to 5.2 GPa the structure transforms to a high-pressure polymorph, termed L-serine monohydrate-II. The structures of both polymorphs have been determined using a combination of X-ray single-crystal and neutron powder diffraction. During the transition the serine interlayer distances reduces further and the water molecules rotate so that both donor interactions are made to the same serine layer. The serine ammonium group adopts an eclipsed conformation, reconfiguring the H-bonding within the serine layers. The disruption of H-bonding as water is pushed into the serine layers suggests that a similar process may occur as a first step in the pressure-denaturation of proteins. Though the water molecules become coordinatively saturated with respect to H-bonding, and interlayer serine-serine Coulombic interactions are strengthened, PIXEL calculations show that overall the intermolecular interactions are weaker in phase-II than phase-I. The lattice enthalpy becomes more negative through the transition as a result of the smaller *PV* term applying to the more efficiently packed phase-II structure.

2.2 Introduction

The experimental parameters that are typically varied during a search for polymorphs of organic and other molecular materials are temperature and choice of recrystallisation solvent. Pressure, which is a powerful thermodynamic variable, is not used extensively. However, an estimate of the relative potential of temperature and pressure can be gauged from the definition of the Gibbs free energy, $G = U - TS + PV$, where the symbols have their usual thermodynamic meanings. For organic

crystals the accessible range of T is commonly limited to *ca.*400-500 K before decomposition occurs. By contrast, 1 GPa represents an increase of four orders of magnitude relative to ambient pressure. 1 GPa is a rather modest figure by the standards of modern high-pressure science, and PV terms equivalent to covalent bond energies are easily accessible.

Research has been carried out on pressure-induced polymorphism in simple organic compounds such as acetic (Allan & Clark, 1999a) and formic acids (Allan & Clark, 1999b) and methanol (Allan *et al.*, 1998), ethanol (Allan & Clark, 1999a; Allan *et al.*, 2001), phenols (Allan *et al.*, 2002; Oswald, Allan, Motherwell *et al.*, 2005; Oswald, Allan, Day *et al.*, 2005) and acetone (Allan *et al.*, 1999) and on more complex systems such as hydrogen-bonded systems (Katrusiak, 2004; Katrusiak, 1992; Katrusiak & Nelmes, 1986; Boldyreva, 2008), amino acids (Moggach *et al.*, 2008), pharmaceuticals, energetic materials (Fabbiani & Pulham, 2006), metal carbonyls (Edwards & Butler, 2000), spin cross-over complexes (Legrand *et al.*, 2008; Guionneau *et al.*, 2005), molecular conductors (Gaultier *et al.*, 1999; Kurmoo *et al.*, 1996; Guionneau *et al.*, 1996) and even single molecule magnets (Prescimone *et al.*, 2008), which may contain 100 atoms per molecule. At the far extreme in terms of the size of system that can now be studied, high-pressure protein crystallography is a rapidly developing field (Girard *et al.*, 2007).

Much of the progress in the field of high-pressure polymorphism has been made possible by the development of area detector systems for single crystal data collection (Dawson *et al.*, 2004). At synchrotron sources, such as Station 9.8 at the SRS, Daresbury, it has been possible for some years to collect routinely in excess of twenty high-pressure data sets per day, integrating data, solving and refining structures as they are collected, achieving perfectly respectable R factors (Moggach, Allan, Parsons *et al.*, 2005). As we shall see, analysis of high-pressure polymorphs can depend critically on accurate H-atom location, and in this regard neutron powder diffraction in combination with the Paris-Edinburgh pressure cell, for example, on the PEARL instrument at ISIS (Le Godec *et al.*, 2001; Marshall & Francis, 2002), has been extremely successful.

The number of molecular crystal structures determined at high pressure is thus increasing rapidly: over 60 structures were deposited in the Cambridge Structural Database in 2005 and 2006, compared to ten in all previous years (Wood, Francis *et al.*, 2008). Pressure-induced phase transitions have been observed in all the classes of compound listed above, and amongst the amino acids they have been crystallographically studied for glycine (Dawson *et al.*, 2005; Goryainov *et al.*, 2006; Goryainov *et al.*, 2005; Boldyreva *et al.*, 2005), serine (Moggach, Allan, Morrison *et al.*, 2005; Moggach, Marshall *et al.*, 2006; Wood, Francis *et al.*, 2008), and cysteine (Moggach, Allan *et al.*, 2006). It seems appropriate at this stage to ask what factors are responsible for driving these phase changes.

Abnormally short intermolecular contacts have never been observed in molecular compounds in the pressure range 0-10 GPa. Instead, as interatomic distances reach a lower limit a phase transition is seen to occur; the lower limit is even predictable on the basis of searches of the Cambridge Structural Database (Allen, 2002). The conclusion that we initially drew from this observation was that as a lower distance limit is approached the intermolecular interactions enter a strongly repulsive region of the potential, which is then relieved by a phase transition.

The development of the PIXEL method (Dunitz & Gavezzotti, 2005; Gavezzotti, 2005, 2007) for the calculation of intermolecular packing energies, has enabled this simple model for the driving forces of phase transitions to be tested. It has been found to be valid in the phase transition from salicylaldoxime-I to II: as the pressure approached 5.9 GPa a hydrogen-bonded pseudo-macrocyclic dimer became rapidly less stable, and a rearrangement of the hydrogen bonds ensued (Wood *et al.*, 2006). By contrast, in serine, where two phase transitions occur at 5 and 8 GPa, no such destabilisations were identified (Wood, Francis *et al.*, 2008). These transitions were found to be driven by the lower volume of the high-pressure polymorph and a rearrangement of the serine molecules to a lower energy conformation.

In this chapter we describe the effect of pressure on L-serine monohydrate (Scheme 2.1) as studied by a combination of single crystal synchrotron X-ray and neutron powder diffraction.

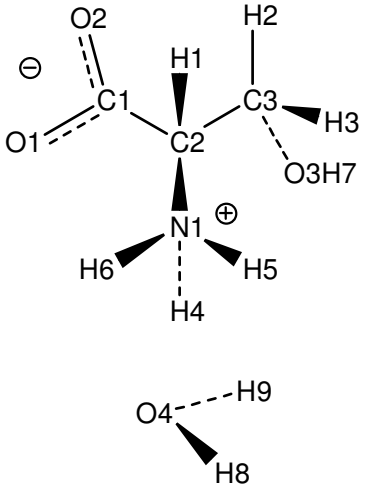

Scheme 2.1: Chemical structure diagram showing the atomic numbering scheme in L-serine monohydrate.

At ambient pressure the compound forms a structure (phase-I) in which layers of serine molecules are connected by layers of water molecules (Frey *et al.*, 1973). We show below that this structure undergoes a transition at about 5 GPa to phase-II, where the layers move closer together and molecular reorientations occur. The results of PIXEL calculations are interpreted to identify what factors drive this phase change.

The study of hydrated amino acids under pressure is to some extent relevant to biological systems. Proteins denature when subjected to pressure, and the mechanism for this is thought to be the forcing of the water molecules into the hydrophobic core of the protein structure where they cause the hydrogen bonds to break and subsequently the secondary structure to unfold (Hummer *et al.*, 1998). This mechanism is hard to prove directly and so the investigation of how amino acid hydrates react to the application of pressure could not only provide fundamental data for computational modelling, but also suggest alternative models for the denaturation mechanism.

2.3 Experimental

2.3.1 Sample preparation

L-Serine (99%) was purchased from Aldrich (catalogue number S2600). A sample (1.594 g) was dissolved in deionised water, and ethanol was then added drop-wise until crystals started to form. Crystals were allowed to grow over a period of 24 h. A small crystal was loaded into a diamond anvil cell. A sample of L-serine-d_7 was obtained from CDN Isotopes and recrystallised from perdeuterated water and ethanol as described above. This was used for high-pressure neutron powder diffraction measurements (see below).

2.3.2 High-pressure single crystal X-ray structure determination

High-pressure experiments were carried out using a Merrill-Bassett diamond anvil cell (half-opening angle 40°), equipped with brilliant-cut diamonds with 600 μm culets, a tungsten gasket and beryllium backing plates (Merrill & Bassett, 1974). A 4:1 mixture of methanol and ethanol was used as a hydrostatic medium. A small ruby chip was also loaded into the cell as the pressure calibrant, and the ruby fluorescence method used to measure the pressure (Piermarini *et al.*, 1975).

Diffraction data were collected on a Bruker-Nonius APEX-II diffractometer with silicon-monochromated synchrotron radiation (λ = 0.4865 Å) on Station 9.8 at the SRS, Daresbury Laboratory. Data collection and processing procedures for the high-pressure experiments followed Dawson *et al.* (2004). Integrations were carried out using dynamic masking of the regions of the detector shaded by the pressure cell with the program SAINT (Bruker-Nonius, 2006). An absorption correction was carried out in a two-stage procedure with the programs SHADE (Parsons, 2004) and SADABS (Sheldrick, 2004).

The results of the first data collection showed the sample to be the phase of L-serine monohydrate originally described in Frey *et al.* (1973); we will refer to this phase hereafter as L-serine monohydrate-I. Data collections were taken in approximately 1.0 GPa steps from ambient pressure up to a final pressure of 5.2 GPa. Determination of the cell constants at 5.2 GPa showed that a single-crystal to single-

crystal phase transition had occurred to a new polymorph (L-serine monohydrate-II). The phase transition resulted in a marked broadening of the diffraction profiles, and no attempt was made to collect data at higher pressures than 5.2 GPa.

Refinements of the compressed form of L-serine monohydrate-I were carried out starting from the co-ordinates determined at ambient pressure (Frey *et al.*, 1973). The structure of L-serine monohydrate-II was solved by direct methods using the program SIR92 (Altomare *et al.*, 1994). Refinements were carried out with $|F|^2$ using all data (CRYSTALS) (Betteridge *et al.*, 2003). Owing to the low completeness of the data sets, all primary bond distances and angles were restrained to the values observed in the ambient pressure structure at room temperature. All non-H atoms were refined with anisotropic displacement parameters, with global rigid-bond and body restraints.

Hydrogen atoms attached to carbon and nitrogen were placed geometrically and their coordinates were refined subject to restraints. The location of the hydrogen atoms attached to oxygen (H7, H8 and H9) could not be determined from Fourier difference maps, and these atoms were placed in order to optimise H-bonding interactions. H-atom positions were subsequently refined subject to standard distance restraints. The positions obtained are consistent with those observed by neutron diffraction reported in Frey *et al.* (1973) and here.

When the H-atoms in phase-II were placed using similar procedures to those described for phase-I, this implied the presence of a short N-H…H(water) contact measuring 1.65 Å. This is rather short in the context of recent work by Wood, McKinnon *et al.* (2008). High pressure neutron powder diffraction experiments were carried out in order to locate the H-atoms in this phase more accurately (see below).

2.3.3 High-pressure neutron powder diffraction

Neutron data were collected using the time-of-flight technique at the PEARL beamline high-pressure diffractometer (HiPr) at ISIS (Le Godec *et al.*, 2001). Data sets between ambient pressure and 5.8 GPa were collected in the range $0.6 < d < 4.3$ Å using a V3b-type Paris-Edinburgh press, with a 16:3:1 mixture of deuterated

methanol, ethanol and water as a hydrostatic medium. Loading of the TiZr capsule gasket (Marshall & Francis, 2002) (volume 55 mm^3) used to hold the sample was hampered by the tendency of serine hydrate to dehydrate. Excess mother liquor was removed from the sample by brief exposure to filter paper; the sample was then moistened with the hydrostatic medium (which contained water) to produce a thick slurry. This procedure was repeated twice, and the capsule then loaded with the slurry together with a small pellet of lead to act as a pressure marker. The pressure was calculated from the refined lead cell lattice parameter using a Birch-Murnaghan equation of state (Birch, 1947) with V_o = 30.3128 $Å^3$, B_o = 41.92 GPa, B' = 5.72. These parameters were derived by Fortes, (2004) as averages of the values determined in three earlier studies (Kuznetsov *et al.*, 2002; Miller & Schuele, 1969; Waldorf & Alers, 1962).

Crystal structure refinements were carried out using TOPAS-Academic version 4.1 (Coelho, 2007). Simultaneous 'X-N refinement' of the structure of L-serine monohydrate-I was performed against single crystal X-ray (collected at 3.7 GPa) and neutron powder data (collected at 3.8 GPa). Cell dimensions used for modelling the X-ray data were derived in the usual way from integration of the X-ray diffraction data and thereafter held fixed; those for modelling the neutron data were refined. The initial structural model was taken from Frey *et al.* (1973) with the serine and water molecules represented using the Z-matrix formalism available in TOPAS, which enables refinements to be parameterised in terms of bond distances and angles rather than fractional atomic coordinates.

In the initial stages of refinement the primary intramolecular geometric parameters were held fixed, and only the positions and orientations of the molecules were allowed to vary. In the final stages all geometric parameters were allowed to refine. Within the serine molecule the NH_3^+ group was constrained to have local three-fold symmetry, C-H distances were also constrained to be equal. A single parameter representing the difference between neutron and X-ray distances involving hydrogen was also refined. Similarity restraints were applied to the C-C distances and the C-O distances within the carboxylate group, but otherwise restraints were

found not to be necessary. Only the HOH angle was held fixed at 105°: free refinement of this parameter yielded <HOH = 99.1(15)°, while having no effect at all on the R_{wp} of the neutron data.

Displacement parameters obtained using X-ray and neutron data are known to differ. Anisotropic displacement parameters (ADPs) for the non-H atoms and a common isotropic displacement parameter for the H-atoms were used to model the X-ray data. A common isotropic displacement parameter was used for the non-H atoms in modelling the neutron data; H-atoms displacement parameters were set to 1.2 × this value.

Preferred orientation in the neutron powder data was modelled using a spherical harmonic expansion to fourth order. Also included in the powder-pattern modelling were structural data for lead (the pressure marker), Ni and WC (components of the Paris-Edinburgh cell anvils), and ice-VII (arising from the residual water in the sample).

The refinement of the structure of serine hydrate-II was carried out in an analogous fashion using X-ray data collected at 5.2 GPa and neutron data collected at 5.8 GPa, except that (*i*) the serine ADPs used for the X-ray modelling were constrained according to the TLS formalism, and (*ii*) the N1-C2 distance was restrained to 1.48 Å. The pressure difference between the neutron and X-ray data is larger than in the case of the phase-I X-N refinement described above.

A refinement in which the positions and orientations of the molecules were varied independently for the neutron and X-ray data sets was tested, though this did not yield any improvement in data fitting, and there is no evidence from improvements in data-fitting that differences between serine-h_7 and serine-d_7 need to be taken into account. They may be present, but if so they are beyond the resolution of our experiments.

The final fits obtained using the refined structures of phase-I at 3.8 GPa and phase-II at 5.8 GPa to the experimental neutron diffraction data are given in Figure 2.1. Listings of crystal and refinement data are given in Table 2.1.

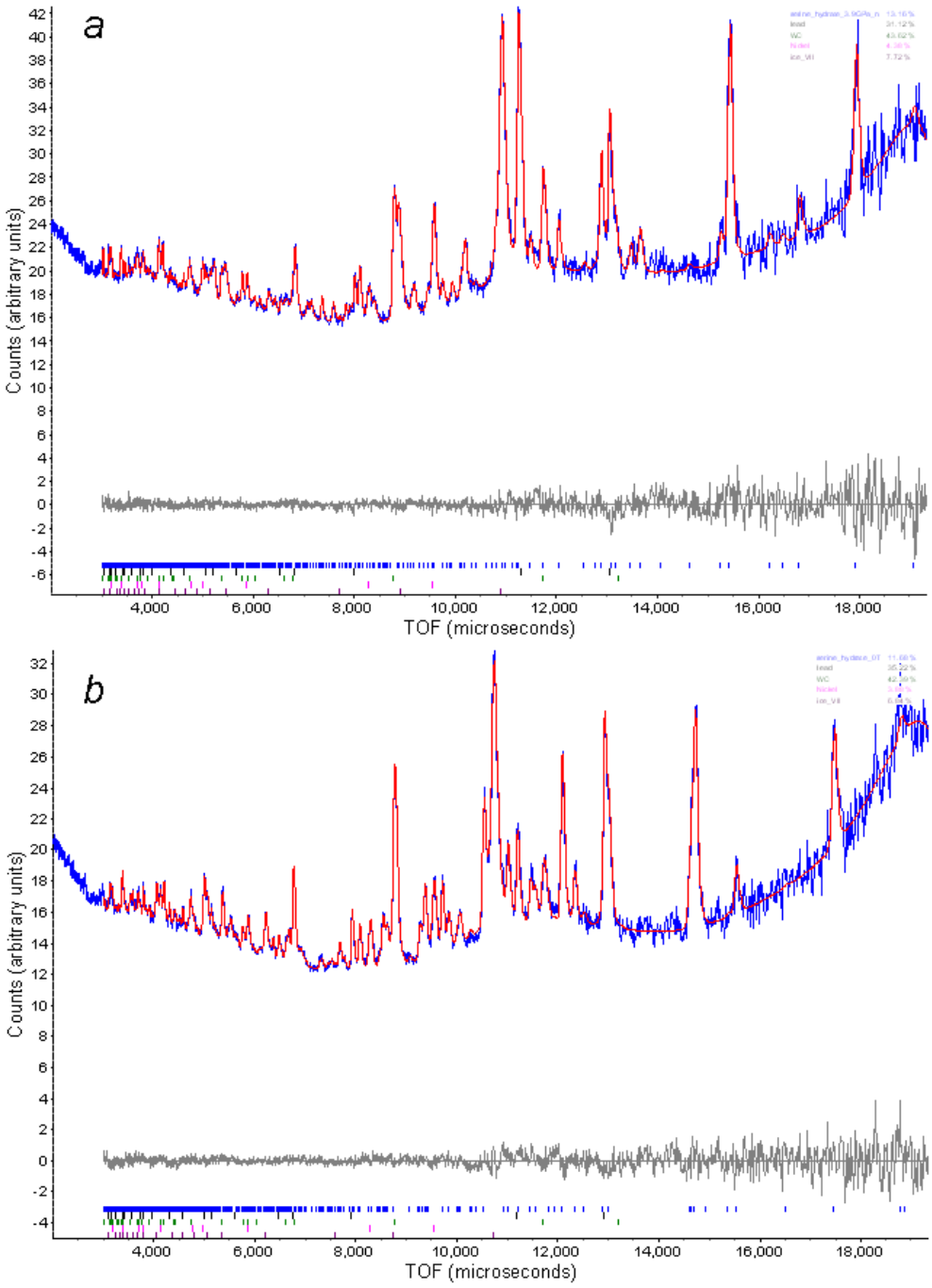

Figure 2.1: Final neutron diffraction Rietveld fits for (*a*) L-serine monohydrate phase-I at 3.8 GPa and (*b*) phase-II at 5.8 GPa. The observed and calculated patterns are given in blue and red respectively. The difference between the two is shown in grey.

Pressure/GPa	1.0	2.6	3.7	3.8
Phase	I	I	I	I
Sample type and radiation used	X-ray single crystal	X-ray single crystal	X-ray single crystal	Neutron powder
Chemical formula	$C_3H_9NO_4$	$C_3H_9NO_4$	$C_3H_9NO_4$	$C_3D_9NO_4$
M_r	123.11	123.11	123.11	132.13
Cell setting, space group	Orthorhombic, $P2_12_12_1$	Orthorhombic, $P2_12_12_1$	Orthorhombic, $P2_12_12_1$	Orthorhombic, $P2_12_12_1$
a, b, c (Å)	9.3344 (6) 11.822 (3) 4.7387 (3)	9.3563 (6) 11.443 (2) 4.6166 (3)	9.3706 (6) 11.204 (2) 4.5341 (3)	9.3701 (14) 11.1831 (10) 4.5294 (6)
V (Å^3)	522.92 (14)	494.28 (10)	476.02 (10)	474.62 (10)
Z	4	4	4	4
D_c (Mg m^{-3})	1.564	1.654	1.718	1.849
No. of measured, independent and observed [$I > 2.0\sigma(I)$] reflections	2795, 306, 256	2930, 311, 264	2574, 288, 233	N/A
R_{int}	0.099	0.090	0.124	N/A
d_{max}, d_{min} (Å)	4.7, 0.8	7.3, 0.8	4.7, 0.8	4.1,0.6
$R[F^2 > 2\sigma(F^2)]$, $wR(F^2)$, S	0.041, 0.043, 1.07	0.042, 0.050, 0.99	0.043, 0.078, 1.56	R_p = 1.956, R_{wp} = 1.565, R_{exp} = 1.395, S = 1.12
Reflection/profile data	299 reflections	307 reflections	275 reflections	2272 data points.
No. of parameters	100	100	Joint X-N refinement with 131 parameters	
$\Delta\rho_{max}$, $\Delta\rho_{min}$ (e Å^{-3})	0.18, –0.19	0.15, –0.19	0.21, –0.18	N/A
Completeness to 0.84 Å	40.9%	51%	48.8%	N/A

(a)

Pressure/GPa	4.5	5.2	5.8
Phase	I	II	II
Sample type and radiation used	X-ray single crystal	X-ray single crystal	Neutron powder
Chemical formula	$C_3H_9NO_4$	$C_3H_9NO_4$	$C_3D_9NO_4$
M_r	123.11	123.11	132.13
Cell setting, space group	Orthorhombic, $P2_12_12_1$	Orthorhombic, $P2_12_12_1$	Orthorhombic, $P2_12_12_1$
a, b, c (Å)	9.3728 (5) 11.0359 (17) 4.4782 (3)	9.8778 (13) 10.155 (4) 4.4175 (7)	9.8641 (14) 10.0991 (9) 4.3986 (7)
V (Å^3)	463.21 (8)	443.1 (2)	438.18 (10)
Z	4	4	4
D_c (Mg m^{-3})	1.765	1.845	2.003
No. of measured, independent and observed [$I > 2.0\sigma(I)$] reflections	2738, 299, 251	2207, 276, 174	N/A
R_{int}	0.101	0.177	N/A
d_{max}, d_{min} (Å)	4.7, 0.8	5.0, 0.8	4.1,0.6
$R[F^2 > 2\sigma(F^2)]$, $wR(F^2)$, S	0.038, 0.044, 0.84	0.074, 0.111, 1.67	R_p = 1.829, R_{wp} = 1.484, R_{exp} = 1.226, S = 1.21
Reflection/profile data	298 reflections	253 reflections	2272 data points
No. of parameters	100	Joint X-N refinement with 109 parameters	
$\Delta\rho_{max}$, $\Delta\rho_{min}$ (e Å^{-3})	0.22, –0.20	0.29, –0.36	N/A
Completeness to 0.84 Å	44.7%	46.4%	N/A

(b)

Table 2.1: Experimental Details. For comparison, cell data at ambient temperature and pressure determined by Frey *et al.* (1973) by single crystal neutron diffraction are: a = 9.365(7), b = 12.239(9), c = 4.835(7) Å. All data sets were collected at room temperature.

2.3.4 PIXEL calculations

The final crystal structures obtained were used to calculate in separate calculations the molecular electron densities of the serine and water molecules at each pressure by standard quantum chemical methods using the program GAUSSIAN98 (Frisch *et al.*, 1998) with the MP2/6-31G** basis set. The calculations are sensitive to H-atom positions (which become difficult to determine especially at higher pressures), and H-atom distances were set to standard neutron values in all calculations (C-H = 1.083 Å, N-H = 1.009 Å, O-H = 0.983 Å). The electron density model of the molecule was then analysed using the program package OPiX (Gavezzotti, 2003) which allows the calculation of dimer and lattice energies. The output from these calculations yields a total energy and a breakdown into its Coulombic (electrostatic), polarisation, dispersion and repulsion components (Gavezzotti, 2005, 2007).

2.3.5 Other programs used

Crystal structures were visualized using the programs CAMERON (Watkin *et al.*, 1993), MERCURY CSD 2 (Bruno *et al.*, 2002) and DIAMOND (Brandenburg & Putz, 2005). Analyses were carried out using PLATON (Spek, 2004), as incorporated in the WIN-GX suite (Farrugia, 1999). Searches of the Cambridge Structural Database (Allen, 2002) utilized the program CONQUEST with database updates up to November 2007.

2.4 Results

2.4.1 The effect of pressure on the structure of L-serine monohydrate-I

The structure of L-serine monohydrate-I has been characterised previously using single crystal neutron diffraction (Frey *et al.*, 1973). Serine molecules were

found to be connected into C(5) chains[†] formed along the a-axis via ammonium-carboxylate N1H5…O2 interactions (Figure 2.2a).

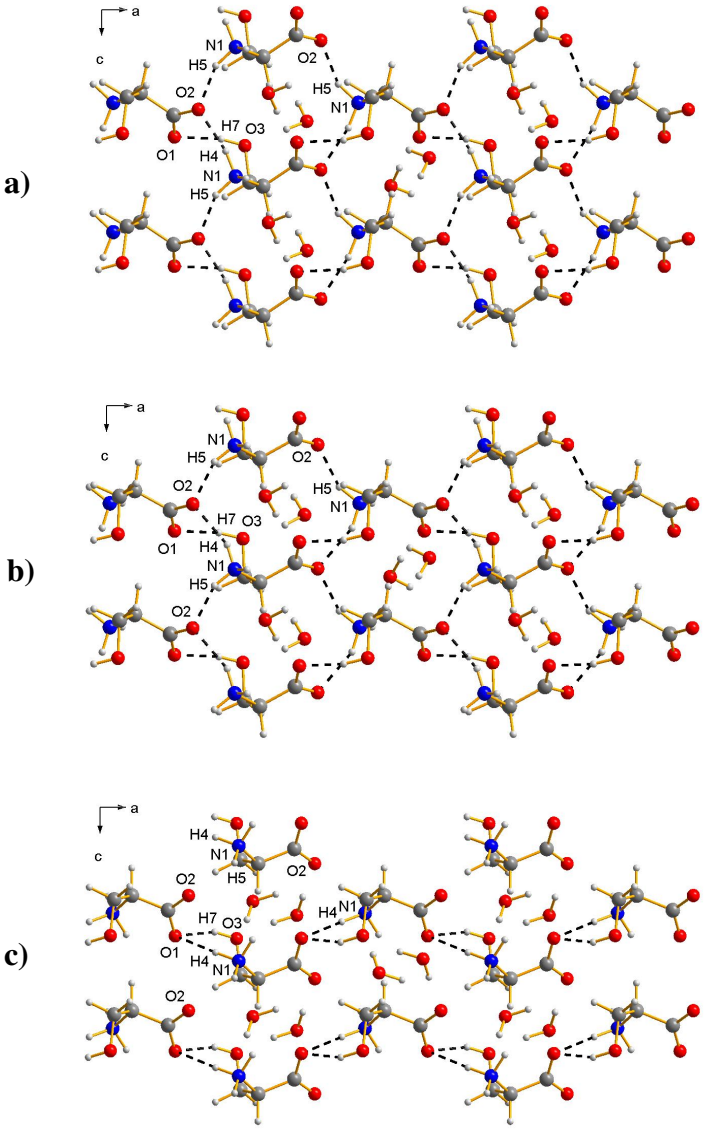

Figure 2.2: L-Serine Monohydrate I (a) at ambient pressure (Frey *et al.*, 1973), (b) at 3.8 GPa and L-Serine Monohydrate II (c) at 5.8 GPa viewed along the *b*-axis.

[†] Here $C(5)$ and $R^4_4(20)$ are graph set descriptors of hydrogen bonding motifs. $C(5)$ refers to a chain motif where the repeat unit in the chain is five atoms in length; $R^4_4(20)$ refers to a 20-membered ring motif containing four H-bond donors and four H-bond acceptors.

Pairs of molecules connected by O3H7…O1 and N1H4…O2 interactions link the C(5) chains into a sinusoidal layer (Figure 2.2a). Taken on their own the O3H7…O1 build primary-level C(6) chains, and together the C(5) and C(6) chains form a secondary-level $R_4^4(20)$ ring motif (Bernstein *et al.*, 1995).

The layers are parallel to the (010) plane and they are linked together via H-bonding contacts involving the water of crystallisation (Figure 2.3a). Each water molecule acts a double H-bond donor: an O4H9…O3 (alcohol) contact is formed to one layer, and an O4H8...O1 carboxylate contact to the layer below. The water is a single H-bond acceptor through an N1H6…O4 contact made to the same layer as the donor contact to the carboxylate function. There are no H-bonds formed between water molecules.

On increasing the hydrostatic pressure on L-serine monohydrate-I there is an anisotropic response in the unit-cell parameters (Figure 2.4). The crystal system is orthorhombic, and the principal axes of the strain tensor coincide with the crystallographic axes. The *b*-axis undergoes the greatest reduction in length (9.7%) between ambient pressure and 4.5 GPa. This corresponds to a change in the serine-serine layer distance from 6.2 Å at ambient pressure to 5.5 Å at 4.5 GPa (then to 5.1 Å at 5.2 GPa). While the *c*-axis shortens by 7.4%, the length of the a-axis is not very sensitive to pressure, and actually appears to increase. The variation of the unit cell volume is also shown in Figure 2.4.

The bulk modulus (K_0), refined for a Birch-Murnaghan equation-of-state (Birch, 1947; Angel, 2002) to second order is 18.9(3) GPa. The data set used to calculate this quantity is admittedly rather limited, and the values of V_0, K' and K'' were fixed at 1424.3 $Å^3$, 4 and -0.1337 GPa^{-1}, respectively. Molecular solids typically have $K_0 < 30$ GPa, (Angel, 2004) and the following K_0 values are useful for comparison: $Ru_3(CO)_{12}$ (6.6 GPa), salicylaldoxime (13.3 GPa), NaCl (25 GPa), cystine (29.1 GPa), quartz (37 GPa), ceramics (50-300 GPa) and diamond (440 GPa) (Moggach, Allan, Parsons *et al.*, 2005; Slebodnick *et al.*, 2004; Wood *et al.*, 2006).

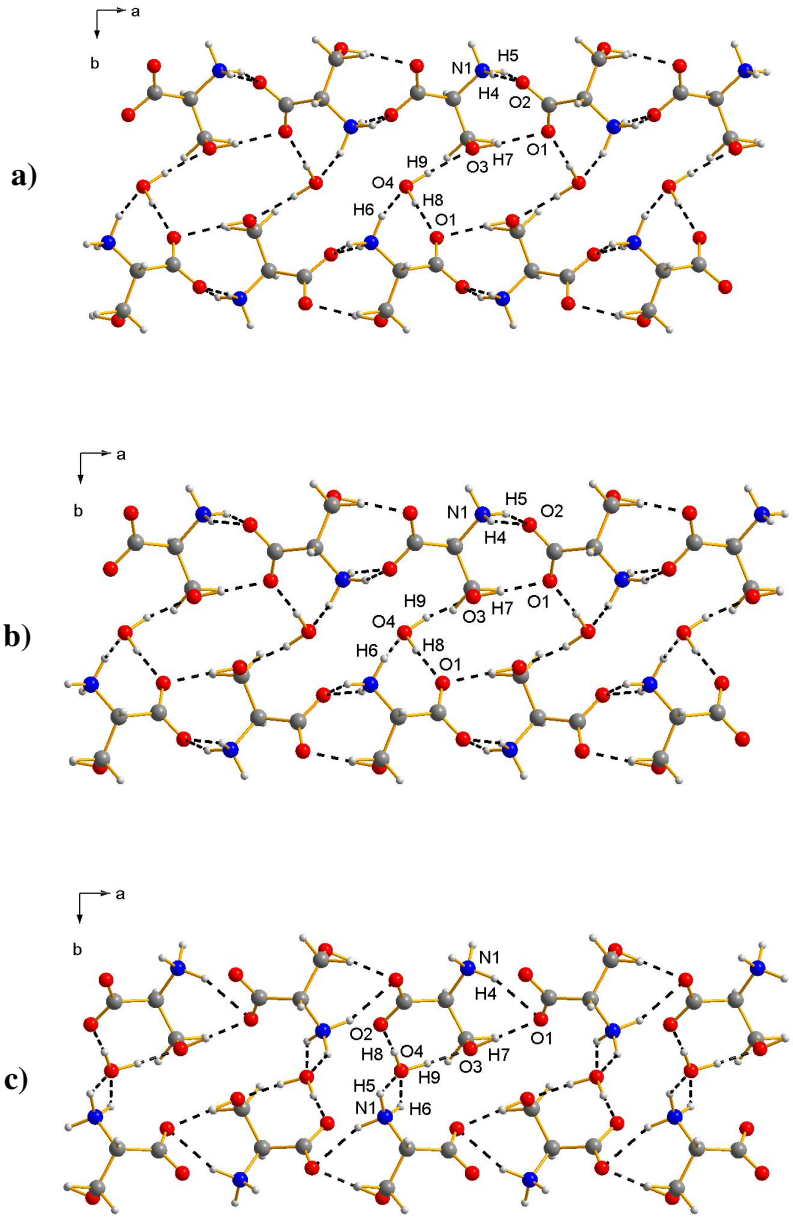

Figure 2.3: L-Serine Monohydrate I (a) at ambient pressure (Frey *et al.*, 1973), (b) at 3.8 GPa and L-Serine Monohydrate II (c) at 5.8 GPa. In (c), O4 appears to form H-bonds to H5 and H6 on the same ammonium group. This is an artefact of the projection: H5 and H6 actually derive from different molecules related by a cell repeat along *c* (Table 2.3).

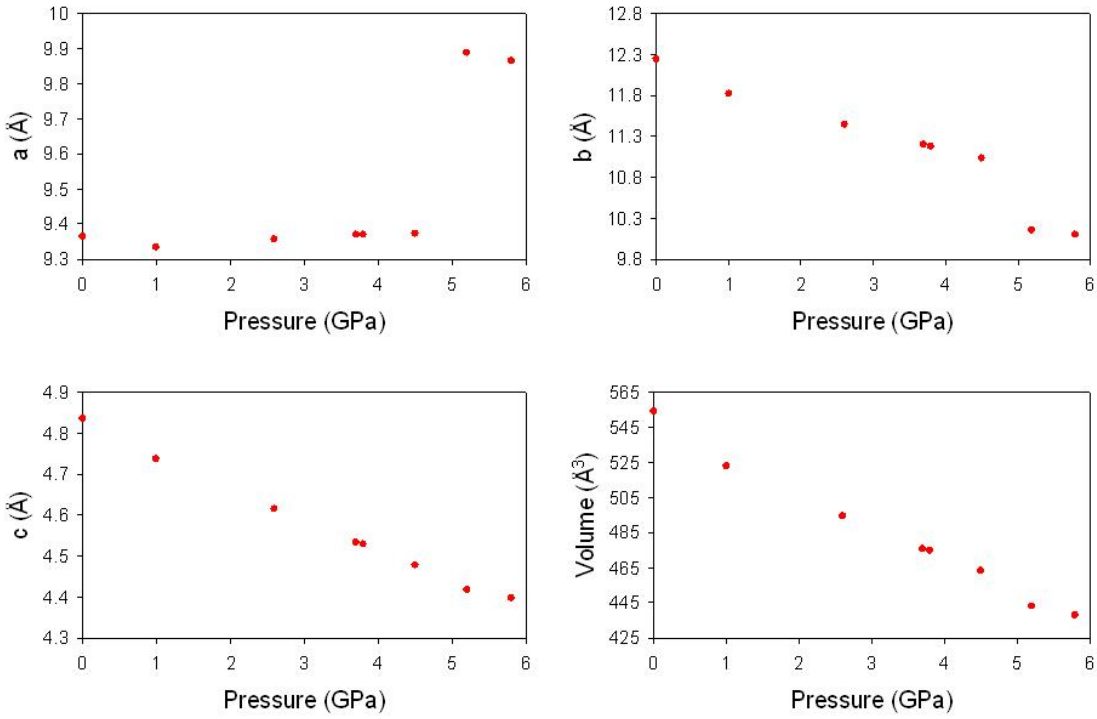

Figure 2.4: Variation of the lattice parameters (*a*, *b* and *c*) and volume of L-serine monohydrate as a function of pressure.

The structure of L-serine monohydrate-I at 3.8 GPa was derived from a joint X-N refinement against single-crystal synchrotron X-ray data and neutron powder data. It is gratifying to note that the standard uncertainties of the bond distances at high pressure are mostly around 0.002 Å (see Table 2.2), and of a similar order of magnitude to those obtained with single-crystal X-ray data under ambient conditions.

Primary bond distances and angles at ambient pressure and 3.8 GPa are compared in Table 2.2. C1-C2 and the C-O distances in the carboxylate group all appear to be slightly shorter at 3.8 GPa than ambient pressure, the differences amounting to about 5σ. Torsion angles (τ) were refined freely, and changes in these parameters are significant, but modest. The largest change up to 3.8 GPa is in τ(N1-C2-C1-O1), which changes from 2.1(3)° to 5.1(8)°.

Atoms Involved	Ambient	3.8 GPa	5.8 GPa
C1-C2/Å	1.527(3)	1.517(2)	1.522(3)
C1-O1/Å	1.248(3)	1.234(2)*	1.254(3)*
C1-O2/Å	1.251(3)	1.233(2)*	1.253(3)*
C2-C3/Å	1.519(3)	1.515(2)	1.521(3)
C2-N1/Å	1.488(2)	1.485(6)	1.475(3)†
C3-O3/Å	1.413(4)	1.406(4)	1.424(7)
<C2-C1-O1/°	118.6(2)	118.0(3)	118.3(3)
<C2-C1-O2/°	116.3(2)	117.2(3)	116.8(4)
<O1-C1-O2/°	125.1(2)	124.8(5)	124.9(5)
<C1-C2-C3/°	110.9(2)	110.2(2)	110.7(3)
<C1-C2-N1/°	110.6(1)	110.0(3)	109.4(3)
<C3-C2-N1/°	111.2(2)	111.6(4)	111.4(5)
<C2-C3-O3/°	111.8(2)	108.8(4)	109.9(5)
τ O1-C1-C2-N1/°	2.1(3)	5.1(8)	-6.3(11)
τ O1-C1-C2-C3/°	126.0(2)	128.5(8)	116.9(10)
τ C1-C2-C3-O3/°	-53.3(2)	-53.9(12)	-63.7(17)
τ N1-C2-C3-O3/°	70.3(2)	68.7(12)	58.4(18)
τ O2-C1-C2-N1/°	-179.2(2)	-174.9(6)	173.7(9)
τ O2-C1-C2-C3/°	-55.3(3)	-51.5(8)	-63.2(10)
τ C1-C2-N1-H4/°	68.7(4)	72.1(14)	130.4(14)
τ C1-C2-N1-H5/°	-168.9(3)	-167.8(14)	109.6(15)
τ C1-C2-N1-H6/°	-54.5(4)	-47.6(14)	10.5(18)

* Subject to similarity restraints (see experimental).

† Restrained to 1.48 Å.

Table 2.2: Intramolecular bond distances, angles (<) and torsions (τ) at ambient pressure (Frey *et al.*, 1973), 3.8 and 5.8 GPa. Frey *et al*. do not quote s.u.s on torsion angles, and so for consistency all torsion angle s.u.s were calculated using variances only in PLATON. Those which can be calculated in TOPAS with the full variance-covariance matrix are slightly lower, for example, τ(O1-C1-C2-N1) at 3.8 GPa and 5.8 GPa are 5.1(3) and -6.3(4)° respectively.

The hydrogen bond parameters for L-serine monohydrate-I between ambient pressure and 3.8 GPa are given in Table 2.3. Within the serine layers (Figure 2.2b) the largest compression occurs for the O3H7…O1 contact, while N1H4…O2 actually appears to increase in length. The water-serine interactions in which the water acts as a hydrogen bond donor decrease in length by 0.13 Å. Consistently, the largest eigenvector of the strain tensor lies along [010], the direction of stacking of the serine layers, and, as noted above, the most prominent effect of pressure is to compress the serine layers together (Figure 2.3b).

2.4.2 The structure of L-serine monohydrate-II

L-serine monohydrate-I is stable to 4.5 GPa; on increasing the pressure to 5.2 GPa the sample underwent a single-crystal-to-single-crystal transition to a new phase, which we refer to as L-serine monohydrate-II. The structure of L-serine monohydrate-II was obtained from a joint X-N refinement against single crystal synchrotron X-ray data (5.2 GPa) and neutron powder data (5.8 GPa). In the following analysis we focus on structural parameters from neutron diffraction at 5.8 GPa, drawing comparisons with those in phase I at 3.8 GPa.

The only significant difference in the primary bond distances and angles (Table 2.2) in phase I at 3.8 GPa and phase II at 5.8 GPa occurs in the carboxylate C-O bond distances (which were restrained to be equal in both refinements), which increase by *ca* 0.02 Å. This effect has also been noted for the carbonyl bond in paracetamol at 4 GPa (Boldyreva *et al.*, 2000). Torsion angles involving non-hydrogen atoms change by relatively small amounts, the largest changes relate to the carboxylate group which rotates about the C1-C2 vector by *ca.* 11.5˚ (Table 2.2).

Much more significant are changes in the orientation of the ammonium group, which rotates anti-clockwise by approximately 52˚ about the vector of the C2-N1 bond. The approximately eclipsed conformation of the ammonium group with respect to the groups attached to C2 was clearly visible in a Fourier map calculated using the neutron data.

H-bond	Ambient (Frey *et al.*, 1973)		3.8 GPa		5.8 GPa	
	Geometry (Å, °)	PIXEL Energy (kJ mol^{-1})	Geometry (Å, °)	PIXEL Energy (kJ mol^{-1})	Geometry (Å, °)	PIXEL Energy (kJ mol^{-1})
O3H7…O1^{i} <O3H7O1	1.843(6) 166.8(4)	-128.4	1.70(3) 169(2)	-120.7	1.68(4) 160(2)	-109.4
N1H4…O2^{i} <N1H4O2	1.901(6) 168.1(4)		1.969(15) 155.1(12)		2.420(19) 130.6(11)	
N1H4…O1^{i} <N1H4O1	- -		- -		2.18(2) 161.0(3)	
N1H5…O2^{ii} <N1H5O2	1.804(6) 153.4(4)	-76.0	1.784(17) 152.3(12)	-81.0	2.41(3) 97.4(11)	-72.1
N1H5…O4^{iii} <N1H5O4	- -	- -	- -	- -	1.81(2) 140.7(11)	-58.0
N1H6…O4^{iii} <N1H6O4	2.130(7) 132.4(4)	-50.6	2.134(18) 121.0(11)	-49.7	3.17(2) 53.5(8)	- -
N1H6…O4^{iv} <N1H6O4	- -	- -	- -	- -	1.902(16) 146.1(13)	-26.4
O4H8…O1^{iii} <O4H8O1	1.868(6) 173.2(5)	-49.2	1.739(15) 172.2(18)	-52.9	- -	- -
O4H8…O2^{ii} <O4H8O2	- -	- -	- -	- -	1.659(18) 174(2)	-24.5
O4H9…O3^{i} <O4H9O3	1.922(7) 177.4(5)	-1.6	1.80(2) 169(2)	+4.5	1.66(3) 174(2)	+6.8

Symmetry Operators

i	-1/2+*x*,1/2-*y*,1-*z*
ii	-1/2+*x*,1/2-*y*,-*z*
iii	1/2-*x*,-*y*,-1/2+*z*
iv	1/2-*x*,-*y*,1/2+*z*

Table 2.3: Hydrogen bonding parameters, with corresponding molecule-molecule PIXEL energies, at ambient pressure, 3.8 and 5.8 GPa.

A single-crystal to single-crystal phase change usually implies that the overall topology of each phase remains the same. This is the case for L-serine monohydrate-II, which displays layers of L-serine molecules formed parallel to the (010) planes (Figure 2.3c). The layers are still sinusoidal, but with a smaller amplitude than in phase-I, which results in a lengthening of the *a*-axis (*cf* Figures 2.2b and c).

Within the layers of serine molecules (Figure 2.2c), the hydrogen bond from the alcohol group (O3H7…O1) is retained through the phase transition. By contrast, the phase-I hydrogen bonds involving the ammonium groups are both broken: N1H5…O2 lengthens by 0.62(3) Å, effectively cleaving the $R_4^4(20)$ ring motif, while N1H4…O2 lengthens by 0.45(2) Å. These changes occur as a result of the rotation of the ammonium group. In phase-II N1H5 forms a new hydrogen bond to the water of crystallisation (O4). N1H4 interacts with the same carboxylate group as in phase-I, forming an H-bond to O1 instead of O2.

In phase-I H-bond donor interactions from the water molecules bridged the serine layers. During the phase transition the water molecule rotates about an axis very close to the O4H9…O3 bond, so that in phase-II both donor interactions are formed to the same layer: the O4H8…O1 contacts formed in phase-I are replaced by O4H8…O2 (*cf.* Figures. 2.3b and c). The interactions in which O4 acts as an acceptor also change as a result of the rotations of the ammonium groups and water molecules. N1H6…O4 breaks and reforms to an oxygen on a different water molecule. In the process a new hydrogen bond is formed to the original water molecule from N1H5. The water of crystallization in phase-II is coordinatively saturated, forming two donor and two acceptor interactions in a tetrahedral arrangement.

2.5 Discussion

2.5.1 PIXEL analysis of intermolecular interaction energies

Overall, the phase transition from serine monohydrate-I to II can be characterized by (*i*) an abrupt decrease of the serine-serine interlayer distance, (*ii*) a change in the orientation of the water of crystallization between the serine layers, and (*iii*) a change in the orientation of the ammonium groups. So far we have presented a conventional analysis of the changes which occur in the crystal structure of L-serine monohydrate based on intermolecular distances. The PIXEL procedure, which has been developed recently by Gavezzotti, enables further insight to be gained by calculation of intermolecular interaction energies. Full details of the PIXEL method,

which has recently been extended to systems with two molecules in the asymmetric unit, are available in Gavezzotti (2007). Application of the PIXEL method to high pressure structures has recently been validated in a joint PIXEL/DFT study on serine (Wood, Francis *et al.*, 2008). PIXEL calculations were carried out on the crystal structures of L-serine monohydrate determined at the pressures reported here.

The total molecule-molecule interaction energies associated with the H-bonding interactions described in the *Results* section are listed in Table 2.3. The strongest interactions in both phases I and II are the charge-assisted H-bonds within the serine layers. The electrostatic term is the dominant contribution in all cases. For example, the first entry (-128.4 kJ mol^{-1}) in Table 2.3 breaks down as follows: Coulombic: -143.8 kJ mol^{-1}, polarisation: -51.5 kJ mol^{-1}, dispersion; -23.8 kJ mol^{-1}, repulsion: 90.7 kJ mol^{-1}. Even though the N1H5…O2 H-bond is formally broken during the I-to-II transition according to the usual geometric criteria, the interaction energy between the two molecules involved is still substantial (-72.1 kJ mol^{-1}) because of the close disposition of the positive ammonium and negative carboxylate groups.

The shortest serine-serine centroid-centroid distance that occurs within the layers (4.82 Å at ambient pressure) is formed across the $R^4_4(20)$ rings between molecules related by a *c*-lattice repeat. This interaction is actually repulsive (+24.7 kJ mol^{-1}, not listed in Table 2.3) because it brings similarly-charged moieties into close proximity. The structure can sustain repulsive interactions because they are out-weighed by attractive forces with larger magnitudes. This effect has also been noted by Gavezzotti in glycine (Gavezzotti, 2002), and similar comments can be applied to the repulsive Na…Na and Cl…Cl interactions present in the structure of NaCl.

The water molecules in phase-I appear to be coordinatively unsaturated with respect to H-bonding, forming two donor and one acceptor interactions (Fig 2.3a and b). The second lone pair acceptor interacts with an NH_3^+ group, which, though it does not form a geometrically typical H-bonding interaction, nevertheless forms a substantial contact with an energy of -25.3 kJ mol^{-1} at ambient pressure.

The O4H9…O3 H-bond (see Table 2.3) has an almost negligibly small energy, -1.6 kJ mol^{-1}, which is surprising given that the O…O, H…O and <OH…O parameters associated with this contact make it appear to be a medium strength interaction. The energy quoted here refers to the total molecule-molecule contact, and its low value may be ascribable to the electrostatic repulsion between O4 and O2, which are both negatively charged, and only 3.15 Å distant (at ambient pressure). In addition, the O4-H9 vector points between the two lone pairs on the alcohol oxygen atom (O3), making the geometry less favourable than it appeared to be on the basis of the geometric parameters around H9 alone. A similarly weak H-bonding contact was noted in serine itself (Wood, Francis *et al.*, 2008).

In addition to 'normal' intermolecular interactions, such as H-bonds, there are numerous longer-range (*ca.* 6 Å) serine-serine Coulombic interactions. The strongest of these (-48.1 kJ mol^{-1} at ambient pressure rising to -94.3 kJ mol^{-1} in phase-II at 5.8 GPa) occurs between the layers of serine, spanning the water molecules. Although water-serine H-bonding interactions are certainly present, and can be said to bind the molecules of the serine layer together, this interpretation overlooks the importance of the longer range Coulombic serine…serine interactions, which have energies similar to or greater than the H-bonding contacts.

2.5.2 What drives the transition from phase-I to II?

The intermolecular lattice energies and a breakdown into the component terms for each structure of L-Serine Monohydrate from ambient pressure up to 5.8 GPa were calculated and are displayed in Table 2.4. PIXEL calculations only take into account *inter*molecular interactions, and energy changes associated with conformation changes within the serine molecules are not considered. Therefore an adjustment to the total energy was calculated as the total lattice energy minus the difference in internal energy of the molecule (as calculated by GAUSSIAN98), and this is listed in Table 2.4 as U_{adj}. Although the conformational change through the phase transition is substantial, the internal energy of the serine molecules appears to change by, at most, 1 kJ mol^{-1}.

Pressure/ GPa	Coulombic	Polarisation	Dispersion	Repulsion	U	U_{adj}	H
0 (Frey *et al.*, 1973)	-375.3	-137.3	-112.2	254.3	-370.5	-370.5	-370.5
1	-386.1	-148.3	-123.9	298.6	-359.7	-360.7	-282.0
2.6	-421.7	-169.4	-139.7	375.9	-354.9	-355.0	-161.5
3.7	-440.9	-181.9	-150.9	425.9	-347.8	-348.0	-82.8
3.8	-442.4	-182.6	-151.8	429.6	-347.2	-347.5	-75.9
4.5	-456.0	-191.4	-159.1	458.2	-348.3	-348.4	-34.5
5.2	-463.2	-212.6	-177.3	519.6	-333.5	-333.8	13.2
5.8	-474.1	-218.2	-180.9	541.2	-332.0	-332.3	50.4

Table 2.4: Components of the lattice energy and enthalpy in L-serine monohydrate-I and II as a function of pressure. All energies are in kJ mol^{-1}. U is the total intermolecular energy. U_{adj} includes a correction for the internal energy difference due to conformation change relative to ambient pressure structure. This was evaluated using GAUSSIAN98 at the MP2/6-31G** level. The enthalpy (H) at each pressure is also listed. $H = U_{adj} + PV$, where P = pressure (in Pascals) and V = molar volume (in $m^3\ mol^{-1}$).

The largest contribution to the total energy is from the Coulombic and repulsion terms, as is expected for a structure containing zwitterions. The value of U_{adj} becomes more positive as pressure is increased, reflecting the large increase in the repulsive interactions between molecules. It is notable that the internal energy becomes slightly *less negative* than would be expected from extrapolation from the phase-I trend through the phase transition at 5.2 GPa (black points in Figure 2.5).

Also listed in Table 2.4 is the value of the lattice enthalpy, $H = U_{adj} + PV$, which also becomes more positive as pressure increases (Figure 2.5). The variation of the lattice enthalpy of phase-I is essentially linear with pressure, and extrapolation

of the trend line confirms that phase-II becomes marginally more stable than phase-I beyond 5 GPa.

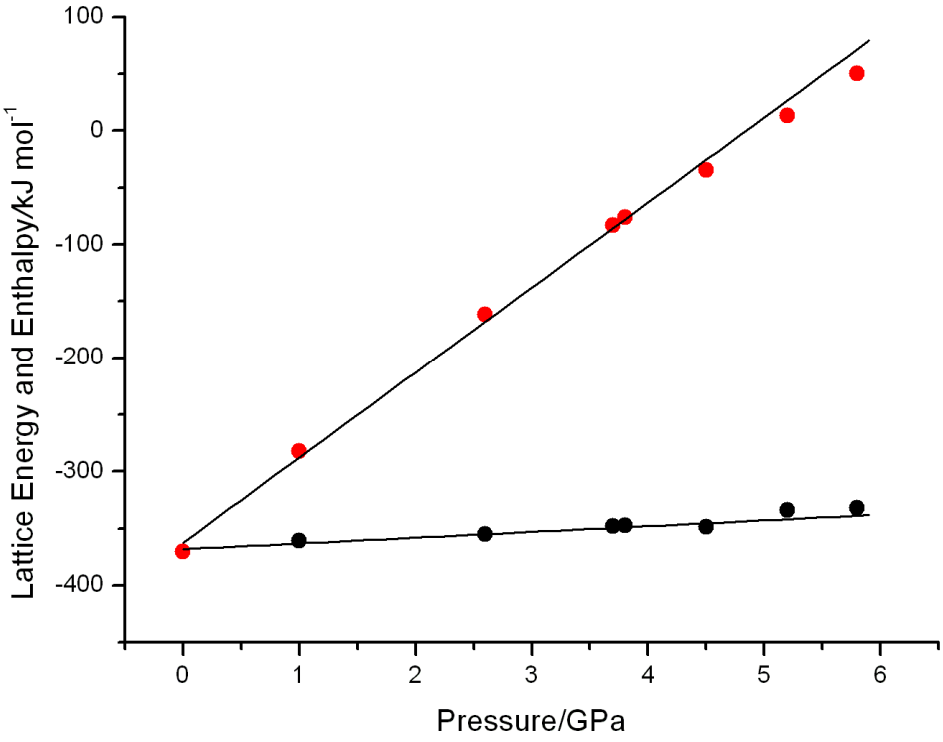

Figure 2.5: Graph showing lattice enthalpy (red points) and U_{adj} (black points) values of L-serine monohydrate I and II at corresponding pressures. The trend lines were calculated using data between 0 and 4.5 GPa (phase-I).

Assuming that the linear relationship between *H* and *P* continues beyond 5 GPa the magnitude of the energy difference between the two polymorphs at 5.2 GPa is estimated to be *ca.* 13 kJ mol^{-1}. This assumption is no doubt an over-simplification, but the energy differences seen here are broadly consistent with Bernstein's observation (Bernstein, 2002) that energy differences between polymorphs are usually no larger than about 10 kJ mol^{-1}. This also illustrates the importance of the inclusion of the *PV* term in the energy calculations: the energetic preference for phase-II above 5 GPa is ascribable to the significant decrease in volume and increase in the efficiency of crystal packing.

The greater packing efficiency of phase-II can be illustrated through examination of the interstitial voids. At ambient pressure the largest voids occur between the layers of serine molecules (Figure 2.6); these voids reduce in size as pressure is increased, and this is why the largest compression occurs along *b*. The voids close-up completely through the phase transition, but as the layers of serine approach one another the water molecules reorientate. A corresponding change in the orientation of the ammonium groups is needed to re-establish favorable H-bonds.

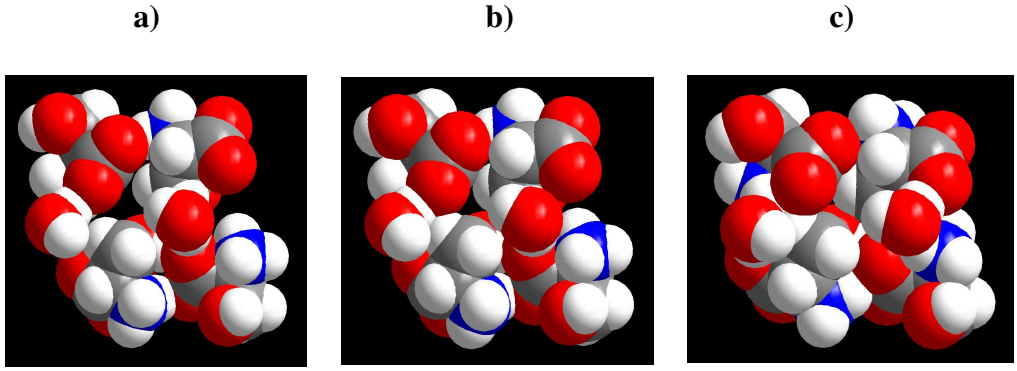

Figure 2.6: Voids occurring between the sheets of serine at a) ambient pressure, b) 3.8 GPa and c) 5.8 GPa

2.6 Conclusions

The effects of the application of pressure on the structure of L-serine monohydrate as studied by a combination of single crystal synchrotron X-ray and neutron powder diffraction have been described. A phase transition occurs at around 5 GPa which is characterised by a diminution of the serine-serine layer distances and a change in the orientations of the water and ammonium moieties. PIXEL analysis shows that overall the intermolecular contact energies are less negative in phase II than phase I by about 15 kJ mol^{-1}. The transition can be said to be driven, not by optimisation of intermolecular contacts, but by the need to reduce the *PV* term which contributes to the lattice enthalpy.

These conclusions parallel those derived from the study on L-serine, where the transition from phase-I to II also occurs between 4.5 and 5.2 GPa. A change in molecular conformation results in a substantial (40 kJ mol^{-1}) stabilisation of the molecular internal energy, and the phase transition was said to be driven by *both* the conformation change and a lowering of the molecular volume. In L-serine monohydrate the change in conformation of the ammonium group has almost no effect on the internal energy of the serine molecules, and the transition can be explained purely in terms of the *PV* contribution to the lattice enthalpy.

Amino acids are rather poor models for proteins. They are zwitterionic, whereas, by and large, the residues which form proteins are not. This means that the energies which characterise residue-residue interactions are much smaller and shorter range than those which have seen shown to occur between serine molecules. However, it is known that pressure can be used to denature proteins, and it is possible that the work described here sheds some light on the mechanism by which this occurs.

Theoretical modelling has been used to suggest that pressure-induced denaturation occurs because water molecules are forced from the hydrophilic protein exterior towards the hydrophobic core. If this is correct then water molecules must move a substantial distance (10s of Å) under the influence of pressure. In the phase transition from serine monohydrate-I to II water molecules are forced into a layer of serine molecules, disrupting the hydrogen bonding within the layer. It seems possible to us that a similar mechanism may apply as a first step in protein denaturation: water molecules are forced by pressure to embed into the outer regions of the protein structure, causing disruption of α-helices and β-sheets which comprise the secondary structure.

2.7 References

Allan, D. R. & Clark, S. J. (1999a). *Physical Review B: Condensed Matter and Materials Physics* **60**, 6328-6334.

Allan, D. R. & Clark, S. J. (1999b). *Physical Review Letters* **82**, 3464-3467.

Allan, D. R., Clark, S. J., Brugmans, M. J. P., Ackland, G. J. & Vos, W. L. (1998). *Physical Review B* **58**, R11809-R11812.

Allan, D. R., Clark, S. J., Dawson, A., McGregor, P. A. & Parsons, S. (2002). *Acta Crystallographica, Section B* **58**, 1018-1024.

Allan, D. R., Clark, S. J., Ibberson, R. M., Parsons, S., Pulham, C. R. & Sawyer, L. (1999). *Chemical Communications* **8**, 751-752.

Allan, D. R., Parsons, S. & Teat, S. J. (2001). *Journal of Synchrotron Radiation* **8**, 10-17.

Allen, F. H. (2002). *Acta Crystallographica, Section B* **58**, 380-388.

Altomare, A., Cascarano, G., Giacovazzo, C., Guagliardi, A., Burla, M. C., Polidori, G. & Camalli, M. (1994). *Journal of Applied Crystallography* **27**, 435-435.

Angel, R. J. (2002). *Reviews in Mineralogy and Geochemistry* **41**, 35-59.

Angel, R. J. (2004). High Pressure Crystallography. NATO Science Series II, edited by A. Katrusiak & P. F. McMillan, pp. 21-36.

Bernstein, J. (2002). Polymorphism in Molecular Crystals. Oxford, UK: Oxford University Press.

Betteridge, P. W., Carruthers, J. R., Cooper, R. I., Prout, K. & Watkin, D. J. (2003). *Journal of Applied Crystallography* **36**, 1487.

Birch, F. (1947). *Physical Review* **71**, 809-824.

Boldyreva, E. V. (2008). *Acta Crystallographica, Section A* **64**, 218-231.

Boldyreva, E. V., Ivashevskaya, S. N., Sowa, H., Ahsbahs, H. & Weber, H.-P. (2005). *Zeitschrift fuer Kristallographie* **220**, 50-57.

Boldyreva, E. V., Shakhtshneider, T. P., Vasilchenko, M. A., Ahsbahs, H. & Uchtmann, H. (2000). *Acta Crystallographica, Section B* **56**, 299-309.

Brandenburg, K. & Putz, H. (2005). *DIAMOND, version 3.2*. Crystal Impact GbR, Postfach 1251, 53002, Bonn, Germany.

Bruker-Nonius (2006). *SAINT version 7, Program for integration of area detector data.* Bruker-AXS, Madison, Wisconsin, USA.

Bruno, I. J., Cole, J. C., Edgington, P. R., Kessler, M., Macrae, C. F., McCabe, P., Pearson, J. & Taylor, R. (2002). *Acta Crystallographica, Section B* **58**, 389-397.

Coelho, A. A. (2007). *TOPAS-Academic.* Version 4.1. Brisbane, Australia.

Dawson, A., Allan, D. R., Belmonte, S. A., Clark, S. J., David, W. I. F., McGregor, P. A., Parsons, S., Pulham, C. R. & Sawyer, L. (2005). *Crystal Growth & Design* **5**, 1415-1427.

Dawson, A., Allan, D. R., Parsons, S. & Ruf, M. (2004). *Journal of Applied Crystallography* **37**, 410-416.

Dunitz, J. D. & Gavezzotti, A. (2005). *Angewandte Chemie, International Edition* **44**, 1766-1787.

Edwards, C. M. & Butler, I. S. (2000). *Coordination Chemistry Reviews* **199**, 1-53.

Fabbiani, F. P. A. & Pulham, C. R. (2006). *Chemical Society Reviews* **35**, 932-942.

Farrugia, L. J. (1999). *Journal of Applied Crystallography* **32**, 837-838.

Fortes, A. D. (2004). PhD thesis, University of London.

Frey, M. N., Lehmann, M. S., Koetzle, T. F. & Hamilton, W. C. (1973). *Acta Crystallographica, Section B* **29**, 876-884.

Frisch, M. J., Trucks, G. W., Schlegel, H. B., Scuseria, G. E., Robb, M. A., Cheeseman, J. R., Zakrzewski, V. G., Montgomery, J. A., Jr, Stratmann, R. E., Burant, J. C., Dapprich, S., Millam, J. M., Daniels, A. D., Kudin, K. N., Strain, M. C., Farkas, O., Tomasi, J., Barone, V., Cossi, M., Cammi, R., Mennucci, B., Pomelli, C., Adamo, C., Clifford, S., Ochterski, J., Petersson, G. A., Ayala, P. Y., Cui, Q., Morokuma, K., Malick, D. K., Rabuck, A. D., Raghavachari, K., Foresman, J. B., Cioslowski, J., Ortiz, J. V., Stefanov, B. B., Liu, G., Liashenko, A., Piskorz, P., Komaromi, I., Gomperts, R., Martin, R. L., Fox, D. J., Keith, T., Al-Laham, M. A., Peng, C. Y., Nanayakkara, A., Gonzalez, C., Challacombe, M., Gill, P. M. W., Johnson, B. G., Chen, W., Wong, M. W., Andres, J. L., Head-Gordon, M., Replogle, E. S. & Pople, J. A. (1998). *Gaussian 98, revision A.7.*

Gaultier, J., Hebrard-Bracchetti, S., Guionneau, P., Kepert, C. J., Chasseau, D., Ducasse, L., Barrans, Y., Kurmoo, M. & Day, P. (1999). *Journal of Solid State Chemistry* **145**, 496-502.

Gavezzotti, A. (2002). *Journal of Physical Chemistry B* **106**, 4145-4154.

Gavezzotti, A. (2003). *OPiX: A computer program package for the calculation of intermolecular interactions and crystal energies.*

Gavezzotti, A. (2005). *Zeitschrift fuer Kristallographie* **220**, 499-510.

Gavezzotti, A. (2007). Molecular Aggregation: Structure Analysis and Molecular Simulation of Crystals and Liquids. Oxford, UK: Oxford University Press.

Girard, E., Dhaussy, A. C., Couzinet, B., Chervin, J. C., Mezouar, M., Kahn, R., Ascone, I. & Fourme, R. (2007). *Journal of Applied Crystallography* **40**, 912-918.

Goryainov, S. V., Boldyreva, E. V. & Kolesnik, E. N. (2006). *Chemical Physics Letters* **419**, 496-500.

Goryainov, S. V., Kolesnik, E. N. & Boldyreva, E. V. (2005). *Physica B: Condensed Matter (Amsterdam, Netherlands)* **357**, 340-347.

Guionneau, P., Gaultier, J., Chasseau, D., Bravic, G., Barrans, Y., Ducasse, L., Kanazawa, D., Day, P. & Kurmoo, M. (1996). *Journal de Physique I* **6**, 1581-1595.

Guionneau, P., Marchivie, M., Garcia, Y., Howard, J. A. K. & Chasseau, D. (2005). *Physical Review B: Condensed Matter and Materials Physics* **72**, 214408/214401-214408/214408.

Hummer, G., Garde, S., Garcia, A. E., Paulaitis, M. E. & Pratt, L. R. (1998). *Proceedings of the National Academy of Sciences of the United States of America* **95**, 1552-1555.

J. Bernstein, Davis, R. E., Shimoni, L. & Chang, N.-L. (1995). *Angewandte Chemie, International Edition* **34**, 1555-1573.

Katrusiak, A. (1992). *Journal of Molecular Structure* **269**, 329-354.

Katrusiak, A. (2004). *NATO Science Series, II: Mathematics, Physics and Chemistry* **140**, 513-520.

Katrusiak, A. & Nelmes, R. J. (1986). *Journal of Physics C: Solid State Physics* **19**, L765-L772.

Kurmoo, M., Day, P., Guionneau, P., Bravic, G., Chasseau, D., Ducasse, L., Allan, M. L., Marsden, I. D. & Friend, R. H. (1996). *Inorganic Chemistry* **35**, 4719-4726.

Kuznetsov, A. Z., Dmitriev, V., Dubrovinsky, L., Prakapenka, V. & Weber, H. P. (2002). *Solid State Communications* **122**.

Le Godec, Y., Dove, M. T., Francis, D. J., Kohn, S. C., Marshall, W. G., Pawley, A. R., Price, G. D., Redfern, S. A. T., Rhodes, N., Ross, N. L., Schofield, P. F.,

Schooneveld, E., Syfosse, G., Tucker, M. G. & Welch, M. D. (2001). *Mineralogical Magazine* **65**, 737-748.

Legrand, V., Le Gac, F., Guionneau, P. & Letard, J. F. (2008). *Journal of Applied Crystallography* **41**, 637-640.

Marshall, W. G. & Francis, D. J. (2002). *Journal of Applied Crystallography* **35**, 122-125.

Merrill, L. & Bassett, W. A. (1974). *Review of Scientific Instruments* **45**, 290-294.

Miller, R. A. & Schuele, D. E. (1969). *Journal of Physics and Chemistry of Solids* **30**, 589-600.

Moggach, S. A., Allan, D. R., Clark, S. J., Gutmann, M. J., Parsons, S., Pulham, C. R. & Sawyer, L. (2006). *Acta Crystallographica, Section B* **62**, 296-309.

Moggach, S. A., Allan, D. R., Morrison, C. A., S. Parsons & Sawyer, L. (2005). *Acta Crystallographica, Section B* **61**, 58-68.

Moggach, S. A., Allan, D. R., Parsons, S., Sawyer, L. & Warren, J. E. (2005). *Journal of Synchrotron Radiation* **12**, 598-607.

Moggach, S. A., Marshall, W. G. & Parsons, S. (2006). *Acta Crystallographica, Section B* **62**, 815-825.

Moggach, S. A., Parsons, S. & Wood, P. A. (2008). *Crystallography Reviews* **14**, 143-184.

Oswald, I. D. H., Allan, D. R., Day, G. M., Motherwell, W. D. S. & Parsons, S. (2005). *Crystal Growth & Design* **5**, 1055-1071.

Oswald, I. D. H., Allan, D. R., Motherwell, W. D. S. & Parsons, S. (2005). *Acta Crystallographica, Section B* **61**, 69-79.

Parsons, S. (2004). *SHADE- Program for empirical absorption corrections to high pressure data.* The University of Edinburgh, Edinburgh, United Kingdom.

Piermarini, G. J., Block, S., Barnett, J. D. & Forman, R. A. (1975). *Journal of Applied Physics* **46**, 2774-2780.

Prescimone, A., Milios, C. J., Moggach, S. A., Warren, J. E., Lennie, A. R., Sanchez-Benitez, J., Kamenev, K., Bircher, R., Murrie, M., Parsons, S. & Brechin, E. K. (2008). *Angewandte Chemie International Edition* **47**, 2828-2831.

Sheldrick, G. M. (2004). *SADABS Version 2004-1, Program for absorption corrections to area detector data.* Bruker-AXS, Madison, Wisconsin, USA.

Slebodnick, C., Zhao, J., Angel, R., Hanson, B. E., Song, Y., Liu, Z. & Hemley, R. J. (2004). *Inorganic Chemistry* **43**, 5245-5252.

Spek, A. L. (2004). *PLATON.* Utrecht University, Utrecht, The Netherlands.

Waldorf, D. L. & Alers, G. A. (1962). *Journal of Applied Physics* **33**, 3266-3269.

Watkin, D. J., Pearce, L. & Prout, K. (1993). *CAMERON - A Molecular Graphics Package.* Chemical Crystallography Laboratory, University of Oxford, Oxford, England.

Wood, P. A., Forgan, R. S., Henderson, D., Parsons, S., Pidcock, E., Tasker, P. A. & Warren, J. E. (2006). *Acta Crystallographica, Section B: Structural Science* B **62**, 1099-1111.

Wood, P. A., Francis, D., Marshall, W. G., Moggach, S. A., Parsons, S., Pidcock, E. & Rohl, A. L. (2008). *CrystEngComm* **10**, 1154-1166.

Wood, P. A., McKinnon, J. J., Parsons, S., Pidcock, E. & Spackman, M. A. (2008). *CrystEngComm* **10**, 368-376.

Chapter 3

Comparison of the Effects of Pressure on Three Layered Hydrates: a Partially Successful Attempt to Predict High-Pressure Polymorphism*

* Johnstone, R. D. L., Lennie, A. R., Parsons, S., Pidcock, E., Warren, J. E. (2008). *Acta Crystallographica, Section B* **65**, 731-748.

3.1 Synopsis

S-4-Sulfo-L-phenylalanine monohydrate and serine monohydrate both contain layers of zwitterions separated by layers of water molecules, and both structures undergo phase transitions at high pressure involving changes in the conformations of the zwitterions and reorientations of the water molecules. The principal directions of compression in these and two other layered hydrates correlate with directions of hydrogen bonds and void distributions.

3.2 Abstract

We report the effect of pressure on the crystal structures of betaine monohydrate (BTM), L-cysteic acid monohydrate (CAM) and S-4-sulfo-L-phenylalanine monohydrate (SPM). All three structures are composed of layers of zwitterionic molecules separated by layers of water molecules. In BTM the water molecules make donor interactions with the same layer of betaine molecules, and the structure remains in a compressed form of its ambient pressure phase up to 7.8 GPa. CAM contains bi-layers of L-cysteic acid molecules separated by water molecules which form donor interactions to the bi-layers above and below. This phase is stable up to 6.8 GPa. SPM also contains layers of zwitterionic molecules with the waters acting as H-bond donors to the layers above and below. SPM undergoes a single-crystal to single-crystal phase transition above 1 GPa in which half the water molecules reorient so as to form one donor interaction with another water molecule within the same layer. In addition, half of the S-4-sulfo-L-phenylalanine molecules change their conformation. The high-pressure phase is stable up to 6.9 GPa, though modest rearrangements in H-bonding and molecular conformation occur at 6.4 GPa. The three hydrates had been selected on the basis of their topological similarity (CAM and SPM) or dissimilarity (BTM) with serine hydrate, which undergoes a phase transition at 5 GPa in which the water molecules change orientation, and the phase transition in SPM shows some common features with that in serine hydrate. Principal directions of compression in all three structures were found to correlate with directions of hydrogen bonds and distributions of interstitial voids.

3.3 Introduction

Pressure-induced polymorphism has been observed in a number of different classes of molecular crystal structure. Simple alcohols, carboxylic acids, phenols and acetone all exhibit new high-pressure phases (Allan *et al.*, 1998; Allan *et al.*, 2001; Allan *et al.*, 2002; Oswald, Allan, Day *et al.*, 2005; Allan & Clark, 1999a, b; Allan *et al.*, 1999; Oswald, Allan, Motherwell *et al.*, 2005). Polymorphism has also been observed in more complex materials like amino acids (Moggach, Parsons *et al.*, 2008), pharmaceuticals and energetic materials (Fabbiani & Pulham, 2006) and even in relatively large single molecule magnets (Prescimone *et al.*, 2008).

One of the motivations for work in the area of high-pressure polymorphism in molecular compounds has been to understand the driving forces behind phase transitions. Packing energy calculations based on the PIXEL method (Gavezzotti, 2005) have shown that some transitions, such as that in salicylaldoxime (Wood *et al.*, 2006) are driven by avoidance of short intermolecular repulsions. In other transitions, such as that in serine (Wood *et al.*, 2008) and serine hydrate (Johnstone *et al.*, 2008), the thermodynamic driving force is the lower volume and more efficient packing in the high-pressure form. These two driving forces can be seen as operating respectively via the U and PV terms in the equation $G = U + PV - TS$.

A number of structures in which the molecules pack in layers have now been studied at high pressure. Examples include α-glycine (Dawson *et al.*, 2005), paracetamol phases I and II (Boldyreva *et al.*, 2002; Boldyreva *et al.*, 2000) and serine hydrate (Johnstone *et al.*, 2008). The layer-stacking direction is often found to be the most compressible, as closer stacking is an effective way to minimise volume. Under ambient conditions, the crystal structure of L-serine monohydrate is built up of layers of hydrogen bonded zwitterionic serine molecules which are linked together by H-bonds to water. The orientation of the water molecules is such that the donor interactions are made to different layers (Scheme 3.1a). With the application of pressure, the crystal structure undergoes a single-crystal to single-crystal phase transition whereby the interlayer distance is reduced so that both donor interactions are made to the same layer (Scheme 3.1b). In order to enable closer stacking of the

serine layers the water molecules have to re-orient, leading to a phase transition. This chapter investigates whether the structural change seen in serine hydrate has any generality: do layered hydrates with the configuration shown in Scheme 3.1a always undergo a transition to a conformation like that in Scheme 3.1b? Can we predict high-pressure polymorphism?

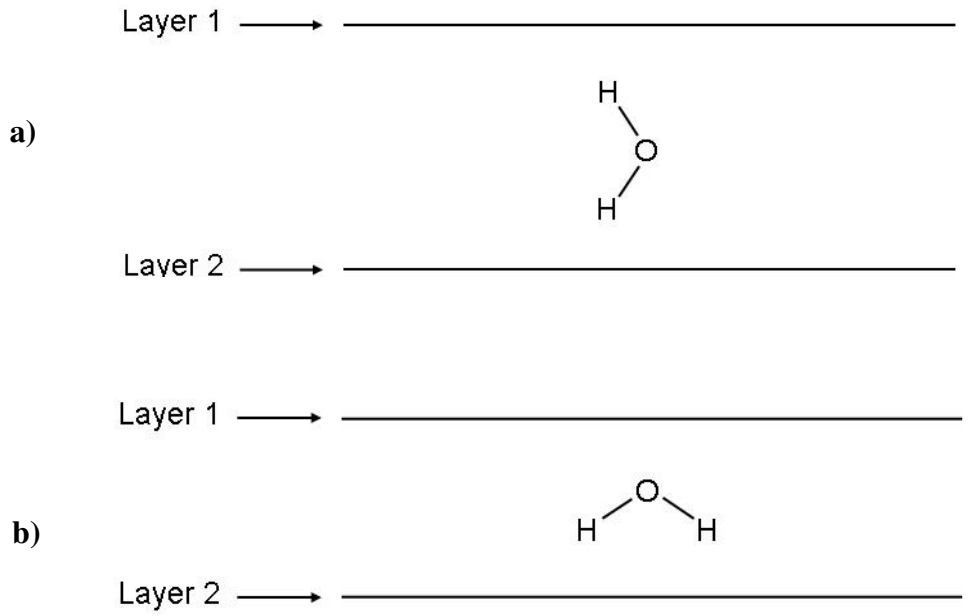

Scheme 3.1: Orientation of the water molecules between the layers of serine in L-serine monohydrate for a) ambient pressure phase and b) high-pressure phase.

In this chapter, the effect of pressure on three layered zwitterionic hydrates (the structures of the zwitterions are shown in Scheme 3.2) is reported. One layered hydrate, betaine monohydrate, has a structure similar to Scheme 3.1b. On the basis of the results on serine hydrate this was expected to be stable with respect to a Scheme 1a structure. S-4-Sulfo-L-phenylalanine monohydrate has a structure analogous to Scheme 3.1a, and we expected this to be unstable with respect to 3.1b on compression. L-Cysteic acid monohydrate has a structure like Scheme 3.1a, but with the L-cysteic acid molecules forming a bi-layer arrangement. This was investigated to determine whether pressure would be 'taken up' by the bi-layers or the water layers.

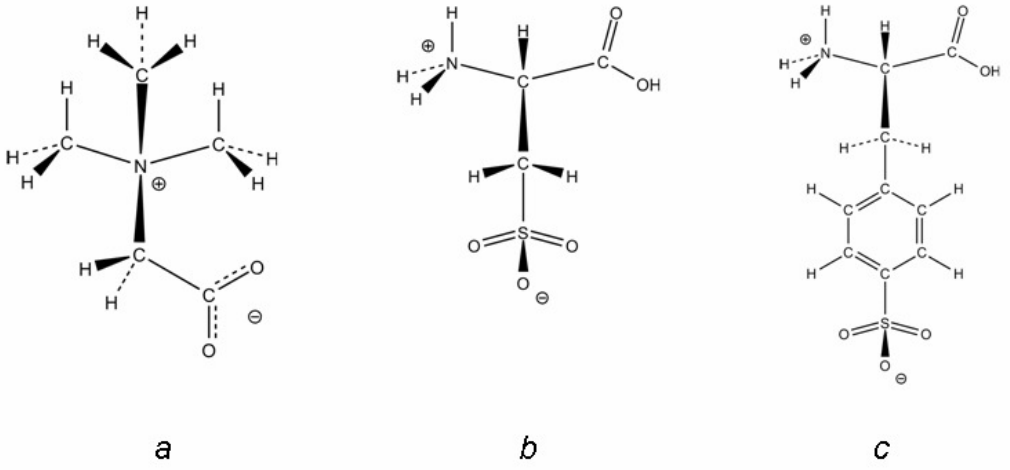

a b c

Scheme 3.2: Molecular structures of (a) betaine, (b) L-cysteic acid and (c) S-4-sulfo-L-phenylalanine.

3.4 Experimental

3.4.1 Crystal growth

Betaine monohydrate ("BTM", 99% purity) was purchased from Sigma-Aldrich (CAS number 590-47-6). The crystals were of sufficient size and quality to be used as received. L-cysteic acid monohydrate ("CAM", 99% purity) was purchased from Sigma-Aldrich (CAS number 23537-25-9). A sample (0.3897 g) was dissolved in deionised water (5 ml), and ethanol was added drop-wise until crystals started to form. These were then allowed to develop into large colourless rods at room temperature over a period of a few hours. S-4-Sulfo-L-phenylalanine monohydrate ("SPM") was synthesised and recrystallised using the method described by Xie *et al.* (2002).The resulting crystals had the appearance of colourless, elongated hexagonal laths. For the high-pressure experiments, a crystalline sample of each hydrate was taken and loaded into a diamond anvil cell.

3.4.2 Determination of ambient pressure structures

The crystal structures of all three systems were determined at ambient pressure and temperature. The crystal used in each case was taken from the same batch as the sample used for the corresponding compression study. Data were

measured on a Bruker SMART APEX diffractometer with graphite-monochromated Mo-Kα radiation (λ = 0.71073 Å) at 293 K. The data were integrated using SAINT (Bruker-Nonius, 2006) and corrected for absorption with SADABS (Sheldrick, 2004). Data were merged in point groups *mmm*, 222 and 2 for BTM, CAM and SPM, respectively.

Structures were solved using the program SIR-92 (Altomare *et al.*, 1994) and were refined against $|F|^2$ using all data (CRYSTALS) (Betteridge *et al.*, 2003). All non-H atoms were refined with anisotropic displacement parameters. Hydrogen atoms attached to carbon and nitrogen were placed geometrically and constrained to ride on their host atoms. Hydrogens attached to oxygen atoms were found in Fourier difference maps, and their positions were refined subject to an O-H distance restraint of 0.84(1) Å. Isotropic displacement parameters were refined for hydrogen atoms attached to oxygen; those on the water molecules were constrained to be equal. Thermal ellipsoid plots with atomic numbering schemes are shown in Figures 3.1a-c. Listings of crystal and refinement data are given in Tables 3.1-3.3.

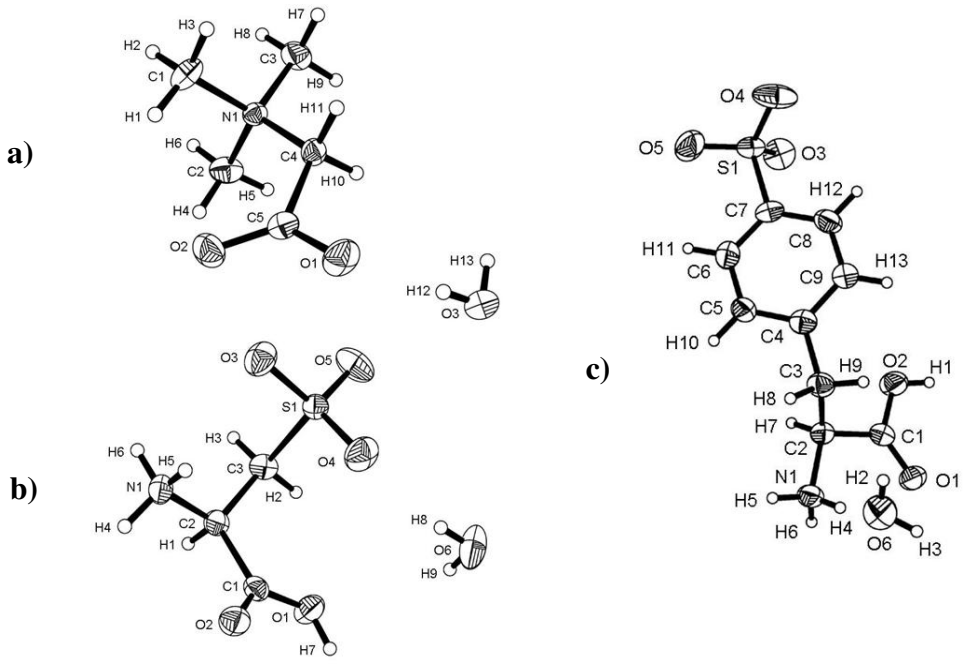

Figure 3.1: The asymmetric unit of a) betaine monohydrate, b) L-cysteic acid monohydrate and c) S-4-sulfo-L-phenylalanine monohydrate at ambient pressure and room temperature. Ellipsoids encompass 30% probability surfaces.

Pressure/ GPa	Ambient	0.1	1.6	2.9
M_r	135.16	135.16	135.16	135.16
Cell setting, space group	Orthorhombic, *Pbca*	Orthorhombic, *Pbca*	Orthorhombic, *Pbca*	Orthorhombic, *Pbca*
a, b, c (Å)	9.4715 (4), 11.4963 (5), 13.0802 (6)	9.431 (3), 11.438 (7), 13.018 (3)	9.1517 (6), 11.1659 (16), 12.5744 (7)	9.0252 (5), 11.0298 (14), 12.3350 (6)
V (Å)	1424.27 (11)	1404.2 (10)	1284.9 (2)	1227.90 (18)
Z	8	8	8	8
D_x (Mg m^{-3})	1.261	1.279	1.397	1.462
μ (mm^{-1})	0.10	0.10	0.11	0.12
Crystal form, colour	Block, Colourless	Block, Colourless	Block, Colourless	Block, Colourless
Crystal size (mm)	0.85 × 0.55 × 0.46	0.20 × 0.20 × 0.10	0.20 × 0.20 × 0.10	0.20 × 0.20 × 0.10
T_{min}	0.80	0.81	0.78	0.79
T_{max}	0.95	0.99	0.99	0.99
No. of measured, independent and observed [$I > 2.0\sigma(I)$] reflections.	14918, 1909, 1761	4791, 578, 414	5289, 708, 535	5995, 695, 545
R_{int}	0.047	0.090	0.079	0.077
d_{max}, d_{min}/ Å	6.54, 0.72	6.35, 0.90	6.16, 0.80	6.07, 0.80
Refinement on	F^2	F	F	F
$R[F^2 > 2\sigma(F^2)]$, $wR(F^2)$, S	0.064, 0.153, 1.08	0.042, 0.047, 0.98	0.046, 0.060, 1.03	0.045, 0.055, 0.98
No. of parameters	89	86	86	86
Weighting Scheme	$w = 1/[\sigma^2(F_o^2) + (0.06P)^2 + 0.75P]$, where $[P = (\max(F_o^2,0) + 2F_c^2)/3]$	$w = 1/[\sigma^2(F_o) + (0.0P)^2 + 0.02P]$, where $[P = (\max(F_o,0) + 2F_c)/3]$	$w = 1/[\sigma^2(F_o) + (0.0P)^2 + 0.02P]$, where $[P = (\max(F_o,0) + 2F_c)/3]$	$w = 1/[\sigma^2(F_o) + (0.01P)^2 + 0.02P]$, where $[P = (\max(F_o,0) + 2F_c)/3]$
$(\Delta/\sigma)_{max}$	<0.0001	<0.0001	<0.0001	<0.0001
$\Delta\rho_{max}$, $\Delta\rho_{min}$ (e Å^{-3})	0.34, –0.23	0.39, –0.36	0.37, –0.41	0.40, –0.37
Completeness	95.1% (0.7 Å)	57.0% (0.9 Å)	54.% (0.8 Å)	54.6% (0.8 Å)
Extinction method	Larson (1970), Equation 22	None	None	None
Exctinion coefficient	0.660 (6)	-	-	-

(a)

Pressure/ GPa	5.6	6.1	4.0	4.9
M_r	135.16	135.16	135.16	135.16
Cell setting, space group	Orthorhombic, *Pbca*	Orthorhombic, *Pbca*	Orthorhombic, *Pbca*	Orthorhombic, *Pbca*
a, b, c (Å)	8.8458 (5), 10.8143 (14), 11.9708 (6)	8.8188 (6), 10.7838 (17), 11.9105 (8)	8.9440 (5), 10.9336 (14), 12.1698 (6)	8.8854 (5), 10.8632 (14), 12.0516 (6)
V (Å)	1145.14 (17)	1132.7 (2)	1190.09 (18)	1163.27 (17)
Z	8	8	8	8
D_x (Mg m^{-3})	1.568	1.585	1.509	1.543
μ (mm^{-1})	0.13	0.13	0.12	0.13
Crystal form, colour	Block, Colourless	Block, Colourless	Block, Colourless	Block, Colourless
Crystal size (mm)	0.20 × 0.20 × 0.10	0.20 × 0.20 × 0.10	0.20 × 0.20 × 0.10	0.20 × 0.20 × 0.10
T_{min}	0.79	0.80	0.81	0.79
T_{max}	0.99	0.99	0.99	0.99
No. of measured, independent and observed [$I > 2.0\sigma(I)$] reflections.	5649, 665, 465	5263, 642, 465	5266, 667, 488	5250, 659, 501
R_{int}	0.086	0.081	0.081	0.073
d_{max}, d_{min}/ Å	5.98, 0.80	5.92, 0.80	6.02, 0.80	6.02, 0.80
Refinement on	*F*	*F*	*F*	*F*
$R[F^2 > 2\sigma(F^2)]$, $wR(F^2)$, *S*	0.043, 0.048, 0.99	0.045, 0.051, 0.98	0.046, 0.054, 1.00	0.045, 0.053, 0.99
No. of parameters	86	86	86	86
Weighting Scheme	$w = 1/[\sigma^2(F_o) + (0.01P)^2 + 0.02P]$, where $[P = (\max(F_o,0) + 2F_c)/3]$	$w = 1/[\sigma^2(F_o) + (0.0P)^2 + 0.03P]$, where $[P = (\max(F_o,0) + 2F_c)/3]$	$w = 1/[\sigma^2(F_o) + (0.0P)^2 + 0.03P]$, where $[P = \max(F_o,0) + 2F_c)/3]$	$w = 1/[\sigma^2(F_o) + (0.0P)^2 + 0.03P]$, where $[P = (\max(F_o,0) + 2F_c)/3]$
$(\Delta/\sigma)_{max}$	<0.0001	<0.0001	<0.0001	<0.0001
$\Delta\rho_{max}$, $\Delta\rho_{min}$ (e Å^{-3})	0.57, –0.52	0.51, –0.50	0.51, –0.59	0.54, –0.57
Completeness	56.4% (0.8 Å)	51.9% (0.8 Å)	53.9% (0.8 Å)	55.3% (0.8 Å)
Extinction method	None	None	None	None
Extinction coefficient	-	-	-	-

(b)

Pressure/ GPa	6.6	7.1	7.8
M_r	135.16	135.16	135.16
Cell setting, space group	Orthorhombic, *Pbca*	Orthorhombic, *Pbca*	Orthorhombic, *Pbca*
a, b, c (Å)	8.7881 (13), 10.735 (2), 11.859 (2)	8.7873 (10), 10.710 (2), 11.8632 (12)	8.778 (2), 10.656 (4), 11.884 (3)
V (Å)	1118.8 (4)	1116.4 (3)	1111.7 (6)
Z	8	8	8
D_x (Mg m^{-3})	1.605	1.608	1.615
μ (mm^{-1})	0.13	0.13	0.13
Crystal form, colour	Block, Colourless	Block, Colourless	Block, Colourless
Crystal size (mm)	0.20 × 0.20 × 0.10	0.20 × 0.20 × 0.10	0.20 × 0.20 × 0.10
T_{min}	0.78	0.78	0.67
T_{max}	0.99	0.99	0.99
No. of measured, independent and observed [$I > 2.0\sigma(I)$] reflections.	5393, 757, 528	5075, 625, 429	2684, 252, 187
R_{int}	0.098	0.109	0.129
d_{max}, d_{min}/ Å	5.90, 0.80	5.89, 0.80	5.94, 1.10
Refinement on	*F*	*F*	*F*
$R[F^2 > 2\sigma(F^2)]$, $wR(F^2)$, *S*	0.053, 0.061, 1.02	0.061, 0.075, 1.02	0.100, 0.135, 1.02
No. of parameters	86	86	41
Weighting Scheme	$w = 1/[\sigma^2(F_o) + (0.0P)^2 + 0.03P]$ where $[P = (\max(F_o,0) + 2F_c)/3]$	$w = 1/[\sigma^2(F_o) + (0.0P)^2 + 0.06P]$, where $[P = (\max(F_o,0) + 2F_c)/3]$	$w = 1/[\sigma^2(F_o) + (0.0P)^2 + 0.27P$, where $[P = (\max(F_o,0) + 2F_c)/3]$
$(\Delta/\sigma)_{max}$	<0.0001	<0.0001	<0.0001
$\Delta\rho_{max}$, $\Delta\rho_{min}$ (e Å^{-3})	0.24, –0.24	0.47, –0.52	0.60, –0.61
Completeness	65.2% (0.8 Å)	52.8% (0.8 Å)	55.8% (1.0 Å)
Extinction method	None	None	None
Extinction coefficient	-	-	-

(c)

Table 3.1: Crystallographic data for betaine monohydrate at increasing pressures: λ = 0.71073 Å for the ambient-pressure data set and 0.4762 Å for the high-pressure data sets.

Pressure/ GPa	Ambient	0.2	1.2	2.8
M_r	187.17	187.17	187.17	187.17
Cell setting, space group	Orthorhombic, $P2_12_12_1$	Orthorhombic, $P2_12_12_1$	Orthorhombic, $P2_12_12_1$	Orthorhombic, $P2_12_12_1$
a, b, c (Å)	6.9233 (2), 19.0222 (5), 5.3030 (2)	6.8922 (2), 19.0021 (19), 5.2919 (2)	6.7622 (2), 18.7945 (19), 5.2343 (2)	6.6284 (3), 18.508 (3), 5.1615 (3)
V (Å)	698.39 (4)	693.06 (8)	665.24 (7)	633.20 (10)
Z	4	4	4	4
D_x (Mg m^{-3})	1.780	1.794	1.869	1.963
μ (mm^{-1})	0.45	0.45	0.47	0.50
Crystal form, colour	Rod, Colourless	Rod, Colourless	Rod, Colourless	Rod, Colourless
Crystal size (mm)	0.20 × 0.20 × 0.10	0.20 × 0.20 × 0.10	0.20 × 0.20 × 0.10	0.20 × 0.20 × 0.10
T_{min}	0.68	0.83	0.83	0.76
T_{max}	0.84	0.96	0.95	0.95
No. of measured, independent and observed [$I > 2.0\sigma(I)$] reflections.	7112, 1129, 1816	4266, 485, 440	4025, 480, 434	3503, 422, 380
R_{int}	0.026	0.045	0.040	0.042
d_{max}, d_{min}/ Å	9.51, 0.72	5.61, 0.70	6.37, 0.70	6.24, 0.70
Refinement on	F^2	F	F	F
$R[F^2 > 2\sigma(F^2)]$, $wR(F^2)$, S	0.032, 0.044, 1.20	0.031, 0.034, 1.04	0.029, 0.029, 0.90	0.033, 0.030, 0.83
No. of parameters	111	108	108	108
Weighting Scheme	Chebychev polynomial (Prince, 1982) (Watkin, 1994)	Chebychev polynomial (Prince, 1982) (Watkin, 1994)	Chebychev polynomial (Prince, 1982) (Watkin, 1994)	Chebychev polynomial (Prince, 1982) (Watkin, 1994)
$(\Delta/\sigma)_{max}$	<0.0001	<0.0001	<0.0001	<0.0001
$\Delta\rho_{max}$, $\Delta\rho_{min}$ (e Å^{-3})	0.27, –0.59	0.14, –0.15	0.15, –0.13	0.22, –0.20
Completeness	95.6% (0.7 Å)	38.4% (0.70 Å)	39.4% (0.70 Å)	36.3% (0.70 Å)
Extinction method	(Larson, 1970) Equation 22	None	None	None
Exctinion coefficient	0.588 (6)	-	-	-
Absolute structure	(Flack, 1983)	As ambient	As ambient	As ambient
Flack parameter	0.056 (6)	-	-	-

(a)

Pressure/ GPa	4.5	5.8	6.8
M_r	187.17	187.17	187.17
Cell setting, space group	Orthorhombic, $P2_12_12_1$	Orthorhombic, $P2_12_12_1$	Orthorhombic, $P2_12_12_1$
a, b, c (Å)	6.5490 (3), 18.259 (3), 5.1169 (3)	6.4955 (4), 18.000 (4), 5.0930 (4)	6.4885 (14), 17.834 (7), 5.0983 (13)
V (Å)	611.88 (10)	595.48 (13)	590.0 (3)
Z	4	4	4
D_x (Mg m^{-3})	2.032	2.088	2.107
μ (mm^{-1})	0.51	0.53	0.53
Crystal form, colour	Rod, Colourless	Rod, Colourless	Rod, Colourless
Crystal size (mm)	0.20 × 0.20 × 0.10	0.20 × 0.20 × 0.10	0.20 × 0.20 × 0.10
T_{min}	0.80	0.75	0.68
T_{max}	0.95	0.95	0.95
No. of measured, independent and observed [$I > 2.0\sigma(I)$] reflections.	3241, 398, 338	3216, 388, 326	1508, 183, 139
R_{int}	0.048	0.065	0.092
d_{max}, d_{min}/ Å	6.17, 0.70	6.11, 0.70	6.10, 0.90
Refinement on	*F*	*F*	*F*
$R[F^2 > 2\sigma(F^2)]$, $wR(F^2)$, *S*	0.033, 0.028, 1.05	0.043, 0.044, 0.92	0.078, 0.093, 0.92
No. of parameters	108	108	58
Weighting Scheme	Chebychev Polynomial (Prince, 1982) (Watkin, 1994)	Chebychev Polynomial (Prince, 1982) (Watkin, 1994)	Chebychev Polynomial (Prince, 1982) (Watkin, 1994)
$(\Delta/\sigma)_{max}$	<0.0001	<0.0001	<0.0001
$\Delta\rho_{max}$, $\Delta\rho_{min}$ (e Å^{-3})	0.16, –0.16	0.27, –0.28	0.36, –0.30
Completeness	35.5% (0.70 Å)	35.3% (0.70 Å)	34.2% (0.90 Å)
Extinction method	None	None	None
Absolute structure	As ambient	As ambient	As ambient

(b)

Table 3.2: Crystallographic date for L-cysteic acid monohydrate at increasing pressures: λ = 0.71073 Å for the ambient-pressure data set and 0.4762 Å for the high-pressure data sets.

Pressure/ GPa	Ambient	0.2	1.0	2.5	4.0
Phase	I	I	I	II	II
M_r	263.27	263.27	263.27	263.27	263.27
Cell setting, space group	Monoclinic, $P2_1$	Monoclinic, $P2_1$	Monoclinic, $P2_1$	Monoclinic, $P2_1$	Monoclinic, $P2_1$
a, b, c (Å)	6.5299 (5), 7.6432 (6), 11.6081 (9)	6.4946 (4), 7.6198 (3), 11.5599 (17)	6.3782 (3), 7.4754 (3), 11.4450 (13)	10.2176 (8), 8.2463 (5), 12.6853 (17)	9.9602 (9), 8.1894 (6), 12.475 (2)
β (°)	93.590 (5)	93.306 (7)	92.591 (7)	114.238 (9)	113.060 (11)
V (Å)	578.22 (8)	571.12 (9)	545.14 (7)	974.61 (18)	936.3 (2)
Z	2	2	2	4	4
D_x (Mg m^{-3})	1.512	1.531	1.604	1.794	936.3 (2)
μ (mm^{-1})	0.30	0.30	0.32	0.35	0.37
Crystal form, colour	Hexagon, Colourless	Hexagon, Colourless	Hexagon, Colourless	Hexagon, Colourless	Hexagon, Colourless
Crystal size (mm)	0.65 × 0.40 × 0.20	0.20 × 0.20 × 0.10	0.20 × 0.20 × 0.10	0.20 × 0.20 × 0.10	0.20 × 0.20 × 0.10
T_{min}	0.80	0.67	0.72	0.81	0.78
T_{max}	0.94	0.97	0.97	0.97	0.96
No. of measured, independent and observed [$I > 2.0\sigma(I)$] reflections.	7731, 1775, 2784	3082, 599, 529	3231, 561, 499	4262, 786, 594	4016, 746, 577
R_{int}	0.033	0.054	0.046	0.071	0.070
d_{max}, d_{min}/ Å	11.58, 0.70	4.47, 0.70	4.41, 0.70	9.37, 0.80	9.11, 0.80
Refinement on	F^2	F	F	F	F
$R[F^2>2\sigma(F^2)]$, $wR(F^2)$, S	0.053, 0.056, 1.18	0.036, 0.035, 0.90	0.029, 0.027, 0.88	0.068, 0.067, 0.95	0.053, 0.053, 0.99
No. of parameters	165	162	162	163	163
Weighting Scheme	Chebychev polynomial (Prince, 1982) (Watkin, 1994)	Chebychev polynomial (Prince, 1982) (Watkin, 1994)	Chebychev polynomial (Prince, 1982) (Watkin, 1994)	Chebychev polynomial (Prince, 1982) (Watkin, 1994)	Chebychev polynomial (Prince, 1982) (Watkin, 1994)
$(\Delta/\sigma)_{max}$	<0.0001	<0.0001	<0.0001	<0.0001	<0.0001
$\Delta\rho_{max}$, $\Delta\rho_{min}$ (e Å^{-3})	0.65, –0.50	0.11, –0.11	0.10, –0.11	0.31, –0.30	0.27, –0.24
Completeness	93.5% (0.7 Å)	32.1% (0.7 Å)	31.7% (0.7 Å)	36.8% (0.8 Å)	36.3% (0.8 Å)
Absolute structure	(Flack, 1983)	As ambient	As ambient	As ambient	As ambient
Flack parameter	0.030 (11)	-	-	-	-

(a)

Pressure/ GPa	5.2	5.8	6.4	6.9
Phase	II	II	II	II
M_r	263.27	263.27	263.27	263.27
Cell setting, space group	Monoclinic, $P2_1$	Monoclinic, $P2_1$	Monoclinic, $P2_1$	Monoclinic, $P2_1$
a, b, c (Å)	9.7934 (8), 8.1603 (5), 12.3534 (17)	9.7046 (5), 8.1477 (3), 12.3071 (13)	9.6213 (11), 8.1290 (8), 12.298 (3)	9.5437 (17), 8.1824 (12), 12.151 (4)
β (°)	112.384 (9)	112.034 (6)	112.049 (13)	111.30 (2)
V (Å)	912.86 (17)	902.05 (12)	891.5 (2)	884.0 (4)
Z	4	4	4	4
D_x (Mg m^{-3})	1.916	1.938	1.961	1.978
μ (mm^{-1})	0.38	0.38	0.39	0.39
Crystal form, colour	Hexagon, Colourless	Hexagon, Colourless	Hexagon, Colourless	Hexagon, Colourless
Crystal size (mm)	0.20 × 0.20 × 0.10	0.20 × 0.20 × 0.10	0.20 × 0.20 × 0.10	0.20 × 0.20 × 0.10
T_{min}	0.80	0.70	0.64	0.64
T_{max}	0.96	0.96	0.96	0.96
No. of measured, independent and observed [$I > 2.0\sigma(I)$] reflections.	4100, 712, 571	3530, 698, 585	3279, 663, 548	1921, 351, 269
R_{int}	0.068	0.077	0.102	0.150
d_{max}, d_{min}/ Å	8.94, 0.80	8.864, 0.80	8.81, 0.80	8.70, 1.00
Refinement on	*F*	*F*	*F*	*F*
$R[F^2 > 2\sigma(F^2)]$, $wR(F^2)$, *S*	0.055, 0.059, 1.02	0.058, 0.064, 1.00	0.067, 0.074, 0.96	0.111, 0.126, 0.74
No. of parameters	163	163	163	163
Weighting Scheme	Chebychev polynomial (Prince, 1982) (Watkin, 1994)	Chebychev polynomial (Prince, 1982) (Watkin, 1994)	Chebychev polynomial (Prince, 1982) (Watkin, 1994)	Chebychev polynomial (Prince, 1982) (Watkin, 1994)
$(\Delta/\sigma)_{max}$	<0.0001	<0.0001	<0.0001	<0.0001
$\Delta\rho_{max}$, $\Delta\rho_{min}$ (e Å^{-3})	0.31, –0.26	0.27, –0.27	0.32, –0.33	0.46, –0.46
Completeness	35.6% (0.8 Å)	35.4% (0.8 Å)	34.0% (0.8 Å)	36.6% (1.0 Å)
Absolute structure	As ambient	As ambient	As ambient	As ambient

(b)

Table 3.3: Crystallographic data for S-4-sulfo-L-phenylalanine monohydrate at increasing pressures: λ = 0.71073 Å for the ambient-pressure data set and 0.4762 Å for the high-pressure data sets

3.4.3 High-pressure crystallography: data processing and general procedures

High-pressure experiments were carried out using a Merrill-Bassett diamond anvil cell (half-opening angle 40°), equipped with Boehler–Almax cut diamonds with 600 μm culets and a tungsten gasket (Merrill & Bassett, 1974, Moggach, Allan *et al.*, 2008).

For each pressure study, a 1:1 mixture of *n*-pentane and isopentane was used as a hydrostatic medium. This hydrostatic medium is very volatile and so the cell was cooled in dry ice prior to loading. A small ruby chip was also loaded into the cell as the pressure calibrant, and the ruby fluorescence method used to measure the pressure (Piermarini *et al.*, 1975).

All diffraction data were collected on a Bruker-Nonius APEX-II diffractometer with silicon-monochromated synchrotron radiation (λ ~ 0.48 Å, see Tables 3.1-3.3) on Station 9.8 at the SRS, Daresbury Laboratory. Data collection and processing procedures for all high-pressure experiments followed Dawson *et al.* (2004). Integrations were carried out using dynamic masking of the regions of the detector shaded by the pressure cell with the program SAINT. An absorption correction was carried out in a two-stage procedure with the programs SHADE (Parsons, 2004) and SADABS. Data were merged using SORTAV (Blessing, 1987) in point groups *mmm*, *mmm* and 2/*m* for BTM, CAM and SPM, respectively. In each study, pressure was increased in regular steps until either the limit of the hydrostatic medium was reached, or peak broadening became too severe for further data collection.

Inspection of the unit cell constants for BTM and CAM upon compression to 7.8 GPa and 6.8 GPa respectively showed that both remain in compressed forms of their respective ambient pressure phases. Compression of the ambient-pressure form of SPM (SPM-I) to 2.5 GPa resulted in a single-crystal to single-crystal phase transition to a new polymorph, hereafter designated SPM-II. Further compression of SPM-II revealed that a more subtle structural change occurs between 6.5 GPa and 6.9 GPa, which resulted in a shortening of the *c*-axis and a lengthening in *b*.

3.4.4 High-pressure crystallography: refinement

The starting coordinates of the compressed forms of BTM, CAM and SPM-I were taken from those determined at ambient pressure, and the structure of SPM-II was solved using SIR-2004 (Burla *et al.*, 2005). All high-pressure refinements were carried out against F using data with $F > 4\ \sigma(F)$ in CRYSTALS. Extreme outlier reflections (e.g. those partially cut-off by the pressure cell, or overlapping with diamond reflections) were omitted from the refinement.

Owing to the low completeness of the data sets (Tables 3.1-3.3), all primary bond distances and angles were restrained to the values observed at ambient pressure conditions. In most cases, non-H atoms were refined with anisotropic displacement parameters, though for some of the higher pressure data sets [BTM (7.8 GPa), CAM (6.8 GPa) and all structures of SPM-II], carbon, nitrogen and oxygen atoms were refined isotropically. Global rigid-bond and -body restraints were applied to all anisotropic displacement parameters.

Hydrogen atoms attached to carbon and nitrogen were placed geometrically and constrained to ride on their host atoms. Hydrogens attached to carboxylic acid groups were found in Fourier difference maps and their positions were refined subject to an O-H distance restraint of 0.84(1) Å, and a <COH angle restraint based on the corresponding ambient-pressure structure. Ambient-pressure structures suggested that the carboxylic acid (CCOOH) groups were planar, and so a restraint was used to enforce this in high-pressure refinements.

Water molecules were treated as rigid bodies: O-H distances were set at 0.84 Å and <OHO angles were constrained to be equal to those observed at ambient conditions; the orientations of the water molecules were allowed to pivot about the oxygen atom positions. In addition to this, restraints were applied to ensure that the water O-H bonds were directed along H-bonding vectors formed at ambient conditions [<(DH…A) = 180(4)°].

The positions of the water hydrogen atoms in SPM-II were just visible in a Fourier difference map, and were confirmed using a maximum entropy enhanced difference map calculated using the program BAYMEM (Smaalen *et al.*, 2003). Isotropic displacement parameters for all O-H hydrogens were refined subject to

restraints, and those attached to the water oxygen atom were constrained to be equal. Planarity restraints were applied to the phenyl rings in all structures of SPM-II. Listings of crystal and refinement data are given in Tables 3.1-3.3; intermolecular interactions are given in Tables 3.4-3.6.

Pressure/GPa	0	0.1	1.6	2.9	4.0	4.9
O3H12...O1[i]						
H12…O1	1.98(2)	1.97(2)	1.93(3)	1.89(2)	1.88(3)	1.87(3)
O3…O1	2.814(2)	2.806(4)	2.764(3)	2.730(3)	2.717(3)	2.700(3)
<O3H12O1	176(2)	173(2)	174(3)	174(2)	174(3)	173(3)
O3H13...O2[ii]						
H13…O2	1.95(2)	1.94(2)	1.90(2)	1.87(2)	1.86(2)	1.84(2)
O3…O2	2.782(2)	2.778(4)	2.728(4)	2.705(4)	2.686(4)	2.672(4)
<O3H13O2	169(2)	173(2)	170(2)	172.5(18)	170(3)	168(3)

(a)

Pressure/GPa	5.6	6.1	6.6	7.1	7.8
O3H12...O1[i]					
H12…O1	1.86(3)	1.83(2)	1.83(3)	1.84(3)	1.83(3)
O3…O1	2.694(3)	2.680(3)	2.665(3)	2.677(5)	2.644(13)
<O3H12O1	175(3)	175(3)	174(4)	175(6)	175(4)
O3H13...O2[ii]					
H13…O2	1.84(2)	1.83(2)	1.82(2)	1.84(3)	1.78(3)
O3…O2	2.665(4)	2.656(4)	2.642(4)	2.634(6)	2.611(14)
<O3H13O2	169(3)	169(3)	170(3)	166(3)	168(4)

(b)

Symmetry Operators:

i	*x*,*y*,*z*
ii	1/2+*x*,*y*,1/2-*z*

Table 3.4: Non-covalent parameters in the crystal structure of betaine monohydrate up to 7.8 GPa. All distances are given in Å and angles are given in °. S.u's are calculated in PLATON; H-positions were as obtained from the refinement and X-H have not been normalised to neutron values.

Pressure/ GPa	0	0.2	1.2	2.8	4.5	5.8	6.8
Bi-layer forming H-bonds:							
N1H4...O2[i]							
H4…O2	2.08	2.09	2.08	2.04	2.02	2.01	1.96
N1…O1	2.820(2)	2.824(5)	2.796(5)	2.735(5)	2.699(6)	2.670(8)	2.628(16)
<N1H4O2	138	137	135	132	130	128	129
N1H5...O3[ii]							
H5…O3	2.16	2.15	2.09	2.02	1.97	1.92	1.93
N1…O3	2.964(2)	2.949(4)	2.894(4)	2.824(4)	2.771(4)	2.724(6)	2.742(13)
<N1H5O3	147	147	146	146	146	146	148
N1H6...O3[iii]							
H6…O3	2.04	2.04	2.03	2.01	1.99	1.99	1.97
N1…O3	2.944(2)	2.943(4)	2.932(4)	2.907(4)	2.891(4)	2.878(6)	2.849(13)
<N1H6O3	174	174	173	170	168	165	163
H-bonds between the water and cysteic acid layers:							
O1H7...O6[iv]							
H7...O6	1.674(17)	1.699(18)	1.677(18)	1.655(17)	1.650(17)	1.641(15)	1.64(2)
O1...O6	2.515(2)	2.530(4)	2.509(4)	2.492(4)	2.488(4)	2.472(5)	2.472(14)
<O1H7O6	176(2)	173(3)	170(3)	174(2)	176(2)	169(3)	171(3)
O6H8...O4[v]							
H8...O4	2.014(16)	1.984(16)	1.934(16)	1.870(12)	1.824(13)	1.78(2)	1.79(3)
O6...O4	2.819(2)	2.812(8)	2.767(6)	2.699(6)	2.653(7)	2.614(8)	2.62(2)
<O6H8O4	165(3)	168(2)	171(3)	168(2)	169(2)	170(3)	170(3)
O6H9...O5[vi]							
H9...O5	1.99(2)	1.98(2)	1.95(2)	1.92(2)	1.90(2)	1.88(2)	1.90(3)
O6...O5	2.790(2)	2.785(5)	2.755(5)	2.731(5)	2.708(6)	2.679(7)	2.702(18)
<O6H9O5	160(2)	160(2)	160(2)	161(2)	160(2)	159(2)	160(3)

Symmetry Operators:

i	-1/2-*x*,1-*y*,-1/2+*z*
ii	1/2-*x*,1-*y*,1/2+*z*
iii	1/2-*x*,1-*y*,-1/2+*z*
iv	-1/2+*x*,1/2-*y*,2-*z*
v	*x*,*y*,*z*
vi	-1/2+*x*,1/2-*y*,1-*z*

Table 3.5: Non-covalent parameters in the crystal structure of L-cysteic acid monohydrate up to 6.8 GPa. All distances are given in Å and angles are given in °. S.u's are calculated in PLATON; H-positions were as obtained from the refinement and X-H have not been normalised to neutron values.

Pressure/GPa	0	0.2	1.0		2.5	4.0
Phase	I	I	I		II	II
Water-Layer H-Bonds						
O6H2...O4[i]				**O61H21...O31[iii]**		
H2…O4	2.11(3)	2.10(2)	2.02(2)	H21…O31	2.04(4)	2.02(3)
O6…O4	2.950(3)	2.922(6)	2.852(6)	O61…O31	2.811(16)	2.788(13)
<O6H2O4	176(3)	168(2)	171(2)	<O61H21O31	152(4)	152(3)
				O62H22...O52[v]		
				H22…O52	2.01(3)	2.00(2)
				O62…O52	2.813(17)	2.800(15)
				<O62H22O52	159(2)	160(3)
O6H3...O4[ii]				**O61H31...O51[vi]**		
H3…O4	2.39(3)	2.33(4)	2.28(3)	H31…O51	2.22(3)	2.14(3)
O6…O4	3.134(3)	3.104(6)	3.055(6)	O61…O51	2.980(18)	2.900(15)
<O6H3O4	149(3)	154(2	154(2)	<O61H31O51	152(2)	151(2)
Water-Water H-Bonds						
				O62H32...O61[vii]		
				H32…O61	2.10(3)	2.15(3)
				O62…O61	2.905(13)	2.954(11)
				<O62H32O61	160(4)	160(4)
Layer-Water H-Bonds						
N1H4...O6[iii]				**N11H41...O61[viii]**		
H4...O6	2.07	2.07	2.03	H41...O61	1.85	1.86
N1...O6	2.906(3)	2.901(5)	2.841(4)	N11...O61	2.728(19)	2.733(15)
<N1H4O6	152	151	148	<N11H41O61	161	159
				N12H42...O62[ix]		
				H42...O62	1.94	1.95
				N12...O62	2.817(14)	2.830(12)
				<N12H42O62	163	163
N1H6...O6[iv]				**N11H61...O62[ix]**		
H6...O6	2.05	2.04	1.99	H61...O62	1.94	1.90
N1...O6	2.940(3)	2.929(5)	2.880(4)	N11...O62	2.792(16)	2.741(14)
<N1H6O6	164	164	164	<N11H61O62	155	154

[(ai)]

Pressure/GPa	0	0.2	1.0		2.5	4.0
Phase	I	I	I		II	II
Layer-layer H-Bonds						
				N12H62...O12[x] H62...O12 N12...O12 <N12H62O12	 2.16 2.995(12) 153	 2.09 2.930(11) 152
O2H1...O4[v] H1…O4 O2…O4 <O2H1O4	 1.77(3) 2.594(3) 163(2)	 1.76(2) 2.598(4) 179(3)	 1.73(2) 2.563(4) 175(2)	**O21H11...O41[xi]** H11…O41 O21…O41 <O21H11O41	 2.09(5) 2.764(12) 137(4)	 2.14(5) 2.723(11) 126(4)
				O22H12...O41[ix] H12…O41 O22…O41 <O22H12O41	 1.77(3) 2.593(9) 167(3)	 1.71(3) 2.551(8) 176(4)
N1H5...O3[vi] H5...O3 N1...O3 <N1H5O3	 1.96 2.782(3) 149	 1.97 2.779(5) 148	 1.98 2.764(5) 143	**N11H51...O32[iv]** H51...O32 N11...O32 <N11H51O32	 2.26 3.078(12) 149	 2.22 3.041(10) 150
				N12H52...O32[iv] H52...O32 N12...O32 <N12H52O32	 2.00 2.820(12) 149	 1.95 2.774(11) 150

[a(ii)]

Pressure/GPa	5.2	5.8	6.4	6.9
Phase	II	II	II	II
Water-layer H-Bonds				
O61H21...O31[iii]				
H21…O31	2.00(4)	2.00(4)	2.00(3)	1.98(3)
O61…O31	2.771(13)	2.767(13)	2.776(14)	2.74(2)
<O61H21O31	153(4)	152(3)	153(4)	152(3)
O62H22...O52[v]				
H22…O52	2.00(3)	2.02(3)	1.99(3)	2.07(3)
O62…O52	2.797(16)	2.815(16)	2.787(16)	2.87(2)
<O62H22O52	159(4)	159(4)	159(4)	159.1(19)
O61H31...O51[vi]				
H31…O51	2.07(3)	2.08(3)	2.05(3)	2.04(3)
O61…O51	2.845(15)	2.844(16)	2.822(16)	2.81(2)
<O61H31O51	153(2)	151(2)	152(2)	152(3)
Water-Water H-Bonds				
O62H32...O61[vii]				
H32…O61	2.14(3)	2.16(3)	2.16(3)	2.17(3)
O62…O61	2.952(12)	2.962(11)	2.954(14)	2.97(2)
<O62H32O61	160(4)	158(2)	158(2)	159(3)
Layer-Water H-Bonds				
N11H41...O61[viii]				
H41...O61	1.84	1.84	1.79	1.78
N11...O61	2.713(16)	2.713(16)	2.658(17)	2.65(2)
<N11H41O61	160	159	159	160
N12H42...O62[ix]				
H42...O62	1.94	1.92	1.93	1.83
N12...O62	2.818(13)	2.794(12)	2.803(13)	2.709(19)
<N12H42O62	163	162	161	161
N11H61...O62[ix]				
H61...O62	1.89	1.87	1.88	1.89
N11...O62	2.730(14)	2.707(14)	2.711(15)	2.69(2)
<N11H61O62	152	151	151	145
N12H52...O32[iv]				
H52...O32	1.92	1.89	1.89	1.95
N12...O32	2.747(11)	2.719(11)	2.713(11)	2.754(14)
<N12H52O32	150	150	149	146

[b(i)]

Pressure/GPa	5.2	5.8	6.4	6.9
Phase	II	II	II	II
Layer-layer H-Bonds				
N12H62...O12[x]				
H62...O12	2.06	2.05	2.03	2.03
N12...O12	2.898(11)	2.887(11)	2.858(12)	2.809(16)
<N12H62O12	153	152	151	142
O21H11...O41[xi]				
H11…O41	2.09(4)	2.13(4)	2.08(4)	2.08(3)
O21…O41	2.690(11)	2.687(11)	2.667(11)	2.708(16)
<O21H11O41	127(4)	123(4)	127(3)	132(2)
O22H12...O41[ix]				
H12…O41	1.70(3)	1.71(3)	1.67(3)	1.698(19)
O22…O41	2.523(8)	2.517(8)	2.501(9)	2.514(13)
<O22H12O41	166(4)	161(4)	172(4)	163(2)
N11H51...O32[iv]				
H51...O32	2.21	2.20	2.22	2.34
N11...O32	3.030(10)	3.025(11)	3.032(11)	3.141(14)
<N11H51O32	150	150	149	147
N12H52...O32[iv]				
H52...O32	1.92	1.89	1.89	1.95
N12...O32	2.747(11)	2.719(11)	2.713(11)	2.754(14)
<N12H52O32	150	150	149	146

[b(ii)]

Symmetry Operators:

i	-*x*,-1/2+*y*,-*z*
ii	*x*,*y*,1+*z*
iii	*x*,*y*,*z*
iv	1-*x*,1/2+*y*,1-*z*
v	-*x*,1/2+*y*,-*z*
vi	1-*x*,-1/2+*y*,-*z*
vii	1-*x*,1/2+*y*,-*z*
viii	2-*x*,1/2+*y*,1-*z*
ix	1-*x*,-1/2+*y*,1-*z*
x	1-x,1/2+y,2-z
xi	2-*x*,-1/2+*y*,1-*z*

Table 3.6: Non-covalent parameters for the crystal structure of in S-4-sulfo-L-phenylalanine monohydrate up to 6.9 GPa. Distances are given in Å and angles are in°. S.u's are calculated in PLATON; H-positions were as obtained from the refinement and X-H have not been normalised to neutron values.

3.4.5 PIXEL calculations

The final crystal structures obtained were used to calculate in separate calculations the molecular electron densities of the zwitterion and water molecules at each pressure by standard quantum chemical methods using the program GAUSSIAN98 (Frisch *et al.*, 1998) with the MP2/6-31G** basis set. The calculations are sensitive to H-atom positions (which become difficult to determine especially at higher pressures), and H-atom distances were set to standard neutron values in all calculations (C-H = 1.083 Å, N-H = 1.009 Å, O-H = 0.983 Å). The electron density model of the molecule was then analysed using the program package OPiX (Gavezzotti, 2003) which allows the calculation of dimer and lattice energies. The output from these calculations yields a total energy and a breakdown into its Coulombic (electrostatic), polarisation, dispersion and repulsion components (Gavezzotti, 2007, 2005).

3.4.6 Other programs used

Crystal structures were visualized using the programs CAMERON (Watkin *et al.*, 1993), Materials-MERCURY 2 (Macrae *et al.*, 2008) and DIAMOND (Brandenburg & Putz, 2005). Void diagrams were created in MERCURY and are shown with a probe radius of 0.2 Å and a default grid spacing of 1 Å. Analyses were carried out using PLATON (Spek, 2004), as incorporated in the WIN-GX suite (Farrugia, 1999). Searches of the Cambridge Structural Database (Allen & Motherwell, 2002) utilized the program CONQUEST with database updates up to November 2008. Calculation of strain tensors were carried out using a locally-written program (Parsons, 2003) using the method described in Hazen & Finger (1982). Eigenvalues and vectors were calculated using JACOBI (Press *et al*., 1992).

3.5 Results

3.5.1 The structure of betaine monohydrate at ambient pressure

The crystal structure of BTM contains one formula unit in the asymmetric unit in the space group *Pbca*, and corresponds to a structure determined previously by Mak (1990). The betaine molecule is zwitterionic with negative charge localised around the carboxylate group and positive charge residing on the quaternary nitrogen atom. Betaine has approximate C_S point symmetry: a least-squares mean plane through the atoms C3, N1, C4, C5, O2 and O1 shows that the average deviation from the plane is 0.016 Å (Figure 3.1a).

The structure comprises layers of betaine molecules which lie parallel to the (010) plane (Figure 3.2a). PIXEL calculations indicate that the betaine molecules within each layer interact via Coulombic attractions between oppositely charged parts of each zwitterion and also by dispersion attractions. Both the betaine and water layers are slightly sinusoidal when viewed along the *a*-axis; a feature emphasised by the colour-coding in Figure 3.2b.

The water molecules reside between the betaine layers (Figure 3.2c) and they interact with the layers through two H-bonds (Table 3.4). Each H-bond is donated to carboxylate oxygen atoms on different molecules in a single layer (Figure 3.2a), forming chains of graph-set descriptor *C*(6) (Bernstein *et al.*, 1995) which run parallel to the *a*-axis (Figures 3.2a and c). There are no geometrically favourable CH…O contacts formed to the water molecules at ambient pressure.

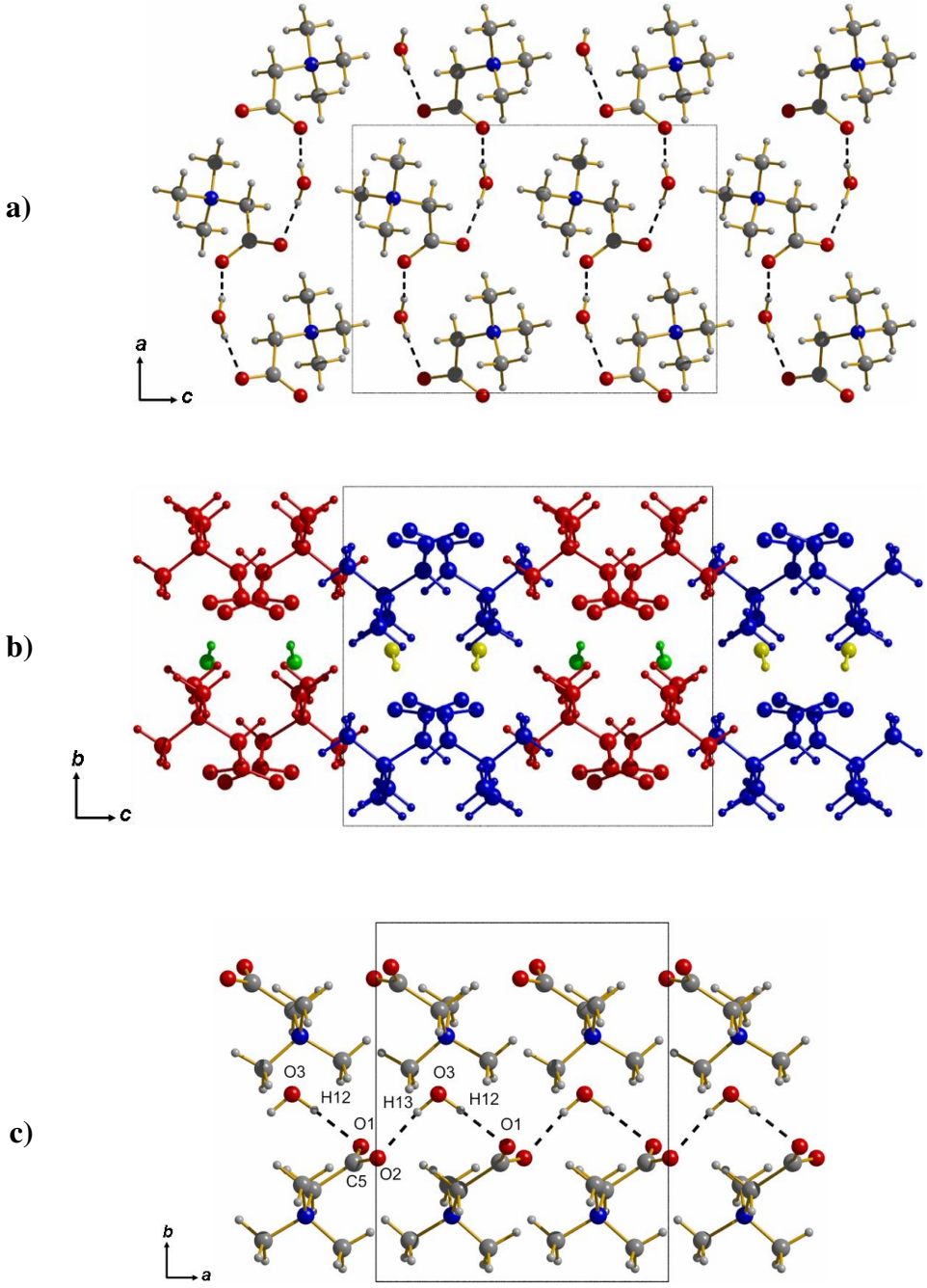

Figure 3.2: a) One layer of betaine molecules viewed along the *b*-axis, betaine molecules interact with each other via Coulombic and dispersive attraction, and with molecules in the water layer by H-bonding. b) Layers of betaine are sinusoidal and are separated by sinusoidal layers of water molecules. The colouring is intended to emphasise the sinusoidal arrangement of the molecules and does not imply crystallographic inequivalence. c) Hydrogen bonds are formed to layers via water molecules (only half a unit cell along *c* is shown for clarity).

3.5.2 Compression of betaine monohydrate

Increasing pressure on BTM produces an anisotropic response in the unit cell parameters (Figure 3.3a). The crystal system is orthorhombic, and the principal axes of the strain tensor coincide with the crystallographic axes (Table 3.7). Though layered structures are often found to compress most along the layer-stacking direction, this is not the case here: the greatest reduction occurs along the *c*-axis (parallel to the layers), which decreases by 9.1% from ambient conditions to 7.8 GPa. The *a*- and *b*-axes are equally compressible (both shortening by 7.3%). The molecular volume reduces by 21.9% at 7.8 GPa with respect to ambient conditions (Figure 3.3b).

a)

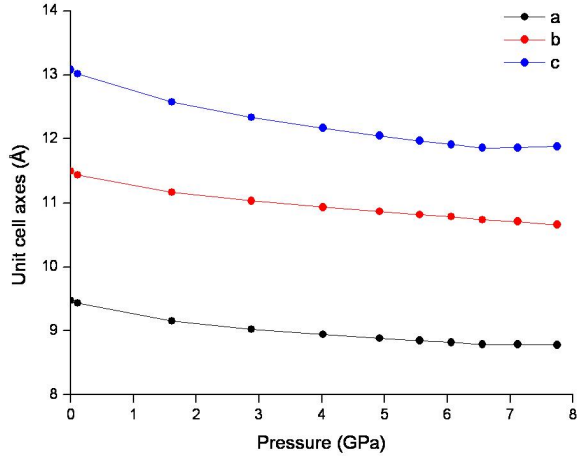

b)

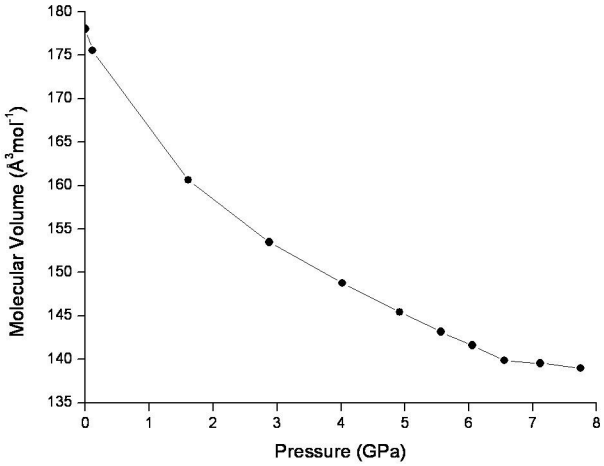

Figure 3.3: a) Unit cell axes for betaine monohydrate with increasing pressure. b) Molecular volume of betaine monohydrate with increasing pressure.

Compound name	Pressure/ GPa	Eigenvalues	Eigenvectors (unit vectors given in the direct axis system)
L-serine monohydrate-I	4.5	0.0008(8) -0.0738(13) -0.0983(7)	0.11 0.00 0.00 0.00 0.00 0.21 0.00 0.08 0.00
L-serine monohydrate-II	5.8	-0.0014(2) -0.0043(2) -0.0055(4)	0.10 0.00 0.00 0.00 0.00 0.23 0.00 0.10 0.00
BTM	7.8	-0.0731(4) -0.0732(2) -0.0915(2)	0.00 0.09 0.00 0.11 0.00 0.00 0.00 0.00 0.08
CAM	6.8	-0.0386(2) -0.0625(1) -0.0628(2)	0.00 0.00 0.19 0.00 0.05 0.00 0.14 0.00 0.00
SPM-I	1.0	-0.0085(1) -0.0220(1) -0.0279(1)	0.08 0.00 0.08 0.00 0.13 0.00 0.13 0.00 -0.04
SPM-II	6.4	-0.0115(3) -0.0142(1) -0.0619(1)	0.07 0.00 0.08 0.00 0.12 0.00 0.09 0.00 -0.02

Table 3.7: Eigenvalues and eigenvectors of the strain tensor for L-serine monohydrate-I and II, BTM, CAM, SPM-I and II.

3.5.3 The structure of L-cysteic acid monohydrate at ambient pressure

The crystal structure of CAM has previously been determined by Ramanadham *et al.* (1973); there is one formula unit in the asymmetric unit and the space group is $P2_12_12_1$. Molecules of L-cysteic acid are zwitterionic: the amino group extracts a hydrogen atom from the sulfonate moiety leaving the carboxyl group protonated (Figure 3.1b).

The structure is made up of bi-layers of L-cysteic acid molecules which lie parallel to the (010) plane (Figure 3.4a). The bi-layers are formed by three hydrogen bonds (Table 3.5, Figure 3.4a), each donated from the ammonium group: two are accepted by sulfonate oxygen atoms in different molecules [N1H5…O3 and N1H6…O3] which together form *C*(4) chains along the *c*-axis; another is accepted by the un-protonated carboxyl oxygen [N1H4…O2].

Water molecules lie between the bi-layers (Figure 3.4b). The orientation of the water molecules with respect to the layers is similar to the form shown in Scheme 3.1a, so that the bi-layers are connected along the *b*-axis through hydrogen bonds

involving the water molecules. The water molecules form H-bonds via their donor atoms to sulfonate groups in the layers above and below (O6H8…O4 and O6H9…O5). Each water molecule also accepts a hydrogen bond from the carboxylic acid group (O1H7…O6).

a)

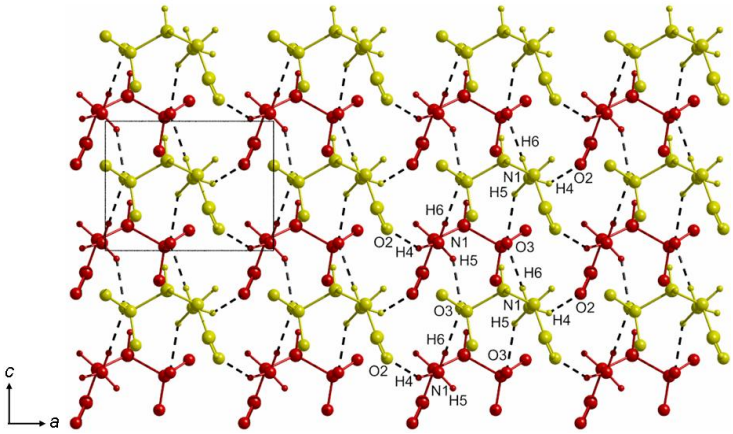

b)

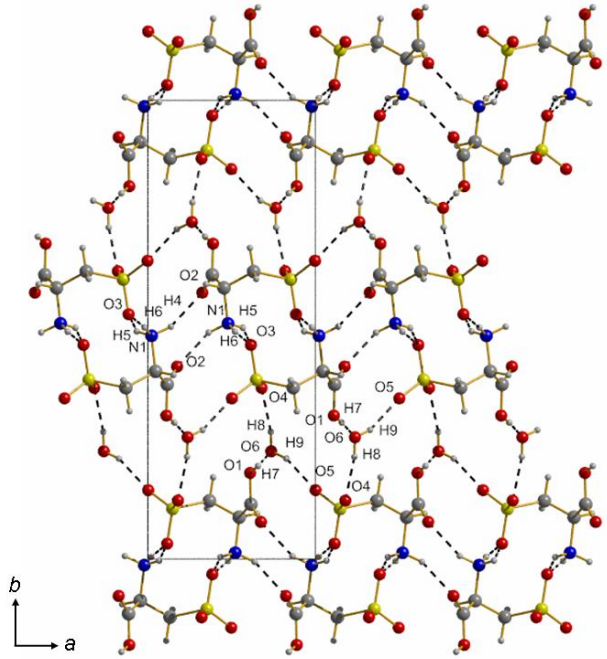

Figure 3.4: a) One bi-layer of L-cysteic acid molecules viewed along the *b*-axis: each half bi-layer is coloured differently for clarity and does not imply crystallographic inequivalence. b) Bi-layers stack along the *b*-axis and are separated by layers of water.

3.5.4 Compression of L-cysteic acid monohydrate

The reduction in the *a*- and *b*-axes as pressure is increased is more or less the same (Figure 3.5a); both shortening by *ca.* 6% upon compression from ambient conditions to 6.8 GPa. As in the compression of BTM, the graphs showing the reduction in the layer-building (*a* and *c*) axes flatten out at high pressure, whereas the graph for the layer stacking axis (*b*) does not, and continues to decrease throughout the pressure range. The molecular volume decreases by 15.5% from ambient conditions to 6.8 GPa (Figure 3.5b).

a)

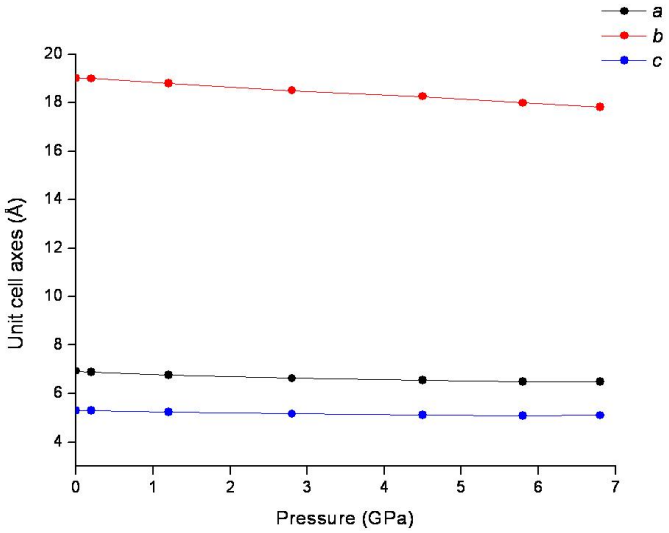

b)

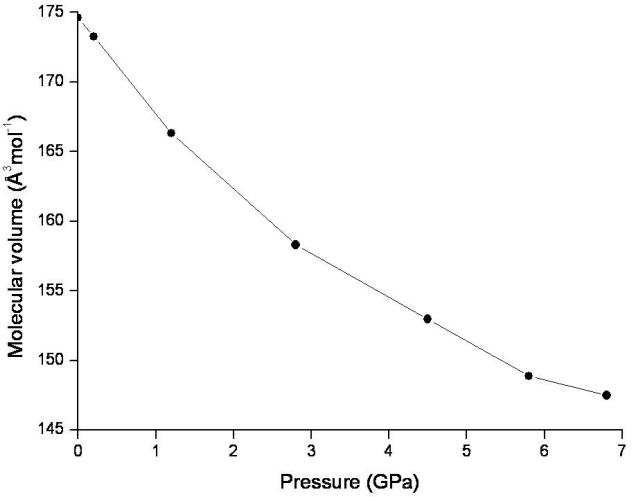

Figure 3.5: a) Unit cell axes for L-cysteic acid monohydrate with increasing pressure. b) Molecular volume of L-cysteic acid monohydrate as a function of pressure.

The molecular geometry of the L-cysteic acid molecules remains essentially unchanged upon compression: the largest change in torsion angle involving non-hydrogen atoms is in the carboxyl group along the C1-C2 bond: O1-C1-C2-N1 changes by *ca* 4º. Overall, at ambient conditions the H-bonds which form the bi-layers are longer than those formed between bi-layers and water molecules (Table 3.5), and on average they compress slightly more. The most compressible hydrogen bond is N1H5…O3 (the longest at ambient conditions) and shortens by 7.5%. The least compressible H-bond is O1H7…O6 (the shortest at ambient conditions) which shortens by 1.7% up to 6.8 GPa to become particularly short [O …O = 2.472(14)].

3.5.5 The structure of S-4-sulfo-L-phenylalanine monohydrate-I at ambient pressure

The crystal structure of SPM-I contains one formula unit in the asymmetric unit, and crystallises in the space group $P2_1$. The S-4-sulfo-L-phenylalanine molecule is zwitterionic, and, as in CAM, it is the sulfonate group (rather than a carboxylic acid group) which is de-protonated (Figure 3.1c). The S1-O5 bond is almost co-planar with the plane of the phenyl ring [τ(O5-S1- C7-C6) = 11.6(3)º], and at the other end of the molecule, the C2–C3 bond is almost perpendicular to the plane of the ring [τ(C5-C4-C3-C2) = 74.3(3)º].

Overall the structure is made up of layers of S-4-sulfo-L-phenylalanine molecules which lie parallel to the (001) plane. The layers are built from two discrete hydrogen bonds: N1H5…O3, and O2H1…O4 (Table 3.6). A figure depicting the layers proves to be rather cluttered, and in Figure 3.6a we have chosen to show only part of each molecule and one of the *C*(9) chains, running in the [110] direction. The remaining halves of the molecules generate another *C*(9) chain running along [-110].

Water molecules are located between the layers with an orientation similar to Scheme 3.1a. Layers are linked together via hydrogen bonding to the water of crystallisation (Fig 3.7a). Water molecules accept two hydrogen bonds from ammonium groups in layers above and below (N1H6…O6 and N1H4…O6), and donate two H-bonds to sulfonate oxygens also in layers above and below (O6H2…O4 and O6H3…O2).

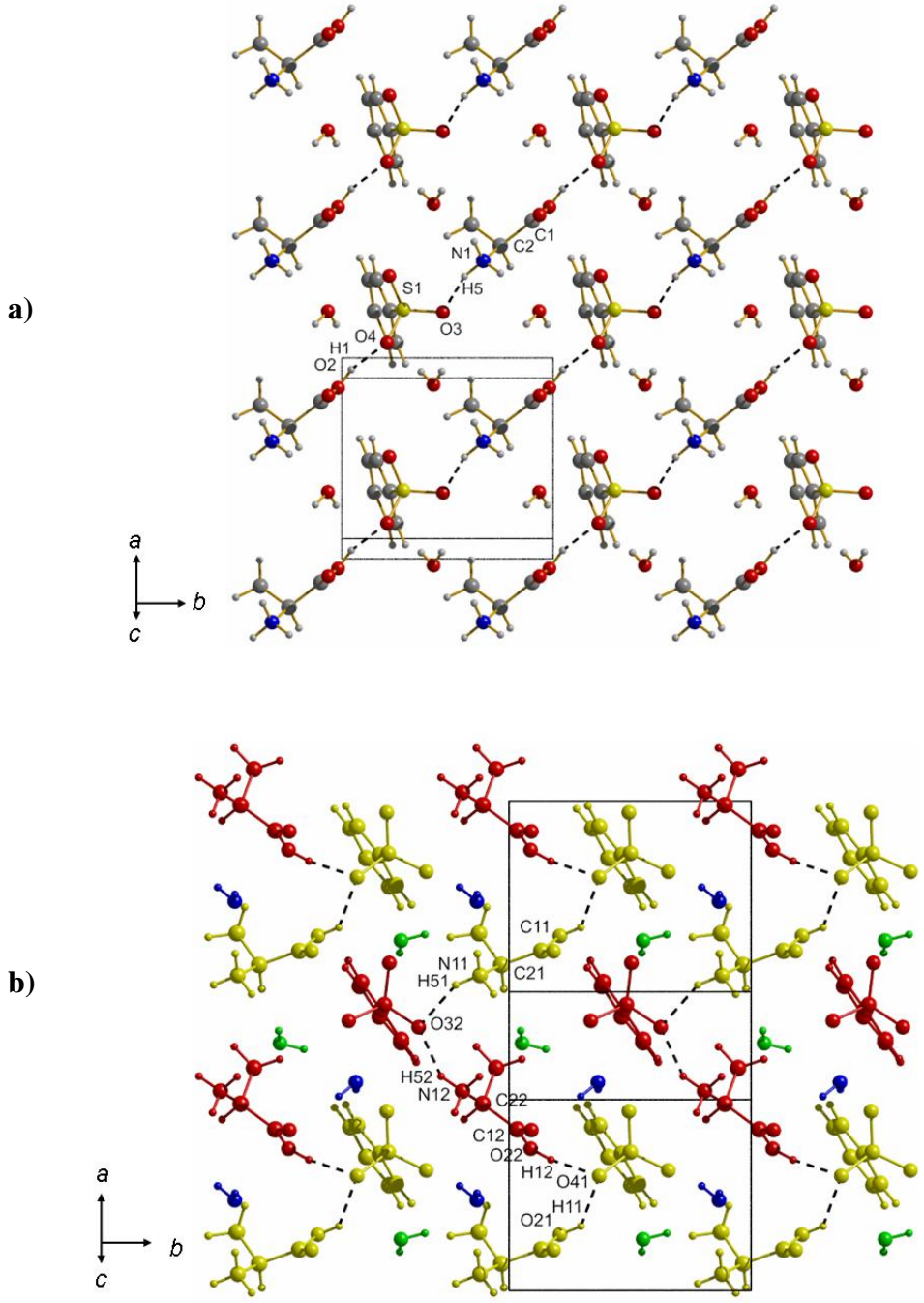

Figure 3.6: Layers of S-4-sulfo-L-phenylalanine monohydrate-I (a) and –II (b) viewed approximately along the reciprocal *c** axis to show the hydrogen bonding within layers. Each molecule is cropped at the C3-C4 bond and hydrogen bonding to water has been omitted for clarity. In b) the molecules are coloured by symmetry equivalence: residue one is red or blue, and residue two is yellow or green.

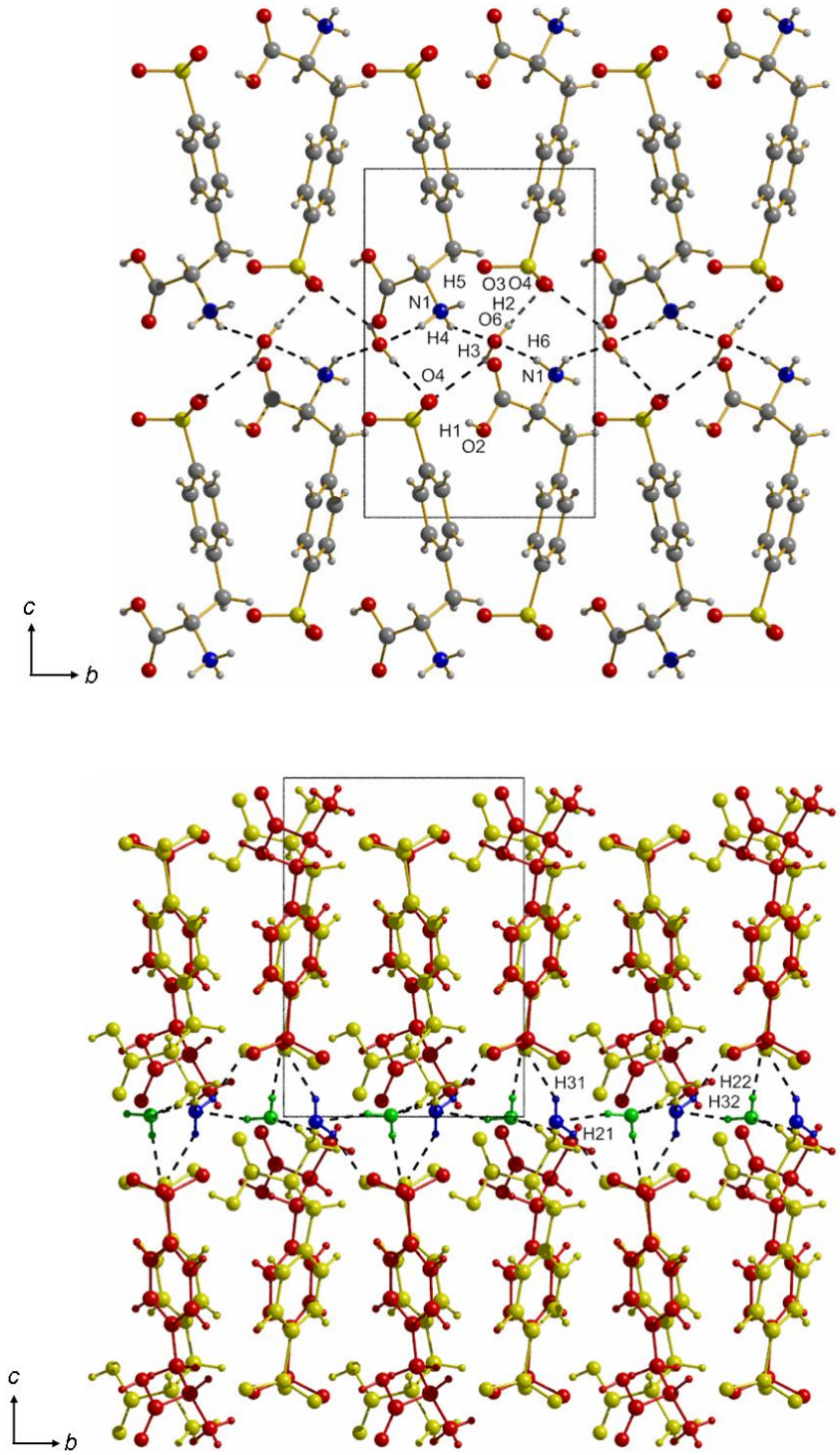

Figure 3.7: Layers of S-4-sulfo-L-phenylalanine monohydrate viewed along the crystallographic *a*-axis for a) SPM-I and b) SPM-II. Hydrogen bonding within layers has been omitted for clarity. In b) the molecules are coloured by symmetry equivalence: residue one is in yellow or blue and residue two is in red or green.

3.5.6 The response of S-4-sulfo-L-phenylalanine monohydrate-I to compression, and the structure of S-4-L-phenylalanine monohydrate-II at 2.5 GPa.

The response of SPM-I to hydrostatic pressure is anisotropic (Fig 3.8). The greatest reduction in the unit cell axes occurs along *a*, which shortens by 2.3% at 1.0 GPa relative to ambient pressure, however, the direction of greatest linear strain lies along [0.13 0.00 -0.04], with other components in the stacking and layer directions (Table 3.7). From ambient conditions to 1.0 GPa, the interlayer separation reduces by 0.15 Å (Fig 3.9).

a)

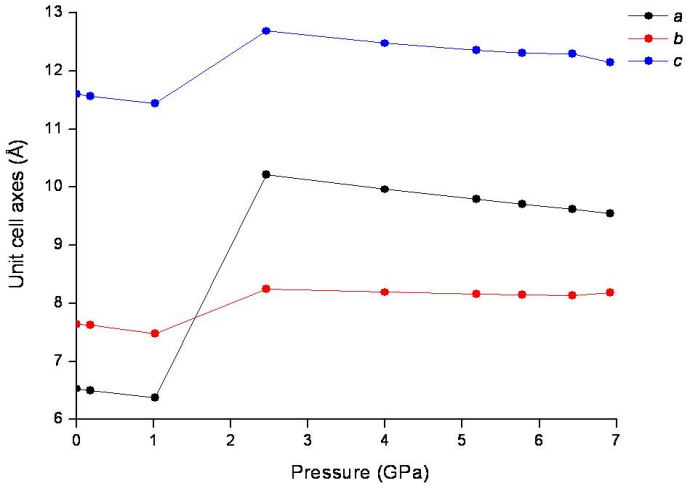

b)

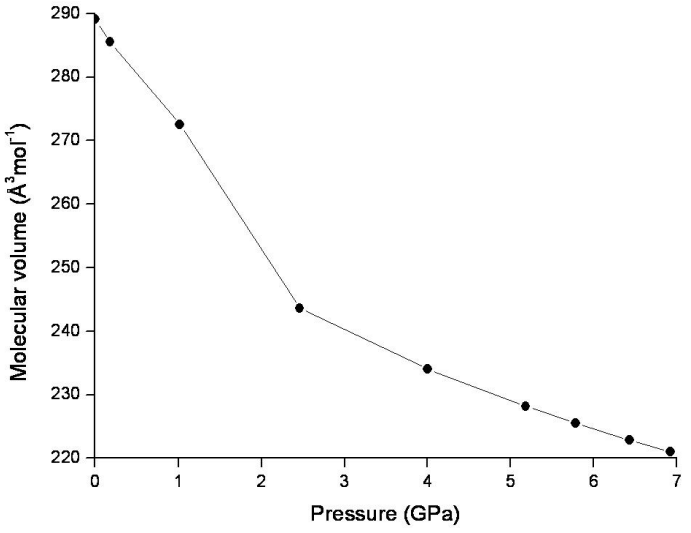

Figure 3.8: a) Unit cell axes for S-4-sulfo-L-phenylalanine monohydrate with increasing pressure. b) Molecular volume of S-4-sulfo-L-phenylalanine monohydrate with increasing pressure.

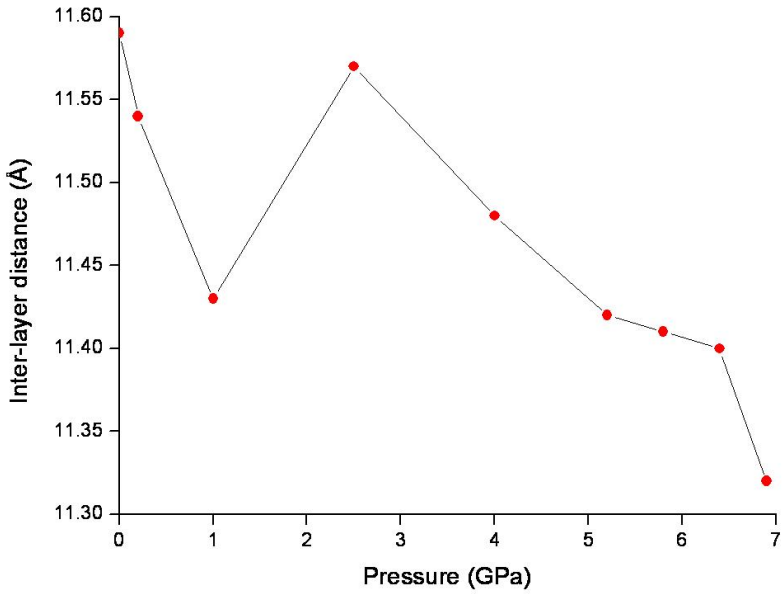

Figure 3.9: Separation between layers of zwitterions in both phases of S-4-sulfo-L-phenylalanine monohydrate with increasing pressure. The layers of zwitterions are parallel to the (001) planes and formed by lattice repeats along *c*, and for the purposes of this figure the interlayer distance is equated with d_{001} (=1/*c**).

The molecular geometry of the zwitterions in SPM-II differ significantly from those in SPM-I: Figure 3.10 shows an overlay of the benzene rings for phase-I (black) and phase-II (red and yellow). In residue 1 (based on S11, and shown in yellow in Figure 3.10) there is a change in the torsion about the S1-C7 vector: τ(O51-S11-C71-C61) changes from 11.6(3)° to -29.7(6)° at 2.5 GPa indicating a rotation of the sulfonate group so that the S11-O51 bond moves away from co-planarity with the ring.

In residue 2 (coloured red in Figure 3.10), there is a larger rotation of the sulfonate group: τ(O52-S12-C72-C62) = -38.0(8)° at 2.5 GPa. There is also a change in the torsion about the C32-C42 bond: τ(C52-C42-C32-C22) = 22.7(11)° at 2.5 GPa, which represents a rotation of the alanine moiety so that the C22-C32 bond is close to the plane of the phenyl ring. This conformational change creates a short *intra*molecular H…H contact of 1.73 Å (hydrogen distances normalised to standard neutron values).

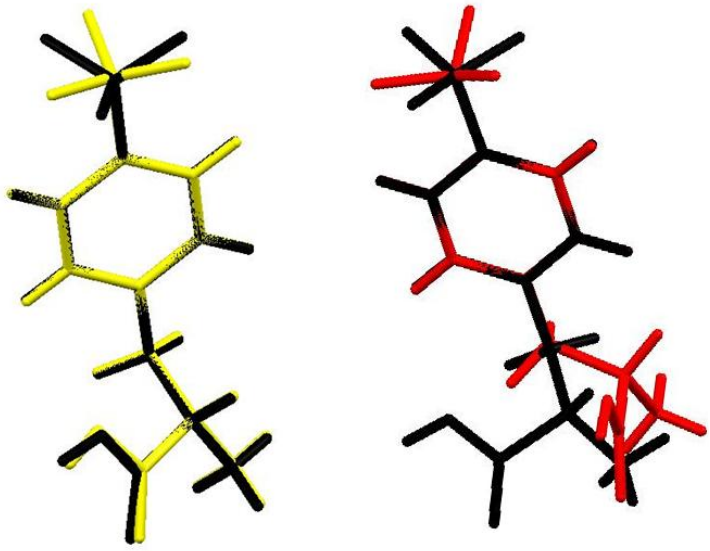

Figure 3.10: Overlay of phase-I (black molecules) and phase-II (red and yellow molecules are residues one and two respectively) in S-4-sulfo-L-phenylalanine monohydrate.

The change in the molecular conformation has an effect on the packing within layers (Fig 3.6b). The *C*(9) chains that occur in phase-I are no longer present in phase-II: two H-bonds are retained throughout transition (O2H1…O4 = O21H11…O41 and N1H5…O3 = N11H51…O32) and both are *longer* in phase-II by *ca.*0.2 Å and 0.3 Å, respectively. Two new discrete H-bonds are formed from carboxyl and ammonium hydrogens as a result in the change in the conformation of residue 2. These are O22H12…O41 and N12H52…O32; note the symmetry operations for O41 and O32 are different from those in the H-bonds which are retained during the transition (full details are in Table 3.6). All four interactions combine to make sinusoidal *C*(14) chains which run along the *a*-axis.

In addition to the change in the packing within layers, the water molecules between layers change orientation. Figure 3.7b shows how the layers interact with the water molecules; each molecule is coloured according to symmetry equivalence. The water molecules in residue one (blue) re-orientate so that the hydrogen bonds that were present in phase-I are broken and new ones are formed to different molecules. However, the overall orientation still conforms to that in Scheme 3.1a, with H-bonds formed to layers above and below.

The water molecules in residue two (green) have re-orientated so that all H-bonds are broken except for N1H6…O6 (= N11H61…O62). In this instance, the water molecules are no longer connecting layers through their hydrogen atoms: one hydrogen bond is now formed to a sulfonate oxygen in one layer and another is formed to the oxygen on a (residue 1) water molecule.

The most compressible hydrogen bond in SPM-I is O6H2…O4, which is an interaction formed from water molecules to layers. The O…O distance decreases by 3.3% from ambient to 1.0 GPa. The shortest H-bond at 1.0 GPa is a layer-layer interaction: O2H1…O4, [O2…O4 = 2.563(4) Å], and this is the least compressible H-bond in the structure, shortening by 1.1% at 1.0 GPa relative to ambient conditions.

3.5.7 Compression of S-4-sulfo-L-phenylalanine monohydrate-II

Compression of the unit cell parameters of SPM-II up to a pressure of 6.4 GPa is anisotropic (Fig 3.8): the greatest reduction occurred for the *a*-axis, and the *b*-axis compressed the least.

Above 6.4 GPa, there was a significant drop in the length of the *c*-axis from 12.298(3) to 12.151(4) at 6.9 GPa, and an increase in the length of the *b*-axis from 8.1290(8) to 8.1824(12) Å. The molecular conformation in residue two also changes slightly: the largest changes occur about the C22-C32 bond [τ(N12-C22-C32-C42) = -157.2(6)º at 6.4 GPa and -165.4(8) at 6.9 GPa] and the C42-C92/C52 bonds where the alanine moiety attaches to the phenyl ring [τ(C32-C42-C92-C82) = -170.6(7)º at 6.4 GPa and -162.8(11) at 6.9 GPa]. As the molecular conformation changes, the short intramolecular H…H contact which was formed upon transition becomes longer, from 1.720 Å at 6.4 GPa to 1.789 Å at 6.9 GPa (hydrogen distances normalised to standard neutron values).

The data quality was nowhere near high enough to be able to locate H-atoms, and in the model presented we have assumed that the orientations of the water molecules remain unchanged during the transition. If this model is correct then there are a number of H-bonds which change abruptly between 6.4 GPa and 6.9 GPa: two H-bonds become markedly longer (O62H22…O52 increases by 0.083 Å and

N11H51…O32 increases by 0.109 Å) and one H-bond (N12H42…O62; the least compressible up to 6.4 GPa) becomes significantly shorter from N…O = 2.803(13) to 2.709(19).

As pressure is increased on SPM-II, the inter-layer separation decreases from 11.57 Å to 11.4 Å at 6.4 GPa. Figure 3.9 shows that the decrease becomes less rapid as pressure is increased, approaching a minimum at 6.4 GPa before undergoing a marked shortening at 6.9 GPa to 11.32 Å.

3.6 Discussion

The aim of this paper was to investigate the extent to which the high-pressure phase behaviour of a series of layered hydrates could be predicted on the basis of the orientation of the water molecules. The idea was a simple one: water molecules in the orientation shown in Scheme 3.1a limit the scope for layers moving closer together on compression, and the need to reduce volume at high pressure would promote reorientation of the water molecules as shown in Scheme 3.1b. Just such a transition was observed previously in L-serine monohydrate, and here in SPM, but overall the results of the present study show that matters are a little more complicated. In particular, in none of the structures does the layer stacking direction correspond to the direction of greatest linear strain. However, the reasons for the differences between the effects of pressure on serine hydrate, BTM, CAM and SPM can be understood by consideration of (*i*) H-bonding directions and (*ii*) void distributions.

H-bonds are amongst the strongest of all intermolecular interactions, they are strongly directional, and, though much depends on the shape of the potential in each specific case, strong H-bonds will tend to inhibit compression along parallel directions in a crystal. For example, amino acids typically form head-to-tail H-bonded chains of molecules, and the chain direction is usually found to have the smallest linear strain under pressure (Dawson *et al.*, 2005; Moggach *et al.*, 2005; Johnstone *et al.*, 2008). Similar conclusions have been reached for chloropyridinium tetrachloro- and bromo-cobaltate (Espallargas *et al.*, 2008).

An alternative guide to distortions at high pressure is the distribution of interstitial voids. In previous publications (Moggach *et al.*, 2005; Wood *et al.*, 2006), void analysis using Voronoi-Dirichlet polyhedra (Blatov & Shevchenko, 2003) has been found to be useful in the identification of the size and distribution of voids within a crystal structure. It was observed that there is a correlation between the positions of the largest voids within the structure and the directions of compression. Void distributions can also be investigated using recently added features in Mercury (Macrae *et al.*, 2008).

In serine hydrate the eigenvalues and vectors of the strain tensor at 4.5 GPa are given in Table 3.7. The numerically smallest strain is along *a*, the direction of head-to-tail chains of molecules. Figure 3.11 shows the void distribution at ambient conditions, 4.5 GPa (just before phase transition) and 5.2 GPa (just after phase transition). At ambient conditions, the voids are distributed more-or-less evenly within and between the layers of serine molecules (shown in black, water molecules are red). Compression to 4.5 GPa results in a significant reduction in the size of all voids in the structure, and this occurs by compression along the *b* and *c* directions.

The H-bonds formed by the water molecules to serine (approximately in the *b*-direction) are weaker than those formed between serine molecules, and as a result the layer stacking *b*-direction experiences a slightly greater linear strain than the *c*-direction. Above 5 GPa the structure transforms to a new phase, a transition that involves re-orientation of the water molecules and a reduction in the inter-layer stacking distance. Interestingly this seems to create small voids within the water layers; these disappear as pressure is increased.

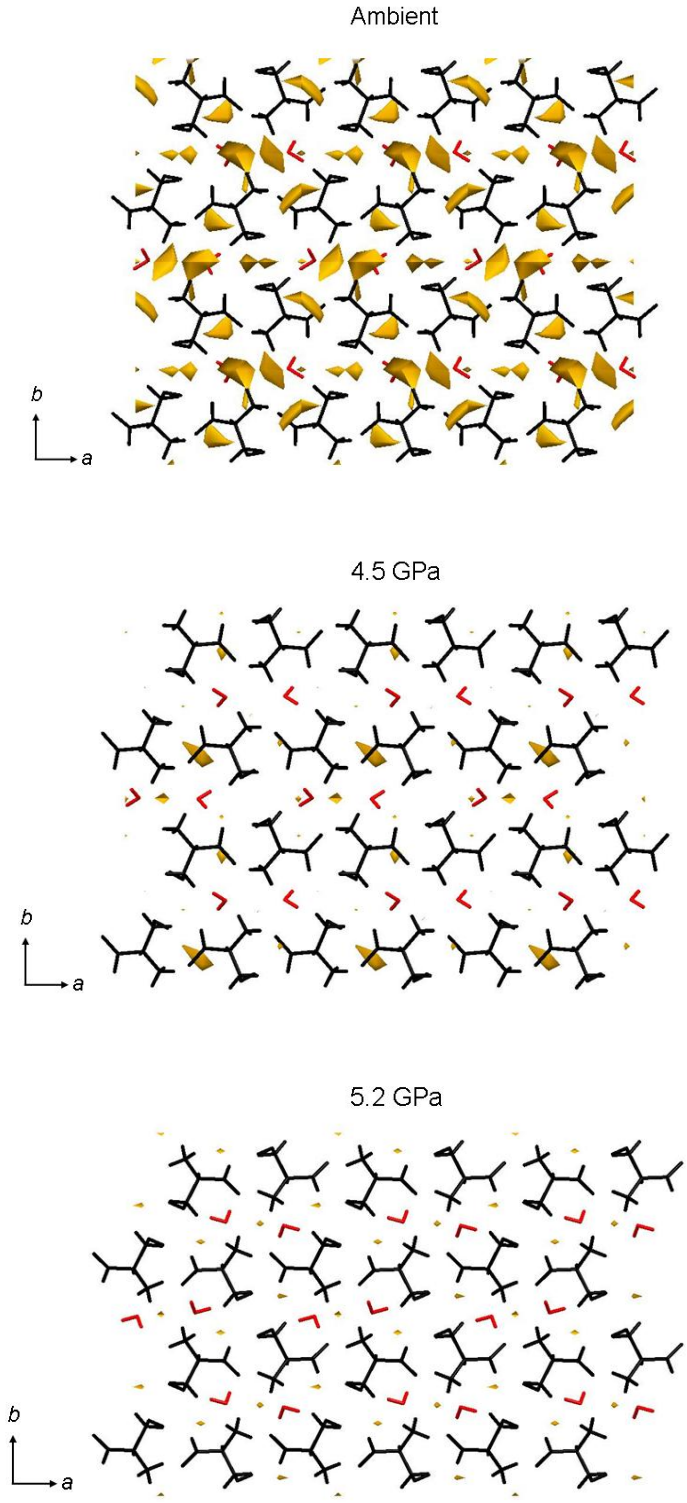

Figure 3.11: Void distribution in L-serine monohydrate at ambient conditions, 4.5 GPa and 5.2 GPa. Four layers of serine run vertically down the page: serine molecules are shown in black, and water molecules are shown in red.

Figure 3.12 shows the distribution of voids in BTM at ambient pressure, 4.0 GPa and 7.8 GPa. The voids are quite uniformly distributed within the structure, and compression is significant along all three principal directions (the range of linear strain is -0.07 to -0.09, Table 3.7). The layer stacking direction (*b*) corresponds to the direction of H-bond formation, and is the least compressible.

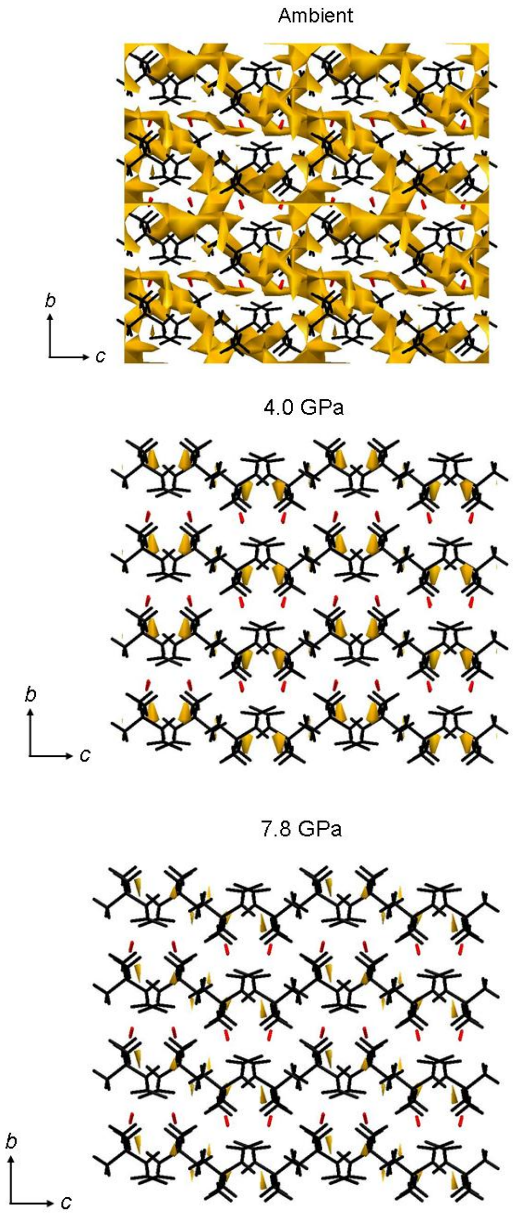

Figure 3.12: Void distribution in betaine monohydrate at ambient conditions, 4.0 GPa and at a final pressure of 7.8 GPa. Four layers of betaine molecules run vertically down the page: betaine molecules are shown in black, and water molecules are shown in red.

By 4.0 GPa the voids in the water layers have closed, a factor which appears to be correlated with a change in the behaviour of the sinusoidal betaine and water layers (Figure 3.2b). At ambient pressure both layers are slightly sinusoidal, and up to 4.0 GPa an increase in pressure increases the amplitude of the modulation. In the case of the betaine layers the modulation can be quantified using the separation between layers calculated using the red and blue molecules in Figure 3.2b; a similar calculation can be carried out for the green and yellow water molecules. These changes can also be visualised in the form of a movie which has been deposited as supplemental material (Movie 1).

The variation in the two modulation distances with pressure is shown in Figure 3.13 a and b. In Figure 3.13a there is a clear transition point from 4.0 GPa to 4.9 GPa where the plane separation remains constant before continuing to increase again. Figure 3.13b, by contrast, proceeds through a distinct maximum at 4.9 GPa. All void space has effectively closed up by 7.8 GPa.

a)

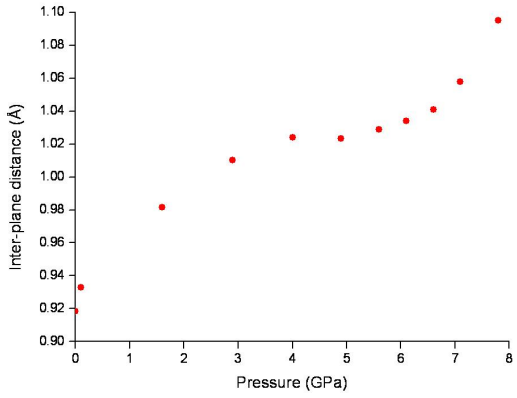

b)

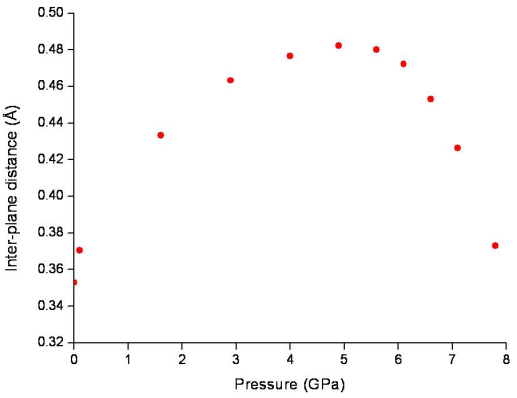

Figure 3.13: Inter-plane separation in betaine monohydrate for a) betaine layers and b) water layers as a function of pressure.

The path of compression in BTM is clearly not uniform, but at no stage does the structure transform to a new phase: this is highlighted in Figure 3.14, where the *normalised holistic RMS deviation* (a packing similarly tool available in Mercury) for the three hydrates is plotted against pressure. For BTM, it is apparent that the largest change in packing occurs within the first few GPa, and after this there is very little change.

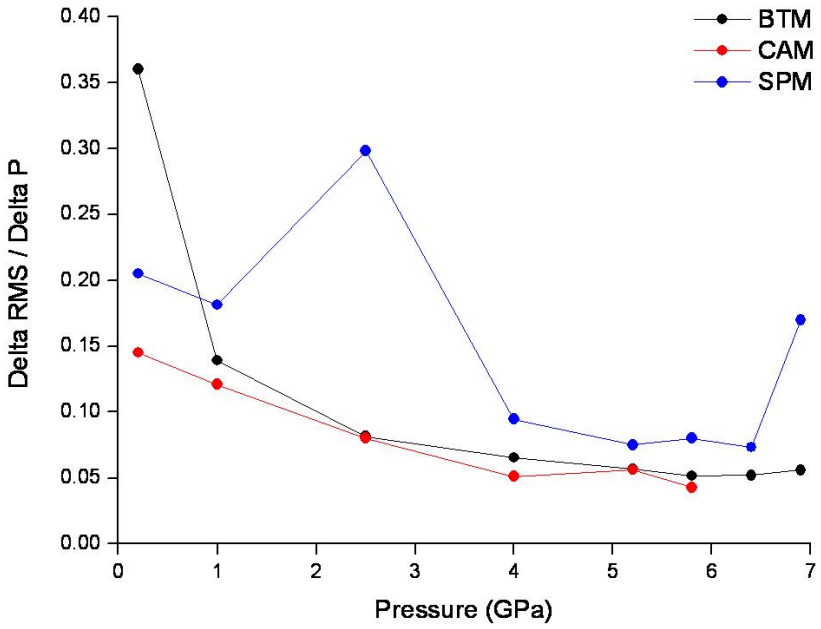

Figure 3.14: A graph showing the normalised holistic RMS deviation for BTM, CAM and SPM as a function of pressure.

The least compressible direction in CAM is the *c*-direction, which is parallel to strong $NH_3^+ \ldots SO_3^-$ hydrogen bonds which build the bi-layers of cysteic acid molecules. When strain is calculated using the cell dimension data at 6.8 GPa (Table 3.7) the *a*- and *b*-axes appear to be equally compressible. A movie showing the compression of the structure viewed along the *c*-axis is available in the supplemental material (Movie 2). The compression along the *a*-direction causes the alignment of pairs of cysteic acid molecules in the bi-layers to become more parallel to the *b*-direction as the voids between them decrease in size (compare the movie with the

void distributions shown in Figure 3.15). At the same time the distance between the bi-layers decreases and the rows of water molecules become less sinusoidal.

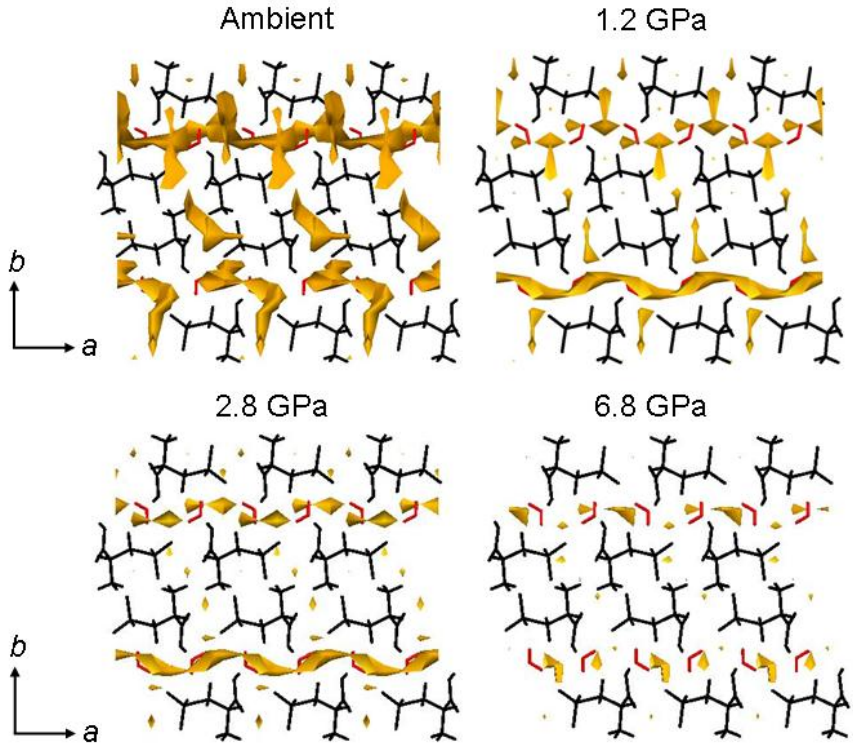

Figure 3.15: Void distribution in L-cysteic acid monohydrate at increasing pressures: L-cysteic acid molecules are shown in black, and water molecules are shown in red.

Between ambient pressure and 5.8 GPa the linear strain along the *a*-axis is greater than along *b* (Figure 3.16), a difference also reflected in the void distributions shown in Figure 3.15: the voids located in the bi-layers are compressed along the *a*-direction more quickly than the extended voids which exist in the water layers are compressed along *b*.

With reference to Figure 3.14, it can be seen that the packing in CAM does not change much throughout the compression study, and as in BTM, most of the compression occurs in the initial stages when the intermolecular interactions are less repulsive.

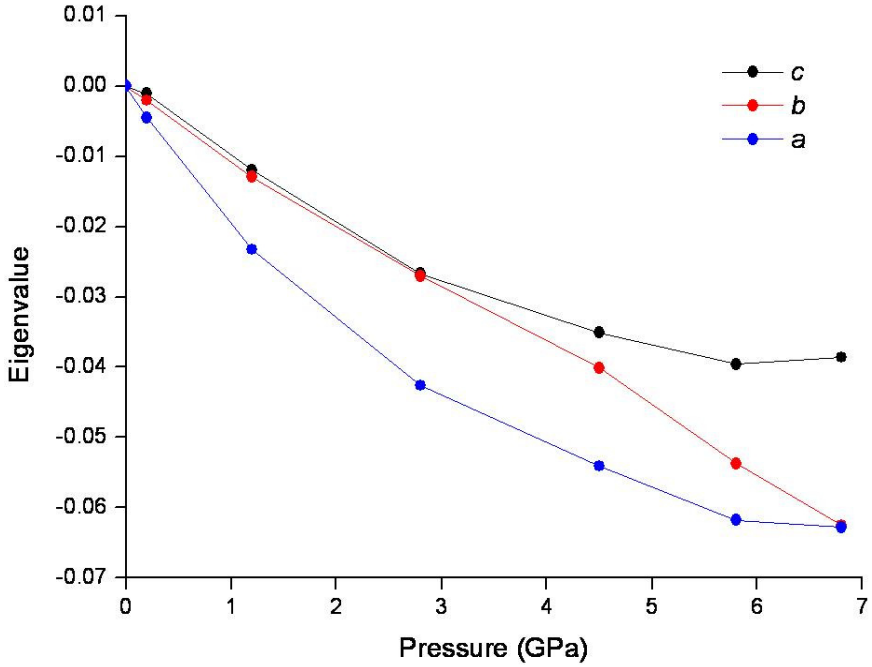

Figure 3.16: Eigenvalues of the strain tensor for L-cysteic acid monohydrate with increasing pressure.

The structure of SPM-I is characterised by elongated voids which run approximately along the *ac* diagonal (Figure 3.17a). The largest component of the strain tensor lies along the [0.13 0.00 -0.04] direction; indicated with a red arrow in Figure 3.17a, which lies perpendicular to the long dimension of the voids. One of the principal axes of the strain tensor must lie along the *b*-axis by symmetry: the strain along this direction is only a little smaller than along [0.13 0.00 -0.04]. The third strain axis makes a right-handed set, lying along [0.08 0.00 0.08], approximately along the length of the voids.

The response of SPM to pressure, as viewed along the *b*-axis, is depicted in the form of a movie in the supplemental material (Movie 3). Even though the precise directions of greatest compression are not necessarily very obvious in the movie, it is clear that the structure compresses most in the horizontal direction. The phase transition which occurs above 1 GPa can be seen as a more abrupt compression in this same direction. The trend persists after the phase transition, and the exact directions of greatest and least strain are illustrated in Figure 3.17b.

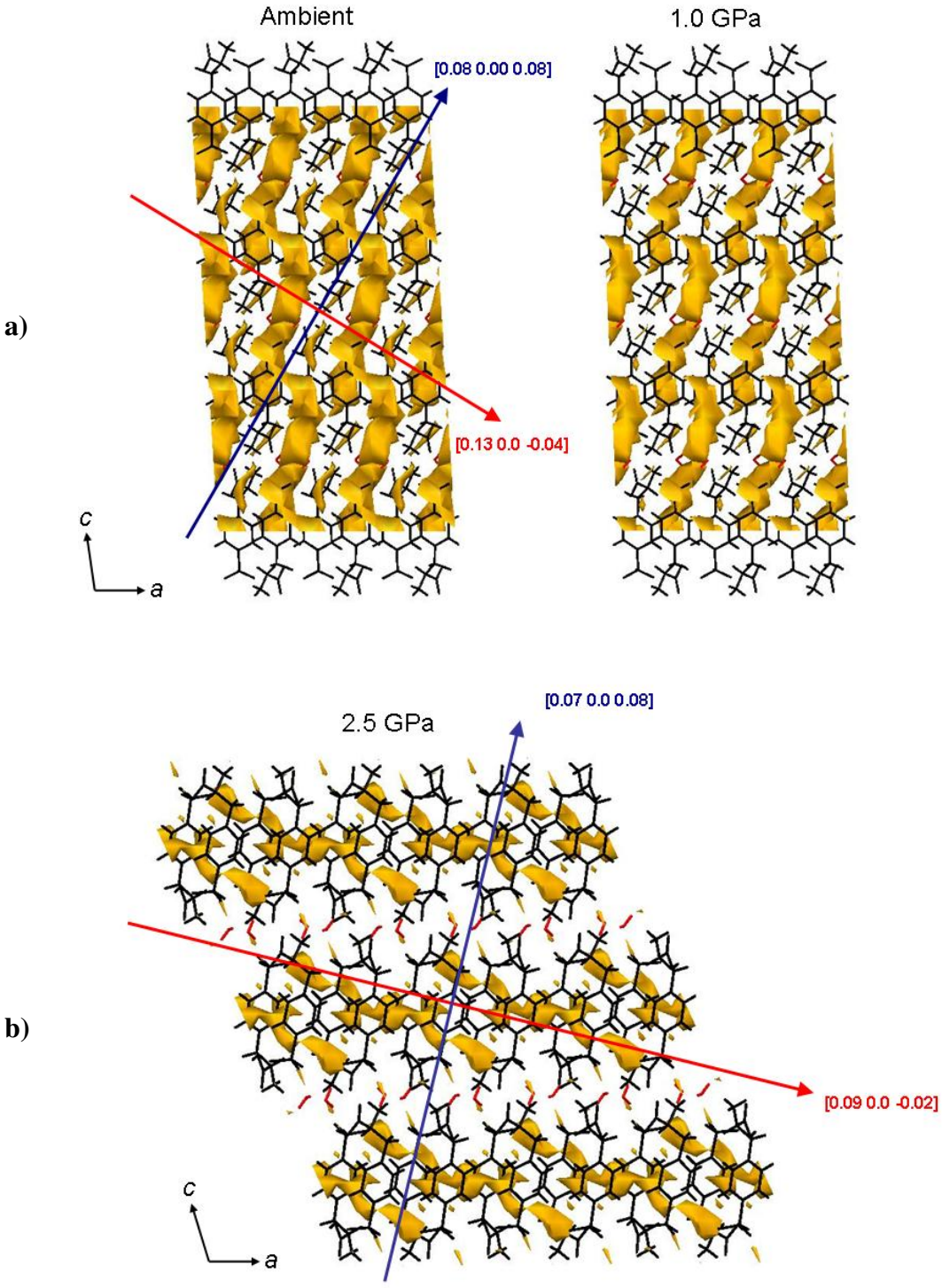

Figure 3.17: Void distribution in a) SPM-I at ambient conditions and 1.0 GPa, and b) SPM-II at 2.5 GPa. S-4-sulfo-L-phenylalanine molecules are shown in black, and water molecules are shown in red. Red and blue arrows indicate the directions of greatest and least strain, respectively (*cf* Table 7).

A common feature in high-pressure studies of layered structures is that the greatest amount of compression occurs along the layer stacking direction: this does not occur in SPM. Part of the reason for this can be traced to the shapes of the voids, but, in addition, this direction is also parallel to the strongest interactions in the structure, namely the H-bonds formed between the layers, and the lengths of the molecules. Rather than decrease the layer stacking distance during the phase transition (as occurs in serine hydrate), the layers actually move further apart, almost as though the system of H-bonds formed between the layers is acting like a compressed spring.

In other respects the transitions in serine hydrate and SPM are quite similar: in both cases water molecules reorient, H-bonding within the layers of zwitterions is disrupted and the zwitterions themselves change conformation.

At 6.9 GPa there is a discontinuity in the cell dimensions of SPM-II versus pressure plots, and in the layer-stacking distance plot shown in Figure 3.9. There are no significant reorientations in the S-4-sulfo-L-phenylalanine molecules, though there is a modest change in a torsion angle which appears to relieve a short intramolecular H…H contact. We can not make a definitive statement about the orientations of the water molecules as H-atoms could not be located precisely.

Figure 3.14 shows the distinct change in packing when the phase transition occurs in SPM at 1 GPa. It is also interesting to see that there is a significant change between the structures at 6.4 GPa and 6.9 GPa when the discontinuity in the cell dimensions occurs.

3.6.1 The driving force of the transition

The character of the phase transition in SPM has similarities to serine hydrate: as pressure is increased on phase-I, layers approach one another, and as the transition occurs hydrogen bonding within layers is disrupted as the geometry of the zwitterions changes. The water molecules also change their orientation, although this is not to allow further approach of the layers: the layers move further apart through the transition (Figure 3.9).

SPM-I contains a very short H-bond [O2H1…O4, O…O = 2.563(4) Å at 1.0 GPa], and a search of the Cambridge Crystallographic Database for RCOOH to RSO_3^- interactions reveals that there are no structures where O…O distances appear to be shorter than this [the shortest occurs in VOJGAC where O…O = 2.561(3)]. PIXEL calculations performed on SPM-I indicate that despite the close proximity of the oxygen atoms, this interaction is strongly stabilising at ambient conditions and becomes even more so upon compression to 1.0 GPa. Similar comments could be made about intermolecular interaction energies in serine and serine hydrate, which are also zwitterionic. In phase-II the interaction becomes even shorter: O22…O42 = 2.514(13) at 6.9 GPa. It is not possible to carry out PIXEL calculations on this structure as there are too many molecules in the asymmetric unit, but we do not see any convincing evidence from the intermolecular distances that would lead us to conclude that the transition is driven by relief of repulsive intermolecular contacts.

The molecular volume decreases significantly throughout the transition (Figure 3.8b). Extrapolation of the phase-I points indicates that the molar volume of SPM-II at 2.5 GPa is *ca.* 6 $Å^3$ mol^{-1} lower than a hypothetical phase-I structure at the same pressure. This equates to a *PV* energy of 9 kJ mol^{-1}, indicating that, as in serine and serine hydrate, the *PV* term is an important factor determining the driving force of the transition.

3.7 Conclusions

We have described the effects of pressure on the crystal structures of betaine monohydrate, L-cysteic acid monohydrate and S-4-sulfo-L-phenylalanine monohydrate using single crystal synchrotron X-ray diffraction. In all cases, the least amount of compression was found to occur along the directions where H-bonds form; and the largest amount of compression occurred along the directions of large voids present within the structure.

A single-crystal to single-crystal phase transition occurs in S-4-sulfo-L-phenylalanine monohydrate at pressures above 1.0 GPa. In common with the phase transition in serine hydrate the SPM-I to -II transition is charactersied by (*i*) a change

in the conformation of the layer-building molecules and (*ii*) reorientation of the water molecules between layers. The original contention was that the water molecules would change their orientation in order to facilitate further shortening of the inter-layer distance: this did not occur, and in fact the layers moved further apart. In other respects the transitions in serine hydrate and SPM are more similar: the water molecules reorient, the zwitterions change conformation and H-bonding within the zwitterionic layers is disrupted.

By analogy with the phase transition in serine hydrate, it is possible that the transition in SPM is driven by the need to increase packing efficiency at high pressure. Above 6.4 GPa, there is a break in the trend of the unit cell parameters: the *b*-axis increases whilst the a-axis decreases, and as this happens the inter-layer separation reduces significantly and a short intramolecular H…H contact is lengthened.

3.8 References

Allan, D. R. & Clark, S. J. (1999a). *Physical Review B: Condensed Matter and Materials Physics* **60**, 6328-6334.

Allan, D. R. & Clark, S. J. (1999b). *Physical Review Letters* **82**, 3464-3467.

Allan, D. R., Clark, S. J., Brugmans, M. J. P., Ackland, G. J. & Vos, W. L. (1998). *Physical Review B: Condensed Matter and Materials Physics* **58**, R11809-R11812.

Allan, D. R., Clark, S. J., Ibberson, R. M., Parsons, S., Pulham, C. R. & Sawyer, L. (1999). *Chemical Communications* **8**, 751-752.

Allan, D. R., Clark, S. J., McGregor, P. A. & Parsons, S. (2002). *Acta Crystallographica, Section B* **58**, 1018-1024.

Allan, D. R., Parsons, S. & Teat, S. J. (2001). *Journal of Synchrotron Radiation* **8**, 10-17.

Allen, F. H. & Motherwell, W. D. S. (2002). *Acta Crystallographica, Section B* **58**, 407-422.

Altomare, A., Cascarano, G., Giacovazzo, C., Guagliardi, A., Burla, M. C., Polidori, G. & Camalli, M. (1994). *Journal of Applied Crystallography* **27**, 435-435.

Bernstein, J., Davis, R. E., Shimoni, L. & Chang, N.-L. (1995). *Angewandte Chemie, International Edition in English* **34**, 1555-1573.

Betteridge, P. W., Carruthers, J. R., Cooper, R. I., Prout, K. & Watkin, D. J. (2003). *Journal of Applied Crystallography* **36**, 1487.

Blatov, V. A. & Shevchenko, A. P. (2003). *Acta Crystallographica, Section A* **59**, 34-44.

Blessing, R. H. (1987). *Crystallography Reviews* **1**, 3-58.

Boldyreva, E. V., Shakhtshneider, T. P., Ahsbahs, H., Sowa, H. & Uchtmann, H. (2002). *Journal of Thermal Analysis and Calorimetry* **68**, 437-452.

Boldyreva, E. V., Shakhtshneider, T. P., Vasilchenko, M. A., Ahsbahs, H. & Uchtmann, H. (2000). *Acta Crystallographica, Section B* **56**, 299-309.

Brandenburg, K. & Putz, H. (2005). *DIAMOND, version 3.2*. Crystal Impact GbR, Postfach 1251, 53002, Bonn, Germany.

Bruker-Nonius (2006). *SAINT version 7, Program for integration of area detector data.* Bruker-AXS, Madison, Wisconsin, USA.

Burla, M. C., Caliandro, R., Camalli, M., Carrozzini, B., Cascarano, G. L., Caro, L. D., Giacovazzo, C., Polidori, G. & Spagna, R. (2005). *Journal of Applied Crystallography* **38**, 381-388.

Dawson, A., Allan, D. R., Belmonte, S. A., Clark, S. J., David, W. I. F., McGregor, P. A., Parsons, S., Pulham, C. R. & Sawyer, L. (2005). *Crystal Growth & Design* **5**, 1415-1427.

Dawson, A., Allan, D. R., Parsons, S. & Ruf, M. (2004). *Journal of Applied Crystallography* **37**, 410-416.

Espallargas, G. M., Brammer, L., Allan, D. R., Pulham, C. R., Robertson, N. & Warren, J. E. (2008). *Journal of the American Chemical Society* **130**, 9058-9071.

Fabbiani, F. P. A. & Pulham, C. R. (2006). *Chemical Society Reviews* **35**, 932-942.

Farrugia, L. J. (1999). *Journal of Applied Crystallography* **32**, 837-838.

Flack, H. D. (1983). *Acta Crystallographica, Section A* **39**, 876-881.

Frisch, M. J., Trucks, G. W., Schlegel, H. B., Scuseria, G. E., Robb, M. A., Cheeseman, J. R., Zakrzewski, V. G., Montgomery, J. A. J., Stratmann, R. E., Burant, J. C., Dapprich, S., Millam, J. M., Daniels, A. D., Kudin, K. N., Strain, M. C., Farkas, O., Tomasi, J., Barone, V., Cossi, M., Cammi, R., Mennucci, B., Pomelli, C., Adamo, C., Clifford, S., Ochterski, J., Petersson, G. A., Ayala, P. Y., Cui, Q., Morokuma, K., Malick, D. K., Rabuck, A. D., Raghavachari, K., Foresman, J. B., Cioslowski, J., Ortiz, J. V., Stefanov, B. B., Liu, G., Liashenko, A., Piskorz, P., Komaromi, I., Gomperts, R., Martin, R. L., Fox, D. J., Keith, T., Al-Laham, M. A., Peng, C. Y., Nanayakkara, A., Gonzalez, C., Challacombe, M., Gill, P. M. W., Johnson, B. G., Chen, W., Wong, M. W., Andres, J. L., Head-Gordon, M., Replogle, E. S. & Pople, J. A. (1998). *Gaussian 98 revision A.7.* Gaussian, Inc., Pittsburgh, PA, USA.

Gavezzotti, A. (2003). *OPIX - A computer program package for the calculation of intermolecular interactions and crystal energies.* University of Milano, Milan, Italy.

Gavezzotti, A. (2005). *Zeitschrift fuer Kristallographie* **220**, 499-510.

Gavezzotti, A. (2007). Molecular Aggregation: Structure Analysis and Molecular Simulation of Crystals and Liquids. Oxford, UK: Oxford University Press.

Hazen, R. M. & Finger, L. W. (1982). Comparative Crystal Chemistry: Temperature, Pressure, Composition and the Variation of Crystal Structure, p. 81. Chichester, New York, USA: John Wiley and Sons.

Johnstone, R. D. L., Francis, D., Lennie, A. R., Marshall, W. G., Moggach, S. A., Parsons, S., Pidcock, E. & Warren, J. E. (2008). *CrystEngComm* **10**, 1758-1769.

Larson, A. C. (1970). Crystallographic Computing, International Summer School 291-294. Munksgaard, Copenhagen, Denmark.

Macrae, C. F., Bruno, I. J., Chisholm, J. A., Edgington, P. R., McCabe, P., Pidcock, E., Rodriguez-Monge, L., Taylor, R., Streek, J. v. d. & Wood, P. A. (2008). *Journal of Applied Crystallography* **41**, 466-470.

Mak, T. C. W. (1990). *Journal of Molecular Structure* **220**, 13-18.

Merrill, L. & Bassett, W. A. (1974). *Review of Scientific Instruments* **45**, 290-294.

Moggach, S. A., Allan, D. R., Morrison, C. A., S. Parsons & Sawyer, L. (2005). *Acta Crystallographica, Section B* **61**, 58-68.

Moggach, S. A., Allan, D. R., Parsons, S. & Warren, J. E. (2008). *Journal of Applied Crystallography* **41**, 249-251

Moggach, S. A., Parsons, S. & Wood, P. A. (2008). *Crystallography Reviews* **14**, 143-184.

Oswald, I. D. H., Allan, D. R., Day, G. M., Motherwell, W. D. S. & Parsons, S. (2005). *Crystal Growth & Design* **5**, 1055-1071.

Oswald, I. D. H., Allan, D. R., Motherwell, W. D. S. & Parsons, S. (2005). *Acta Crystallographica, Section B* **61**, 69-79.

Parsons, S. (2003). *STRAIN - Program for calculation of linear strain tensors* University of Edinburgh, Edinburgh, UK.

Parsons, S. (2004). *SHADE- Program for empirical absorption corrections to high pressure data.* The University of Edinburgh, Edinburgh, United Kingdom.

Piermarini, G. J., Block, S., Barnett, J. D. & Forman, R. A. (1975). *Journal of Applied Physics* **46**, 2774-2780.

Prescimone, A., Milios, C. J., Moggach, S. A., Warren, J. E., Lennie, A. R., Sanchez-Benitez, J., Kamenev, K., Bircher, R., Murrie, M., Parsons, S. & Brechin, E. K. (2008). *Angewandte Chemie, International Edition* **47**, 2828-2831.

Press, W. H., Teukolsky, S. A., Vetterling, W. T. & Flannery, B. P. (1992). Numerical Recipes in Fortran, Second Edition. Cambridge University Press, Cambridge, England.

Prince, E. (1982). Mathematical Techniques in Crystallography and Materials Science. New York, USA: Springer-Verlag.

Ramanadham, M., Sikka, S. K. & Chidambaram, R. (1973). *Acta Crystallographica Section B* **29**, 1167.

Sheldrick, G. M. (2004). *SADABS Version 2004-1, Program for absorption corrections to area detector data.* Bruker-AXS, Madison, Wisconsin, USA.

Smaalen, S. v., Palatinus, L. & Schneider, M. (2003). *Acta Crystallographica, Section A* **59**, 459-469.

Spek, A. L. (2004). *PLATON.* Utrecht University, Utrecht, The Netherlands.

Watkin, D. J. (1994). *Acta Crystallographica, Section A* **50**, 411-437.

Watkin, D. J., Pearce, L. & Prout, K. (1993). *CAMERON - A Molecular Graphics Package.* Chemical Crystallography Laboratory, University of Oxford, Oxford, England.

Wood, P. A., Forgan, R. S., Henderson, D., Parsons, S., Pidcock, E., Tasker, P. A. & Warren, J. E. (2006). *Acta Crystallographica Section B* **62**, 1099-1111.

Wood, P. A., Francis, D., Marshall, W. G., Moggach, S. A., Parsons, S., Pidcock, E. & Rohl, A. L. (2008). *CrystEngComm* **10**, 1154 - 1166.

Xie, Y.-R., Xiong, R.-G., Xue, X., Chen, X.-T., Xue, Z. & You, X.-Z. (2002). *Inorganic Chemistry* **41**, 3323–3326.

Chapter 4

Use of the Allen Key in Crystal Engineering: Pressure-Induced Polymorphism in a High *Z'* Structure*

*Johnstone, R. D. L., Ieva, M., Lennie, A. R., McNab, H., Parsons, S., Pidcock, E., Warren, J. E. *CrystEngComm*. In Press.

4.1 Abstract

Methyl 2-(9H-carbazol-9-yl)benzoate is unusual in crystallising with eight molecules in the crystallographic asymmetric unit (Z' = 8). Under high pressure it transforms to a Z' = 2 structure. The molecules in the Z' = 2 phase have unfavourable conformations, but these are stabilised in the crystal by their efficient packing at high pressure.

4.2 Introduction

A feature of crystal structures that is frequently commented on, but rarely explained, is the number of molecules in the asymmetric unit (*Z*'). A survey of the Cambridge Crystallographic Database (Allen, 2002) carried out in 2000 (Steiner, 2000) showed that 96.6% of organic crystal structures have *Z*' = ½, 1 or 2, and by far the most common situation in organic crystal structures is for the asymmetric unit to contain one molecule (*Z*' = 1). This occurs in approximately 65% of cases. Values of *Z*' < 1 occur when a molecule crystallises on a special position, most commonly a centrosymmetric molecule crystallising about a position with -1 crystallographic symmetry. About 25% of organic crystal structures fall into this category. The remaining 10% or so [8.42% in 2000 (Steiner, 2000) rising to 8.8% in 2006 (Anderson, Goeta *et al.*, 2006)] of structures contain *Z*' > 1. Of structures with *Z*' > 1 the largest category have *Z*' = 2. Though structures with *Z*' = 3 or 4 occur in 0.5% of cases, values greater than this are very rare indeed. A database of structures with *Z*' > 4 has been compiled by Steed and co-workers (Steed, 2006-2009); the highest value of *Z*' for any structure listed in Steed's database is 32, for trimethyltin hydroxide (CSD refcode TMESNH) (Kasai *et al.*, 1965).

While an overall predictive high-*Z*' theory is lacking, a number of classes of compound have been identified as being particularly susceptible to formation of high *Z*' crystal structures. For example, 60% of chirally pure carboxylic acids and amides crystallise with *Z*' > 1 (Anderson, Afarinkia *et al.*, 2006; Dey & Pidcock, 2008): there is an incompatibility between the tendencies of acid or amide groups to form centrosymmetric H-bonded dimers and the enantiopurity of the compound, which

precludes the presence of an inversion centre in the crystal structure. In forming a crystal, the molecules 'solve' their problem by crystallising in a *Z*' = 2 structure in which pairs of crystallographically distinct molecules are related by a pseudo inversion centre (indeed, 83% of *Z*' = 2 crystals show some form of pseudosymmetry) (Gavezzotti, 2008). Systems such as these have been termed 'structurally frustrated' (Anderson *et al.*, 2008), and it can also occur when two or more competing supramolecular synthons are present within the same molecule. For example competition between strongly directional hydrogen bonding and less strongly directional π…π stacking interactions can lead to structural frustration and the formation of high *Z*' crystal structures (Anderson *et al.*, 2008).

Another factor which is associated with the formation of high *Z*' structures is the existence of a number of different conformations within a narrow range of energy: different conformations can co-exist within the same crystal, leading to a high-*Z*' structure (Desiraju, 2007; Roy *et al.*, 2006). It would appear that this is the source of the high value of *Z*' in the crystal structure of methyl 2-(9H-carbazol-9-yl)benzoate, **1** (Scheme 4.1).

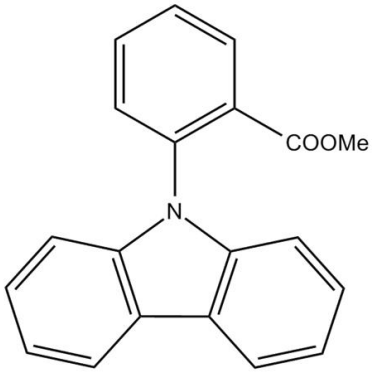

Scheme 4.1:
Methyl 2-(9H-carbazol-9-yl)benzoate, **1**

4.3 Results and Discussion

When crystallised from hexane/ethyl acetate under ambient conditions, **1** forms crystals with *Z*' = 8. The structure is in the polar space group *Pn*, but the positions of the orientations of the eight molecules which comprise the asymmetric unit make the space group close to $P2_1nb$ (a non-standard setting of $Pna2_1$) (Spek, 2003).

A view of one of the molecules is shown in Figure 4.1a, with a super-position of all eight molecules in Figure 4.1b. The main conformational differences arise from the torsional flexibility about the N1-C13 and C14-C19 bonds (Figure 4.1a). *Ab initio* calculations in which the conformations were held fixed while allowing all other structural parameters to vary (Roy *et al.*, 2006) indicate that the energies of the eight molecules span a range of 6 kJ mol^{-1}. There is approximate mirror-symmetry about a vertical plane through the middle of Figure 4.1b, but, since the space group is *Pn*, conformers with positive and negative torsion angles are present in the structure in equal amounts. The β-angle of the monoclinic unit cell is very close to 90°, and the crystal is twinned.

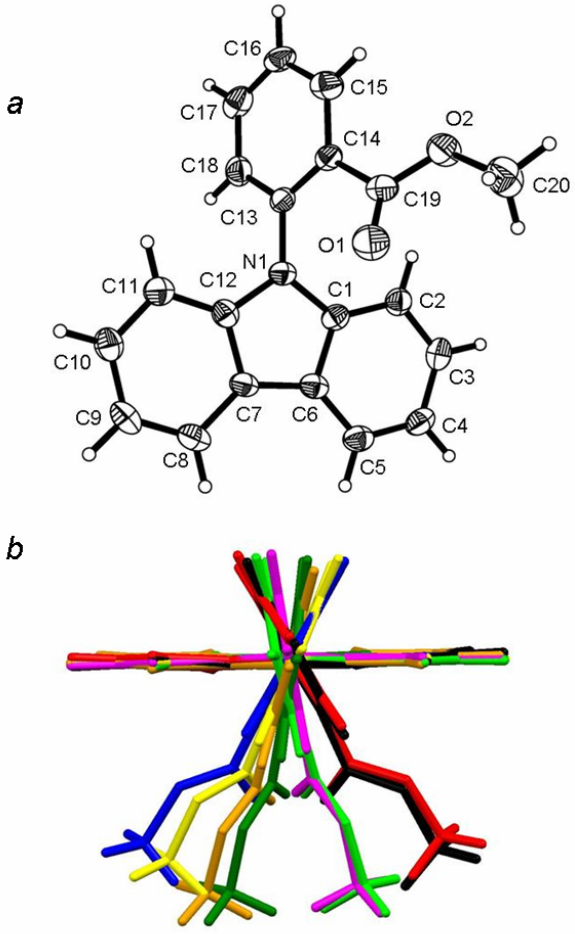

Figure 4.1 a) Molecular geometry of **1** at 150 K. Ellipsoids enclose 50% probability surfaces. b) Overlay of the carbazole rings for the eight symmetry inequivalent molecules in the ambient pressure phase (**1**-I).

The free energy of a system is expressed by the equation $G = U + PV - TS$, where the symbols have their usual thermodynamic meanings. At low pressures small differences in the conformational energies (which contribute to U) can be accommodated, but as pressure is increased on a sample the PV term becomes ever larger, and the need to pack molecules efficiently becomes ever more important. At high pressure the need to minimise volume should select conformers which are consistent with efficient packing, reducing the value of Z'. In this paper we describe the effect of high pressure on the crystal structure of **1**, and our attempts to force the crystal structure into one with a lower value of Z'.

A crystal of **1** was loaded into a Merrill-Bassett diamond anvil cell (Merrill & Bassett, 1974) (half-opening angle 40°), equipped with Boehler–Almax cut diamonds with 600 μm culets and a tungsten gasket (Moggach *et al.*, 2008). A 4:1 mixture of methanol and ethanol was used as a hydrostatic medium, and pressures were measured from the wavelength of the fluorescence from a small ruby chip which was also loaded into the cell (Piermarini *et al.*, 1975). The pressure inside the cell can be increased by tightening the Allen screws which hold the components of the cell together. Single crystal synchrotron diffraction data were collected in steps of *ca.* 1 GPa up to a final pressure of 6.8 GPa.

Up to 4.9 GPa the structure remained in a compressed form of its ambient-pressure phase (which we will label **1**-I). Pairs of molecules form pseudo-centrosymmetric dimers through CH…O interactions, and the dimers are then linked into ribbons by more CH…O and CH…π contacts. The ribbons run along the *a*-direction and there are four crystallographically distinct types. Ribbons interact with each other by more CH…π contacts, generating pseudo-2_1 screw axes along the *a*-direction (Figure 4.2a). The H…O distances in the CH…O contacts lie between 2.48 and 2.78 Å at ambient pressure and 2.11 and 2.46 Å at 4.9 GPa; the H….ring centroid distances in the CH…π interactions lie between 2.62 and 3.04 Å at ambient pressure and 2.31 and 2.88 Å at 4.9 GPa.

On increasing the pressure from 4.9 GPa to 5.3 GPa the structure underwent a phase transition to a new phase (**1**-II, Figure 4.2b). The value of Z' in the new phase is only 2, forming in space group $P2_12_12_1$. The pseudo-2_1 symmetry which related

the ribbons in phase-I is now a genuine crystallographic symmetry element; equally the twin law present in phase-I becomes a symmetry operation of the whole crystal. The structures are nevertheless quite different: a packing similarity search in Mercury 2.2 (Macrae *et al.*, 2008) indicates that only 4 molecules match in a cluster of 20.

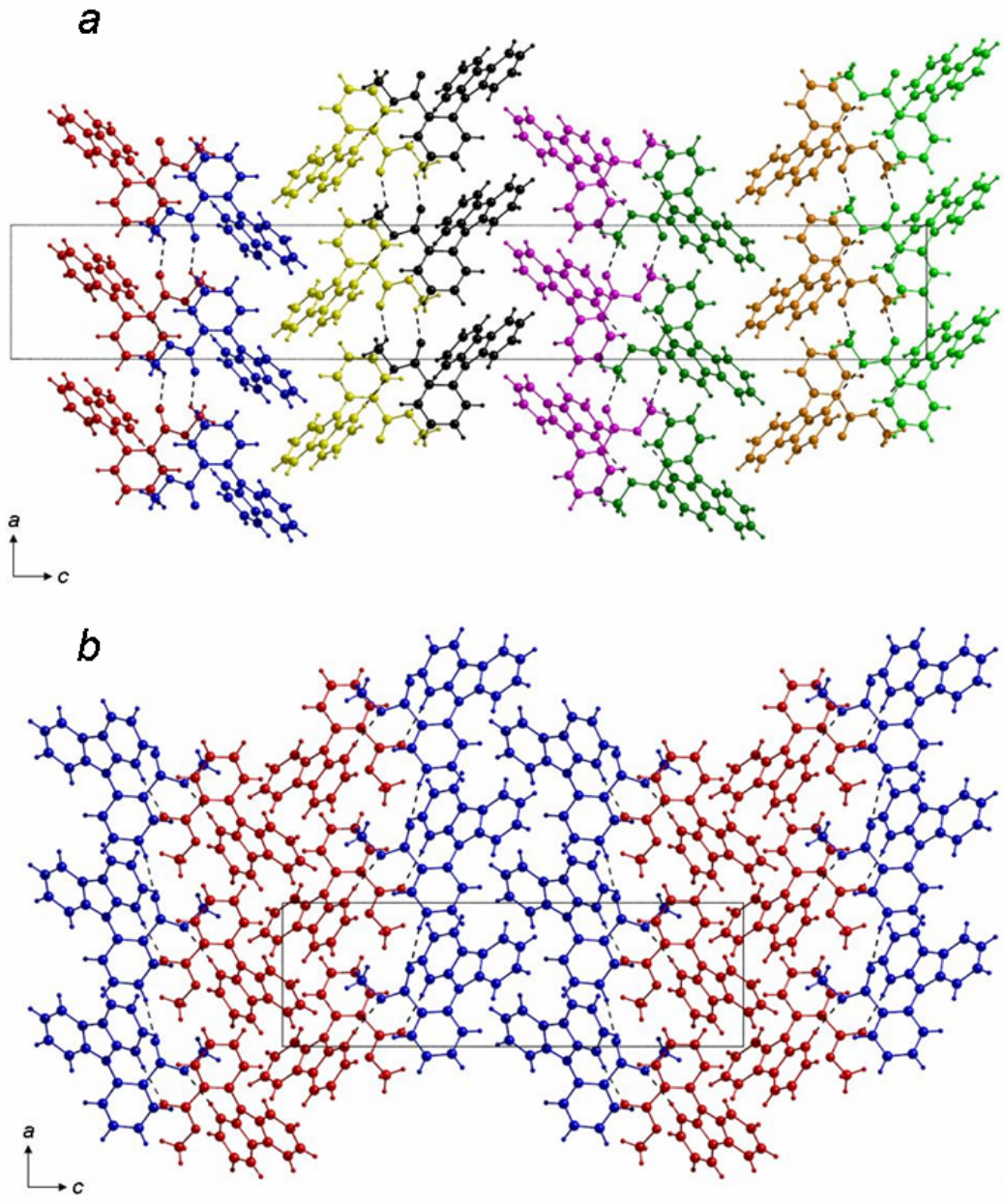

Figure 4.2: Packing in **1** in a) phase-I and b) phase-II, viewed along the *b*-direction. Molecules are coloured according to symmetry equivalence.

In phase-I there were eight conformations present in the unit cell; in phase-II there are just two (Figure 4.3). The ester group adopts two conformations relative to the phenyl ring [τ(C13-C14-C19-O1) = -166.7(6)° and -22.6(10)° in molecules 1 and 2, respectively]. In molecule 1 the methyl group of the ester is placed immediately above the carbazole ring, and as a result of this τ(C1-N1-C13-C14) is numerically larger [-110.9(7)°] than in molecule 2 [-39.8(9)°]. Somewhat unusually, the crystal and diffraction quality improved markedly after the phase transition; this may be the result of a reduction in the volume of the unit cell by a factor of two. H-atoms could be located easily, and it is clear that the methyl group adopts a near-eclipsed conformation. The carbazole ring becomes twisted: the largest deviations from the mean plane of the carbazole moiety in molecules 1 and 2 are 0.06 and 0.08 Å respectively. An attempt to restrain these moieties to planarity resulted in an increase in R_1 by 3%.

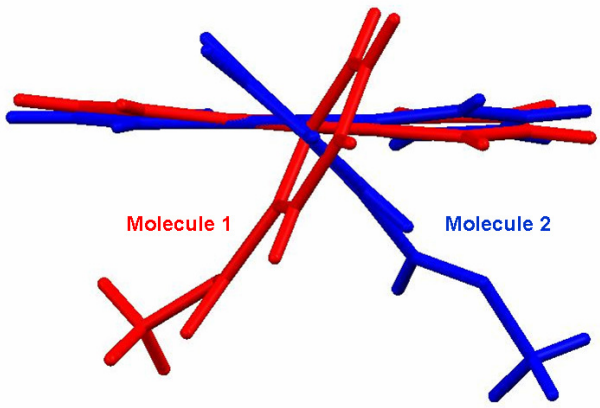

Figure 4.3: Overlay of the carbazole rings for the two unique molecules in phase-II (**1**-II) at 5.3 GPa.

The energies of the molecules in phase-I had a range of 6 kJ mol^{-1}. The energy difference between the molecules in phase-II is only 0.6 kJ mol^{-1} in favour of molecule 1. However, the molecules in phase-II are between 22 and 26 kJ mol^{-1} less stable than those in phase-I. This is a remarkably high energy difference. While molecules in crystal structures may deviate from the hypothetical minimum energy

structure of an isolated molecule at 0 K in order to minimise the energy of the crystal as a whole, energies are rarely more than about 5 kJ mol^{-1} above the global minimum (Allen *et al.*, 1996). The source of the energy difference lies mostly in the distortion of the carbazole rings from planarity (*ca.* 10 kJ mol^{-1}), the change in the orientation of the ester group (*ca.* 7 kJ mol^{-1}) and the eclipsed conformation of the methyl group (*ca.* 3 kJ mol^{-1}). But how can the structure sustain such unstable molecular conformations?

Our original idea in studying the effect of pressure on **1** was to force the molecules to adopt conformations consistent with more efficient packing. That this has occurred is demonstrated by the change in molecular volume that occurs during the phase transition (Figure 4.4). Extrapolation of the trend of the volume versus pressure curve established for phase-I suggests that it would have an estimated volume of 4909 $Å^3$ at 5.3 GPa had it not transformed to phase-II. This gives an estimated molecular volume of 307 $Å^3$ in phase-I at 5.3 GPa, compared to an observed molecular volume of 299.9 $Å^3$ for phase-II at the same pressure. At 5.3 GPa this volume difference gives phase-II an *PV* energy advantage of 23 kJ mol^{-1}, a value which is of a similar size to the energy differences between the molecules in phases-I and II. These data show that it is the more efficient packing which enables the structure of phase-II to accommodate such unfavourable molecular conformations.

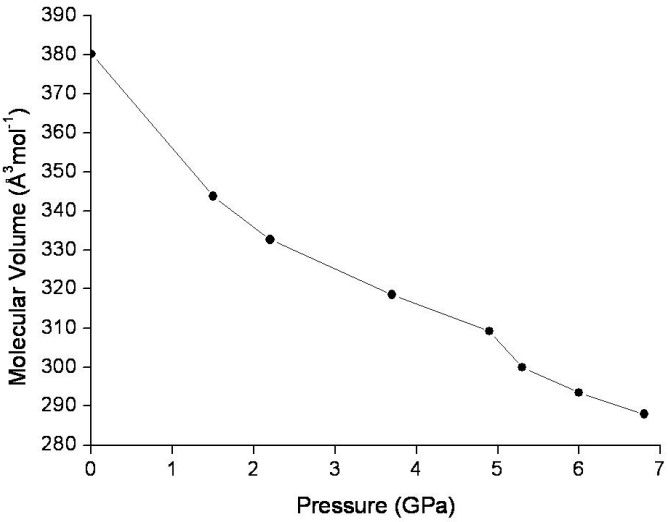

Figure 4.4: Molecular volume of **1** as a function of pressure.

If pressure is released the *PV* advantage of phase-II diminishes, and the molecules would be expected to 'spring back' to their more stable conformations. Consistent with this model, when the pressure was released the structure transformed back to phase-I at 4.6 GPa, demonstrating the thermodynamic stability of phase-I at lower pressures. Given the differences between the structures, the ability to go back-and-forth between phases in single-crystal to single-crystal transitions is remarkable.

4.4 Conclusions

Some authors have described high *Z*' structures as 'fossil relics' of fast growing crystal nuclei which become kinetically stabilised as the crystal grows [see for example Desiraju (2007)]. It has even been suggested that high *Z*' structures are metastable forms obtained under kinetic conditions, implying that generally a lower energy, thermodynamically more stable polymorph with a lower value of *Z*' must exist. This idea has been criticised by Anderson & Steed (2007) while a systematic investigation of energetics in high *Z*' structures found no proof that fully symmetric structures are more stable (Gavezzotti, 2008). The results described here for **1**, for which a high *Z*' structure is thermodynamically preferred over a lower *Z*' alternative at low pressure, are also consistent with the idea that high *Z*' structures can be thermodynamically stable.

4.5 Experimental

A mixture of carbazole (3.34 g, 20 mmol), methyl 2-iodobenzoate (7.86 g, 30 mmol), copper powder (0.90 g) and anhydrous potassium carbonate (4.14 g, 30 mmol) was heated in nitrobenzene (2 cm^3) at 175 °C for 48 h. After cooling, a mixture of water and chloroform (1 : 1) was added and the two layers separated. The aqueous layer was extracted twice with chloroform and the organic layers were combined and dried over $MgSO_4$. The solvent was removed under reduced pressure and the residual oil was purified by flash dry chromatography on silica using hexane:ethyl acetate (85:15) as the eluant to give colourless crystals of **1** (5.30 g, 88%) mp 149-151 °C [lit., (Glaser *et al.*, 1980) 150-151 °C]. δ_H (360 MHz, $CDCl_3$)

8.20-8.10 (3H, m), 7.78 (1H, m), 7.61 (2H, m), 7.40 (2H, ddd, *J* 8.3, 7.2, 1.3 Hz), 7.29 (2H, ddd, *J* 8.0, 7.3, 1.0 Hz), 7.15 (2H, td, *J* 8.2, 0.8) 3.21 (3H, s) [consistent with reported data (Glaser *et al.*, 1980)]; δ_C 166.3 (quat), 141.5 (2 quat), 136.8 (quat), 133.2 (CH), 131.9 (CH), 129.99 (CH), 129.96 (quat), 128.2 (CH), 125.8 (2 CH), 123.2 (2 quat), 120.1 (2 CH), 119.7 (2 CH), 109.2 (2 CH) 52.0 (CH_3).

Crystal data for **1-I** at ambient pressure: monoclinic *Pn*, a = 7.6168(2), b = 15.2552(5), c = 52.3376(16) Å, β = 89.976(2)°, V = 6081.4(3) Å^3, Z = 16¸ D_c = 1.316 g cm^{-3}, T = 150 K. 39621 data were collected on a Bruker SMART APEX diffractometer with graphite-monochromated Mo-Kα radiation (λ = 0.71073 Å) to θ_{max} = 23.3°, giving a unique set of 8753 data (R_{int} = 0.0497) (Blessing, 1997). Refinements started from coordinates taken from the Cambridge Structural Database (CSD refcode: CARZIF). A multiscan absorption correction was applied (SADABS) (Sheldrick, 2008). Minimisation was carried out against F using 8633 data with $F > 4\sigma(F)$ in CRYSTALS (Betteridge *et al.*, 2003). Anisotropic displacement parameters for non-hydrogen atoms were restrained to ideal rigid body values derived from TLS analysis of unrestrained parameters. Global rigid-bond and body restraints were also applied. Distances and angles within phenyl rings were restrained to be equal, and planarity restraints were also applied. All hydrogen atoms were placed geometrically and constrained to ride on their host atoms. The structure was pseudo-merohedrally twinned via a two-fold axis along [100]; the twin scale factor was 0.4611(5). The final unweighted R factor was 0.0365, R_w = 0.0241, and the final difference map extremes were ±0.14 eÅ^{-3}.

High-pressure diffraction data were collected on a Bruker-Nonius APEX-II diffractometer with silicon-monochromated synchrotron radiation (λ = 0.4792 Å) on Station 9.8 at the SRS, Daresbury Laboratory. Data collection and processing procedures for high-pressure experiments followed (Dawson *et al.*, 2004). Refinements of the compressed form of **1-I** obtained between ambient pressure and 4.9 GPa were carried out starting from the ambient pressure coordinates; minimisation was against F using data with $F > 4\ \sigma(F)$ using CRYSTALS. All primary bond distances and angles were restrained to the values observed at ambient pressure. Owing to the low completeness of the data sets, displacement parameters

were only modelled at the isotropic level with global rigid-bond restraints applied. Planarity restraints were also applied to the phenyl rings. Twinning was modelled using the same twin law as used for the ambient pressure refinements, although a different crystal was used for the high-pressure data collections, and the scale factors were also different [0.111(3)]. Crystal data for **1-I** at 4.9 GPa: monoclinic *Pn*, a = 7.0316(6), b = 14.0254(19), c = 50.157(8) Å, β = 89.796(9)°, V = 4946.5(11) Å^3, Z = 16, D_c = 1.618 g cm^{-3}. 15990 data were collected to θ_{max} = 13.6°, giving a unique set of 3698 reflections (R_{int} = 0.1028), corresponding to a completeness of 74%. The final value of R was 0.0767, R_w = 0.0762, Δρ = ±0.17 eÅ^{-3}.

The structure of **1-II** was solved using the program SIR-2004 (Burla *et al.*, 2005). Refinements were carried out against F using data with $F > 4\sigma(F)$ in CRYSTALS. The data quality improved considerably after the phase transition, all non-hydrogen atoms were refined anisotropically with global rigid-bond and body restraints. Hydrogen atoms attached to phenyl rings were placed geometrically and constrained to ride on their host atoms. Geometric placement of methyl hydrogens resulted in a close H…H contact of *ca.* 1.2 Å (hydrogen distances normalised to standard neutron values), and subsequently, their positions were refined using distance and angle restraints. Crystal data for **1-II** at 5.3 GPa: orthorhombic $P2_12_12_1$. a = 7.701(2), b = 12.569(6), c = 24.786(13) Å, V = 2399.2(18) Å^3, Z = 8, D_c = 1.668 gcm^{-3}. 9206 data were collected to θ_{max} = 15.3°, yielding a unique data set of 1574 reflections (R_{int} = 0.145), corresponding to a completeness of 79%. The value of R was 0.0510, R_w = 0.0570 and Δρ = ±0.30 eÅ^{-3}.

Gasket failure occurred above 5.3 GPa and a second loading was required using a slightly different pressure cell with 400 μm culets in order to reach higher pressures. Diffraction profiles broadened significantly above 6.8 GPa, and no attempt was made to collect data at higher pressures. Instead the pressure was reduced back down to 4.6 GPa in order to test the reversibility of the phase transition. Enough data were collected at 4.6 GPa to enable indexing, which showed that the sample had reverted to phase-I.

Ab initio calculations were carried out with GAUSSIAN03 (Frisch *et al.*, 2003) at the B3LYP/6-31G(d,p) level of theory.

4.6 References

Allen, F. H. (2002). *Acta Crystallographica, Section B* **58**, 380-388.

Allen, F. H., Harris, S. E. & Taylor, R. (1996). *Journal of Computer-Aided Molecular Design* **10**, 247-254.

Anderson, K. M., Afarinkia, K., Yu, H.-W., Goeta, A. E. & Steed, J. W. (2006). *Crystal Growth and Design* **6**, 2109–2113.

Anderson, K. M., Goeta, A. E., Hancock, K. S. B. & Steed, J. W. (2006). *Chemical Communications* 2138-2140.

Anderson, K. M., Goeta, A. E. & Steed, J. W. (2008). *Crystal Growth and Design* **8**, 2517–2524.

Anderson, K. M. & Steed, J. W. (2007). *CrystEngComm* **9**, 328-330.

Betteridge, P. W., Carruthers, J. R., Cooper, R. I., Prout, K. & Watkin, D. J. (2003). *Journal of Applied Crystallography* **36**, 1487.

Blessing, R. H. (1997). *Journal of Applied Crystallography* **30**, 421-426.

Burla, M. C., Caliandro, R., Camalli, M., Carrozzini, B., Cascarano, G. L., Caro, L. D., Giacovazzo, C., Polidori, G. & Spagna, R. (2005). *Journal of Applied Crystallography* **38**, 381-388.

Dawson, A., Allan, D. R., Parsons, S. & Ruf, M. (2004). *Journal of Applied Crystallography* **37**, 410-416.

Desiraju, G. R. (2007). *CrystEngComm* **9**, 91-92.

Dey, A. & Pidcock, E. (2008). *CrystEngComm* **10**, 1258-1264.

Frisch, M. J., Trucks, G. W., Schlegel, H. B., Scuseria, G. E., Robb, M. A., Cheeseman, J. R., Montgomery Jr., J. A., Vreven, T., Kudin, K. N., Burant, J. C., Millam, J. M., Iyengar, S. S., Tomasi, J., Barone, V., Mennucci, B., Cossi, M., Scalmani, G., Rega, N., Petersson, G. A., Nakatsuji, H., Hada, M., Ehara, M., Toyota, K., Fukuda, R., Hasegawa, J., Ishida, M., Nakajima, T., Honda, Y., Kitao, O., Nakai, H., Klene, M., Li, X., Knox, J. E., Hratchian, H. P., Cross, J. B., Bakken, V., Adamo, C., Jaramillo, J., Gomperts, R., Stratmann, R. E., Yazyev, O., Austin, A. J., Cammi, R., Pomelli, C., Ochterski, J. W., Ayala, P. Y., Morokuma, K., Voth, G. A., Salvador, P., Dannenberg, J. J., Zakrzewski, V. G., Dapprich, S., Daniels, A. D., Strain, M. C., Farkas, O., Malick, D. K., Rabuck, A. D., Raghavachari, K., Foresman, J. B., Ortiz, J. V., Cui, Q., Baboul, A. G., Clifford, S., Cioslowski, J., Stefanov, B. B., Liu, G., Liashenko, A., Piskorz, P., Komaromi, I., Martin, R. L., Fox, D. J., Keith, T., Al-Laham, M. A., Peng, C. Y., Nanayakkara, A., Challacombe,

M., Gill, P. M. W., Johnson, B., Chen, W., Wong, M. W., Gonzalez, C. & Pople, J. A. (2003). *Gaussian 03, Revision E.01*. Gaussian, Inc., Wallingford CT, 2004. .

Gavezzotti, A. (2008). *CrystEngComm* **10**, 389 - 398.

Glaser, R., Blount, J. F. & Mislow, K. (1980). *Journal of the American Chemical Society* **102**, 2777-2786.

Kasai, N., Yasuda, K. & Okawara, R. (1965). *Journal of Organometallic Chemistry* **3**, 172-173.

Macrae, C. F., Bruno, I. J., Chisholm, J. A., Edgington, P. R., McCabe, P., Pidcock, E., Rodriguez-Monge, L., Taylor, R., Streek, J. v. d. & Wood, P. A. (2008). *Journal of Applied Crystallography* **41**, 466-470.

Merrill, L. & Bassett, W. A. (1974). *Review of Scientific Instruments* **45**, 290-294.

Moggach, S. A., Allan, D. R., Parsons, S. & Warren, J. E. (2008). *Journal of Applied Crystallography* **41**, 249-251

Piermarini, G. J., Block, S., Barnett, J. D. & Forman, R. A. (1975). *Journal of Applied Physics* **46**, 2774-2780.

Roy, S., Banerjee, R., Nangia, A. & Kruger, G. J. (2006). *Chemistry-A European Journal* **12**, 3777-3788.

Sheldrick, G. M. (2008). *SADABS, Program for absorption corrections to area detector data.* Bruker-AXS, Madison, WIsconsin, USA.

Spek, A. L. (2003). *Journal of Applied Crystallography* **36**, 7-13.

Steed, J. W. (2006-2009). *Z',* http://www.dur.ac.uk/zprime/.

Steiner, T. (2000). *Acta Crystallographica Section B* **56** 673-676.

Chapter 5

High-Pressure Polymorphism in Salicylamide*

* Johnstone, R. D. L., Lennie, A. R., Parker, S. F., Parsons, S., Pidcock, E., Richardson, P., Warren, J. E., Wood, P. A. *CrystEngComm*. In press.

5.1 Abstract

The compression of a single crystal (grown at ambient conditions) of salicylamide to 5.1 GPa is reported. The ambient phase appears to be stable up to this pressure, and Raman spectra do not indicate any change in phase above this point. In addition, we show that pressure-induced crystallisation (0.2 GPa) of a saturated solution of salicylamide in a 4:1 mixture of methanol: ethanol results in a polymorphic form of the ambient phase. Processing of three crystallites within the cell as if the data were non-merohedrally twinned resulted in data which were >90% complete. The polymorph obtained from *in situ* growth is favoured due to the *PV* term, the zero point energy and entropy.

5.2 Introduction

Understanding and prediction of polymorphism in the organic solid state is one of Chemistry's 'big questions'. Different polymorphs differ in solubility, ease of processing and reproducibility of formation. These properties are of particular importance to the pharmaceutical industry, which spends many millions of pounds each year on investigations of polymorphism of drug compounds, and our big question is one of real practical and commercial importance. Understanding why a polymorph forms under certain conditions but not under others forms an important component to work in the areas of polymorphism and crystal engineering.

Over the past ten years high pressure has been shown to be a powerful tool for studying polymorphism. Numerous new high pressure polymorphs have been generated for simple molecules such as alcohols and carboxylic acids (Allan & Clark, 1999a, b; Allan *et al.*, 1998; Oswald *et al.*, 2005), for more complex systems, such as amino acids (Moggach, Parsons *et al.*, 2008), and for substantially larger systems such as energetic materials, pharmaceuticals (Fabbiani & Pulham, 2006), metal-organic frameworks (Moggach *et al.*, 2009) and transition metal complexes (Allan *et al.*, 2006; Moggach & Parsons, 2009). Over the course of our work in this area we have tried to understand the driving forces for pressure-induced phase transitions. In salicylaldoxime, for example, a transition between one form and another occurs at *ca*. 5 GPa, which we have shown relieves the strain generated in

hydrogen bonds and π-π stacking interactions which are driven into repulsive regions of their potentials (Wood *et al.*, 2006).

In this paper we describe a study on the effect of pressure on salicylamide (Scheme 5.1), a compound closely related to salicylaldoxime, the two being related by replacement of an oxime group by an amide. We show that although a new polymorph of salicylamide can be formed by *in situ* crystal growth from solution at 0.2 GPa, compression of the known ambient-pressure form does not result in any phase transformations, even up to 5 GPa. This result illustrates the need for the existence of an energetically accessible pathway for a phase transition to occur in a solid, a feature also seen in compression studies of glycine, where different starting polymorphs yield different high-pressure forms (Dawson *et al.*, 2005).

When new polymorphs are generated by application of pressure, packing energy calculations can track the effects of compression on individual intermolecular interactions, revealing which interactions become repulsive, and which of these are relieved after a phase transition. When a new form crystallises directly from solution this conceptually simple means for understanding why polymorphism occurs is not available, and in this chapter, the features that make the new high-pressure polymorph of salicylamide thermodynamically competitive with the known form are addressed.

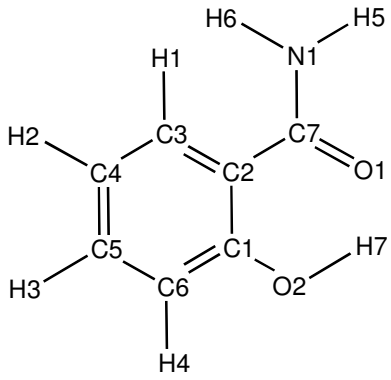

Scheme 5.1: Chemical structure diagram showing atomic numbering scheme in salicylamide.

5.3 Experimental

The effect of pressure on salicylamide was investigated in two separate experiments. In one case pressure was applied to a crystal grown at ambient pressure. In the second experiment, a crystal was grown *in situ* at high pressure.

Salicylamide (99% purity, Scheme 5.1) was purchased from Aldrich (catalogue number 860417). A sample (0.5103 g) was dissolved in a 4:1 mixture of methanol and ethanol (5 ml) and recrystallised by slow evaporation of the solvent. The solvent system used here is commonly used as a hydrostatic medium in high-pressure crystallography.

For one set of experiments a small, colourless, block-shaped crystal was loaded into a diamond anvil cell and used to study the effect of pressure on a single crystal grown *ex situ*. For the second set of experiments, a sample of the mother liquor from the same crystal growth experiment described above was loaded into a separate diamond anvil cell and used for *in situ* crystal growth at high pressure (0.2 GPa). Crystal growth is described below.

5.3.1 Determination of the crystal structure of salicylamide under ambient conditions

In order to facilitate a comparison between ambient and high-pressure structures, diffraction data were also collected on salicylamide at ambient temperature and pressure. The crystal used was taken from the same batch as the sample used for the compression study. Data were measured on a Bruker SMART APEX diffractometer with graphite-monochromated Mo-Kα radiation (λ = 0.71073 Å) at room temperature. The data were integrated using SAINT (Bruker-Nonius, 2006) and corrected for absorption with SADABS (Sheldrick, 2004). The structure was solved using the program SIR-92 (Altomare *et al.*, 1994) and initial structure refinement against $|F|^2$ using all data in CRYSTALS (Betteridge *et al.*, 2003), yielded a conventional *R*-factor of 0.075 (crystal and refinement data are given in Table 5.1).

The results of the ambient pressure data collection showed the sample to have the same unit cell parameters and space group as those determined by Sasada *et al.* (1964) and Pertlik (1990). Direct refinement of Pertlik's coordinates against our data set yielded a very high *R*-factor (0.51). The solution we present here differs from those given in the above references by an origin-shift of [¼,-¼ ,¼]. We discuss the implication of this on crystal packing below.

Pressure/ GPa	Ambient	0.3	2.0
Phase	I	I	I
M_r	137.14	137.14	137.14
Cell setting, space group	Monoclinic, *I*2/*a*	Monoclinic, *I*2/*a*	Monoclinic, *I*2/*a*
a, b, c (Å)	12.8887 (8), 4.9700 (3), 20.9607 (19)	12.7925 (11), 4.9356 (5), 20.415 (5)	12.5438 (6), 4.8464 (3), 19.203 (3)
α, β, γ (˚)	90, 91.546 (4), 90	90, 92.266 (14), 90	90, 93.648 (7), 90
V (Å)	1342.19 (17)	1288.0 (4)	1165.0 (2)
Z	8	8	8
D_x (Mg m^{-3})	1.357	1.414	1.564
μ (mm^{-1})	0.10	0.11	0.12
Crystal form, colour	Block, colourless	Block, colourless	Block, colourless
Crystal size (mm)	0.57 x 0.36 x 0.32	0.2.0 x 0.20 x 0.10	0.2.0 x 0.20 x 0.10
T_{min}	0.82	0.86	0.86
T_{max}	0.97	0.99	0.99
No. of measured, independent and observed reflections.	9399, 1778, 1434	4875, 814, 520	4594, 753, 564
R_{int}	0.037	0.084	0.062
d_{max}, d_{min}/ Å	10.4, 0.72	4.6, 0.70	4.52, 0.70
$R[F^2 > 2\sigma(F^2)]$, $wR(F^2)$, S	0.075, 0.138, 1.10	0.054, 0.128, 0.99	0.047, 0.111, 1.00
No. of parameters	95	95	95
Weighting Scheme	Calculated Method = Modified Sheldrick w = 1/[$s^2(F^2)$ + (0.02P)^2 + 2.68P] ,where P = (max(F_o^2,0) + 2F_c^2)/3	Calculated Method = Modified Sheldrick w = 1/[$s^2(F^2)$ + (0.02P)^2 + 2.68P] ,where P = (max(F_o^2,0) + 2F_c^2)/3	Calculated Method = Modified Sheldrick w = 1/[$s^2(F^2)$ + (0.02P)^2 + 2.68P] ,where P = (max(F_o^2,0) + 2F_c^2)/3
$(\Delta/\sigma)_{max}$	<0.0001	<0.0001	<0.0001
$\Delta\rho_{max}$, $\Delta\rho_{min}$ (e Å^{-3})	0.34, -0.31	0.37, -0.36	0.27, -0.23
Completeness to 0.8 Å	100%	45.7%	46.7%

(a)

Pressure/ GPa	4.0	5.1	0.2
Phase	I	I	II
M_r	137.14	137.14	137.14
Cell setting, space group	Monoclinic, *I*2/*a*	Monoclinic, *I*2/*a*	Orthorhombic, $P2_12_12_1$
a, b, c (Å)	12.3706 (7), 4.7918 (3), 18.398 (3)	12.2791 (7), 4.7643 (3), 17.9649 (17)	3.8938 (4), 5.5612 (6), 28.566 (8)
α, β, γ (˚)	90, 94.078 (8), 90	90, 93.960 (4), 90	90, 90, 90
V (Å)	1087.8 (2)	1048.46 (13)	618.6 (2)
Z	8	8	4
D_x (Mg m^{-3})	1.675	1.737	1.472
μ (mm^{-1})	0.13	0.13	0.11
Crystal form, colour	Block, colourless	Block, colourless	Block, colourless
Crystal size (mm)	0.2.0 x 0.20 x 0.10	0.2.0 x 0.20 x 0.10	Three crystallites, each 0.20 x 0.07 x 0.04
T_{min}	0.84	0.79	0.74
T_{max}	0.99	0.99	0.99
No. of measured, independent and observed reflections.	4172, 721, 542	3937, 695, 566	10956, 720, 434
R_{int}	0.058	0.059	0.149
d_{max}, d_{min}/ Å	4.46, 0.70	4.44, 0.70	5.46, 0.8
$R[F^2 > 2\sigma(F^2)]$, $wR(F^2)$, *S*	0.050, 0.119, 1.00	0.048, 0.124, 1.05	0.049, 0.126, 1.05
No. of parameters	95	95	95
Weighting Scheme	Calculated Method = Modified Sheldrick w = 1/[$s^2(F^2)$ + (0.02P)^2 + 2.68P] ,where P = (max(F_o^2,0) + 2F_c^2)/3	Calculated Method = Modified Sheldrick w = 1/[$s^2(F^2)$ + (0.02P)^2 + 2.68P] ,where P = (max(F_o^2,0) + 2F_c^2)/3	Calculated Method = Modified Sheldrick w = 1/[$s^2(F^2)$ + (0.02P)^2 + 2.68P] ,where P = (max(F_o^2,0) + 2F_c^2)/3
$(\Delta/\sigma)_{max}$	<0.0001	<0.0001	<0.0001
$\Delta\rho_{max}$, $\Delta\rho_{min}$ (e Å^{-3})	0.31, -0.31	0.27 -0.27	0.27, -0.30
Completeness to 0.8 Å	46.5%	47.9%	90.9%

(b)

Table 5.1: Crystallographic data for salicylamide.

5.3.2 High-pressure crystallography: compression of a single crystal

High-pressure experiments were carried out using a Merrill-Bassett diamond anvil cell (half-opening angle 40°), equipped with Boehler–Almax cut diamonds with 600 μm culets and a tungsten gasket (Merrill & Bassett, 1974; Moggach, Allan *et al.*, 2008). A 1:1 mixture of *n*-pentane and isopentane was used as a hydrostatic medium. This hydrostatic medium is very volatile, and the cell was cooled in dry ice prior to loading. A small ruby chip was also loaded into the cell and the ruby fluorescence method used to measure the pressure (Piermarini *et al.*, 1975).

Diffraction data were collected on a Bruker-Nonius APEX-II diffractometer with silicon-monochromated synchrotron radiation (λ = 0.4754 Å) on Station 9.8 at the SRS, Daresbury Laboratory. Data collection and processing procedures for the high-pressure experiments followed Dawson *et al.* (2004). Integrations were carried out using dynamic masking of the regions of the detector shaded by the pressure cell with the program SAINT. An absorption correction was carried out in a two-stage procedure with the programs SHADE (Parsons, 2004) and SADABS. Data were merged using SORTAV (Blessing, 1997, 1987).

Data collections were taken at regular intervals from ambient pressure up to a final pressure of 5.1 GPa. The sample remained in a compressed form of phase-I (see Table 5.1). A further increase in pressure resulted in a marked broadening of the diffraction profiles, and no attempt was made to collect data at higher pressures.

Refinements of the compressed form of salicylamide-I were carried out using the starting coordinates determined at ambient pressure and were refined against $|F|^2$ using all data, in CRYSTALS. Owing to the low completeness of the data sets (Table 5.1), global rigid bond and body restraints were applied to the anisotropic displacement parameters. Restraints were also applied to all non-hydrogen primary intramolecular bond distances and angles based on the ambient pressure values.

Hydrogen atoms attached to carbon and nitrogen were placed geometrically and positions were not refined, isotropic displacement parameters were respectively set to 1.2 and 1.5 times those of the C or N host atoms. Hydrogens attached to oxygen atoms were located in Fourier difference maps and their positions were refined subject to an O-H distance restraint of 0.84(1) Å. A planarity restraint was

applied to atoms H7, O2, C1, C2, C7 and O1. Since the orientation of the OH group is the only H-atom structural parameter not fixed by the geometry of the rest of the molecule an isotropic displacement parameter for H7 was refined independently with a restraint based on the ambient pressure value.

5.3.3 Compression of salicylamide as studied by Raman spectroscopy

For the purposes of Raman spectroscopic measurements a single crystal of salicylamide-I was loaded into a Merrill-Bassett cell in the manner described above. Raman measurements were carried out as a function of pressure by excitation with a 632.417 nm line from a He-Ne laser, the fluorescence being detected with a Jobin-Yvon LabRam 300 Raman spectrometer.

5.3.4 High Pressure Recrystallisation

High-pressure recrystallisation of salicylamide from solution was performed using a Merrill-Basset diamond cell (half opening angle 40°), equipped with brilliant-cut diamonds with 600 μm culets, a tungsten gasket and beryllium backing plates. At 0.2 GPa polycrystalline material precipitated. This was then almost completely redissolved with a heat gun, leaving a small seed crystallite. Slow cooling to room temperature produced three colourless crystals, each differently orientated inside the gasket hole. Diffraction data were collected using synchrotron radiation in the same manner as described above for the compression study. Determination of the cell constants showed the formation of a new polymorph of salicylamide (salicylamide-II) in space group $P2_12_12_1$ (Table 5.1).

The three domains were indexed and integrated separately, and then scaled and merged together in the program SORTAV (Blessing, 1987, 1997) to yield a data set of better than 90% completeness. The structure was solved using the program SIR-2004 (Burla *et al.*, 2005). Refinement was carried out against $|F|^2$ using all data (CRYSTALS) from all three domains to give a conventional *R*-factor of 0.049. All non-H atoms were refined with anisotropic displacement parameters. Hydrogen atom treatment was the same as for high-pressure structures of salicylamide-I.

Release of pressure from the cell caused the crystal to re-dissolve, and we were not able to recover it at ambient conditions.

5.3.5 DFT calculations

Periodic density functional theory (DFT) calculations were carried out using the DMOL^3 code (Delley, 1990) as incorporated in the Materials Studio suite of software (*Materials Studio Release Notes, Release 4.4, Accelrys Software Inc.*, 2008). The PW91 GGA exchange-correlation functional (Perdew & Wang, 1992) was used with the DND basis set. DND is a numerical basis set which includes polarizing d-functions on all non-H atoms; it is thought to provide reasonable accuracy at modest computational cost.

The *k*-point sampling was 4×4×2 with a grid size of 0.05 Å^{-1}; the optimisation energy convergence criterion was $\Delta E_{\text{opt}} < 2 \times 10^{-5}$ Hartree. The coordinates of the atoms in the solid state structure were allowed to optimise, while keeping the unit cell dimensions fixed. Following geometry optimisation vibrational frequencies were calculated at the Γ-point in the harmonic approximation. The structures studied in this way were salicylamide-I at ambient pressure and 0.3 GPa and salicylamide-II at 0.2 GPa.

5.3.6 Inelastic neutron scattering

Inelastic neutron scattering (INS) data were collected on the TOSCA instrument (Colognesi *et al.*, 2002) at the ISIS neutron spallation facility. A polycrystalline sample of salicylamide-h_7 (3.2243 g) was used as obtained from Aldrich. The spectra were recorded using a flat sample can at 20 K. INS data were visualised and compared to the results of the DFT calculations using the ACLIMAX program (Ramirez-Cuesta, 2004).

5.3.7 PIXEL Calculations

The final crystal structures obtained were used to calculate the molecular electron densities of the salicylamide molecules at each pressure by standard quantum chemical methods using the program GAUSSIAN03 (Frisch *et al.*, 2004)

with the MP2/6-31G** basis set. H-atom distances were set to standard neutron values in all calculations (C-H = 1.083 Å, N-H = 1.009 Å, O-H = 0.983 Å). The electron density was used to evaluate packing energies using the PIXEL method as implemented in the program OPiX (Gavezzotti, 2003). The output from these calculations yields a total packing energy and a breakdown into component interactions. Each energy is further broken down into its Coulombic (electrostatic), polarisation, dispersion and repulsion contributions (Gavezzotti, 2005, 2007).

5.3.8 Hirshfeld surface calculations

Hirshfeld surface calculations were carried out using CrystalExplorer (McKinnon *et al.*, 2004; Wolff *et al.*, 2007). The wavefunction for electrostatic potential mapping was obtained at the HF/6-31G* level of theory using the TONTO package embedded in CrystalExplorer. The electrostatic potential was mapped between -0.04 (red, indicating regions of negative charge) and +0.04 (blue, for positively charged regions).

5.3.9 Other programs used

Crystal structures were visualised using the programs CAMERON (Watkin *et al.*, 1993), MERCURY 2.2 (Macrae *et al.*, 2008) and DIAMOND (Brandenburg & Putz, 2005). Movies showing compression of the structures were made using CRYSTALMAKER (CrystalMaker, 2009). Analyses were carried out using PLATON (Spek, 2003), as incorporated in the WIN-GX suite (Farrugia, 1999). Searches of the Cambridge Structural Database (Allen, 2002) utilized the program CONQUEST with updates up to November 2008. Calculation of strain tensors were carried out using a locally-written program (Parsons, 2003) using the method described in Hazen & Finger (1982). Eigenvalues and vectors were calculated using the JACOBI routine in Press *et al.* (1992).

5.4 Results

5.4.1 Salicylamide-I at ambient conditions

Salicylamide crystallises at ambient conditions with one molecule in the asymmetric unit in the space group *I*2/*a*. Each molecule is effectively planar: a least-squares mean plane calculated using all non-hydrogen atoms shows that the average deviation of these atoms from the plane is 0.014 Å.

Non-covalent interactions are listed in Table 5.2. Also included are estimates of the energies of each intermolecular interaction as calculated by the PIXEL method (Dunitz & Gavezzotti, 2005; Gavezzotti, 2005, 2007). A breakdown of each energy term is available in Table 5.3. Note that PIXEL treats interactions at a *molecular* and not at an atomic level, and one must beware of falling into the trap of attributing a particular contact energy to a single prominent interatomic interaction, such as a hydrogen bond.

Each molecule forms one intramolecular H-bond from the hydroxyl group to the amidic oxygen (O2H7…O1) and two intermolecular H-bonds (N1H5…O1 and N1H6…O2) (Table 5.2). Pairs of N1H5…O1 contacts form across an inversion centre to create a dimer with a ring motif, graph set descriptor $R^2_2(8)$ (Bernstein *et al.*, 1995) (Table 5.2). The two molecules involved in each dimer are almost coplanar with a distance between least squares planes of 0.13 Å. This is the strongest interaction in the structure; the N…O distance is 2.923(3) Å and according to the PIXEL calculations the total intermolecular interaction energy is -55.7 kJ mol^{-1} (labeled interaction #1 in Table 5.2). N1H6…O2 (interaction #2 in Table 5.2) connects the dimers along the *a*-axis via glide symmetry; the N…O distance is 3.000(2) Å and the molecule-molecule energy is estimated to be -33.0 kJ mol^{-1}.

PIXEL Interaction no.	Interaction type	0 GPa	0.3 GPa	2.0 GPa	4.0 Gpa	5.1 GPa
Intramolecular interactions						
-	**O2H7...O1[i]**					
	H7…O1	1.71(3)	1.72(2)	1.69(2)	1.69(3)	1.68(3)
	O2…O1	2.514(2)	2.509(3)	2.489(3)	2.475(3)	2.467(3)
	<O2H7O1	156(3)	154(2)	155(2)	155(3)	153(3)
Network-building interactions						
#1	**N1H5...O1[ii]**					
	H5…O1	2.05	2.02	1.95	1.90	1.88
	N1…O1	2.923(3)	2.898(4)	2.832(3)	2.782(3)	2.758(3)
	<N1H5O1	175	176	177	178	177
	Energy	-55.7	-56.3	-56.8	-53.4	-52.1
#2	**N1H6...O2[iii]**					
	H6…O2	2.14	2.10	1.99	1.91	1.88
	N1…O2	3.000(2)	2.956(3)	2.841(2)	2.773(14)	2.735(2)
	<N1H6O2	164	164	164	165	165
	Energy	-33.0	-33.5	-32.5	-28.7	-25.5
Inter-network interactions						
#3	**π...πi[iv]**					
	Plane-plane	3.203	3.149	2.967	2.828	2.750
	Offset	6.551	6.519	6.458	6.396	6.347
	Energy	-23.6	-23.9	-21.8	-17.8	-15.6
#6	**π...π[vii]**					
	Plane-plane	3.368	3.260	3.050	2.927	2.859
	Offset	3.655	3.706	3.766	3.794	3.811
	Energy	-7.2	-6.9	-1.4	3.4	8.1
Inter-slab interactions						
#4	**π...πi[v]**					
	Plane-plane	2.680	2.642	2.580	2.566	2.556
	Offset	5.094	4.976	4.689	4.473	4.352
	Energy	-10.3	-11.1	-12.3	-11.2	-10.3
#5	**C4H2...π[vi]**					
	H2...π	3.23	3.11	2.83	2.67	2.61
	C4...π	4.035(3)	3.902(4)	3.626(4)	3.473(5)	3.411(3)
	<C4H2π	143	143	142	143	143
	Energy	-10.0	-10.5	-10.0	-7.5	-6.2

Symmetry Operators:

i	*x,y,z*	v	1/2-*x*, -1/2-*y*, 3/2-*z*
ii	1- *x*,1-*y*,1-*z*	vi	1-*x*, -1/2+*y*, 3/2-*z*
iii	1/2+*x*,-*y*,*z*	vii	*x*, *y*-1, *z*
iv	1-*x*, -*y*, 1-*z*		

Table 5.2: Geometry of intermolecular interactions in salicylamide-I. Distances are in Å, and angles in °. S.u's were calculated in PLATON. Total interaction energies are also included from PIXEL calculations and are given in kJ mol^{-1}. For CH…π interactions, distances and angles are measured with respect to the centroid of the rings.

Structure and Pressure	Interaction no. (see text)	ECoul	Epol	Edisp	Erep	Etot	Symmetry operators
CSD Refcode SALMID01 (Pertlik, 1990) (Ambient pressure)	-	-74.9	-24.9	-15.5	62.0	-53.3	-*x*+1/2, -*y*+3/2, -*z*+1/2
	-	-37.7	-26.8	-35.5	135.4	35.4	-*x* +1/2, *y*, -z+1
	-	-18.0	-3.3	-16.9	13.6	-24.6	-*x*+1/2, -*y*+1/2, -*z*+1/2
	-	-3.9	-0.6	-8.3	3.1	-9.6	-*x*, -*y*, -*z*+1
	-	2.9	-2.3	-20.3	12.0	-7.7	*x*, *y*+1, *z* / *x*, *y*-1, *z*
	-	-6.0	-7.2	-13.0	19.0	-7.2	*x*-1/2, -*y*, *z* / *x*+1/2, -*y*, *z*
Phase-I at ambient pressure – This work	#1	-76.3	-25.0	-15.2	60.8	-55.7	-*x*+1, -*y*+2, -*z*+1
	#2	-36.7	-12.7	-16.3	32.6	-33.0	*x*-1/2, -*y*+1, *z* / *x*+1/2, -*y*+1, *z*
	#3	-17.3	-3.3	-17.2	14.2	-23.6	-*x*+1, -*y*+1, -*z*+1
	#4	-4.3	-0.6	-8.9	3.5	-10.3	-*x*+1/2, -*y*+1/2, -*z*+3/2
	#5	-3.6	-1.3	-11.7	6.7	-10.0	-*x*+1, *y*-1/2, -*z*+3/2 / -*x*+1, *y*-1/2, -*z*+3/2
	#6	3.3	-2.5	-19.9	11.9	-7.2	*x*, *y*+1, *z* / *x*, *y*-1, *z*
Phase-I at 0.3 GPa – This work	#1	-80.5	-27.7	-15.7	67.7	-56.3	-*x*+1, -*y*+2, -*z*+1
	#2	-40.5	-14.6	-17.5	39.1	-33.5	*x*-1/2, -*y*+1, *z* / *x*+1/2, -*y*+1, *z*
	#3	-19.3	-3.9	-18.6	18.0	-23.9	-*x*+1, -*y*+1, -*z*+1
	#4	-5.1	-0.9	-10.4	5.2	-11.1	-*x*+1/2, -*y*+1/2, -*z*+3/2
	#5	-4.7	-1.9	-13.8	9.8	-10.5	-*x*+1, *y*-1/2, -*z*+3/2 / -*x*+1, *y*-1/2, -*z*+3/2
	#6	1.9	-3.3	-22.7	17.2	-6.9	*x*, *y*+1, *z* / *x*, *y*-1, *z*

(a)

Structure and Pressure	Interaction no. (see text)	ECoul	Epol	Edisp	Erep	Etot	Symmetry operators
Phase-II at 0.2 GPa – This work	#7	-23.0	-7.0	-13.1	16.2	-26.9	*x*-1, *y*+1, *z* / *x*+1, *y*-1, *z*
	#8	-27.6	-10.8	-8.6	27.5	-19.5	-*x*+1, *y*+1/2, -*z*+1/2 / -*x*+1, *y*-1/2, -*z*+1/2
	#9	-5.5	-3.3	-17.6	10.2	-16.2	*x*, *y*+1, *z* / *x*, *y*-1, *z*
	#10	0.4	-4.0	-33.0	23.4	-13.2	*x*+1, *y*, *z* / *x*-1, *y*, *z*
	#11	-2.8	-1.2	-9.6	5.8	-7.7	*x*-1/2, *y*-1/2, *z*+1 / *x*+1/2, *y*-1/2, *z*+1
	#12	-0.8	-1.1	-7.9	4.8	-5.1	*x*+1/2, -*y*-3/2, -*z*+1 / *x*-1/2, -*y*-3/2, -*z*+1

(b)

Table 5.3: Total energy breakdown for the six most energetically significant interactions in SALMID01, salicylamide-I at ambient pressure and 0.3 GPa and salicylamide-II at 0.2 GPa. Energies are calculated using the PIXEL method and are given in kJ mol^{-1}.

The hydrogen bonding creates a rather 'open' network (Figure 5.1a), and efficient packing is achieved by the interweaving of two networks (coloured red and blue in Figure 5.1b). The networks interact by the two stacking interactions; labelled #3 and #6 in Table 5.2 and illustrated in Figure 5.2. Interaction #3 is relatively strong for a stacking interaction (-23.6 kJ mol^{-1}), a feature which can be traced to large the electrostatic component (an energy breakdown is given in Table 5.3).

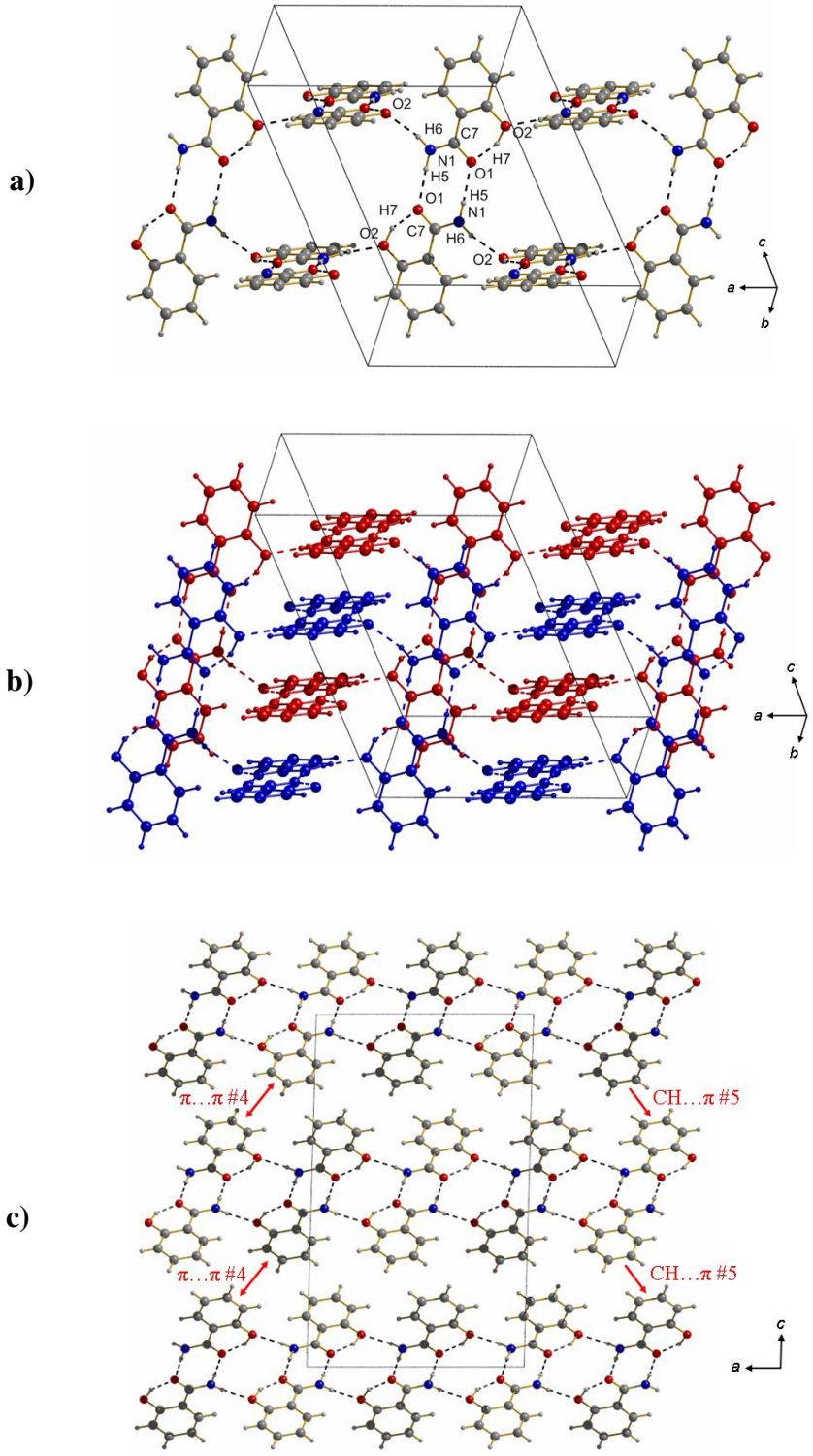

Figure 5.1: a) Hydrogen bonding in salicylamide-I creates an 'open' network of dimer interactions. b) Two networks combine via π…π stacking interactions to form slabs parallel to the *ab* plane. c) Slabs are connected to each other along the *c*-axis via π-interactions. Labels #4 and #5 refer to the specific interactions studied using the PIXEL method (see Tables 5.2 and 5.3).

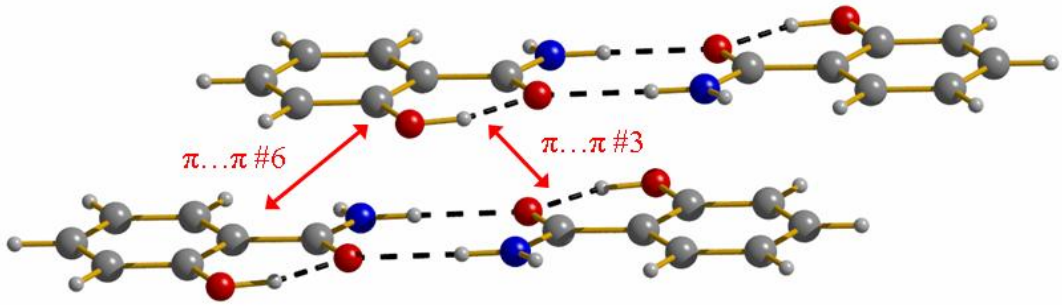

Figure 5.2: The π...π stacking interactions between the $R_2^2(8)$ dimers formed within the slabs in salicylamide-I. Labels #3 and #6 refer to the interactions studied using the PIXEL method (Tables 5.2 and 5.3).

Hirshfeld shape-index[†] plots (McKinnon *et al.*, 2004) (Figure 5.3) indicate that the interaction occurs between highly polar amide groups at points *a* and *b* in Figure 5.3a, placing NH_2 groups directly on top of C=O groups. The electrostatic complementarity of these regions is very clear when the Hirshfeld surface is colour-coded according to the electrostatic potential (Figure 5.3b) (Spackman *et al.*, 2008).

Interaction #6 is a more typical stacking contact which is dominated by dispersion (Table 5.3). It is formed through points *c*, *d* and *e* on the Hirshfeld shape index surface (Figure 5.3a). The contact is offset so that centre of the phenyl ring on one molecule is positioned over the carboxyl group on the other.

The pairs of H-bonded networks yield slabs, which are connected along the *c*-axis via π…π and CH… π interactions (#4 and #5 in Figure 5.1c, respectively), which both have energies of *ca.* -10 kJ mol^{-1} (Table 5.3). Dispersion is the largest component in the energy breakdown for both interactions. The CH…π contact in interaction #5 is labelled *f* in the Hirshfeld shape index plot of Figure 5.3a.

[†] Hirshfeld surfaces provide a useful way of looking at the packing environment in a crystal structure. The surface is created by applying the Hirshfeld stockholder partitioning method to divide the crystal into regions in which the electron density of the crystal is dominated by the electron density of a specific molecule. A number of useful properties can be mapped onto the surface including d_e (distances to nearest external atom) and d_i (distances to nearest internal atom) and the electrostatic potential. Patterns of π…π contacts can be illustrated by mapping the *shape index* onto the Hirshfeld surface; this is determined using the principal curvatures of the surface and shows concave regions as negative (red) and convex regions as positive (blue). Concave and convex regions in one surface fit into the convex and concave regions on a contacting surface.

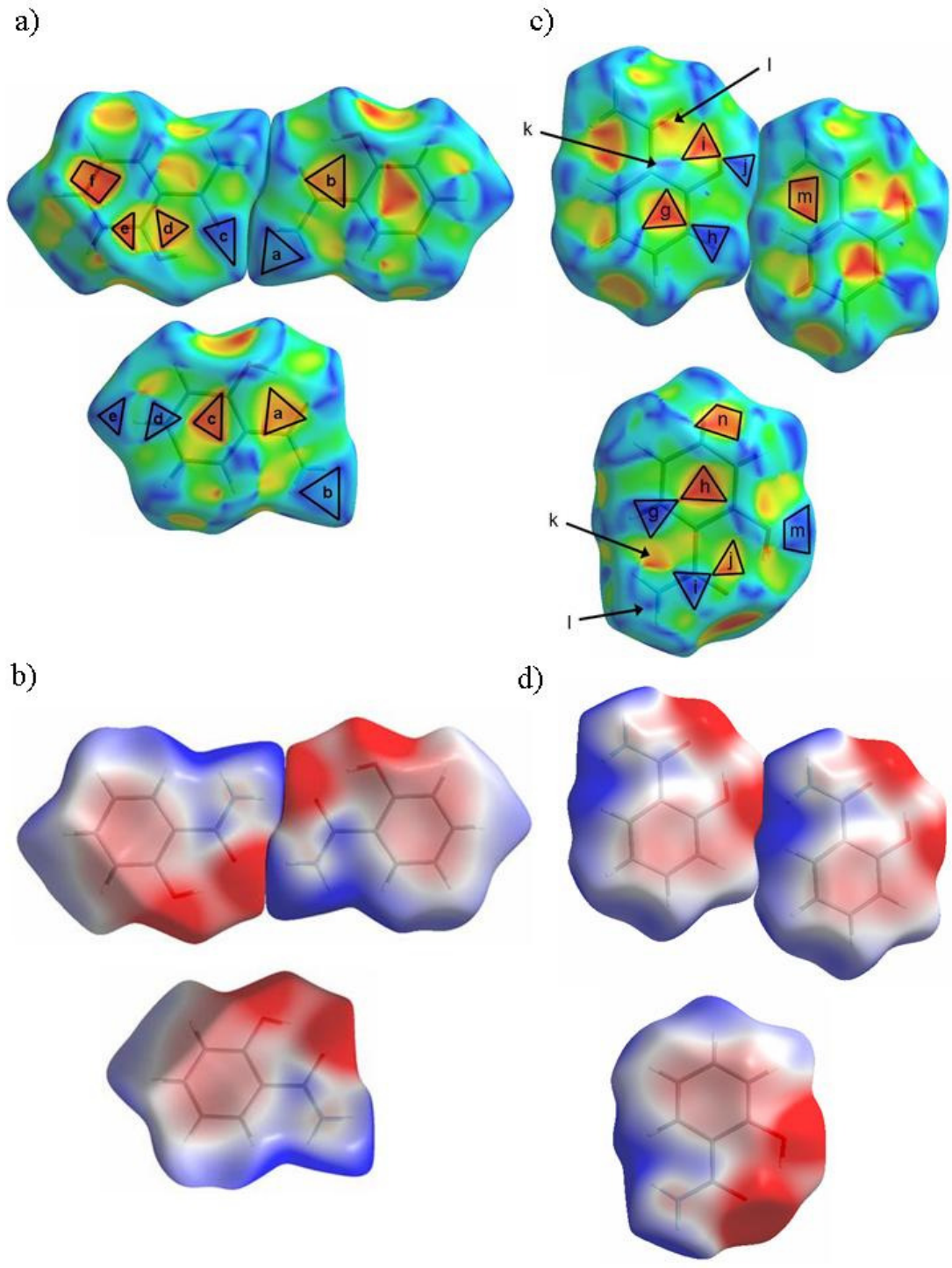

Figure 5.3: a) Shape index plots illustrating the contact points of interactions #3 and #6 in salicylamide-I. The same surfaces are shown in (b) with electrostatic potential mapped onto them in blue (+ve charge) and red (-ve charge). c) Shape index plots illustrating the contact points of interactions #9 and #10 in salicylamide-II, also with corresponding electrostatic potential plots.

5.4.2 Compression of salicylamide-I to 5.1 GPa

Increasing hydrostatic pressure on salicylamide-I produces an anisotropic response in the unit cell parameters (Figure 5.4a). The greatest reduction occurs in the length of the *c*-axis (the slab-stacking axis) which decreases by 14.5% from ambient conditions to 5.1 GPa, whilst the *a*- and *b*-axes reduce by 4.7% and 4.1% respectively.

a)

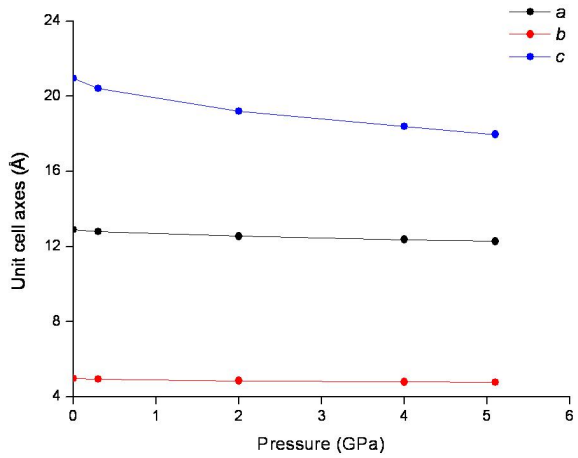

b)

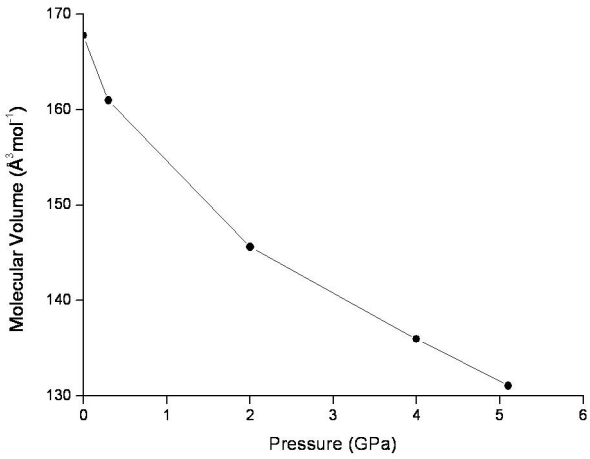

Figure 5.4: Variation of a) the unit cell parameters and b) the molecular volume in salicylamide-I as a function of pressure.

The direction of greatest linear strain lies along [0.016 0.000 0.047], a vector corresponding to the closing up of large voids in the structure which occur in and between the slabs of salicylamide dimers (Figure 5.5). As pressure is applied, the voids between the slabs close up more quickly than those within them and at 5.1 GPa the inter-slab voids have almost disappeared (Figure 5.5a-c).

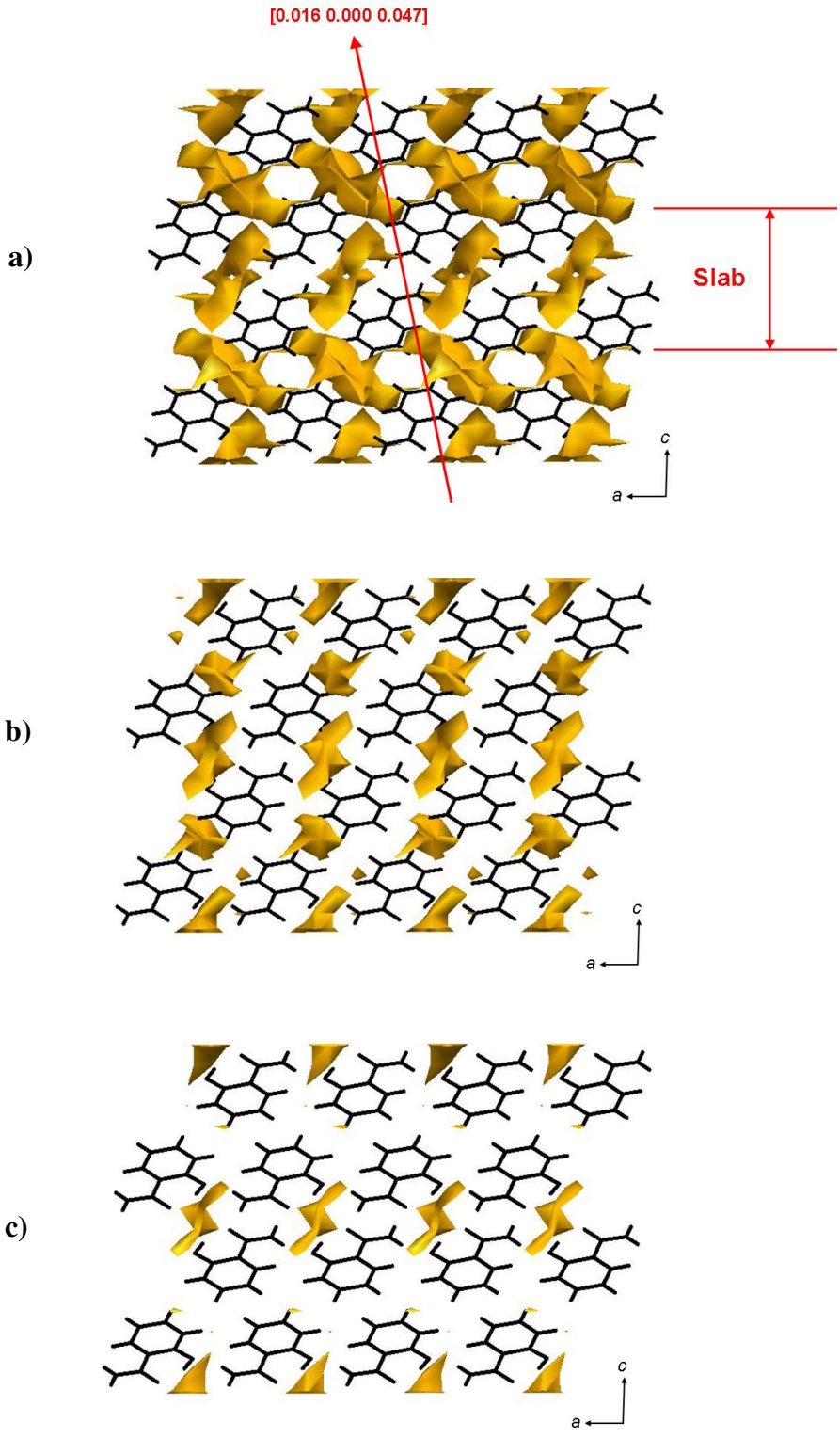

Figure 5.5: Void diagrams (Macrae *et al.*, 2008) of salicylamide-I at a) ambient conditions, b) 2.0 GPa and c) 5.1 GPa. Salicylamide molecules are coloured black. The vector which represents the direction of greatest compression is shown as a red arrow in a).

One eigenvector of the strain tensor must correspond to the *b*-axis by symmetry, and this is the direction of least compression in the structure. Quicktime movies showing the compression of salicylamide-I when viewed along the *a*- and *b*-axes are included in the supplemental material (files layers_viewed_along_a.mov and layers_viewed_along_b.mov), and they clearly show that the most prominent effect of pressure is to push the slabs closer together.

The effect of pressure on the molecular geometry is small: the largest change occurs for τ(C3-C2-C7-N1), which is 1.7(3)˚ at ambient conditions and -4.9(5)˚ at 5.1 GPa. The hydroxyl oxygen also moves out of the plane of the ring: τ(O2-C1-C6-C5) is 179.8(2)˚ at ambient conditions and 176.7(3)˚ at 5.1 GPa. The combination of these two factors affects the intramolecular hydrogen bond O2H7…O1, which compresses by a little less than 2% as pressure is increased to 5.1 GPa (Table 5.2). The two intermolecular hydrogen bonds are not constrained by the rigidity of the molecule: N1H6…O2 and N1H5…O1 compress by 8.8% and 5.6% respectively as the molecules are forced closer together.

The π…π stacking interactions in salicylamide-I compress more than the hydrogen bonds (Table 5.2): inter-planar separations for interactions #3 and #6 both decrease by *ca.*15% up to 5.1 GPa. The offset distance for interaction #3 *reduces* from 6.551 Å at ambient conditions to 6.347 Å at 5.1 GPa, and for interaction #6, it *increases* from 3.655 Å to 3.811 Å as the $R^2_2(8)$ dimers slide relative to one another (this is demonstrated with two movies available in the supplemental material, files R22(8)_dimers_along_a.mov and R22(8)_dimers_perpendicular_a.mov). The offset distance for π…π interaction #4 shortens by 14.6% upon compression to 5.1 GPa as the slabs of molecules are pushed closer together.

All of the interactions become weaker as pressure is increased, and the variation of their energy with centroid-centroid distance is given in Figure 5.6. The graph shows that interactions #4 and #5 are relatively unchanged upon compression despite the closing of large voids between slabs. The slopes for interactions #1, #2, #3 and #6 all become much steeper as pressure increases; indicating that they are all becoming weaker as they are driven into the repulsive region of the intermolecular potential. Interaction #6 becomes destabilising above a pressure of 2.0 GPa; the

contact has become very short with an inter plane distance of 2.859 Å at 5.1 GPa (Table 5.2).

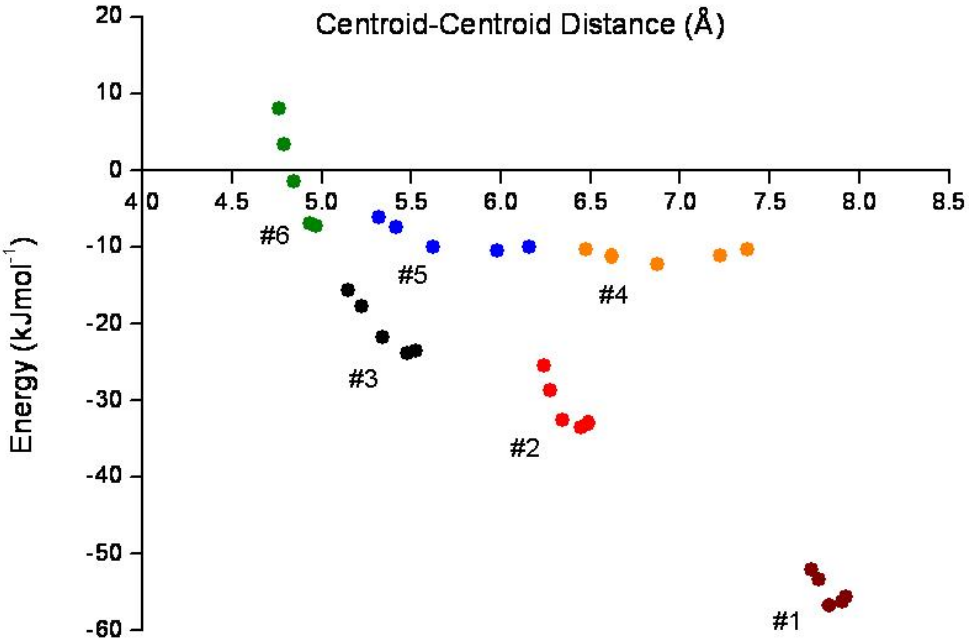

Figure 5.6: Graph of total interaction energy (in kJ mol^{-1}) against the distance between the molecular centroids of the molecules involved in the interaction (in Å) in salicylamide-I. The numbers #1, #2 *etc.* refer to the contacts listed in Table 5.2.

In other systems (Wood *et al.*, 2006), energetic features like the ones described above have been observed prior to phase transitions, and beyond 5.1 GPa the diffraction profiles began to broaden significantly. This might be taken to indicate that a phase transition occurred, and Raman spectra were measured between ambient pressure and 5.8 GPa to test this idea. Regrettably the results are somewhat ambiguous (Figure 5.7). Above 5.4 GPa a weak peak at 700 cm^{-1} increases in intensity and a weak shoulder develops at about 750 cm^{-1}. There is also a great reduction in peak intensity and sharpness between 5.0 GPa to 5.4 GPa. Such effects have been taken as indicative of phase transformations in other systems (Gonçalves *et al.*, 2009; Teixeira *et al.*, 2000). By-and-large however, the spectra shown in blue and green towards the top of Figure 5.7 just look like broader, weaker versions of the spectra below. On balance we believe the broadening observed in the diffraction profiles is probably owed to build-up of strain in the crystal rather than a phase

transition. Similar effects were seen in γ-glycine in the lead-up to a transition to the ε-phase (Dawson *et al.*, 2005).

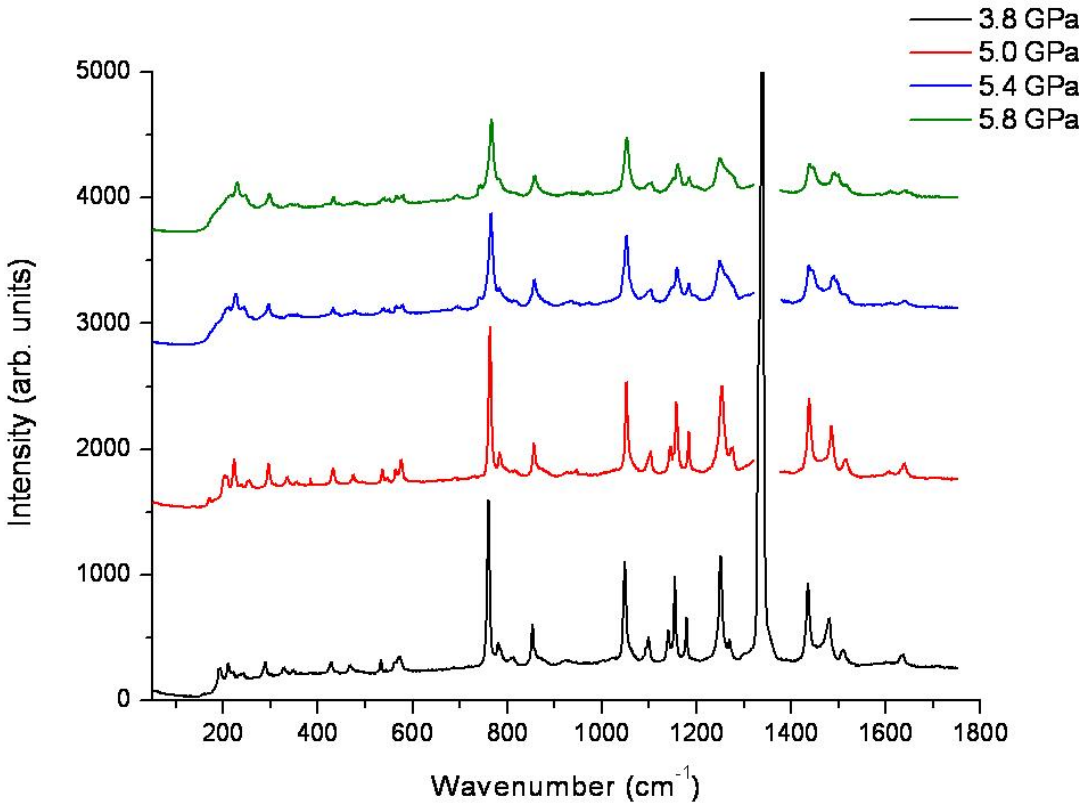

Figure 5.7: Raman spectra of compressed forms of salicylamide-I either side of 5.1 GPa. The intense peak at *ca.*1300 cm^{-1} is the result of a diamond C-C stretch and is omitted from the red, blue and green spectra for clarity.

5.4.3 Salicylamide-II at 0.2 GPa

Pressure-induced recrystallisation of salicylamide at 0.2 GPa resulted in a new polymorph, hereafter designated salicylamide-II. The molecular conformation of salicylamide in phase-II is similar to that in phase-I at ambient conditions: the largest difference in non-hydrogen-atom torsion angle is 4.1(6)°, and arises from a twist in the amide group about the C2-C7 bond. This accords with *ab initio* calculations (GAUSSIAN03) (Frisch *et al.*, 2004), which show that the lowest frequency internal vibration in salicylamide is a twisting motion about the C2-C7 bond (75 cm^{-1}). The energy difference between the two conformations is thus very small (0.2 kJ mol^{-1}).

Intermolecular interactions distances and angles along with PIXEL energy estimates are listed in Table 5.4; an energy breakdown is given in Table 5.3.

PIXEL Interaction number	Interaction type	0.2 GPa
Intramolecular interactions		
-	**O2H7..O1[i]** H7…O1 O2…O1 <O2H7O1	 1.74(3) 2.530(5) 153(3)
Network-building interactions		
#7	**N1H6..O2[ii]** H6…O2 N1…O2 <N1H6O2 Energy	 2.26 3.027(4) 146 -26.9
#8	**N1H5..O1[iii]** H5…O1 N1…O1 <N1H5O1 Energy	 2.06 2.893(5) 157 -19.5
#9	**π...πi[iv]** Plane-plane Offset Energy	 2.633 4.898 -16.2
#10	**π...π[v]** Plane-plane Offset Energy	 3.375 1.942 -13.2
Inter-slab interactions		
#11	**C5H3...π** H3...π C5...π <C5H3π Energy	 3.80 4.682 157 -7.7
#12	**C4H2...π** H2...π C4...π <C4H2π Energy	 4.15 5.056 161 -5.1

Symmetry Operators:

i	*x*,*y*,*z*	v	1+*x*, *y*, *z*
ii	1+*x*, -1+*y*,*z*	vi	1/2+*x*, 3/2+*y*, 1-*z*
iii	1-*x*,1/2+*y*,1/2-*z*	vii	1/2+*x*, 1/2-*y*, 1-*z*
iv	*x*, 1+*y*, *z*		

Table 5.4: Geometry of intermolecular interactions in salicylamide-II. Distances are in Å, and angles in °. S.u's were calculated in PLATON. Total interaction energies are also included from PIXEL calculations and are given in kJ mol^{-1}. For CH…π interactions, distances and angles are measured with respect to the centroid of the rings.

Salicylamide-II features the same intramolecular hydrogen bond O2H7…O1 that is observed in phase-I, but because of the small conformational change, O…O distance is slightly longer [2.530(5) Å *vs.* 2.514(2) Å] (*cf.* Tables 5.2 and 5.4). As in phase-I there are two conventional intermolecular H-bonds; the identity of donor and acceptor atoms remains the same in both phases, but the symmetry relationships are different. An overlay of the H-bonding environment of the two phases is given in Figure 5.8.

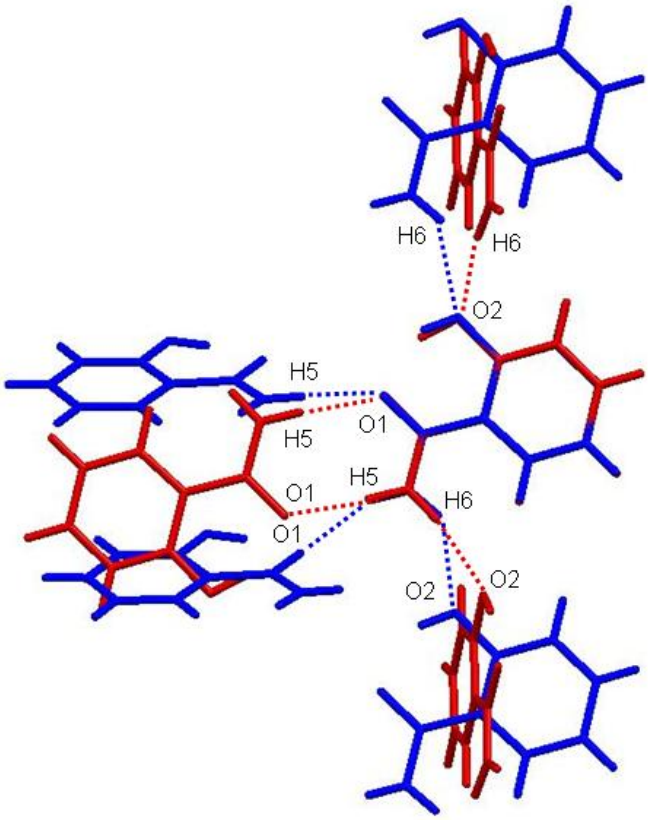

Figure 5.8: Overlay of the H-bonding environments in salicylamide-I (red) and salicylamide-II (blue). Intramolecular O2H7…O1 H-bonds are omitted for clarity.

The molecules of salicylamide no longer form dimers: N1H5…O1 (interaction #8 in Table 5.4, -19.5 kJ mol^{-1}) now links the molecules into a ribbon motif which runs parallel to the *b*-axis via a 2_1 screw axis (Figure 5.9a). N1H6…O2 (#7, -26.9 kJ mol^{-1}) connects the ribbons into slabs via lattice translations along *a* (Figure 5.9b). Unlike in phase-I, the slabs in phase-II are formed by one H-bonded network only.

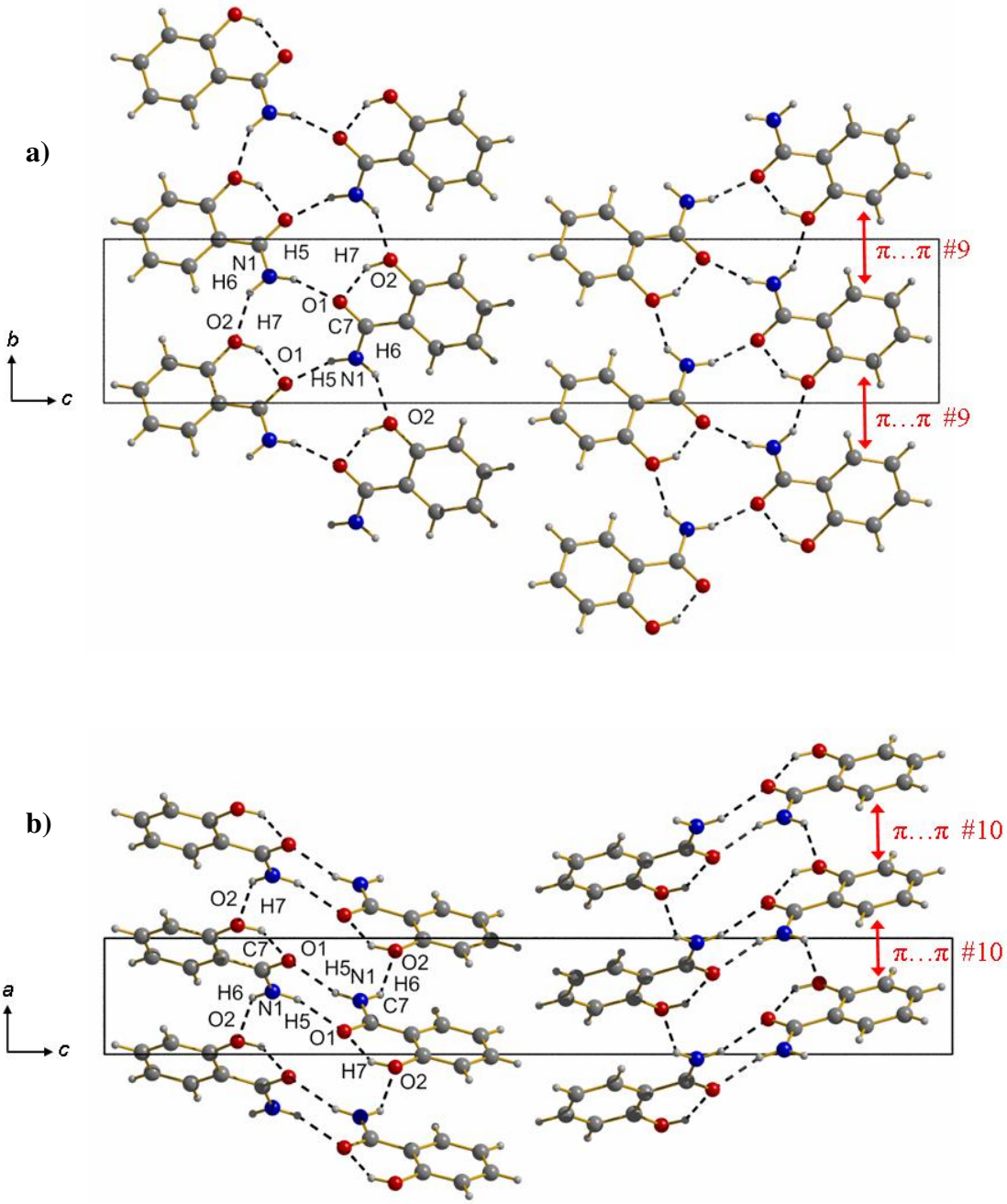

Figure 5.9: Salicylamide-II at 0.2 GPa, a) viewed along the *a*-axis and b) viewed along the *b*-axis. Labels 9 and 10 refer to the specific interactions studied in using the PIXEL method (Tables 5.3 and 5.4).

Intermolecular bonding within the slabs is reinforced by π…π stacking interactions created by lattice repeats along the *b*- and *a*-axes; interactions are labelled as #9 and #10 in Figures 5.9a and b respectively. They have total energies of -16.2 kJ mol^{-1} and -13.2 kJ mol^{-1} respectively (Table 5.4), and these should be compared with -23.9 and -6.9 kJ mol^{-1} in phase-I (at 0.3 GPa). Interaction #10, which, due to a small offset between the phenyl rings (1.944 Å), has a relatively large number of contact points on its shape index surface (labelled *g*-*l* in Figure 5.3c), whilst interaction #9 arises almost entirely from the point labelled *m*, which lacks the triangular shape typically observed for π…π stacking interactions. These contacts are all dominated by their dispersion terms (Table 5.3); the electrostatic components are weak, a feature which can be understood by considering the electrostatic potential surfaces shown in Figure 5.3d.

The slabs stack parallel to the (001) plane and each interacts with another along the *c*-axis through CH…π contacts (#11 and #12 in Table 5.4, the first of these is labelled *n* in Figure 5.3c). There are now no significant slab-slab π…π stacking interactions. PIXEL calculations show that the combined slab-slab interactions in Tables 5.2 and 5.4, are weaker in phase-II than phase-I at 0.3 GPa by 8.8 kJ mol^{-1}.

5.4.4 Vibrational contributions to the thermodynamic functions of salicylamide-I and II

Periodic DFT calculations were carried out on the structures of salicylamide-I and II obtained at 0.3 and 0.2 GPa, respectively, with the aim of obtaining zero point energies and the vibrational contributions to the enthalpy and entropy in the two phases at room temperature.

Inelastic neutron scattering data were collected on salicylamide-I at ambient pressure with the aim of validating the periodic DFT calculations. The positions of bands in an INS spectrum correspond to vibrational frequencies, as is also the case for IR and Raman spectroscopy. While intensities of IR and Raman bands are still rather difficult to calculate, INS intensities depend only on the motions of the atoms. This means that both positions and intensities can be quite reliably calculated from a theoretical frequency calculation, making INS amongst the best techniques available

for assessing the accuracy of periodic quantum mechanical calculations. A comparison of the observed and calculated INS spectra for salicylamide-I (calculated with the cell dimensions fixed to measured ambient pressure values) is shown in Figure 5.10. By and large the agreement between frequencies and intensities is very good, suggesting that the level of theory used here for determination of the thermodynamic properties of different phases of salicylamide is appropriate.

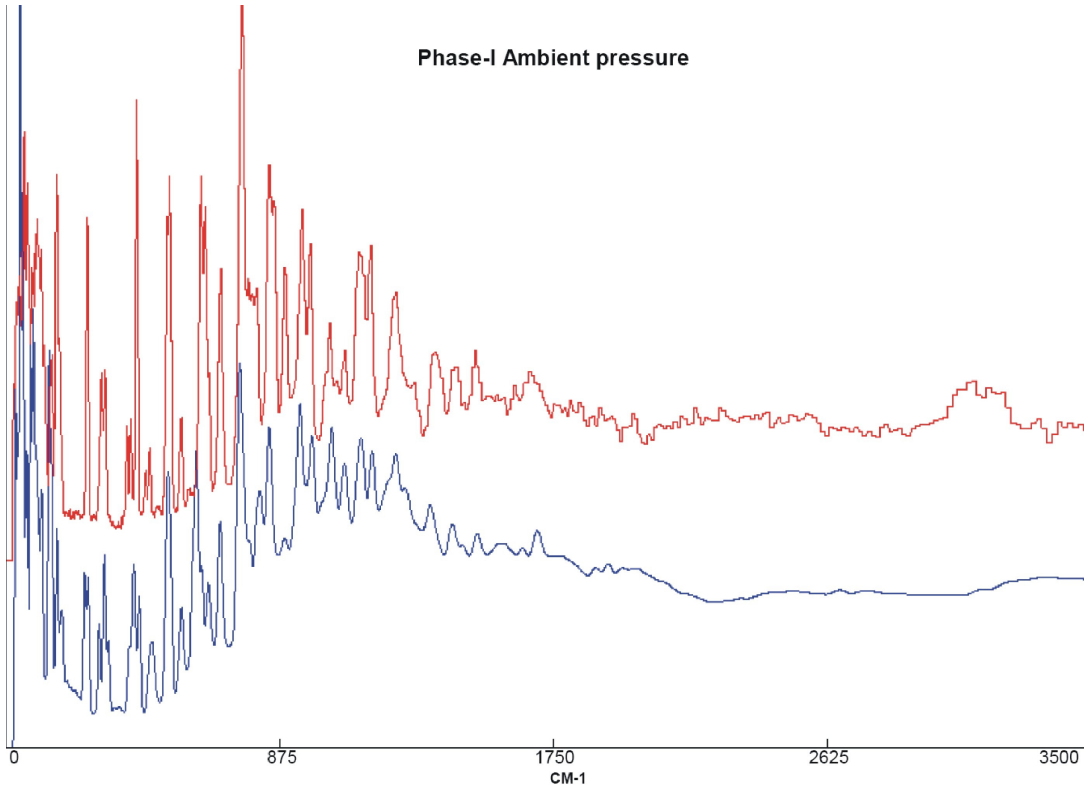

Figure 5.10: Observed (red) and calculated (blue) INS spectra for salicylamide-I at ambient pressure.

The largest deviation between the optimised and experimental non-H atomic positions in the crystal structures of salicylamide-I at ambient pressure and 0.3 GPa, and in salicylamide-II at 0.2 GPa, were 0.049, 0.047 and 0.063 Å, respectively. This excellent level of agreement also validates the theoretical approach used.

The values of the zero-point energy and the vibrational contributions to enthalpy, entropy and the free energy can be calculated from the vibrational frequencies using standard formulae of statistical thermodynamics [see, for example,

Equ 12.2, 12.9 and 12.16 in Maczek (2002)], and these quantities are listed in Table 5.5.

Phase	**ZPE/kJ mol^{-1}**	***H*/kJ mol^{-1}**	***S*/J mol^{-1} K^{-1}**	***G*/kJ mol^{-1}**
I at 0.3 GPa	343.58	22.99	152.35	321.14
II at 0.2 GPa	342.52	23.82	163.64	317.55
II - I	-1.06	0.83	11.292	-3.59

Table 5.5: Vibrational contributions to the thermodynamic functions for salicylamide phases I and II calculated using harmonic frequencies obtained from periodic DFT calculations. ZPE = zero point energy.

5.5 Discussion

5.5.1 The crystal structure of salicylamide at ambient pressure

Interactions 1-6 in phase-I (Table 5.2) can be categorised as (*i*) intra-network (hydrogen bonding within networks; contacts #1 and #2), (*ii*) network-network (interactions which occur within slabs, between different networks; contacts #3 and #6), and (*iii*) slab-slab (interactions occurring between slabs; contacts #4 and #5). On average, the interactions which form the networks are stronger (Table 5.3) than the slab-building interactions which form between the networks, and these, in turn, are stronger than the interactions between the slabs.

The lattice energy calculated for the CSD entry SALMID01 is -42.5 kJ mol^{-1} (Table 5.6), and is much less stable than the structure of salicylamide-I reported here (-98.9 kJ mol^{-1}). The latter is in very good agreement with the literature sublimation enthalpy values of 101.9(4) kJ mol^{-1}, (Bernades & Piedade, 2008) and 99.3(23) kJ mol^{-1} (Silva & Araujo, 2007).

Structure Pressure	Pressure/ GPa	E_{Coul}	E_{pol}	E_{disp}	E_{rep}	U	U_{adj}	H
SALMID01	0	-73.6	-37.3	-88.7	157.1	-42.5	-42.5	-42.5
Phase-I 0 GPa	0	-81.3	-29.0	-80.1	91.5	-98.9	-98.9	-98.9
Phase-I 0.3 GPa	0.3	-91.1	-34.0	-89.6	113.1	-101.6	-101.1	-67.9
Phase-II 0.2 GPa	0.2	-63.8	-24.6	-99.0	88.5	-98.9	-98.7	-76.1

Table 5.6: Components of the lattice energy and enthalpy for SALMID01, salicylamide-I and salicylamide-II. All energies are given in kJ mol^{-1}. U_{adj} includes a correction for the small internal energy difference due to conformation change relative to ambient pressure structure. This was calculated in GAUSSIAN at the MP2/6-31G** level. Enthalpy values are calculated as $H = U + PV$, where P = pressure (in Pa) and V = molar volume (in m^3mol^{-1}).

The difference between the two models lies in the location of the origin on either one of the two crystallographically distinct inversion centres in space group *I*2/*a*. We assume that a non-standard setting must have been used for the refinements quoted in references (Sasada *et al.*, 1964) and (Pertlik, 1990), though no mention of this is made in either publication.[‡] The structures of both proposed models consist of slabs of molecules connected by π-interactions. However, the instability of SALMID01 results from the large repulsive component (Table 5.6), which arises because of a number of short H…H contacts at *ca.* 1.96 Å (X-H distances normalised to standard neutron values) which occur between slabs. Though not unprecedented, these distances are very short by comparison of other H…H distances in the Cambridge Database [see Figure 6 in (Wood, McKinnon *et al.*, 2008)], and there is a large a repulsive contribution of 135.4 kJ mol^{-1} to this contact which is destabilising with an overall energy of +35.4 kJ mol^{-1} (Table 5.3, top section). Indeed, it was the existence of these short H…H interactions which first attracted our interest in the behaviour of salicylamide at high pressure! If PIXEL calculations are performed on SALMID01 in the same setting as our model (by shifting the coordinates and using

[‡] We have contacted Dr. Pertlik, the author of the second of these papers, but regrettably the original diffraction and refinement data have been lost.

the same symmetry operators) the lattice energy becomes -99.2 kJ mol^{-1}; a value very close to ours (Table 5.6).

The information that is contained in a Hirshfeld surface analysis can be condensed into a 2D histogram of d_i (x-axis) against d_e (y-axis) known as a *fingerprint plot* which are useful for observing packing differences between structures (Spackman & McKinnon, 2002; McKinnon *et al.*, 2004). The fingerprint plot for SALMID01 is shown in Figure 5.11a. This plot looks quite bizarre by comparison with examples of other H-bonded solids quoted in McKinnon *et al.* (2004). For example the feature which is circled in red indicates the presence of numerous very short H…H contacts. The strangeness of the fingerprint plot supports our contention that the coordinates quoted in the two previously published crystal structures of salicylamide are incorrect (at least with respect to the usual setting of the space group).

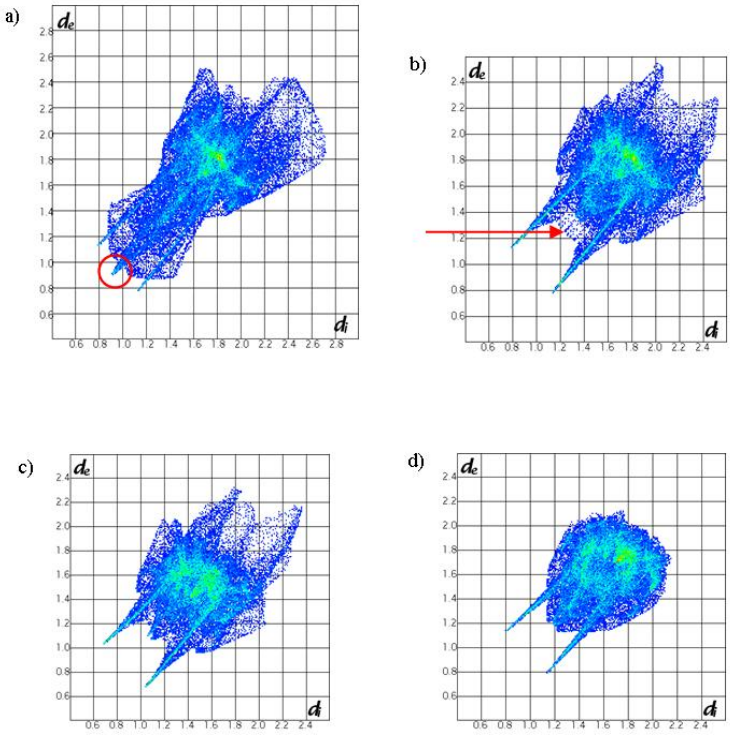

Figure 5.11: Fingerprint plots: a) SALMID01 (Pertlik, 1990) (red circle indicates an elongated nose region due to short intermolecular H…H contacts), b) salicylamide-I at ambient conditions (the red arrow points towards a region corresponding to short H…H contacts across a dimer), c) salicylamide-I at 5.1 GPa, d) salicylamide-II at 0.2 GPa.

The fingerprint plot for our model of the crystal structure of salicylamide, which is shown in Figure 5.11b, is more normal for H-bonded materials (McKinnon *et al.*, 2004). Two prominent 'prongs' are characteristic of NH…O H-bond formation, while the 'skirt' of points (indicated with a red arrow) between the prongs derive from short H…H contacts formed across the $R^2_2(8)$ dimers. The various π…π contacts are represented by the green area in the middle of Figure 5.11b. The compression of salicylamide-I results in the shortening of contacts, and Figure 5.11c shows that overall, the fingerprint plot moves towards the origin upon compression to 5.1 GPa. A feature develops in the skirt region as H…H contacts shorten. Development of short H…H contacts is characteristic of compressed organic crystal structures (Wood, McKinnon *et al.*, 2008).

5.5.2 Formation of salicylamide-II at 0.2 GPa

Salicylamide-II was grown *in-situ* by recrystallisation of a saturated solution at pressure. Crystal growth resulted in three crystallites and the integration was performed as though the sample was a non-merohedral twin, harvesting reflections from all three crystallites. Refinement of the merged data resulted in a completeness of over 90% whereas integration of one domain alone gave a completeness of *ca.* 30%. This is a good example illustrating a situation where twinning can be beneficial: high-pressure datasets often suffer from low completeness because of shading from the steel pressure cell body, and inclusion of multiple crystals in different orientations within the gasket hole can improve this.

Whereas phase-I crystallises in the centrosymmetric space group *I*2/*a*, phase-II forms in the Sohncke group $P2_12_12_1$, which is relatively unusual for achiral molecules (Pidcock, 2005). Inversion centres are very common features in crystal structures of achiral compounds, but if a molecule has approximate mirror or inversion symmetry an inversion relationship can be mimicked by a rotational operator. The appearance of a polymorph in $P2_12_12_1$ may be ascribable to approximate mirror symmetry of the planar and rigid salicylamide molecule, (Pidcock, 2005) which means that when nucleating the $P2_12_12_1$ structure does not

have the problem of "rejecting" the wrong hand of molecule for the growing crystallite.

There is no evidence that phase-II is formed on compression of phase-I, and the only route by which we have observed it is via direct recrystallisation from solution at high pressure. It is important to recognise that transformations between very different crystal structures involving substantial reorganisation of the crystal packing are likely to be subject to a large activation barrier, and are kinetically hindered. The results on salicylamide imply that there is no energetically favourable route for transformation of phase-I directly into phase-II. Related features were observed in a study of the effect of pressure on different polymorphs of glycine (Dawson *et al.*, 2005). α-Glycine remains in the same phase up to at least 6 GPa, and Raman data suggest that it is stable to over 20 GPa (Murli *et al.*, 2003). By contrast β-glycine transforms to δ-glycine at 0.8 GPa, and γ-glycine transforms to ε-glycine at 2 GPa. Thus the polymorph formed depends on the identity of the starting phase, and there is a close topological relationship between the β and δ forms and between the γ and ε-forms (Dawson *et al.*, 2005).

The molecular structures in phases I and II are essentially the same. Both phases comprise slabs of hydrogen-bonded molecules which stack parallel to the (001) plane. The identity of the donor and acceptor atoms for the hydrogen bonds is the same in both cases, but the symmetry operations are different. This means that in phase-II the slabs are made up of a single hydrogen-bonded network, whereas in phase-I it was an inter-weaving of two networks. The density of phase-II is greater than phase-I at 0.3 GPa by 0.058 Mg m^{-3} (Table 5.1), which is nicely illustrated with the fingerprint plot in Figure 5.11d with the disappearance of the diffuse blue regions which represent long-range contacts across voids. The disappearance of the skirt region in Figure 5.11d represents the loss of the $R^2_2(8)$ dimers in phase-II.

Table 5.6 shows the intermolecular lattice energy values for both phases and a breakdown of energy terms: at 0.3 GPa, the overall cohesive energy of phase-I (-101.6 kJ mol^{-1}) is slightly more negative than phase-II (-98.9 kJ mol^{-1}). Interpolation of the total intermolecular interaction energy for phase-I to 0.2 GPa (-100.7 kJ mol^{-1}) suggests that the difference in cohesive energies is less at 0.2 GPa,

ca. 2 kJ mol^{-1} in favour of phase-I. Comparison of the rows in Table 5.6 for phase-I and 0.3 GPa and phase-II at 0.2 GPa shows that phase-I is favoured by the Coulombic and polarisation terms, while phase-II is favoured by the dispersion and lower repulsion terms. This picture is unchanged if the phase-I energies are interpolated to 0.2 GPa (E_{Coul} = -87.4, E_{Pol} = -32.1, E_{Disp} = -87.0 and E_{Rep} = +104.8 kJ mol^{-1}). It is interesting that even though phase-II is denser, its repulsion term is lower.

The differences in the Coulombic energies of phases I and II can be traced to differences in the most important Coulombic interactions, namely the H-bonds. The top interaction in phase-I is the dimer mediated by N1H5…O1 H-bonds. The electrostatic component of this bond is -80.5 kJ mol^{-1}, but for the purposes of comparisons between different H-bonds this value should be halved (-40.3 kJ mol^{-1}) as the interaction involves two H-bonds. In phase-II, the electrostatic component of the N1H5…O1 H-bonds is only -27.6 kJ mol^{-1}. It is notable that though the N1H5…O1 H-bonds have similar N…O distances in phases I and II (Tables 5.2 and 5.4), that in phase-II is much less linear (157°) than in phase-I (176°). Moreover, the N1-H5 vector is more closely aligned with the lone pair on O1 in phase-I than in phase-II. While the less ideal geometry of the H-bonding in phase-II likely contributes to the differences in the Coulombic energies, it is important to bear in mind that the figures quoted refer to whole molecule interactions, and not just the H-bonds, and it is not possible on the basis of the PIXEL results to ascribe the differences to changes in H-bond geometry alone.

The second strongest interaction in phase-I is N1H6…O2, which has a Coulombic component of -40.5 kJ mol^{-1}, compared to -23.0 kJ mol^{-1} for the related N1H6…O2 interactions in phase-II. The N1…O2 distance is shorter, more linear (164º *vs.* 146º), and more optimally aligned with the O2 lone pair in phase-I.

The repulsion components of the H-bonds in phase-II are lower, but this is not enough to outweigh the differences in the Coulombic terms, and the H-bonds in phase-II are overall weaker than those in phase I by 15 kJ mol^{-1}, and it would appear that the Coulombic advantage of phase-I can be traced to the more favourable H-bonding geometry in the structure. The data in Table 5.3 also show that, by contrast,

the dispersion components of the various stacking and CH-π interactions in phase-II are both more numerous and more energetic than in phase-I. Broadly speaking, what is lost in H-bonding in phase-I is made up by improved dispersion interactions in phase-II.

The energy data in Table 5.3 and in the paragraphs above indicate that intermolecular interactions in phases I and II are energetically competitive overall. In addition, the data in Table 5.1 show that phase-II is denser than phase-I, with a volume of 154.7 $Å^3$ per molecule at 0.2 GPa, compared to 161.0 $Å^3$ per molecule for phase-I at 0.3 GPa. Interpolation of the phase-I volume to 0.2 GPa gives a value of 163.3 $Å^3$ per molecule. This volume difference equates to a *PV* advantage of *ca.* 1 kJ mol^{-1} for phase-II at 0.2 GPa.

The *PV* term becomes a progressively more important contributor to free energy as *P* increases, and eventually it would be expected to outweigh the cohesive energy derived from efficient H-bonding. In the phase-I to II transitions in serine (Moggach *et al.*, 2006; Wood, Francis *et al.*, 2008) and serine hydrate (Johnstone *et al.*, 2008) (both at 5 GPa), for example, the change in cohesive energy is actually positive, but this is out-weighed by the negative change in the *PV* term. In the transition from serine-II to III at 8 GPa H-bonds actually become longer, but there is an increase in H…H contacts pointing to enhanced dispersion terms. It is interesting to speculate that at very high pressures H-bonded polymorphs may become disfavoured relative to efficiently-packed structures dominated by dispersion.

5.5.3 Zero point energy and vibrational contributions to free energy

Hudson and co-workers have recently pointed-out that differences in zero point energy can be similar to, or even larger than, overall differences in polymorph energies (Rivera *et al.*, 2008). It is therefore important to take zero point energies into account when discussing relative polymorph stabilities, particularly where H-bonding is involved as this has a strong effect on vibrational energies. In Hudson's study, it was shown that for glycine the dominant effect on ZPE differences between the α- and γ- polymorphs comes from the internal bending modes. These modes tend to deform H-bonds from linearity, and so they increase in frequency when H-bonding

is strong and linear. Strong H-bonding can therefore act to *destabilise* a structure through this zero point energy contribution. On the face of it therefore, salicylamide-II, with its weaker H-bonding, should also be favoured over phase-I by a smaller zero point energy.

Vibrational frequencies of phases I and II were calculated using periodic DFT and used to estimate the vibrational contributions to the thermodynamic functions at 298.15 K. The results, which are listed in Table 5.5, show that indeed, the zero point energy of phase II of salicylamide is *ca.* 1 kJ mol^{-1} smaller than that of phase-I. Break-down of the contributions to the zero-point energy in the manner described by Hudson shows that the ZPE difference can be traced to lower vibrational frequencies of phase-II in the 0-400, 1000-1200, 1600-1800 and 2000-3000 cm^{-1} regions of the vibrational spectrum. The 0–400 cm^{-1} region consists mostly of whole molecule lattice vibrations, and it seems intuitively reasonable that these modes are lower in frequency in phase-II with its weaker H-bonding (see also below). The regions from 1000-1200 and 1600-1800 cm^{-1} contain rocking and bending modes centred on the NH_2 groups. As Hudson has observed in glycine, these modes are higher in frequency in phase-I because they lead to deformations of H-bonds which are more linear (and energetic) than in phase-II. The region between 2000 and 3000 cm^{-1} contains the stretching mode of the OH groups involved in internal OH…O H-bonding. This is higher in frequency in phase-I; the reason for this is not altogether obvious as the O…O distance is longer in phase-II, so that the OH stretch would be expected to be higher in phase-II.

Phase-II is also favoured by entropy, $T\Delta S$ is *ca.* -3 kJ mol^{-1} at 298.15 K. Entropic contributions drop off quite rapidly with wavenumber, and the largest differences are seen in the lattice modes below about 200 cm^{-1}. As described above in the context of the ZPE, the lower frequencies in phase-II are consistent with a less rigid network of H-bonds.

The generally lower frequencies of phase-II mean that the vibrational enthalpy favours phase-I, but not enough to over-ride the contributions of the ZPE and entropy.

In summary, the formation of salicylamide-II at 0.2 GPa can be understood in terms of (a) the replacement of H-bonds by dispersion-dominated stacking and CH…π interactions; (b) its higher density and (c) its lower vibrational frequencies. The last of these occurs because of weaker H-bonding in phase-II which, paradoxically perhaps, gives this polymorph an advantage in both zero point energy and entropy.

5.6 Conclusions

We have shown that the published structures of salicylamide-I at ambient pressure, though not exactly wrong, appear to have been described with respect to a non-standard space group origin. The overall features of the published and revised structures are similar: the molecules are connected through H-bonding into layers, and these layers are then stacked through π-π interactions. However, our structure does not contain the short H…H contacts which were a notable feature of the previously proposed structure. Packing energy calculations using the PIXEL method and Hirshfeld surface analysis were both very useful for verifying the structure of salicylamide-I presented here.

Application of pressure to salicylamide-I up to 5 GPa does not result in any phase transitions, though the interactions within the layers do enter a destabilising region of their potentials. Above 5 GPa the crystal appears to deteriorate. Although this behaviour is usually taken to imply that a transition has occurred, Raman spectra taken after the collapse are rather similar to those taken at lower pressures, and while we are not able to make a definitive comment on the phase of the collapsed material, we are not convinced by the suggestion that a phase transition has occurred.

When a crystal of salicylamide is grown directly from solution at 0.2 GPa a new high-pressure phase, salicylamide-II, is formed. The structure was determined from data collected on three crystallites, each differently orientated within the sample chamber. The data set had an unusually high completeness for a high-pressure structure determination, and is an example of where twinning can be beneficial.

Our aim in this paper has been to establish what makes the new form energetically competitive with phase-I. PIXEL calculations show that although

phase-II features similar NH…O_{phenol} and NH…O_{amide} interactions to those present in phase-I, these interactions are substantially weaker. This deficit in the cohesive energy is made up by increases in the strengths of π-π and CH…π interactions in phase-II, and at 0.2 GPa the cohesive energies favour phase-I by *ca.* 2 kJ mol^{-1}. However, phase-II is denser than phase-I, and the lower molecular volume gives phase II an advantage of 1 kJ mol^{-1} via the *PV* contribution to its free energy. Finally, DFT frequency calculations (validated by experimental inelastic neutron scattering data) show that the zero point energy of phase-I is *ca.* 1 kJ mol^{-1} higher than phase-II because in phase-I the frequencies of NH bending modes are increased by the need to deform strong, linear NH…O hydrogen bonds. The presumably more rigid H-bonding network of phase-I also means that its low frequency phonon modes are higher in energy than in phase-II, and this leads to an entropic advantage of some 3 kJ mol^{-1} for phase-II. Entropy is often neglected when comparing the thermodynamic stabilities of different polymorphs, but in the present study it is the largest of all terms considered.

Overall we estimate that at 0.2 GPa the free energy of phase-II is lower than that of phase-I by about 3 kJ mol^{-1}.

5.7 References

Allan, D. R., Blake, A. J., Huang, D., Prior, T. J. & Schroeder, M. (2006). *Chemical Communications* 4081-4083.

Allan, D. R. & Clark, S. J. (1999a). *Physical Review B: Condensed Matter and Materials Physics* **60**, 6328-6334.

Allan, D. R. & Clark, S. J. (1999b). *Physical Review Letters* **82**, 3464-3467.

Allan, D. R., Clark, S. J., Brugmans, M. J. P., Ackland, G. J. & Vos, W. L. (1998). *Physical Review B: Condensed Matter and Materials Physics* **58**, R11809-R11812.

Allen, F. H. (2002). *Acta Crystallographica, Section B* **58**, 380-388.

Altomare, A., Cascarano, G., Giacovazzo, C., Guagliardi, A., Burla, M. C., Polidori, G. & Camalli, M. (1994). *Journal of Applied Crystallography* **27**, 435-435.

Bernades, C. E. S. & Piedade, M. E. M. (2008). *Journal of Physical Chemistry A* **112**, 10029-10039.

Bernstein, J., Davis, R. E., Shimoni, L. & Chang, N.-L. (1995). *Angewandte Chemie, International Edition in English* **34**, 1555-1573.

Betteridge, P. W., Carruthers, J. R., Cooper, R. I., Prout, K. & Watkin, D. J. (2003). *Journal of Applied Crystallography* **36**, 1487.

Blessing, R. H. (1987). *Crystallography Reviews* **1**, 3-58.

Blessing, R. H. (1997). *Journal of Applied Crystallography* **30**, 421-426.

Brandenburg, K. & Putz, H. (2005). *DIAMOND, version 3.2*. Crystal Impact GbR, Postfach 1251, 53002, Bonn, Germany.

Bruker-Nonius (2006). *SAINT version 7, Program for integration of area detector data.* Bruker-AXS, Madison, Wisconsin, USA.

Burla, M. C., Caliandro, R., Camalli, M., Carrozzini, B., Cascarano, G. L., Caro, L. D., Giacovazzo, C., Polidori, G. & Spagna, R. (2005). *Journal of Applied Crystallography* **38**, 381-388.

Colognesi, D., Celli, M., Cilloco, F., Newport, R. J., Parker, S. F., Rossi-Albertini, V., Sacchetti, F., Tomkinson, J. & Zoppi, M. (2002). *Applied Physics* A **74**, S64-S66.

CrystalMaker (2009). *A crystal and molecular structures program for MAC and Windows.* CrystalMaker Software Ltd., Oxford, England. (www.crystalmaker.com)

Dawson, A., Allan, D. R., Belmonte, S. A., Clark, S. J., David, W. I. F., McGregor, P. A., Parsons, S., Pulham, C. R. & Sawyer, L. (2005). *Crystal Growth & Design* **5(4)**, 1415-1427.

Dawson, A., Allan, D. R., Parsons, S. & Ruf, M. (2004). *Journal of Applied Crystallography* **37**, 410-416.

Delley, B. (1990). *Journal of Chemical Physics* **92**, 508-517.

Dunitz, J. D. & Gavezzotti, A. (2005). *Angewandte Chemie, International Edition* **44**, 1766-1787.

Fabbiani, F. P. A. & Pulham, C. R. (2006). *Chemical Society Reviews* **35**, 932-942.

Farrugia, L. J. (1999). *Journal of Applied Crystallography* **32**, 837-838.

Frisch, M. J., Trucks, G. W., Schlegel, H. B., Scuseria, G. E., Robb, M. A., Cheeseman, J. R., J. A. Montgomery, J., Vrevren, T., Kudin, K. N., Burant, J. C., Millam, J. M., Iyengar, S. S., Tomasi, J., Barone, V., Mennucci, B., Cossi, M., Scalmani, G., Rega, N., Petersson, G. A., Nakatsuji, H., Hada, M., Ehara, M., Toyota, K., Fukuda, R., Hasegawa, J., Ishida, M., Nakajima, T., Honda, Y., Kitao, O., Nakai, H., Klene, M., Li, X., Knox, J. E., Hratchian, H. P., Cross, J. B., Bakken, V., Adamo, C., Jaramillo, J., Gomperts, R., Stratmann, R. E., Yazyev, O., Austin, A. J., Cammi, R., Pomelli, C., Ochterski, J. W., Ayala, P. Y., Morokuma, K., Voth, G. A., Salvador, P., Dannenberg, J. J., Zakrzewski, V. G., Dappricj, S., Daniels, A. D., Strain, M. C., Farkas, O., Malick, D. K., Rabuck, A. D., Raghavachari, K., Foresman, J. B., Oritz, J. V., Cui, Q., Baboul, A. G., Clifford, S., Cioslowski, J., Stefanov, B. B., Liu, G., Liashenko, A., Piskorz, P., Komaromi, I., Martin, R. L., Fox, D. J., Keith, T., Al-Laham, M. A., Peng, C. Y., Nanayakkara, A., Challacombe, M., Gill, P. M. W., Johnson, B., Chen, W., Wong, M. W., Gonzalez, C. & Pople, J. A. (2004). *Gaussian 03 revision E.01.* Gaussian, Inc., Wallington CT.

Gavezzotti, A. (2003). *OPIX - A computer program package for the calculation of intermolecular interactions and crystal energies.* University of Milano, Milan, Italy.

Gavezzotti, A. (2005). *Zeitschrift fuer Kristallographie* **220**, 499-510.

Gavezzotti, A. (2007). *Molecular Aggregation: Structure Analysis and Molecular Simulation of Crystals and Liquids*, p. 323. Oxford, UK: Oxford University Press.

Gonçalves, R. O., Freire, P. T. C., Bordallo, H. N., Lima Jr, J. A., Melo, F. E. A., Mendes Filho, J., Argyriou, D. N. & Lima, R. J. C. (2009). *Journal of Raman Spectroscopy* **40**, In press. DOI 10.1002/jrs.2209.

Hazen, R. M. & Finger, L. W. (1982). Comparative Crystal Chemistry: Temperature, Pressure, Composition and the Variation of Crystal Structure, p. 81. Chichester, New York, USA: John Wiley and Sons.

Johnstone, R. D. L., Francis, D., Lennie, A. R., Marshall, W. G., Moggach, S. A., Parsons, S., Pidcock, E. & Warren, J. E. (2008). *CrystEngComm* **10**, 1758-1769.

Macrae, C. F., Bruno, I. J., Chisholm, J. A., Edgington, P. R., McCabe, P., Pidcock, E., Rodriguez-Monge, L., Taylor, R., Streek, J. v. d. & Wood, P. A. (2008). *Journal of Applied Crystallography* **41**, 466-470.

Maczek, A. (2002). Statistical Thermodynamics. Oxford: Oxford University Press.

Materials Studio Release Notes, Release 4.4, Accelrys Software Inc. (2008).

McKinnon, J. J., Spackman, M. A. & Mitchell, A. S. (2004). *Acta Crystallographica, Section B* **60**, 627-668.

Merrill, L. & Bassett, W. A. (1974). *Review of Scientific Instruments* **45**, 290-294.

Moggach, S. A., Allan, D. R., Parsons, S. & Warren, J. E. (2008). *Journal of Applied Crystallography* **41**, 249-251

Moggach, S. A., Bennett, T. D. & Cheetham, A. K. (2009). *Angewandte Chemie* **48,** 7087-7089.

Moggach, S. A., Marshall, W. G. & Parsons, S. (2006). *Acta Crystallographica, Section B* **62**, 815-825.

Moggach, S. A. & Parsons, S. (2009). *Specialist Periodic Reports: Spectroscopic Properties of Inorganic and Organometallic Compounds* **40**, 324-354.

Moggach, S. A., Parsons, S. & Wood, P. A. (2008). *Crystallography Reviews* **14**, 143-184.

Murli, C., Sharma, S. M., Karmakar, S. & Sikka, S. K. (2003). *Physica B: Condensed Matter (Amsterdam, Netherlands)* **339**, 23-30.

Oswald, I. D. H., Allan, D. R., Day, G. M., Motherwell, W. D. S. & Parsons, S. (2005). *Crystal Growth & Design* **5**, 1055-1071.

Parsons, S. (2003). *STRAIN - Program for calculation of linear strain tensors* University of Edinburgh, Edinburgh, UK.

Parsons, S. (2004). *SHADE- Program for empirical absorption corrections to high pressure data.* The University of Edinburgh, Edinburgh, United Kingdom.

Perdew, J. P. & Wang, Y. (1992). *Physical Review B* **45**, 13244-13249.

Pertlik, F. (1990). *Monatshefte fuer Chemie* **121**, 129-139.

Pidcock, E. (2005). *Chemical Communications* 3457-3459.

Piermarini, G. J., Block, S., Barnett, J. D. & Forman, R. A. (1975). *Journal of Applied Physics* **46**, 2774-2780.

Press, W. H., Teukolsky, S. A., Vetterling, W. T. & Flannery, B. P. (1992). Numerical Recipes in Fortran, Second Edition. Cambridge University Press, Cambridge, England.

Ramirez-Cuesta, A. J. (2004). *Computer Physics Communications* **157**, 226-238.

Rivera, S. A., Allis, D. G. & Hudson, B. S. (2008). *Crystal Growth & Design* **8**, 3905-3907.

Sasada, Y., Takano, T. & Kakudo, M. (1964). *Bulletin of the Chemical Society of Japan* **37**, 940-946.

Sheldrick, G. M. (2004). *SADABS Version 2004-1, Program for absorption corrections to area detector data.* Bruker-AXS, Madison, Wisconsin, USA.

Silva, M. D. M. C. R. d. & Araujo, N. R. M. (2007). *Journal of Chemical Thermodynamics* **39**, 1372-1376.

Spackman, M. A. & McKinnon, J. J. (2002). *CrystEngComm* **4**, 378-392.

Spackman, M. A., McKinnon, J. J. & Jayatilaka, D. (2008). *CrystEngComm* **10**, 377-388.

Spek, A. L. (2003). *Journal of Applied Crystallography* **36**, 7-13.

Teixeira, A. M. R., Freire, P. T. C., Moreno, A. J. D., Sasaki, J. M., Ayala, A. P., Mendes Filho, J. & Melo, F. E. A. (2000). *Solid State Communications* **116**, 405-409.

Watkin, D. J., Pearce, L. & Prout, K. (1993). *CAMERON - A Molecular Graphics Package.* Chemical Crystallography Laboratory, University of Oxford, Oxford, England.

Wolff, S. K., Grimwood, D. J., McKinnon, J. J., Jayatilaka, D. & Spackman, M. A. (2007). *CrystalExplorer 2.0,* University of Western Australia, Australia.

Wood, P. A., Forgan, R. S., Henderson, D., Parsons, S., Pidcock, E., Tasker, P. A. & Warren, J. E. (2006). *Acta Crystallographica Section B* **62**, 1099-1111.

Wood, P. A., Francis, D., Marshall, W. G., Moggach, S. A., Parsons, S., Pidcock, E. & Rohl, A. L. (2008). *CrystEngComm* **10**, 1154 - 1166.

Wood, P. A., McKinnon, J. J., Parsons, S., Pidcock, E. & Spackman, M. A. (2008). *CrystEngComm* **10**, 368-376.

Chapter 6

The Effect of Pressure on the Crystal Structure of Bianthrone*

* Johnstone, R. D. L., Lennie, A. R., Parsons, S., Pidcock, E. *Acta Crystallographica*, *Section B*. In preparation

6.1 Abstract

The crystal structure of bianthrone consists of layers of molecules which stack along the [010] direction. The structure remains in a compressed form of the ambient phase when subjected to hydrostatic pressure up to 6.5 GPa, and the most prominent effect of pressure is to push the layers closer together. PIXEL calculations show that the strongest intermolecular interactions within the structure occur between layers; these interactions become considerably less stable as the inter-layer separation reduces. CH…O contacts within layers involving the carbonyl oxygen also become significantly less stable, and Raman spectra indicate that as the C…O distance shortens there is a shift in the C=O stretch to higher frequency; a relationship which points to a hardening of potential in this region of the structure. Bianthrone appears to undergo a subtle colour change from bright yellow to dark orange as pressure is applied, and it is likely that this is caused by changes in π-π stacking distances as the layers of bianthrone approach each other.

6.2 Introduction

Bianthrone (Scheme 6.1) is part of a family of compounds which are commonly known as bistricyclic aromatic enes. Crystals of bianthrone formed at ambient pressure and temperature are bright yellow, and the molecules adopt a 'folded' conformation (Figure 6.1a) (Harnik & Schmidt, 1954).

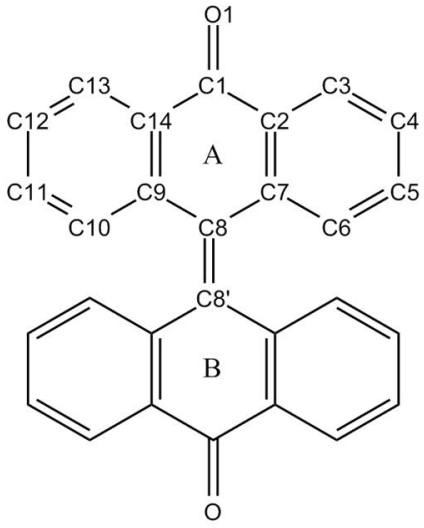

Scheme 6.1: 9,9'-bi-9(10*H*)-anthracenylidene-10,10'dione (bianthrone).

a)

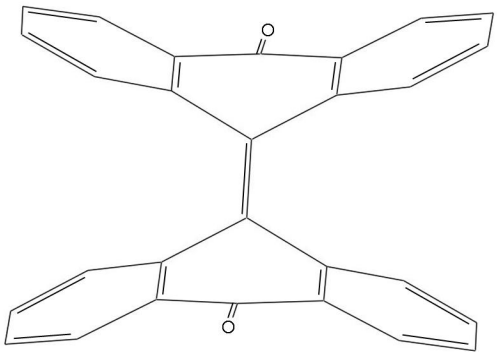

b)

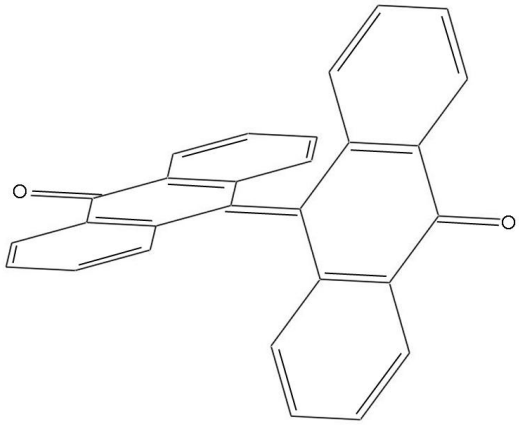

Figure 6.1: a) The ambient temperature/pressure, 'folded' conformation of bianthrone (Harnik & Schmidt, 1954). b) The proposed twisted form (Harnik, 1956; Korenstein *et al.*, 1973): the tricyclic rings are planar and the torsion about the central double bond is *ca*. 55˚.

In solution, bianthrone changes colour reversibly from bright yellow to dark green when subjected to heat (thermochromism) (Meyer, 1909a, b), light (photochromism) (Kortum, 1974) and pressure between 0.13 and 10.6 GPa (piezochromism) (Fanselow & Drickamer, 1974). Proton nmr spectroscopy and minimum energy strain calculations (Korenstein *et al.*, 1973) indicate that the bianthrone molecules in the green form take-on a 'twisted' conformation (Figure 6.1b), which is marginally less stable than the folded conformer (Harnik, 1956).

The yellow crystals of bianthrone are neither photochromic nor thermochromic; however, they are reported to change colour to dark green on grinding in a pestle and mortar (Wasserman & Davies, 1959). Although the structure

of the green form has not been established by X-ray crystallography, it is thought to be in the twisted form. Further support for this contention comes from the polymorphic behaviour of other bistricyclic aromatic enes which exhibit dark-coloured twisted and brightly-coloured folded polymorphic forms. For example, the twisted form of 9-(2,7-dimethyl-9*H*fluoren-9-ylidene)-9*H*-xanthene is deep-purple and the folded form is yellow (Biedermann *et al.*, 2006).

The principal aim of the present study was to investigate whether the colour change that is observed in bianthrone upon grinding could be reproduced by the application of hydrostatic pressure to a single crystal in a diamond anvil cell. In the event this was not observed, highlighting the important differences between hydrostatic and non-hydrostatic conditions. However, there did appear to be a subtle colour change from yellow to dark orange as a result of the compression.

6.3 Experimental

6.3.1 Crystal growth

Bianthrone [9,9'-bi-9(10*H*)-anthracenylidene-10,10'dione] (Scheme 6.1) was purchased from Sigma-Aldrich (Catalogue number R750077). A sample (50 mg) was dissolved in dichloromethane (5 ml), and slow evaporation over the course of two weeks at room temperature of the solvent resulted in the formation of small, yellow crystals on the side of the vial.

6.3.2 Determination of the ambient pressure structure

Data were measured on a Bruker SMART APEX diffractometer with graphite-monochromated Mo-Kα radiation (λ = 0.71073 Å) at 293 K. The data were integrated using SAINT (Bruker-Nonius, 2006) and corrected for absorption with SADABS (Sheldrick, 2004). The structure was solved using direct methods (SIR-92) (Altomare *et al.*, 1994) and refined against F using data with $F > 4\ \sigma(F)$ in CRYSTALS (Betteridge *et al.*, 2003). All non-H atoms were refined with anisotropic displacement parameters. Hydrogen atoms attached to carbon were placed geometrically and constrained to ride on their host atoms. Crystal and refinement data are given in Table 6.1.

Pressure/ GPa	Ambient	1.2	2.2	3.3
Formula	$C_{28}O_2H_{16}$	$C_{28}O_2H_{16}$	$C_{28}O_2H_{16}$	$C_{28}O_2H_{16}$
M_r	384.43	384.43	384.43	384.43
Cell setting, space group	Monoclinic, $P2_1/n$	Monoclinic, $P2_1/n$	Monoclinic, $P2_1/n$	Monoclinic, $P2_1/n$
a, b, c (Å)	10.1860 (3), 8.4277 (2), 11.6457 (3)	9.9825 (11), 7.8892 (15), 11.4879 (9)	9.9021 (14), 7.6543 (18), 11.4225 (11)	9.8354 (13), 7.4567 (19), 11.3543 (12)
β (°)	109.591 (2)	109.780 (6)	109.860 (9)	109.939 (8)
V (Å)	941.85 (4)	851.3 (2)	814.3 (2)	782.8 (2)
Z	2	2	2	2
D_x (Mg m^{-3})	1.355	1.500	1.568	1.631
μ (mm^{-1})	0.08	0.09	0.10	0.10
Crystal form, colour	Block, Yellow	Block, Yellow	Block, Yellow	Block, Yellow
Crystal size (mm)	0.57 × 0.33 × 0.31	0.20 × 0.20 × 0.10	0.20 × 0.20 × 0.10	0.20 × 0.20 × 0.10
T_{min}	0.82	0.86	0.78	0.84
T_{max}	0.97	0.99	0.99	0.99
No. of measured, independent and observed [$I > 2.0\sigma(I)$] reflections.	12386, 2349, 1867	4044, 852, 644	3792, 818, 625	3798, 772, 583
R_{int}	0.049	0.087	0.087	0.093
d_{max}, d_{min}/ Å	8.84, 0.75	6.14, 0.90	8.63, 0.90	6.04, 0.90
Refinement on	*F*	*F*	*F*	*F*
$R[F^2>2\sigma(F^2)]$, $wR(F^2)$, *S*	0.055, 0.051, 1.11	0.045, 0.044, 1.01	0.044, 0.047, 1.04	0.042, 0.043, 1.04
No. of parameters	136	136	136	136
Weighting Scheme	Chebychev polynomial (Prince, 1982) (Watkin, 1994)	Chebychev polynomial (Prince, 1982) (Watkin, 1994)	Chebychev polynomial (Prince, 1982) (Watkin, 1994)	Chebychev polynomial (Prince, 1982) (Watkin, 1994)
$(\Delta/\sigma)_{max}$	<0.0001	<0.0001	<0.0001	<0.0001
$\Delta\rho_{max}$, $\Delta\rho_{min}$ (e Å^{-3})	0.24, –0.19	0.12, –0.13	0.14 –0.15	0.15, –0.16
Completeness	99.8% (0.75 Å)	69.2% (0.9 Å)	68.7% (0.9 Å)	69.6% (0.9 Å)

a)

Pressure/ GPa	4.2	5.1	6.0	6.5
Formula	$C_{28}O_2H_{16}$	$C_{28}O_2H_{16}$	$C_{28}O_2H_{16}$	$C_{28}O_2H_{16}$
M_r	384.43	384.43	384.43	384.43
Cell setting, space group	Monoclinic, $P2_1/n$	Monoclinic, $P2_1/n$	Monoclinic, $P2_1/n$	Monoclinic, $P2_1/n$
a, b, c (Å)	9.7854 (7), 7.2988 (11), 11.3074 (7)	9.7527 (9), 7.2058 (15), 11.2786 (9)	9.7286 (10), 7.1123 (17), 11.2468 (11)	9.7119 (14), 7.041 (2), 11.2282 (18)
β (°)	110.028 (4)	110.132 (6)	110.186 (7)	110.229 (10)
V (Å)	758.75 (14)	744.19 (18)	730.4 (2)	720.4 (3)
Z	2	2	2	2
D_x (Mg m^{-3})	1.683	1.716	1.748	1.772
μ (mm^{-1})	0.11	0.11	0.11	0.11
Crystal form, colour	Block, Yellow	Block, Yellow	Block, Yellow	Block, Yellow
Crystal size (mm)	0.20 × 0.20 × 0.10	0.20 × 0.20 × 0.10	0.20 × 0.20 × 0.10	0.20 × 0.20 × 0.10
T_{min}	0.84	0.79	0.76	0.81
T_{max}	0.99	0.99	0.99	0.99
No. of measured, independent and observed [$I > 2.0\sigma(I)$] reflections.	3269, 689, 554	3280, 649, 506	3365, 623, 487	3016, 641, 473
R_{int}	0.074	0.093	0.081	0.117
d_{max}, d_{min}/ Å	4.64, 0.90	5.98, 0.90	5.96, 0.90	5.95, 0.90
Refinement on	*F*	*F*	*F*	*F*
$R[F^2>2\sigma(F^2)]$, $wR(F^2)$, *S*	0.042, 0.044, 1.07	0.041, 0.047, 1.08	0.041 0.029 1.09	0.051, 0.039, 1.09
No. of parameters	136	136	136	136
Weighting Scheme	Chebychev polynomial (Prince, 1982) (Watkin, 1994)	Chebychev polynomial (Prince, 1982) (Watkin, 1994)	Chebychev polynomial (Prince, 1982) (Watkin, 1994)	Chebychev polynomial (Prince, 1982) (Watkin, 1994)
$(\Delta/\sigma)_{max}$	<0.0001	<0.0001	<0.0001	<0.0001
$\Delta\rho_{max}$, $\Delta\rho_{min}$ (e Å^{-3})	0.16, –0.16	0.12, –0.12	0.14, –0.15	0.19, –0.19
Completeness	65.7% (0.9 Å)	65.1% (0.9 Å)	62.4% (0.9 Å)	67.3% (0.9 Å)

b)

Table 6.1: Crystallographic data for bianthrone at increasing pressures.

6.3.3 High-pressure crystallography: data processing and general procedures

High-pressure experiments were carried out using a Merrill-Bassett diamond anvil cell (half-opening angle 40°), equipped with Boehler–Almax cut diamonds with 600 μm culets and a tungsten gasket (Merrill & Bassett, 1974; Moggach *et al.*, 2008). A 4:1 mixture of methanol and ethanol was used as a hydrostatic medium. A small ruby chip was also loaded into the cell as the pressure callibrant, and the ruby fluorescence method used to measure the pressure (Piermarini *et al.*, 1975).

All diffraction data were collected on a Bruker-Nonius APEX-II diffractometer with silicon-monochromated synchrotron radiation (λ = 0.4780 Å) on Station 9.8 at the SRS, Daresbury Laboratory. Data collection and processing procedures for all high-pressure experiments followed Dawson *et al.* (2004). Integrations were carried out using dynamic masking of the regions of the detector shaded by the pressure cell with the program SAINT. An absorption correction was carried out in a two-stage procedure with the programs SHADE (Parsons, 2004) and SADABS. Data were merged using SORTAV (Blessing, 1987).

Refinements of the compressed form of bianthrone were carried out starting from the co-ordinates determined at ambient pressure. Refinement procedures followed those at ambient conditions, though owing to the low completeness of the data-sets, all primary bond distances and angles were restrained to the values observed at ambient conditions. All non-H atoms were refined with anisotropic displacement parameters, with global rigid-bond and body restraints.

6.3.4 Compression of bianthrone as studied by Raman spectroscopy

For the purposes of Raman spectroscopic measurements a polycrystalline sample of bianthrone was loaded into a Merrill-Bassett cell in the manner described above. Raman measurements were carried-out at room temperature as a function of pressure by excitation with a 632.417 nm line from a He-Ne laser, the fluorescence being detected with a Jobin-Yvon LabRam 300 Raman spectrometer.

6.3.5 PIXEL calculations

The final crystal structures obtained were used to calculate the molecular electron densities of the bianthrone molecules at each pressure by standard quantum chemical methods using the program GAUSSIAN03 (Frisch *et al.*, 2004) with the MP2/6-31G** basis set. H-atom distances were set to standard neutron values in all calculations (C-H = 1.083). The electron density was used to evaluate packing energies using the PIXEL method as implemented in the program OPiX (Gavezzotti, 2003). The output from these calculations yields a total packing energy and a breakdown into component interactions. Each energy is further broken down into its Coulombic (electrostatic), polarisation, dispersion and repulsion contributions (Gavezzotti, 2005, 2007).

6.3.6 Other programs used

Crystal structures were visualised using the programs CAMERON (Watkin *et al.*, 1993), MERCURY 2.2 (Macrae *et al.*, 2008) and DIAMOND (Brandenburg & Putz, 2005). Analyses were carried out using PLATON (Spek, 2004), as incorporated in the WIN-GX suite (Farrugia, 1999). Searches of the Cambridge Structural Database utilized the program CONQUEST with database updates up to November 2008 (Allen, 2002).

6.4 Results

6.4.1 The crystal structure of bianthrone at ambient pressure

Bianthrone crystallises in the space group $P2_1/n$ with half a molecule in the asymmetric unit, the crystallographic inversion centre lies at the mid-point of the C=C bond connecting the two tricyclic moieties (Scheme 6.1). At ambient temperature and pressure each molecule adopts a 'folded' conformation (Figure 6.1a) where the two central six-membered rings (labelled A and B in Scheme 6.1) take on a boat-like conformation [τ(C8'-C8-C9-C10) = 44.5(2)° and τ(C8'-C8-C9-C14) = 137.22(15)°]. The tricyclic groups are non-planar: a least-squares mean plane calculated using carbon atoms 1-14 (Scheme 6.1), shows that the average deviation of these atoms from the plane is 0.37 Å.

Table 6.2 gives the energies of the five energetically most significant (>2 kJmol^{-1}) intermolecular interactions in bianthrone calculated at ambient conditions. The PIXEL method calculates molecule-molecule intermolecular energies and therefore some interactions comprise more than one contact. The geometrical parameters for each contact are also included in Table 6.2.

Pressure (GPa)	**0**	**1.2**	**2.2**	**3.3**
Interaction #1 (Inter-layer)				
C11H6...O1[i]				
H6…O1	2.59	2.40	2.35	2.32
C11…O1	3.309(2)	3.055(3)	2.962(3)	2.898(4)
<C11H6O1	133	126	122	119
C10H5...R1[i]				
H5…R2	3.75	3.66	3.61	3.59
C10…R2	4.624(3)	4.525(4)	4.474(4)	4.441
<C10H5R2	155	153	153	150
R2…R1 [ii]				
R2...R1	4.367(1)	4.088(2)	3.964(2)	3.855(2)
Offset	2.114	1.905	1.794	1.677
C4H2...R3 [iii]				
H2…R3	3.07	2.88	2.82	2.77
C4…R3	3.489(3)	3.255(4)	3.162(4)	3.082(4)
<C4H2R3	108	105	103	100
Energy (kJmol^{-1})	-34.7	-33.3	-30.4	-23.6
Interaction #2 (Intra-layer)				
C5H3...R3[iv]				
H3…R3	3.51	3.42	3.35	3.29
C5…R3	4.450(3)	4.236(4)	4.157(4)	4.093(4)
<C5H3R3	146	145	144	144
Energy (kJmol^{-1})	-18.4	-18.2	-17.4	-16.4
Interaction #3 (Inter-layer)				
C12H7...R3[v]				
H7…R3	3.45	3.17	3.03	2.92
C12…R3	4.090(3)	3.791(4)	3.650(4)	3.536(4)
<C12H7R3	127	124	124	124
C6H4…H7C12[vi]	2.52	2.30	2.21	2.14
H4…H7				
Energy (kJmol^{-1})	-17.0	-18.0	-19.2	-19.1
Interaction #4 (Intra-layer)				
C13H8...O1[vii]				
H8…O1	2.49	2.40	2.35	2.32
C13…O1	3.396(2)	3.256(3)	3.186(3)	3.132(3)
<C13H8O1	159	150	147	143
Energy (kJmol^{-1})	-15.1	-14.0	-14.5	-14.5
Interaction #5 (Intra-layer)				
C3H1…H1C3 [viii]				
H1…H1	2.72	2.41	2.29	2.19
C4H2…H1C3 [viii]				
H2…H1	2.89	2.78	2.72	2.65
Energy (kJmol^{-1})	-10.3	-12.6	-13.7	-13.7

a)

Pressure (GPa)	4.2	5.1	6.0	6.5
Interaction #1 (Inter-layer)				
C11H6...O1[i]				
H6…O1	2.29	2.27	2.26	2.23
C11…O1	2.840(3)	2.812(4)	2.784(4)	2.750(5)
<C11H6O1	116	116	114	113
C10H5...R1[i]				
H5…R2	3.56	3.55	3.53	3.53
C10…R2	4.411(4)	4.391(4)	4.373(4)	4.363(5)
<C10H5R2	150	149	149	148
R2…R1 [ii]				
R2...R1	3.775(2)	3.725(2)	3.678(2)	3.642(3)
Offset	1.590	1.515	1.448	1.345
C4H2...R3 [iii]				
H2…R3	2.73	2.75	2.71	2.70
C4…R3	3.027(4)	3.005(4)	2.972(4)	2.950(5)
<C4H2R3	99	96	97	96
Energy (kJmol^{-1})	-19.4	-15.6	-9.4	-3.5
Interaction #2 (Intra-layer)				
C5H3...R3[iv]				
H3…R3	3.25	3.22	3.20	3.18
C5…R3	4.046(4)	4.018(4)	3.996(5)	3.976(5)
<C5H3R3	143	143	143	143
Energy (kJmol^{-1})	-14.7	-13.6	-10.9	-9.5
Interaction #3 (Inter-layer)				
C12H7...R3[v]				
H7…R3	2.84	2.80	2.74	2.70
C12…R3	3.454(4)	3.406(4)	3.348(4)	3.312(5)
<C12H7R3	123	123	123	123
C6H4…H7C12[vi]				
H4…H7	2.09	2.06	2.03	2.01
Energy (kJmol^{-1})	-18.0	-17.4	-16.2	-14.7
Interaction #4 (Intra-layer)				
C13H8...O1[vii]				
H8…O1	2.29	2.28	2.27	2.25
C13…O1	3.077(3)	3.054(3)	3.029(3)	3.006(4)
<C13H8O1	140	138	137	136
Energy (kJmol^{-1})	-13.8	-13.0	-12.4	-11.0
Interaction #5 (Intra-layer)				
C3H1…H1C3 [viii]				
H1…H1	2.10	2.05	1.99	1.96
C4H2…H1C3 [viii]				
H2…H1	2.59	2.56	2.52	2.49
Energy (kJmol^{-1})	-13.6	-13.9	-13.9	-12.9

b)

Symmetry Operators:

i	1/2+*x*, 1/2-*y*, 1/2+*z*
ii	3/2-*x*, 1/2+*y*, 1/2-*z*
iii	3/2-*x*, -1/2+*y*, 1/2-*z*
iv	-1+*x*, *y*, *z*
v	5/2-*x*, 1/2+*y*, 1/2-*z*
vi	1/2+*x*, 3/2-*y*, -1/2+*z*
vii	2-*x*, 1-*y*, -*z*
viii	1-*x*, 1-*y*, -*z*

Ring Identities:

R1	C2-C3-C4-C5-C6-C7
R2	C1-C2-C7-C8-C9-C14
R3	C9-C10-C11-C12-C13-C14

c)

Table 6.2: The main non-covalent interactions for the crystal structure of bianthrone with increasing pressure. Distances are in Å and angles are given in °. S.u's are calculated in PLATON. Interactions involving rings are measured from the centroid of the ring. Hydrogen distances are not normalised to standard neutron values.

The crystal structure consists of chains of molecules which run parallel to the *c*-axis, interacting with each other via C13H8…O1 contacts (Interaction #4 in Table 6.2: Total energy = -15.1 kJmol^{-1}) which form in pairs across inversion centres (Figure 6.2a). Chains of molecules interact with each other through CH…π interactions (Interaction #2: Total energy = -18.4 kJmol^{-1}) and H…H contacts (Interaction #5: Total energy = -10.3 kJmol^{-1}) to form layers which stack along the *b*-axis. The layers interact with one another via C11H6…O1 contacts, π-interactions and H…H contacts (Interactions #1 and #3: Total energies = -34.7 kJmol^{-1} and -17.0 kJmol^{-1} respectively) (Figures 6.2b and c). The total energy of the interactions within the layers (intra-layer: #'s 2, 4 and 5 in Table 6.2) is -43.8 kJmol^{-1}, and is less than the total energy of interactions between the layers (inter-layer: #'s 1 and 3 in Table 6.2), which is -51.7 kJmol^{-1}.

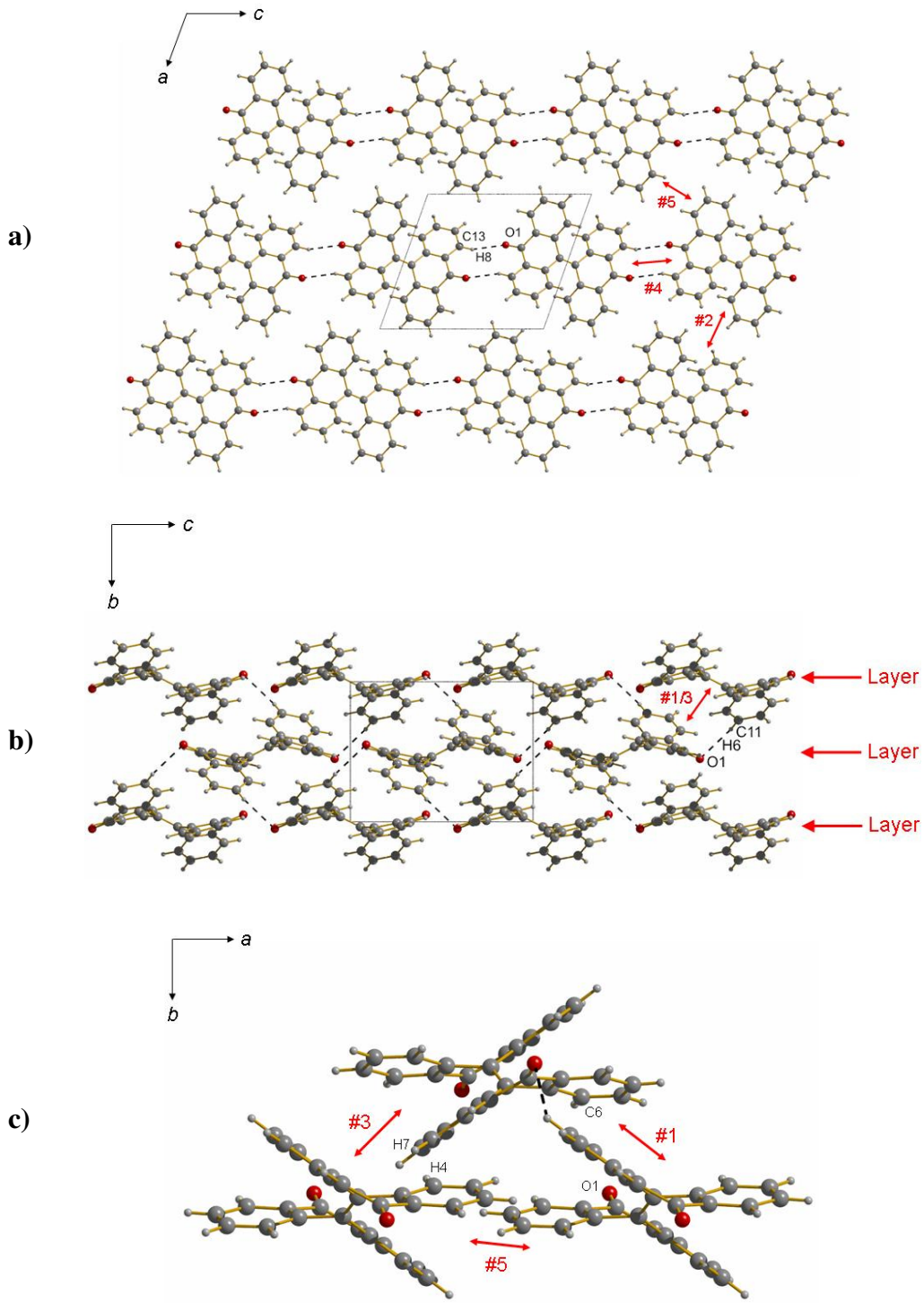

Figure 6.2: a) One layer of bianthrone molecules viewed along the *b*-axis. b) Layers of bianthrone viewed along *a*. For clarity the C13H8…O1 contacts shown in (a) are not present in (b). The numbers 1-5 represent the PIXEL interactions in Table 6.2. Interactions #1 and #3 are shown in (c) viewed along the *c*-axis in order to clarify (b).

A breakdown of the total energy for the contacts is given in Table 6.3. At ambient conditions all five interactions are dominated by the dispersion term, except for #4 (a CH…O contact), where dispersion and Coulombic terms are approximately the same (-11.6 and -12.2 kJmol^{-1}, respectively). The total lattice energy calculated by the PIXEL method at ambient conditions is -146.8 kJmol^{-1} (E_{Coul}= -47.5 kJmol^{-1}, E_{pol}= -19.7 kJmol^{-1}, E_{disp}= -183.8 kJmol^{-1}, E_{rep}= 104.3 kJmol^{-1}). PIXEL lattice energies can be validated by comparison with experimental sublimation enthalpies. However, to our knowledge there is no literature value for the sublimation enthalpy of bianthrone.

Energy Breakdown (kJmol^{-1})	**0 GPa**	**1.2 GPa**	**2.2 GPa**	**3.3 GPa**
Interaction #1				
E_{Coul}	-10.0	-20.1	-27.3	-34.8
E_{pol}	-5.3	-10.7	-14.6	-18.5
E_{disp}	-46.2	-65.3	-78.0	-86.4
E_{rep}	26.8	63.1	89.4	116.1
E_{tot}	-34.7	-33.0	-30.5	-23.6
Interaction #2				
E_{Coul}	-5.1	-10.4	-14.2	-18.0
E_{pol}	-2.6	-5.2	-7.6	-10.6
E_{disp}	-23.8	-33.6	-38.6	-42.6
E_{rep}	13.1	31.1	42.9	54.7
E_{tot}	-18.4	-18.2	-17.4	-16.4
Interaction #3				
E_{Coul}	-4.4	-7.8	-10.6	-13.1
E_{pol}	-2.7	-5.4	-7.9	-10.1
E_{disp}	-20.3	-28.3	-34.4	-39.5
E_{rep}	10.4	23.5	33.6	43.4
E_{tot}	-17.0	-18.0	-19.3	-19.2
Interaction #4				
E_{Coul}	-12.2	-15.4	-17.7	-19.1
E_{pol}	-5.4	-6.7	-8.2	-8.6
E_{disp}	-11.6	-13.3	-15.2	-16.8
E_{rep}	14.1	21.4	26.6	30.1
E_{tot}	-15.1	-14.0	-14.5	-14.5
Interaction #5				
E_{Coul}	-3.3	-5.0	-6.2	-7.7
E_{pol}	-0.9	-2.1	-3.3	-4.5
E_{disp}	-8.8	-12.4	-14.5	-16.5
E_{rep}	2.7	6.9	10.2	15.0
E_{tot}	-10.3	-12.6	-13.7	-13.7

a)

Energy Breakdown ($kJmol^{-1}$)	4.2 GPa	5.1 GPa	6.0 GPa	6.5 GPa
Interaction #1				
E_{Coul}	-43.9	-48.8	-55.2	-60.4
E_{pol}	-23.5	-25.8	-29.6	-31.6
E_{disp}	-99.0	-104.6	-111.1	-115.4
E_{rep}	146.7	163.7	186.5	204.0
E_{tot}	-19.6	-15.6	-9.4	-3.5
Interaction #2				
E_{Coul}	-21.7	-23.5	-26.6	-28.4
E_{pol}	-14.3	-15.6	-17.4	-18.6
E_{disp}	-46.3	-48.7	-49.8	-51.0
E_{rep}	67.6	74.2	83.0	88.6
E_{tot}	-14.7	-13.6	-10.9	-9.5
Interaction #3				
E_{Coul}	-15.9	-17.9	-20.1	-22.0
E_{pol}	-12.5	-14.1	-16.2	-17.6
E_{disp}	-43.4	-46.3	-48.6	-50.4
E_{rep}	53.7	61.0	68.7	75.3
E_{tot}	-18.1	-17.4	-16.2	-14.7
Interaction #4				
E_{Coul}	-21.0	-21.5	-21.7	-22.3
E_{pol}	-9.7	-10.1	-10.5	-10.8
E_{disp}	-18.3	-18.8	-19.7	-20.3
E_{rep}	35.2	37.3	39.5	42.4
E_{tot}	-13.8	-13.0	-12.4	-11.0
Interaction #5				
E_{Coul}	-9.4	-10.7	-12.4	-13.9
E_{pol}	-6.2	-7.1	-8.9	-10.4
E_{disp}	-18.9	-20.7	-22.3	-23.0
E_{rep}	20.8	24.7	29.6	34.5
E_{tot}	-13.6	-13.9	-13.9	-12.9

b)

Table 6.3: Breakdown of the total interaction energy for each contact (#'s 1-5) featured in Figures 6.2 (a-c) and Table 6.2.

6.4.2 Compression of bianthrone to 6.5 GPa.

Compression of bianthrone is anisotropic (Figure 6.3), and the crystal remains in a compressed form of its ambient phase up to 6.5 GPa. The colour change from yellow to green that occurs on grinding is not observed, though there does appear to be a subtle change from yellow to orange which becomes more apparent at higher pressures.

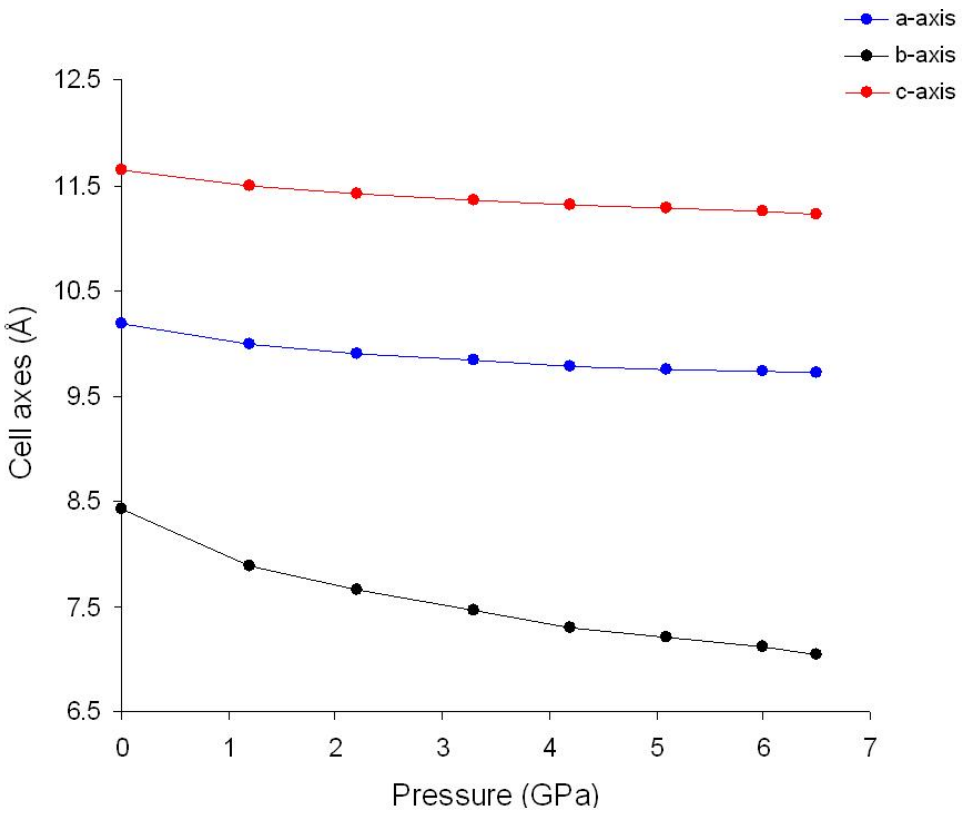

Figure 6.3: Unit cell axes of bianthrone as a function of pressure.

Although the strongest interactions occur between the layers (Table 6.2) which stack along the *b*-direction, the greatest amount of compression also occurs along the same direction, which decreases by 16.5% between ambient pressure and 6.5 GPa. Compression along the *b*-axis is substantially more than along either of the layer-building axes (*a* and *c*) which compress by 4.7% and 3.6% respectively.

The H…O distances in the CH…O contacts (Table 6.2) are 2.49 and 2.59 Å at ambient pressure and 2.25 and 2.23 Å at 6.5 GPa respectively; the H….ring centroid distances in the CH…π interactions lie between 3.07 and 3.70 Å at ambient pressure and 2.70 and 3.53 Å at 6.5 GPa; the H…H distances lie between 2.52 and 2.89 Å at ambient conditions and 1.96 and 2.49 Å at 6.5 GPa. The centroid to centroid distance of the π…π stacking interaction decreases by 16.6 % upon compression to 6.5 GPa.

These features are summarised effectively in Hirshfeld finger-print plots of the structures of bianthrone at ambient pressure and 6.5 GPa (Figure 6.4).[†] The two prongs which represent CH…O interactions are prominent at ambient conditions (red arrows) whilst they become masked as a result of the relatively larger contraction in the short H…H contacts. The compressed stacking interactions lead to an increase in the number of distances in the middle of the plots (black arrow), while the void-space reduction is seen in the disappearance of the diffuse region at high values of (d_i,d_e).

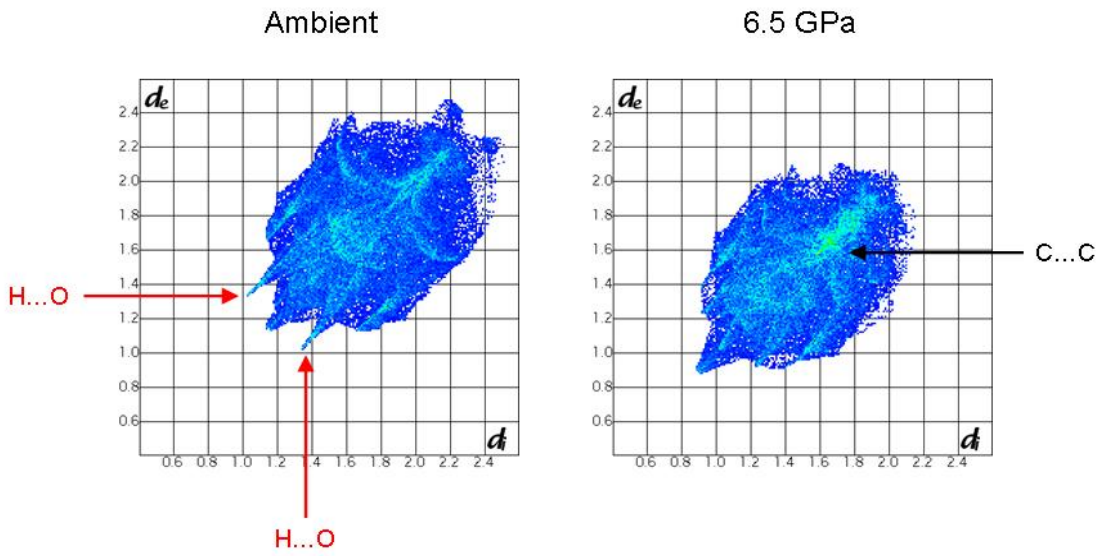

Figure 6.4: *Fingerprint* plots for bianthrone at ambient conditions and at 6.5 GPa. Green areas represent an increased frequency of contact distances compared to the blue areas. The red arrows point towards the two 'prongs' which represent H…O distances, and the black arrow points towards an area of C…C distances.

[†] Hirshfeld surfaces provide a useful way of looking at the packing environment in a crystal structure. The surface is created by applying the Hirshfeld stockholder partitioning method to divide the crystal into regions in which the electron density of the crystal is dominated by the electron density of a specific molecule. A number of useful properties can be mapped onto the surface including d_e (distances to nearest external atom) and d_i (distances to nearest internal atom) and the electrostatic potential.

The bulk modulus (K_0) and its pressure derivative (K') refined for a Vinet equation-of-state (Vinet *et al.*, 1987; Angel *et al.*, 2000; Vinet *et al.*, 1986) were 8.1(5) GPa and 8.6(5), respectively. The value of V_0, the volume at ambient pressure, was fixed at 941.85 Å^3. Molecular solids typically have $K_0 < 30$ GPa (Angel, 2004) and the following K_0 values are useful for comparison: $Ru_3(CO)_{12}$ (K_0 = 6.6 GPa); alanine (K_0 = 13.6 GPa and K' = 6.7), NaCl (K_0 = 25 GPa), quartz (37 GPa, K' = 6), ceramics (K_0 = 50-300 GPa) and diamond (K_0 = 440 GPa). Softer, molecular structures have relatively high values of K', which indicates a large amount of compression at low pressure.

The overall folded shape of the bianthrone molecules remains throughout the compression study, though some of the torsion angles do change significantly. The average change in non-H torsion angle between ambient conditions and 6.5 GPa is *ca*. 4º, and the largest differences occur in τ(C8'-C8-C9-C10) and τ(C8'-C8-C9-C14) which both change by *ca*. 10 º.

As pressure is increased on bianthrone, the relative magnitudes of the cohesive energy component terms for each interaction remain consistent with those at ambient conditions (Table 6.3); for example, the dispersion component in contacts 1, 2, 3 and 5 still dominates at 6.5 GPa and for contact #4, the Coulombic and dispersion components are effectively equal.

6.4.3 High-pressure Raman spectroscopy

Raman spectra of a solid crystalline sample of bianthrone at pressures similar to those in the crystallographic study are presented in Figure 6.5. The spectrum at ambient conditions corresponds well to that reported by Sanchez-Cortes *et al.* (1997). At ambient conditions the peak corresponding to the C=O stretch lies at 1661.5 cm^{-1}, and as pressure is applied to 6 GPa it shifts to 1671.6 cm^{-1}. At higher pressures the peaks in each spectrum become increasingly broad and no C=O peak could be located at 6.6 GPa. Other features of the spectra include a splitting of a peak at *ca*. 200 cm^{-1} and the introduction of two new peaks at *ca*. 400 cm^{-1}.

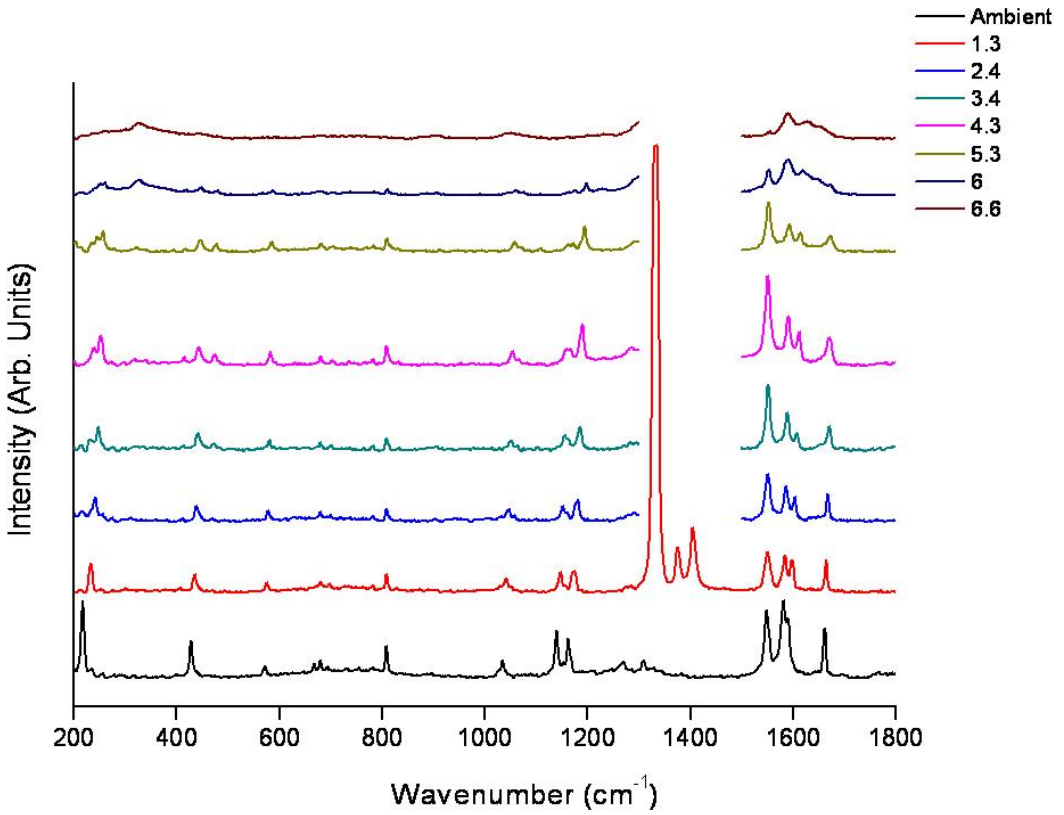

Figure 6.5: Raman spectra of bianthrone with increasing pressure. For pressures above 1.3 GPa, the large peak arising from a diamond C-C stretch (*ca.*1300cm^{-1}) and the doublet at *ca.*1400cm^{-1} (ruby) are omitted for clarity.

6.5 Discussion

The compression of a crystal structure can often be understood in terms of relative intermolecular interaction strength. In most cases, relatively weak and non-directional interactions like π…π stacking contacts will tend to compress more than stronger, more directional types like H-bonds (Espallargas *et al.*, 2008). In bianthrone however, the largest amount of compression occurs along the direction of the strongest interactions (contacts occurring between layers, see *Results*) and in this case, compression can be understood in terms of the relative distribution of voids within the structure. Structures like bianthrone, which have a layered topology, will often compress to reduce the inter-layer separation [*cf.* serine hydrate (Johnstone *et al.*, 2008), glycine (Dawson *et al.*, 2005) and paracetamol phase I and II (Boldyreva *et al.*, 2002; Boldyreva *et al.*, 2000)] as this is the most efficient way to reduce

volume. Figures 6.6(a-c) show that large voids which are present between the layers at ambient conditions significantly reduce in size as the inter-layer separation reduces with pressure.

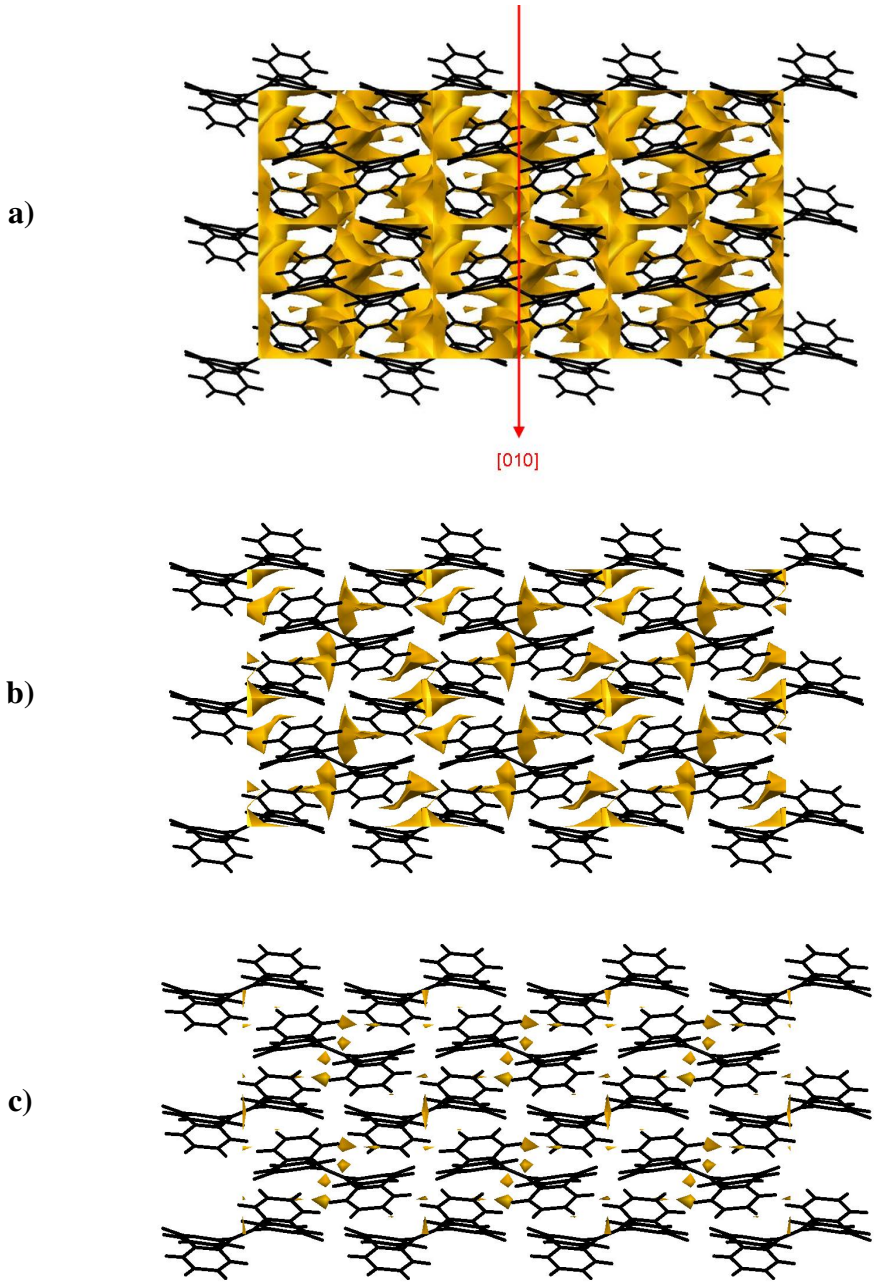

Figure 6.6: Void diagrams of bianthrone at ambient conditions (a), 2.2 GPa (b) and 6.5 GPa. The red arrow in (a) represents the direction of greatest linear strain throughout the compression study.

Figure 6.7 gives the total energy of the top five intermolecular interactions in bianthrone as a function of the centroid-centroid distance. Interactions #1, 3 and 4 all show similar behaviour: as pressure is applied the total interaction energies become rapidly more positive.

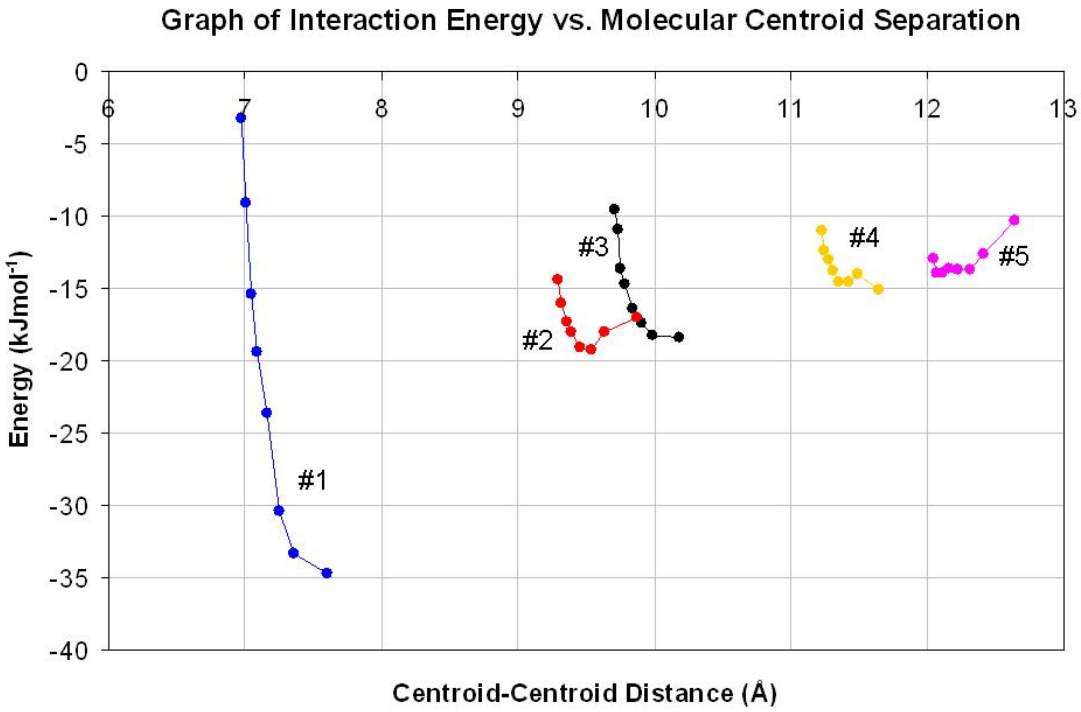

Figure 6.7: Graph of total interaction energy against the distance between the molecular centroids of the molecules involved in the interaction in bianthrone. The numbers 1-5 refer to the contacts listed in Table 6.2.

The energy of interaction #2 becomes more negative initially, but this too becomes more positive above 2.2 GPa. Only interaction #5 appeared to be stabilised with pressure, but only slightly. PIXEL calculations do not enable these energy changes to be broken down into atom-atom interaction energies, but it is notable that in contact #1 the distance between atoms C6 and O1 (Figure 6.2c) which is 3.27 Å at ambient conditions is 2.69 Å at 6.5 GPa (well within the sum of the van der Waals radii). Similarly, in contact #3 the distance between atoms H7 and H4 (Figure 6.2c) which is 2.52 Å at ambient conditions and 2.01 Å at 6.5 GPa, which is very short in the context of other H…H contacts in the CSD (hydrogen distances are not

normalised to standard neutron values). Supporting evidence for the shape of the curve corresponding to interaction #4 in Figure 6.7 is provided by Raman spectroscopy (see Figure 6.5). Figure 6.8 shows the relationship between the wavenumber of the C=O stretch and the C…O distance in contact #4 (C13H8…O1) as pressure is increased: the negative correlation points to a hardening of potential in this region of the structure, as indicated in Figure 6.7.

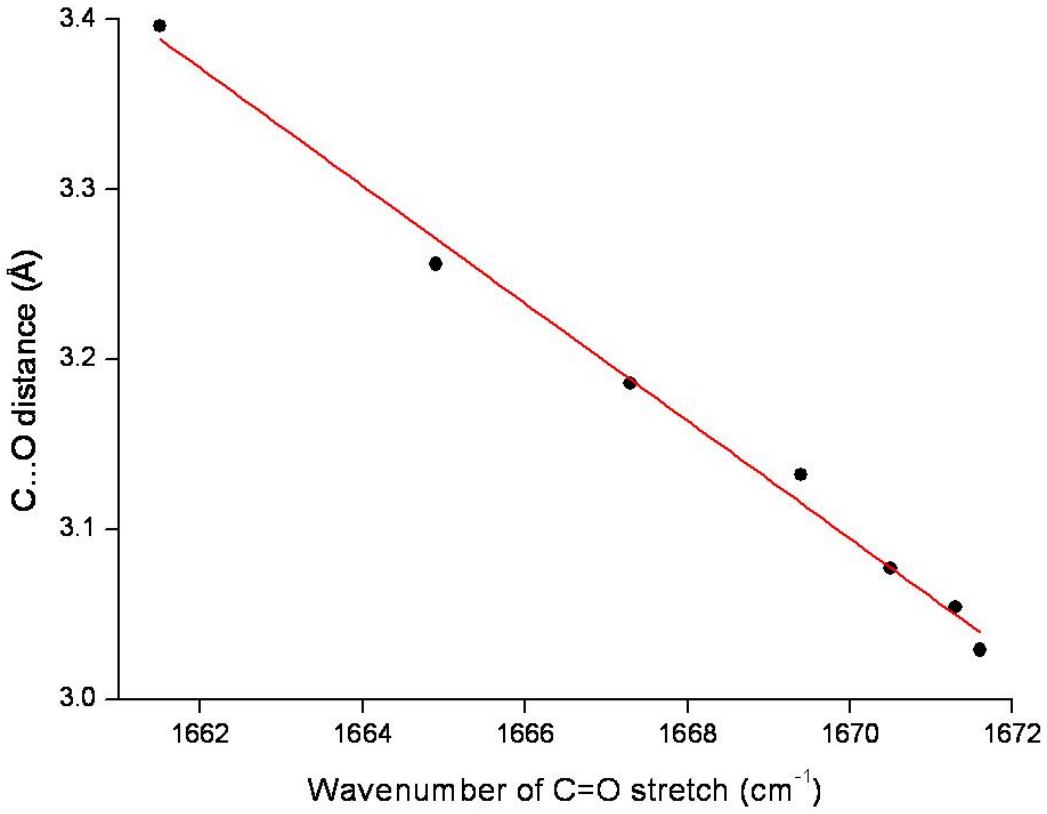

Figure 6.8: A graph to show the relationship between the wavenumber of the C=O stretch in the Raman spectra (Figure 6.5) and the C…O distance of the C13H8...O1 contact (#4 in Table 6.2).

It is clear from Figure 6.7 that several intermolecular interactions in bianthrone are driven well into the repulsive regions of their potentials at 6.5 GPa. This contrasts with what was observed in salicylaldoxime (Wood *et al.*, 2006): in that structure strain in H-bonding and stacking interactions with energy-distance curves similar to those in Figure 6.7 were found to be relieved by a phase transition. Why should a transition occur in salicylaldoxime but not in bianthrone?

The dominant contributors to free energy changes in phase transitions are usually assumed to be the internal energy and the pressure × volume term. In high pressure phase transitions there is *always* a reduction in volume, leading to a negative $P\Delta V$ contribution to ΔG. As pressure increases this term becomes ever more important, and, as was seen in serine hydrate, transitions can be driven entirely by this term, even at the expense of making the internal energy (U) more positive.

In other phase transitions both the U and PV terms are important. The transition from salicylaloxime-I to II above 5.3 GPa, for example, occurs with almost no change in volume. The molecular volume in phase-II at 5.93 GPa is 126.1 $Å^3$, the extrapolated molecular volume for phase-I at the same pressure is 126.4 $Å^3$, and the $P\Delta V$ term is only -1 $kJmol^{-1}$. This compares to an estimated ΔU of -25 $kJmol^{-1}$. The implication of Figure 6.7 is that in bianthrone the molecules are packed efficiently enough that the PV term overcomes any tendency to relieve the strain built up in interactions 1-4. Similar remarks could also be made about 3-aza-bicyclo(3.3.1)nonane-2,4-dione (Wood *et al.*, 2008), which remains stable up to 7.1 GPa and salicylamide-I (unpublished work), which is stable on compression to 5.1 GPa.

Our initial motive for studying the effect of pressure on bianthrone was to investigate whether the colour change from yellow to green that occurs on grinding could be reproduced on application of hydrostatic pressure. We have shown that this does not occur up to 6.5 GPa, a pressure well in excess of those that can be achieved in a pestle and mortar (10s of atmospheres). The colour change on grinding is thought to be associated with a change in the conformation of the bianthrone molecules; the change in colour from yellow to orange observed under hydrostatic pressure may be due to changes in π-π stacking distances. Our findings suggest that transition on grinding is induced by shear stresses. The occurrence of different phase behaviour under either hydrostatic or non-hydrostatic conditions has also been observed, for example, in $CuGeO_3$ (Dera *et al.*, 2002).

6.6 Conclusions

We have shown that the crystal structure of bianthrone remains in a compressed form of its ambient pressure phase when subjected to hydrostatic pressures up to 6.5 GPa. As the structure is compressed, a subtle colour change from yellow to orange is observed which is likely to be caused by changes in the distances of π…π stacking interactions. The colour change from yellow to green that takes place upon grinding is not observed under hydrostatic conditions.

PIXEL calculations show that as pressure is applied the main intermolecular interactions in the structure become significantly less stable. High-pressure Raman spectra support this observation, and indicate that a CH…O interaction becomes weaker as it shortens with pressure. Even though the structure evidently becomes a lot more strained as pressure is applied, there is apparently no need for this to be relieved by a phase transition; it is primarily due to the overwhelming contribution of the *PV* term to the free energy.

6.7 References

Allen, F. H. (2002). *Acta Crystallographica, Section B* **58**, 380-388.

Altomare, A., Cascarano, G., Giacovazzo, C., Guagliardi, A., Burla, M. C., Polidori, G. & Camalli, M. (1994). *Journal of Applied Crystallography* **27**, 435-435.

Angel, R. J. (2004). High Pressure Crystallography. NATO Science Series II, edited by A. Katrusiak & P. F. McMillan, pp. 21-36.

Angel, R. J., Downs, R. T. & Finger, L. W. (2000). *Reviews in Mineralogy and Geochemistry* **41**, 559-596.

Betteridge, P. W., Carruthers, J. R., Cooper, R. I., Prout, K. & Watkin, D. J. (2003). *Journal of Applied Crystallography* **36**, 1487.

Biedermann, P. U., Stezowski, J. J. & Agranat, I. (2006). *Chemistry--A European Journal* **12**, 3345-3354.

Blessing, R. H. (1987). *Crystallography Reviews* **1**, 3-58.

Boldyreva, E. V., Shakhtshneider, T. P., Ahsbahs, H., Sowa, H. & Uchtmann, H. (2002). *Journal of Thermal Analysis and Calorimetry* **68**, 437-452.

Boldyreva, E. V., Shakhtshneider, T. P., Vasilchenko, M. A., Ahsbahs, H. & Uchtmann, H. (2000). *Acta Crystallographica, Section B* **56**, 299-309.

Brandenburg, K. & Putz, H. (2005). *DIAMOND, version 3.2*. Crystal Impact GbR, Postfach 1251, 53002, Bonn, Germany.

Bruker-Nonius (2006). *SAINT version 7, Program for integration of area detector data.* Bruker-AXS, Madison, Wisconsin, USA.

Dawson, A., Allan, D. R., Belmonte, S. A., Clark, S. J., David, W. I. F., McGregor, P. A., Parsons, S., Pulham, C. R. & Sawyer, L. (2005). *Crystal Growth & Design* **5**, 1415-1427.

Dawson, A., Allan, D. R., Parsons, S. & Ruf, M. (2004). *Journal of Applied Crystallography* **37**, 410-416.

Dera, P., Jayaraman, A., Prewitt, C. T. & Gramsch, S. A. (2002). *Physical Review B* **65**, 134105.

Espallargas, G. M., Brammer, L., Allan, D. R., Pulham, C. R., Robertson, N. & Warren, J. E. (2008). *Journal of the American Chemical Society* **130**, 9058-9071.

Fanselow, D. L. & Drickamer, H. G. (1974). Journal of *Chemical Physics* **61**, 4567-4574.

Farrugia, L. J. (1999). *Journal of Applied Crystallography* **32**, 837-838.

Frisch, M. J., Trucks, G. W., Schlegel, H. B., Scuseria, G. E., Robb, M. A., Cheeseman, J. R., J. A. Montgomery, J., Vrevren, T., Kudin, K. N., Burant, J. C., Millam, J. M., Iyengar, S. S., Tomasi, J., Barone, V., Mennucci, B., Cossi, M., Scalmani, G., Rega, N., Petersson, G. A., Nakatsuji, H., Hada, M., Ehara, M., Toyota, K., Fukuda, R., Hasegawa, J., Ishida, M., Nakajima, T., Honda, Y., Kitao, O., Nakai, H., Klene, M., Li, X., Knox, J. E., Hratchian, H. P., Cross, J. B., Bakken, V., Adamo, C., Jaramillo, J., Gomperts, R., Stratmann, R. E., Yazyev, O., Austin, A. J., Cammi, R., Pomelli, C., Ochterski, J. W., Ayala, P. Y., Morokuma, K., Voth, G. A., Salvador, P., Dannenberg, J. J., Zakrzewski, V. G., Dappricj, S., Daniels, A. D., Strain, M. C., Farkas, O., Malick, D. K., Rabuck, A. D., Raghavachari, K., Foresman, J. B., Oritz, J. V., Cui, Q., Baboul, A. G., Clifford, S., Cioslowski, J., Stefanov, B. B., Liu, G., Liashenko, A., Piskorz, P., Komaromi, I., Martin, R. L., Fox, D. J., Keith, T., Al-Laham, M. A., Peng, C. Y., Nanayakkara, A., Challacombe, M., Gill, P. M. W., Johnson, B., Chen, W., Wong, M. W., Gonzalez, C. & Pople, J. A. (2004). *Gaussian 03 revision E.01.* Gaussian, Inc., Wallington CT.

Gavezzotti, A. (2003). *OPIX - A computer program package for the calculation of intermolecular interactions and crystal energies.* University of Milano, Milan, Italy.

Gavezzotti, A. (2005). *Zeitschrift fuer Kristallographie* **220**, 499-510.

Gavezzotti, A. (2007). *Molecular Aggregation: Structure Analysis and Molecular Simulation of Crystals and Liquids*, p. 323. Oxford, UK: Oxford University Press.

Harnik, E. (1956). *Journal of Chemical Physics* **24**, 297.

Harnik, E. & Schmidt, G. M. J. (1954). *Journal of the Chemical Society* 3295-3302.

Johnstone, R. D. L., Francis, D., Lennie, A. R., Marshall, W. G., Moggach, S. A., Parsons, S., Pidcock, E. & Warren, J. E. (2008). *CrystEngComm* **10**, 1758-1769.

Korenstein, R., Muszkat, K. A. & Sharafy-Ozeri, S. (1973). *Journal of the American Chemical Society* **95**, 6177.

Kortum, G. (1974). *Berichte der Bunsen-Gesellschaft* **78**, 391-403.

Macrae, C. F., Bruno, I. J., Chisholm, J. A., Edgington, P. R., McCabe, P., Pidcock, E., Rodriguez-Monge, L., Taylor, R., Streek, J. v. d. & Wood, P. A. (2008). *Journal of Applied Crystallography* **41**, 466-470.

Merrill, L. & Bassett, W. A. (1974). *Review of Scientific Instruments* **45**, 290-294.

Meyer, H. (1909a). *Berichte der Deutschen Chemischen Gesellschaft* **42**, 143-145.

Meyer, H. (1909b). *Monatshefte fuer Chemie* **30**, 165-177.

Moggach, S. A., Allan, D. R., Parsons, S. & Warren, J. E. (2008). *Journal of Applied Crystallography* **41**, 249-251.

Parsons, S. (2004). *SHADE- Program for empirical absorption corrections to high pressure data.* The University of Edinburgh, Edinburgh, United Kingdom.

Piermarini, G. J., Block, S., Barnett, J. D. & Forman, R. A. (1975). *Journal of Applied Physics* **46**, 2774-2780.

Prince, E. (1982). Mathematical Techniques in Crystallography and Materials Science. New York, USA: Springer-Verlag.

Sanchez-Cortes, S., Jancura, D., Miskovsky, P. & Bertoluzza, A. (1997). *Spectrochimica Acta Part A* **53**, 769-779.

Sheldrick, G. M. (2004). *SADABS Version 2004-1, Program for absorption corrections to area detector data.* Bruker-AXS, Madison, Wisconsin, USA.

Spek, A. L. (2004). *PLATON.* Utrecht University, Utrecht, The Netherlands.

Vinet, P., Ferrante, J., Rose, J. H. & Smith, J. R. (1987). *Journal of Geophysical Research* **92**, 9319-9325.

Vinet, P., Ferrante, J., Smith, J. R. & Rose, J. H. (1986). *Journal of Physics C: Solid State* **19**, L467-L473.

Wasserman, E. & Davies, R. E. (1959). *Journal of Chemical Physics* **30**, 1367.

Watkin, D. J. (1994). *Acta Crystallographica, Section A* **50**, 411-437.

Watkin, D. J., Pearce, L. & Prout, K. (1993). *CAMERON - A Molecular Graphics Package.* Chemical Crystallography Laboratory, University of Oxford, Oxford, England.

Wood, P. A., Forgan, R. S., Henderson, D., Parsons, S., Pidcock, E., Tasker, P. A. & Warren, J. E. (2006). *Acta Crystallographica, Section B* **62**, 1099-1111.

Wood, P. A., Haynes, D. A., Lennie, A. R., Motherwell, W. D. S., Parsons, S., Pidcock, E. & Warren, J. E. (2008). *Crystal Growth & Design* **8**, 549-558.

Chapter 7

Conclusion

7.1 Conclusion

The initial aim of this project was to investigate whether pressure could be used to force unusual crystal structures to conform to more conventional behaviour. The results indicate that in some cases it can. In all cases where a phase transition occurred, the need to pack more efficiently at pressure was a major contributor to the thermodynamic driving force of the transition.

The crystal structure of L-serine monohydrate at ambient conditions is unusual in terms of the orientation of water molecules, which are positioned between layers of serine. Application of pressure to the ambient phase resulted in a phase transition which was characterised by *i*) a reduction in the inter-layer separation, *ii*) a rearrangement of the zwitterion molecular geometry and *iii*) a change in the orientation of the water molecules to one which is more commonly observed in the CSD. PIXEL calculations have enabled the driving force of the transition to be pinpointed as the *PV* term in the equation for the free energy $G = U - TS + PV$.

The idea that a phase transition can be predicted on the basis of topology has been tested, and has been partially successful. The crystal structure of S-4-sulfo-L-phenylalanine monohydrate has the same topology as the ambient phase of serine hydrate. It undergoes a pressure-induced phase transition at 1 GPa which was also characterised by a rearrangement of the internal structure of the zwitterions and a change in the orientations of the water molecules, though as the transition occurs the layers move further apart instead of closer together. Inspection of the interstitial voids in the two phases indicates that, as in serine hydrate, the high-pressure phase is more efficiently packed than the ambient phase, and the *PV* term is an important factor in the driving force of the transition.

Application of pressure of methyl 2-(9H-carbazole-9-yl)benzoate, a structure with an unusually large number of molecules in the asymmetric unit ($Z' = 8$) resulted in a phase transition at 5 GPa. The high-pressure polymorph was determined to be a $Z' = 2$ structure. $Z' = 8$ structures comprise *ca.* 0.02% of the whole of the CSD, whilst ones with $Z' = 2$ represent *ca*. 7%. The transition resulted in a significant drop in the molecular volume, indicating that the *PV* term is important in the driving force of the transition. The molecular geometries in the high-pressure phase are less stable

than in the ambient pressure phase. As pressure is released on phase-II, the *PV* advantage diminishes, and the $Z' = 8$ structure is re-established.

We have re-determined the crystal structure of salicylamide at ambient conditions, which appears to be described with respect to a non-standard origin in previous determinations. Application of pressure to a single crystal grown at ambient conditions to 5 GPa does not result in a phase transition, though *in situ* crystal growth from solution resulted in the formation of a new polymorph at 0.2 GPa. PIXEL calculations show that the high–pressure phase is favoured by the *PV* contribution to the free energy (phase-II is denser than phase-I), the zero point energy and the entropy. We have also shown that the amount of reciprocal space that can be accessed during high-pressure data collection can be increased (in this case) three-fold by inclusion of multiple crystals in the sample chamber of a pressure cell.

Bianthrone changes colour from yellow to green on grinding, but this does not occur when a single crystal is subjected to hydrostatic pressure up to 6.5 GPa. This implies that the structure reacts differently to hydrostatic and non-hydrostatic conditions. A gradual colour change from yellow to orange was observed, which could be a result of changes in π…π stacking distances as the crystal compresses. PIXEL calculations indicate that the structure becomes significantly more strained as pressure is applied, however, the efficiency of packing is presumably enough to overcome any need for this strain to be relieved by a phase transition.